

VOLUME 11

NUMBER 1-2

2024

ISSN 2409-6121; eISSN 2522-1361

# Physical Sciences and Technology

National Nanotechnological Laboratory of Open Type  
Institute of Experimental and Theoretical Physics

Physical Sciences and Technology is publishing two number in a year by al-Farabi Kazakh National University, al-Farabi ave., 71, 050040, Almaty, the Republic of Kazakhstan  
website: <http://phst.kaznu.kz/>

Any inquiry for subscriptions should be send to:  
Gauhar Mussabek, al-Farabi Kazakh National University  
al-Farabi ave., 71, 050040, Almaty, the Republic of Kazakhstan  
e-mail: [gauharmussabek@gmail.com](mailto:gauharmussabek@gmail.com)

## SCOPE AND AIM

*Physical Sciences and Technology* provides an original paperback for the publication of peerreviewed research and review articles in all fields of Physics and related Technology. The topics, included in the scope, especially emphasize understanding of the physics underlying modern technology.

Subject areas may include, but are not limited to the following fields: Astronomy and Space Research, Theoretical Physics and Astrophysics, Plasma Physics and Related Technology, Chemical Physics and Related Technology, Condensed Matter Physics and Related Technology, Thermal physics and Related Technology, Nuclear Physics and Related Technology, Nanomaterials and Nanotechnology, Applied Atomic and Molecular Physics, Material Sciences and Related Technology, Electronics and Related Technology, Instrumentation, Photonics and Quantum Electronics, Signal processing.

The Journal is issued under the auspices of the National Nanotechnological Laboratory of Open Type and Institute of Experimental and Theoretical Physics and is published two times a year by the «Kazakh University» Publishing House. The International Editorial Board of the Journal consists of leading researchers from different countries of the world. The Journal is wide open for contributions that both lie at the far frontiers of contemporary physics and are particularly aimed at applications of the scientific principles of physics to modern technological problems.

## High-temperature analysis of silicon properties with manganese-oxygen binary complexes

M.O. Tursunov<sup>1\*</sup> , Kh.M. Iliev<sup>2</sup>  and B.K. Ismaylov<sup>3</sup> 

<sup>1</sup>Termez State University, Termez, Uzbekistan

<sup>2</sup>Tashkent State Technical University, Tashkent, Uzbekistan

<sup>3</sup>Karakalpak State University, Nukus, Uzbekistan

\*e-mail: m.tursunov@tersu.uz

(Received December 05, 2023; received in revised form April 16, 2024; accepted May 10, 2024)

The properties of KDB-5 grade silicon, including the concentration of electroactive manganese atoms, were studied after doping with manganese using the diffusion method in the temperature range of 1100–1300 °C. It was observed that as the diffusion temperature increased within this range, the concentration of electroactive manganese atoms decreased. At 1300 °C, the concentration of these atoms became significantly lower than that of the initial boron impurity. We propose that this behavior of manganese atoms may be due to the formation of electrically neutral quasi-molecular complexes between oxygen and manganese atoms located in neighboring lattice sites. During the formation of these electrically neutral complexes, tetrahedral cells of the  $\text{Si}_2\text{O}^{++}\text{Mn}^-$  type are created within the silicon lattice. These cells slightly disturb the lattice periodicity but are significantly different in properties from the elementary silicon cell. The chemical bond in these complexes is ionic-covalent, and the binding energy of the electron differs. As the concentration of these tetrahedral cells increases, various combinations can form, potentially leading to the creation of nanocrystals of a new phase with distinct fundamental parameters.

**Key words:** silicon, manganese diffusion, oxygen, electrically neutral complex, solubility, binding energy.  
**PACS number(s):** 61.46.+w.

### 1 Introduction

As is well known, thermal and radiation defects in silicon are primarily caused by optically active oxygen atoms. Therefore, controlling the state of oxygen atoms is of significant technological interest. Studying the interaction of nickel atoms with oxygen provides a useful model, as manganese atoms in silicon have a relatively high solubility ( $N \sim 10^{18} \text{ cm}^{-3}$ ) comparable to oxygen, and are mostly in an electrically neutral state [1-2]. The formation of electrically neutral  $\text{O}^{++}\text{Mn}^-$  type in the silicon lattice. These new unit cells exhibit properties that differ significantly from those of the silicon unit cell. The chemical bonds in these new structures are ionic-covalent, and the binding energy of the electrons differs as well. As the concentration of these unit cells increases, various combinations can form, potentially leading to the creation of nanocomplexes of a new phase with distinct fundamental parameters [3-5].

### 2 Materials and methods

Single-crystal p-type silicon with a resistivity of  $\rho=5 \Omega \cdot \text{cm}$ , obtained by the Czochralski method, was used as the starting material. The oxygen concentration in the samples was  $N_{\text{O}_2}=(5 \div 6) \cdot 10^{17} \text{ cm}^{-3}$ , and the dislocation density was  $S=10^3 \text{ cm}^{-2}$ . All samples underwent identical mechanical and chemical treatment. Manganese diffusion was carried out from the gas phase in evacuated quartz ampoules with a residual pressure of no more than  $P \sim 10^{-4} \text{ mm Hg}$ ; each ampoule contained two samples of both types of material [6-8]. The diffusion time ranged from  $t=0.5$  to 1 hour.

The electrical parameters of the samples were determined by the Hall effect method, and the photoelectric properties were measured using an IKS-14 installation equipped with a special cryostat. An SEM-MIRA-3 electron microscope was used for analysis. The results of the study indicated that the

samples were uniformly doped throughout their volume.

Manganese diffusion was carried out at a temperature of  $T=1300^{\circ}\text{C}$  and a diffusion time of 0.5 hours. The diffusion time was chosen in such a way as to ensure uniform doping of the samples throughout the entire volume. For all samples, the contacts were obtained by chemical nickel deposition.

### 3 Results and discession

We studied the effect of thermal annealing at specific temperatures for durations ranging from  $t=1$

to 10 hours, including oxidation in silicon (see Fig. 1). We examined the impact of thermal annealing for  $t=1$  to 10 hours on the parameters of control (initial) p-type samples with  $\rho=5 \Omega\cdot\text{cm}$  and on samples doped with Mn at  $T=1300^{\circ}\text{C}$ , which after doping had parameters close to the original. The results of these studies are presented in Figure 2. In the control (initial) samples annealed for more than  $t>5$  hours, an increase in resistivity is observed, indicating the generation of thermal donors (curve 1). Meanwhile, the electrical parameters of the manganese-doped samples remain practically unchanged (curve 2) [8-10].

Electrical parameters of the studied samples at  $T=300\text{K}$  are given in Table 1.

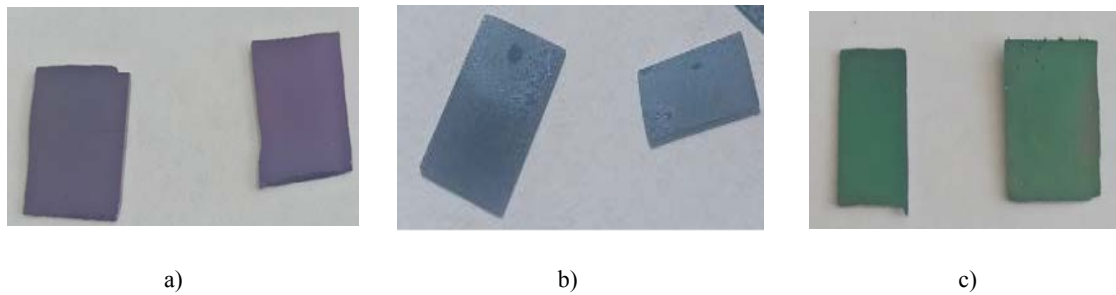


**Figure 1** – Oxidation at different temperatures in silicon:  
a)  $800^{\circ}\text{C}$ ; b)  $1100^{\circ}\text{C}$  and c)  $1300^{\circ}\text{C}$

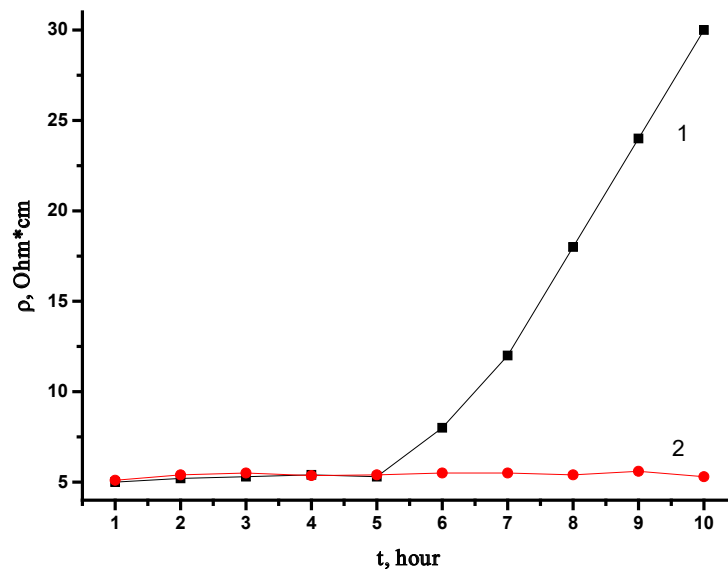


**Figure 2** – Effect of thermal annealing. 1-control (initial) samples,  
2-samples alloyed with Mn at  $T = 1300^{\circ}\text{C}$

**Table 1** – Values of electrical parameters of samples after diffusion at T=1300°C (vacuum P~10<sup>-6</sup> mm Hg, rapid cooling)

Si <B,Mn>				
Conductivity type	R <sub>x</sub> , 1/Ω•cm <sup>-1</sup>	ρ, Ω•cm	μ, cm <sup>2</sup> /V•s	p, cm <sup>-3</sup>
p	1,3•10 <sup>3</sup>	5÷7	260÷270	(3,5÷3,8)10 <sup>15</sup>
Control (Si<B>)				
Conductivity type	R <sub>x</sub> , 1/Ω•cm <sup>-1</sup>	ρ, Ω•cm	μ, cm <sup>2</sup> /V•s	p, cm <sup>-3</sup>
p	1,8•10 <sup>3</sup>	5,0	360	3,5•10 <sup>15</sup>

The oxygen content (concentration of optically active interstitial oxygen atoms N<sub>O</sub><sup>opt</sup>) was assessed using IR transmission spectra in the region of 1106 cm<sup>-1</sup> (9 μm) measured on an FSM-1202 infrared spectrometer at room temperature (see Fig. 3).

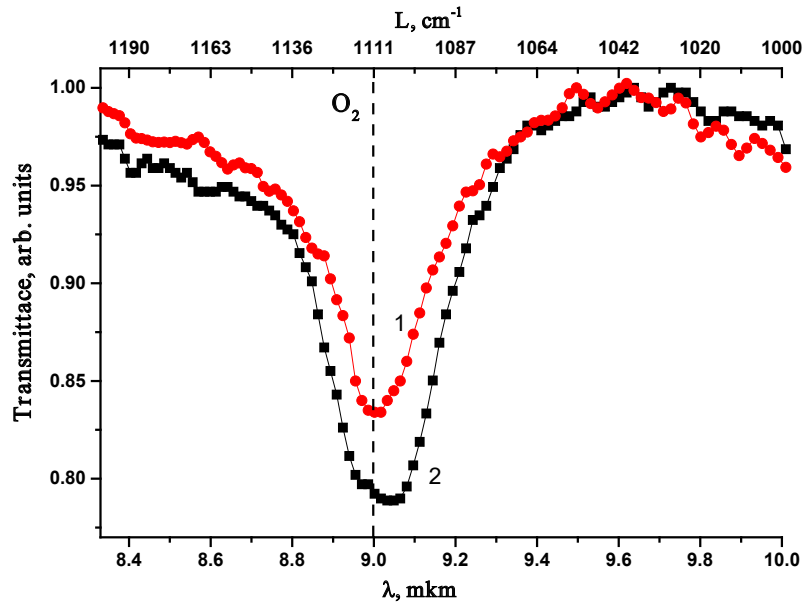


**Figure 3** – Dependence of the relative transmittance of the sample on the wavelength of the incident radiation. 1 – Si<Mn> 2 – control sample

Estimations of N<sub>O</sub><sup>opt</sup> were made using the well-known formula [11-12]:

$$N_o^{OPT} = 3.3 \cdot 10^{17} \cdot \frac{1}{d} \cdot \ln \frac{I}{I_0} \quad (1)$$

where I and I<sub>0</sub> are the intensities of incident and transmitted light, d is the thickness of the sample.

Using formula (1), we determined the concentration of optically active oxygen in silicon for the manganese-doped and control samples. Then we have:

1. Si < Mn >

$$N_o^{OPT} = 3.3 \cdot 10^{17} \cdot \frac{1}{d} \cdot \ln \frac{I}{I_0} = 2.5 \cdot 10^{17} \text{ cm}^{-3}$$

2. Si < control >

$$N_o^{OPT} = 3.3 \cdot 10^{17} \cdot \frac{1}{d} \cdot \ln \frac{I}{I_0} = 5.4 \cdot 10^{17} \text{ cm}^{-3}$$

$$3. N_o^{opt(control)} - N_o^{opt(Mn)} = 5.4 \cdot 10^{17} - 2.5 \cdot 10^{17} = 2.9 \cdot 10^{17} \text{ cm}^{-3}$$

The results show that the oxygen concentration decreases by a factor of 2.16. Therefore, it can be assumed that doping with manganese significantly reduces the amount of optically active oxygen.

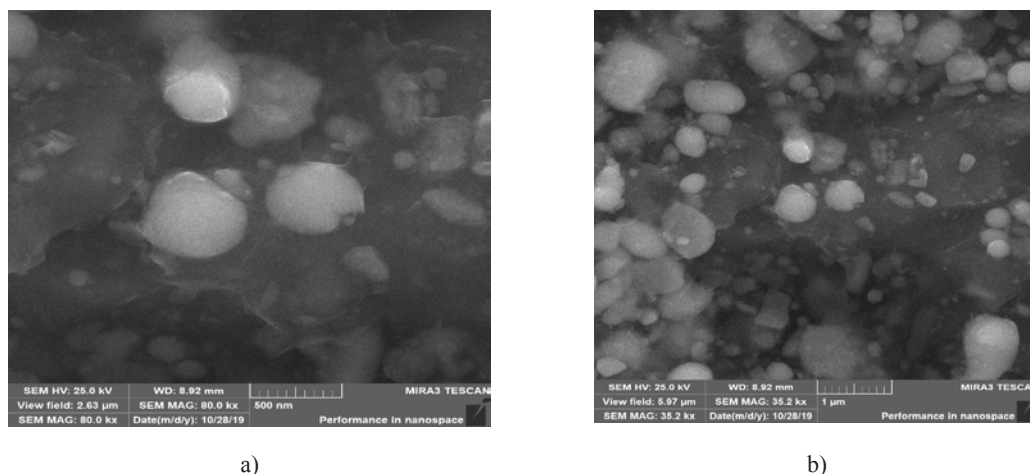


**Figure 4** – Electron diffraction patterns "for reflection" from a single-crystalline film of manganese oxide on silicon: a) at a resolution of 500 nm; b) at a resolution of 1  $\mu$ m

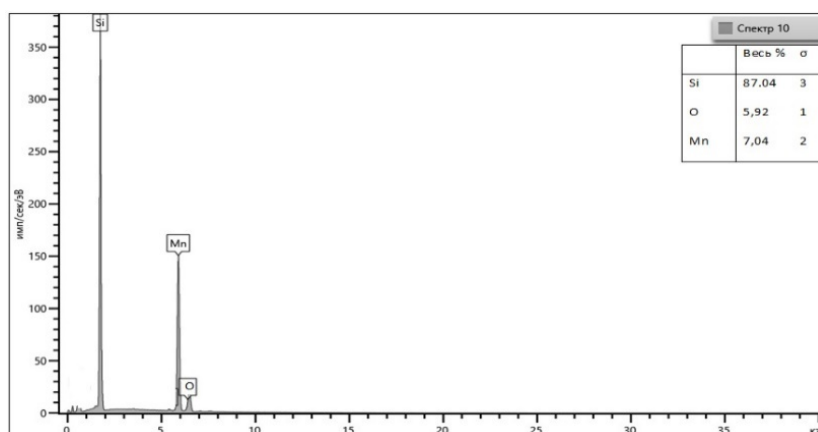


**Figure 5** – Electron diffraction patterns "for reflection" from a single-crystalline film of manganese and oxygen on silicon

#### 4 Consideration of the possible structures of manganese-oxygen complexes.

From a formal perspective, such formations can have the composition  $\text{Si}_k\text{Mn}^m\text{O}^n$ , where the value of  $k$  is determined by the need to integrate the complex into the tetrahedral silicon lattice, with different possible charge states for all atoms. In this scenario, the requirements of tetrahedral coordination of surrounding bonds within the lattice, the absence of mechanical stress, and the presence of electronic configurations in the constituent atoms that ensure stable chemical bonding must be met.

In the simplest case, where  $m=n=1$ , the manganese-oxygen complex can formally adopt structures such as  $\text{Mn}^{+2}\text{O}^{-2}$ ,  $\text{Mn}^{+1}\text{O}^{-1}$ ,  $\text{Mn}^0\text{O}^0$ ,  $\text{Mn}^{-1}\text{O}^{+1}$  and  $\text{Mn}^{-2}\text{O}^{+2}$ , supplemented with the required

number of silicon atoms ( $k$ ) to complete the lattice [13-15].

It is particularly important to emphasize that in such complexes, the conventional concepts of atomic valence and electronegativity may be altered. This is because the complex is not an isolated manganese-oxygen molecule or a crystal of such molecules, but rather a part of the silicon crystal lattice. Consequently, the system must achieve a minimum of free energy within the silicon lattice environment. The presence of the silicon lattice imposes additional requirements on the structure of the complexes: tetrahedral coordination of surrounding bonds within the lattice, absence of significant mechanical stress, and appropriate electronic configurations of the constituent atoms to ensure stable chemical bonds both within and around the complex.

1. *Structure of  $Mn^{+2}O^{-2}$* . The bond between atoms is ionic, consistent with their electronegativity values. This structure aligns with traditional concepts of the chemical bond between oxygen and metals. The sum of the ionic radii of  $O^{-2}$  (0.14 nm) and  $Mn^{+2}$  (0.083 nm) totaling 0.223 nm, closely matches the two covalent radii of silicon ( $2 \times 0.111$  nm), preventing lattice stress. However, the oxygen atom, with a fully completed (inert) outer shell, cannot effectively interact with the surrounding three silicon atoms, breaking these bonds. Even if two silicon bonds are closed to a neighbor, one broken bond remains, potentially detaching an electron and exhibiting electrical activity. Manganese in the  $Mn^{+2}$  state also has a stable outer shell, posing similar issues with external lattice bonds.

2. *Structure of  $Mn^{+1}O^{-1}$* . The bond between atoms is ionic, matching their electronegativity. The oxygen atom, with an incompletely filled (7-electron) outer shell, can interact effectively with one silicon atom, forming an oxygen-silicon ionic bond, while the other two bonds break. If two silicon bonds are closed to a neighbor, oxygen's electrical activity is absent. Manganese in the  $Mn^{+1}$  state also has one weakly bound electron and can form an ionic bond with one silicon atom, breaking the other two bonds. If two silicon bonds close to a neighbor, manganese's electrical activity is also absent.

3. *Structure of  $Mn^0O^0$* . The bond between atoms is potentially covalent, not matching their electronegativity values. In this case, the oxygen atom, with an incompletely filled (6-electron) outer shell, should exhibit acceptor properties towards surrounding silicon atoms. Manganese in the  $Mn^0$  state also lacks a stable outer shell, leading to issues with external bonds.

4. *Structure  $Mn^{-1}O^{+1}$* . The bond between atoms is ionic, not consistent with their electronegativity values. The oxygen atom, with an incompletely filled (5-electron) outer shell, can interact effectively with three silicon atoms, similar to a covalent bond, leaving two excess oxygen electrons that could create electrical activity. Manganese in the  $Mn^{-1}$  state also lacks a stable outer shell, introducing the possibility of electrical activity.

5. *Structure of  $Mn^{-2}O^{+2}$* . The bond between atoms is ionic, not matching their electronegativity values. The oxygen atom, with an incompletely filled (4-electron) outer shell, can interact effectively with three silicon atoms and manganese, forming an ionic-covalent bond. This configuration should avoid electrical activity. Manganese in the  $Mn^{-2}$  state also

has a 4-electron outer shell, allowing tetrahedral covalent bonds with neighbors without causing electrical activity.

The structure of site complexes between Mn atoms and Group VI elements in the silicon lattice is shown in Fig. 6. The distance between the atoms included in the complex differs slightly from the silicon-silicon distance in the lattice, since impurities during the formation of complexes are in site positions and are held in these positions by covalent bonds. Then distance = 2.27 Å.

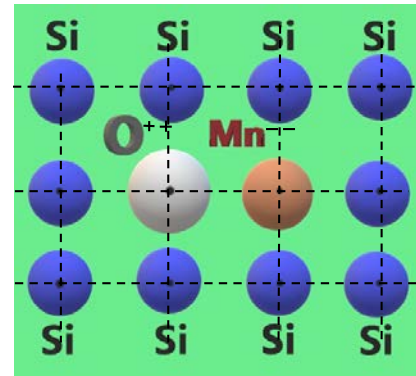


Figure 6 – Structure of site complexes between Mn atoms and Group VI elements in the silicon lattice

Calculated binding energy based on experimental results.

1)  $Si < MnO >$  dielectric constant of the interaction medium (silicon lattice) = 12. Considering the impurity-impurity bond to be ionic and taking the charge multiplicity equal to unity, we can estimate the force of attraction between the oxygen and manganese atoms [16-18]:

$$F_{MnO} = \frac{4kq^2}{\epsilon r_l^2} = 1,49 \cdot 10^{-9} \quad (2)$$

Where:  $q = 1.6 \cdot 10^{-19}$  C – electron charge, coefficient  $k = 9 \cdot 10^9 \frac{N \cdot m^2}{C^2}$

Then the minimum value of the binding energy between atoms in the complex can be estimated by the expression:

$$E_{MnO} = Fr_l = 1,49 \cdot 10^{-9} \cdot 2.34 \cdot 10^{-10} = 3,48 \cdot 10^{-19} J = 2.17 eV \quad (3)$$



$$2) \text{ For Si<MnS>} \\ \varepsilon = 12, r_l = 2,73 \text{ \AA}, q = 1.6 \cdot 10^{-19} \text{ C}, \\ k = 9 \cdot 10^9 \frac{N \cdot m^2}{C^2}; F_{MnS} = \frac{4kq^2}{\varepsilon r_l^2} = 1,03 \cdot 10^{-9} \quad (4)$$

$$E_{MnS} = Fr_l = 1,03 \cdot 10^{-9} \cdot 2,34 \cdot 10^{-10} = \\ = 2.41 \cdot 10^{-19} \text{ J} = 1,5 \text{ eV} \quad (5)$$

$$3) \text{ For Si<MnSe>} \\ \varepsilon = 12, r_l = 2,84 \text{ \AA}, q = 1.6 \cdot 10^{-19} \text{ C}, \\ k = 9 \cdot 10^9 \frac{N \cdot m^2}{C^2};$$

$$F_{MnSe} = \frac{4kq^2}{\varepsilon r_l^2} = 9,52 \cdot 10^{-10} \quad (6)$$

$$E_{MnSe} = Fr_l = 9,52 \cdot 10^{-10} \cdot 2,34 \cdot 10^{-10} = \\ = 2.2 \cdot 10^{-19} \text{ J} = 1,39 \text{ eV} \quad (7)$$

4) Si&lt;MnTe&gt;

$$\varepsilon = 12, r_l = 3.01 \text{ \AA}, q = 1.6 \cdot 10^{-19} \text{ C},$$

$$k = 9 \cdot 10^9 \frac{N \cdot m^2}{C^2}; F_{MnTe} = \frac{4kq^2}{\varepsilon r_l^2} = 8.5 \cdot 10^{-10} \quad (8)$$

$$E_{MnTe} = Fr_l = 8.5 \cdot 10^{-10} \cdot 2.34 \cdot 10^{-10} = \\ = 1.98 \cdot 10^{-19} \text{ J} = 1,24 \text{ eV} \quad (9)$$

$$E_{MnO} \sim 2,17 > E_{MnS} \sim 1,5 > E_{MnSe} \sim 1,39 > E_{MnTe} \sim 1,24$$

The concentrations of Mn impurity atoms, group VI elements and their complexes are shown in Table 3 [19-20].

**Table 2** – Binding energies between Mn atoms and Group VI elements in the silicon lattice, calculated from the Coulomb interaction

Binary complexes	Minimum binding energy $E$ , eV
Si <sub>2</sub> O <sup>++</sup> Mn <sup>-</sup>	2,17
Si <sub>2</sub> S <sup>++</sup> Mn <sup>-</sup>	1,5
Si <sub>2</sub> Se <sup>++</sup> Mn <sup>-</sup>	1,39
Si <sub>2</sub> Te <sup>++</sup> Mn <sup>-</sup>	1,24

**Table 3** – Concentrations of impurity Mn atoms, group VI elements and their complexes

$t, ^\circ\text{C}$	$C_{Mn}, \text{cm}^{-3}$	$C_O, \text{cm}^{-3}$	$C_{MnO}, \text{cm}^{-3}$	$N_s, \text{cm}^{-3}$
1300	$2 \cdot 10^{16}$	$5 \cdot 10^{17}$	$4 \cdot 10^{16}$	$5 \cdot 10^{22}$
$t, ^\circ\text{C}$	$C_{Mn}, \text{cm}^{-3}$	$C_S, \text{cm}^{-3}$	$C_{MnS}, \text{cm}^{-3}$	$N_s, \text{cm}^{-3}$
1100	$1,5 \cdot 10^{16}$	$5 \cdot 10^{16}$	$4 \cdot 10^{15}$	$3 \cdot 10^{22}$
$t, ^\circ\text{C}$	$C_{Mn}, \text{cm}^{-3}$	$C_{Se}, \text{cm}^{-3}$	$C_{MnSe}, \text{cm}^{-3}$	$N_s, \text{cm}^{-3}$
1250	$2 \cdot 10^{16}$	$1 \cdot 10^{17}$	$1 \cdot 10^{15}$	$2,5 \cdot 10^{22}$
$t, ^\circ\text{C}$	$C_{Mn}, \text{cm}^{-3}$	$C_{Te}, \text{cm}^{-3}$	$C_{MnTe}, \text{cm}^{-3}$	$N_s, \text{cm}^{-3}$
1250	$2 \cdot 10^{16}$	$5 \cdot 10^{17}$	$1 \cdot 10^{15}$	$2,5 \cdot 10^{22}$

In this table:

$T$  – complexation temperature for complex formation Si<sub>2</sub>Mn<sup>-</sup>B<sup>VI++</sup>.

$C_{Mn}$  – solubility of manganese at a given diffusion temperature.

$C_O$  – solubility of group VI elements at a given diffusion temperature.

$C_{MnO}$  – concentration of complexes of group VI elements and manganese.

$N_s$  – atomic concentration.

Using the Arrhenius equation written for the equilibrium between complexes and individual impurity atoms at temperature  $T$ , we can write [21-22]

$$\frac{d \ln \alpha}{dT} = \frac{E_a}{RT^2} \quad (10)$$

$$\begin{aligned} E_{\text{MnO}} &\sim 1,46 \text{ eV} > E_{\text{MnS}} \sim 1,24 \text{ eV} > \\ &> E_{\text{MnSe}} \sim 1,09 \text{ eV} > E_{\text{MnTe}} \sim 0,87 \text{ eV} \end{aligned}$$

$$E_a = kT \ln \left( \frac{N \cdot C_{AB}}{4C_A C_B} \right) \quad (11)$$

It should be noted that the binding energy in complexes decreases with increasing sizes of Group VI element atoms.

**Table 4** – Binding energies between Mn atoms and Group VI elements in the silicon lattice, calculated using the Arrhenius equation

Binary complexes	Binding energy, $E$ , eV
$\text{Si}_2\text{O}^{++}\text{Mn}^-$	1,46
$\text{Si}_2\text{S}^{++}\text{Mn}^-$	1,24
$\text{Si}_2\text{Se}^{++}\text{Mn}^-$	1,09
$\text{Si}_2\text{Te}^{++}\text{Mn}^-$	0,87

The patterns of decreased binding energy in complexes involving Mn and Group VI elements (O, S, Se, Te), as calculated from Coulomb interactions, align with the Gibbs energy trends [23-25]. Additionally, the calculated binding energies, using experimental values for the concentration of impurities and complexes, confirm this decrease in binding energy. From the analysis of experimental data and numerical calculations, we can conclude that the physical model of complex formation between manganese and Group VI element atoms is generally accurate.

## 5 Conclusions

Based on the results obtained, we propose a model for the formation of electrically neutral molecules resulting from the interaction between manganese and oxygen atoms. This model considers both lattice site and interstitial arrangements of manganese and oxygen atoms. The resulting silicon material contains a relatively high concentration  $N \sim (3 \div 4) \cdot 10^{16} \text{ cm}^{-3}$  of tetrahedral cells of the  $\text{Si}_2\text{O}^{++}\text{Mn}^-$  type in the silicon lattice, which is of significant scientific and practical interest.

Research into methods to increase the concentration of these binary cells and explore their properties could pave the way for creating a new class of silicon-based materials for optoelectronic and

photoelectric devices. Silicon enriched with binary cells of the  $\text{Si}_2\text{Mn}^- \text{B}^{\text{VI}++}$  type holds the potential to facilitate the development of innovative optoelectronic and nanoelectronic devices, as well as highly efficient silicon-based solar cells with parameters comparable to or better than those of expensive multi-stage photocells based on AIIIBV materials.

The diffusion conditions allow for a significant increase in the concentration of electroactive manganese atoms, thereby enhancing the described phenomena and expanding the functionality of manganese-doped silicon in optoelectronics and spintronics. Consequently, developing technology to boost the concentration of these binary cells in silicon is of great scientific and practical interest. This advancement could lead to the future creation of a new class of silicon-based materials for optoelectronic and photoelectric devices.

## Acknowledgements

The work was financially supported by the Ministry of Innovative Development of the Republic of Uzbekistan within the framework of the project F-OT-2021-497 – “Development of the scientific foundations for the creation of solar cogeneration plants based on photovoltaic thermal batteries”.

## References

1. Milvidsky M.G., Chaldyshev V.V. Nanosized atomic clusters in semiconductors – a new approach to the formation of material properties // *Physics and technology of semiconductors*. – 1998. – Vol. 32. – no. 5. – P. 513-522. <https://doi.org/10.1134/1.1187418>
2. Zainobiddinov S. Physical foundations of the formation of deep levels in silicon // *Tashkent, Fan* – 1984. – P. 160.
3. Boltaks B.I. Diffusion and point defects in semiconductors // *Science, Leningrad* – 1972. – P. 384.
4. Boltaks B.I., Bakhadirkanov M.K., Gorodetsky S.M., Kulikov G.S. Compensated silicon // *Leningrad, Nauka* – 1972. – P. 122.
5. Bakhadyrkhanov M.K., Isamov S.B., Zikrillayev N.F., Tursunov M.O. Anomalous photoelectric phenomena in silicon with nanoclusters of manganese atoms // *Semiconductors*. – 2021. Vol. 55. – No. 6. – P. 636–639. <https://doi.org/10.1134/s1063782621060038>
6. Ismailov K.A., Iliev X.M., Tursunov M.O., Ismaylov B.K. Formation of complexes consisting of impurity Mn atoms and group VI elements in the crystal lattice of silicon. // *Semiconductor Physics, Quantum Electronics & Optoelectronics*. – 2021. – Vol. 24. – No. 3. – P. 255–260. <http://dx.doi.org/10.15407/spqeo24.03.255>
7. Ismailov, K.A., Kenzhaev, Z.T., Koveshnikov, S.V., Kosbergenov, E.Z., Ismaylov, B.K. Radiation Stability of nickel doped solar cells // *Physics of the Solid State*. – 2022. – Vol. 64(3). – P. 154–156. <https://doi.org/10.1134/S1063783422040011>
8. Zikrillayev, N.F., Mavlonov, G.Kh., Trabzon, L., Koveshnikov S.V., Kenzhaev Z.T., Ismailov, T.B., Abduganiev, Y.A., Magnetic properties of silicon with paramagnetic impurity atoms // *East European Journal of Physics*. – 2023. Vol.15(6). – P. 380–384. [http://dx.doi.org/10.21272/jnep.15\(6\).06001](http://dx.doi.org/10.21272/jnep.15(6).06001)
9. Ismaylov, B.K., Zikrillayev, N.F., Ismailov, K.A., Kenzhaev, Z.T. Clusters of impurity nickel atoms and their migration in the crystal lattice of silicon // *Physical Sciences and Technology* – 2023. – Vol.10(1). – P. 13–18; <https://doi.org/10.26577/phst.2023.v10.i1.02>
10. Zikrillayev, N.F., Isamov, S.B., Koveshnikov, S.V., Kenzhaev, Z.T., Turekeev, K.S. Codiffusion of gallium and phosphorus atoms in silicon // *Surface Engineering and Applied Electrochemistry*.- 2023. – Vol.59(2).- P. 210–215. <https://doi.org/10.3103%2Fs1068375523020199>
11. M.K. Bakhadirkanov, Kh.M. Iliev, M.O. Tursunov, S.B. Isamov, S.V. Koveshnikov, M.Kh. Majitov. Electrical properties of silicon doped with manganese via high-temperature diffusion // *Inorganic Materials* – 2021. – Vol. 57. – No. 7. – P. 655-662. <https://doi.org/10.1134/S0020168521070013>
12. Nakashima H., Hashimoto K. Deep impurity levels and diffusion coefficient of manganese in silicon // *J. Appl. Phys.* – 1991. – Vol. 69. – № 3 – P. 1440-1445. <https://doi.org/10.1063/1.347285>
13. Bakhadyrkhanov, M.K., Kenzhaev, Z.T. Optimal conditions for nickel doping to improve the efficiency of silicon photoelectric cells // *Technical Physics*. – 2021. – Vol. 66(7). P. 851–856. <https://doi.org/10.21883/JTF.2021.06.50868.332-20>
14. Bakhadyrkhanov, M.K., Isamov, S.B., Kenzhaev, Z.T., Koveshnikov, S.V. Studying the effect of doping with nickel on silicon-based solar cells with a deep p–n-junction // *Technical Physics Letters*.- 2019.- Vol. 45(10). P. 959–962. <http://dx.doi.org/10.1134/S1063785019100031>
15. Bakhadyrkhanov, M.K., Isamov, S.B., Kenzhaev, Z.T., Melebaev D., Zikrillayev, Kh.F., Ikhtiyarova, G.A. Silicon photovoltaic cells with deep p–n-junction // *Applied Solar Energy (English translation of Geliotekhnika)*. – 2020.- Vol. 56(1).- P. 13–17. <https://doi.org/10.3103/S0003701X2001003X>
16. Bakhadyrkhanov M.K., Iliev Kh.M., Sattorov O.E., Ismailov K.A., Saparniyazova Z.M., Norkulov N., Asanov D. Zh. Interaction between multiply charged manganese nanoclusters and sulfur atoms in silicon // *Inorganic Materials*. – 2012. – V.48. – № 3. – P.325-328. <http://dx.doi.org/10.1134/S0020168515070031>
17. Zainabidinov, S.Z., Musayev, K.N., Turgunov, N.A. et al. Dopant micro association mechanisms in Si ⟨Mn⟩ and Si ⟨Ni⟩ // *Inorganic Materials*. – 2012. – V.48. – P. 1065–1069. <https://doi.org/10.1134/S0020168512110192>
18. Bakhadyrkhanov, M.K., Kenzhaev, Z.T., Koveshnikov, S.V., Usmonov, A.A., Mavlonov, G.K. Formation of complexes of phosphorus and boron impurity atoms in silicon // *Inorganic Materials*. – 2022. Vol. 58(1). <https://doi.org/10.1134/S0020168522010034>
19. Taskin A.A., Tishkovsky E.G. Formation of complexes associated with selenium atoms in silicon // *Physics and Technology of Semiconductors*. – 2002. Vol. 36(6), P. 641-649. <https://doi.org/10.1134/1.1485656>
20. Iliev Kh.M., Tursunov M.O., Koveshnikov S.V., Khudaynazarov Z.B. Research of properties of silicon with binary nanoclusters with participation of Mn and Se atoms // *Semiconductor Physics and Microelectronics*. – 2020. – Vol. 2. – Is 2. – P. 59-62. <https://doi.org/10.5281/zenodo.100096>
21. Weixin Ouyang, Feng Teng, Jr-Hau He, Xiaosheng Fang. Enhancing the photoelectric performance of photodetectors based on metal oxide semiconductors by charge-carrier engineering // *Adv. Funct. Mater.* – 2019. – Vol.29(9). <http://dx.doi.org/10.1002/adfm.201807672>
22. R. Mainz, A. Singh, S. Levchenko, M. Klaus, C. Genzel, K.M. Ryan, T. Phase-transition-driven growth of compound semiconductor crystals from ordered metastable nanorods // *Nature Communications*. – 2014. – Vol. 3133. <https://doi.org/10.1038/ncomms4133>
23. Bakhadyrkhanov M.K., Askarov Sh.I, and Norkulov N. Some features of chemical interaction between a fast diffusing impurity and a group VI element in silicon. // *Physics state solid*. – 1994. – No. 142. – P. 339-346. <https://doi.org/10.1002/pssa.2211420206>
24. Glushko V.P. Thermodynamic constant for materials // *Issue. 7 – Pt 1, Nauka, Moscow* -1974.
25. Björk M. T., Schmid H., Knoch J., Riel H., Riess W. Donor deactivation in silicon nanostructures // *Nature Nanotechnology*.- 2009. -Vol. 4. – P. 103-107. <https://doi.org/10.1038/nnano.2008.400>

**Information about authors:**

*Tursunov Mamasobir Ochildiyevich (corresponding author), PhD in physical and mathematical sciences, is an Associate professor at Termez State University, (Termez, Uzbekistan) e-mail: mtursunov@tersu.uz;*

*Iliev Khalmurat Midzhitovich, Doctor of Physical and Mathematical Sciences, is a Professor at Tashkent State Technical University (Tashkent, Uzbekistan) e-mail: xolmurodov.iliev@tdtu.uz;*

*Ismaylov Bayrambay Kanatbaevich, PhD in physical and mathematical sciences, is a DSc student at Karakalpak State University (Nukus, Uzbekistan) e-mail: i.bairam@bk.ru*

## Physical mechanisms of gettering properties of nickel clusters in silicon solar cells

Z.T. Kenzhaev<sup>1\*</sup>, Kh.M. Iliev<sup>1</sup>, K.A. Ismailov<sup>2</sup>, G.Kh. Mavlonov<sup>1</sup>,  
S.V. Koveshnikov<sup>1</sup>, B.K. Ismaylov<sup>1</sup> and S.B. Isamov<sup>1</sup>

<sup>1</sup>Tashkent State Technical University, Tashkent, Uzbekistan

<sup>2</sup>Karakalpak State University, Nukus, Uzbekistan

\*e-mail: zoir1991@bk.ru

(Received December 03, 2023; received in revised form April 13, 2024; accepted April 27, 2024)

This study demonstrates that the concentration of nickel atoms near the surface of solar cells is 2–3 orders of magnitude higher than in the bulk material, significantly enhancing the gettering rate at the surface. Using IR-microscopy, SEM, and SIMS, we found that the surface density of nickel clusters is approximately  $10^6$ – $10^7$  cm<sup>-2</sup>, with an average cluster diameter of 20–100 nm and a cluster concentration of  $10^{11}$ – $10^{15}$  cm<sup>-3</sup>. Experimental results revealed that nickel clusters on the surface of silicon samples contain a substantial amount of oxygen and recombination impurities (Cu, Fe, Cr), indicating excellent gettering properties. We identified the physical mechanisms underlying the effects of nickel impurity atom diffusion and additional thermal annealing on the state of nickel atoms near the surface and base of the solar cells. Physical models were developed for the structure of nickel atom clusters in silicon and for the gettering process of fast-diffusing impurities by these clusters. The binding energy of fast-diffusing impurity atoms with a nickel cluster was estimated to be approximately 1.39 eV. Calculations indicated that nickel doping can increase the lifetime of minority charge carriers by a factor of 2–4, and experimental results confirmed an increase in the lifetime of minority charge carriers by up to a factor of 2. These findings highlight the potential of nickel doping to enhance the performance and efficiency of silicon-based solar cells, offering a promising avenue for future research and development in photovoltaic technology.

**Key words:** silicon solar cell, diffusion, nickel clusters, recombination centers, gettering, minority carrier lifetime, binding energy.

**PACS number(s):** 61.46.+w.

### 1 Introduction

In modern industrial production of solar cells (SCs), there is a trend toward increasing the use of solar-grade silicon due to its lower cost [1]. However, solar-grade silicon has a shorter minority carrier lifetime, making it challenging to achieve high conversion efficiency [2, 3]. To enhance the efficiency of silicon SCs, it is necessary to increase the collection coefficient and the lifetime of photogenerated charge carriers [4, 5], and to reduce optical and electrical energy losses [6]. Increasing the minority carrier lifetime in SCs [7, 8] can be achieved through the gettering of recombination centers by nickel clusters.

The effectiveness of complex formation and gettering processes depends significantly on the mobility of impurity atoms in the lattice and their

binding energy with the getter [9–11]. Therefore, an important task is to assess the structure of nickel clusters and the binding energy of impurity atoms with these clusters [12–15].

In work [16], the mechanisms and basic methods for obtaining atomic clusters were studied, and the possibilities for controlling the properties of cluster materials were analyzed. The physical essence of cluster formation in semiconductors is the system's tendency to achieve a state with minimal free energy, i.e., gradually restoring equilibrium.

Works [17, 18] investigate changes in the size and density of nickel clusters depending on the annealing temperature ( $T=650$ – $900$  °C) and cooling rate. It was found that as the annealing temperature decreases, cluster density decreases while their size increases. Similarly, a decrease in the cooling rate leads to a reduction in cluster density and an increase

in size. Using IR microscopy, studies [19, 20] discovered the self-organization of nickel clusters in a silicon lattice under conditions of diffusion doping and additional thermal annealing.

Nickel clusters easily form during both diffusion and additional thermal annealing, but they have minimal impact on the electrical parameters of the material itself during thermal annealing in the temperature range of  $T = 400\text{--}1000\text{ }^{\circ}\text{C}$  [21, 22].

While the above studies focused on nickel clusters in bulk silicon, they did not explore the formation of nickel clusters in the near-surface nickel-enriched region of silicon. For small clusters, the surface's contribution to the system's free energy change is significant, and the influence of elastic deformation increases with cluster size. Rigorous quantitative assessments of these effects are challenging because they require accurate cluster models. Therefore, as mentioned in [16], the concepts of “crystal lattice” or “surface” of a cluster are often used arbitrarily.

If clusters of nickel atoms possess gettering properties and can remove harmful impurities from the crystal, they positively affect the efficiency of solar cells (SCs). Based on this, it is assumed that additional doping of silicon SCs with nickel atoms should increase their efficiency by extending the minority carrier lifetime.

Systematic research into the effect of nickel impurity clusters on the parameters of silicon SCs is of significant practical interest, as nickel shows great promise due to the technological advantages of doping [23–25]. From a technological perspective, the deposition of a nickel metal layer onto the silicon surface can be achieved chemically [26, 27], allowing simultaneous processing of multiple wafers. Additionally, the diffusion of nickel atoms can be performed in open air at relatively low temperatures ( $T_{\text{diff}} = 800\text{--}850^{\circ}\text{C}$ ). Consequently, the method of doping silicon with nickel atoms from a chemically deposited layer can be seamlessly integrated into existing industrial SC production processes.

However, models of nickel clusters are currently lacking, and the physical mechanisms by which nickel atom clusters affect the parameters of silicon SCs remain unclear. The purpose of this study was to demonstrate the effectiveness of introducing nickel impurities into silicon wafers used in photovoltaic converters, to elucidate the physical mechanisms by which nickel clusters influence the lifetime of minority charge carriers in silicon SCs, and to develop an appropriate physical model.

## 2 Methods and materials

To study the formation of clusters and silicides on the surface due to high nickel concentrations, the following investigations were carried out. The wafers were obtained using the Czochralski method, with a resistivity of  $0.5\text{ }\Omega\cdot\text{cm}$ , a thickness of  $380\text{ }\mu\text{m}$ , a minority carrier lifetime ( $\tau$ ) greater than  $6\text{ }\mu\text{s}$ , an oxygen content of approximately  $N_{\text{O}_2} \sim 7 \times 10^{17}\text{ cm}^{-3}$ , and a dislocation density ( $N$ ) less than  $10^2\text{ cm}^{-2}$ . In a vacuum, a layer of pure nickel  $1\text{ }\mu\text{m}$  thick was deposited onto the surface of the samples. Diffusion was carried out at  $T_{\text{diff}} = 800\text{--}950\text{ }^{\circ}\text{C}$  for 30 to 60 minutes, and at  $T_{\text{diff}} = 1000\text{--}1200\text{ }^{\circ}\text{C}$  for 5 to 60 minutes in an air atmosphere, followed by air cooling (without a boat). After diffusion, additional thermal annealing was conducted at  $T_{\text{ann}} = 700\text{--}900\text{ }^{\circ}\text{C}$  for 30 to 60 minutes in an air atmosphere ( $\sim 50\text{--}60\text{ }^{\circ}\text{C/s}$ ) to activate the gettering process of uncontrolled recombination impurities [26–28].

After each technological stage, chemical treatment was performed to remove residues of metallic nickel and silicon oxide from the surface (using a 3:1 mixture of HCl and HNO<sub>3</sub>, followed by 49% HF and a water rinse). The surface was then cleaned with a hydrogen peroxide–ammonia solution. The samples were not ground or polished.

To study the formation of nickel clusters in silicon and their parameters, silicon samples doped with nickel were examined using an INFRAM-I infrared microscope and a scanning electron microscope. The elemental composition of nickel clusters in the samples was analyzed using a TESCAN MIRA3 scanning electron microscope in X-ray microanalysis mode. Measurements were taken on both the front surface and the fracture surface of the samples. The fracture surfaces were scanned with a step size of  $0.5\text{ }\mu\text{m}$ , starting from the front side (the side doped with nickel).

## 3 Results

Previously [26], the distribution of nickel atoms in the near-surface layer of silicon after diffusion was measured with a CAMECA IMS-6f Magnetic Sector SIMS mass spectrometer. It was found that the surface concentration of nickel reaches approximately  $n_s \approx (2\text{--}4) \times 10^{21}\text{ cm}^{-3}$ , the thickness of the enriched layer is about  $d \sim 2\text{--}3\text{ }\mu\text{m}$ , and nickel is distributed almost uniformly throughout the bulk with a concentration of  $n_{\text{Ni}} \approx 10^{16}\text{--}7 \times 10^{17}\text{ cm}^{-3}$ , which confirms the published results [29].

The sizes of nickel atom clusters in the obtained samples were measured with a TESCAN MIRA 3 scanning electron microscope (see Fig. 1).

Based on the obtained results (IR microscopy, SEM, and SIMS), it was found that the surface density of nickel clusters is approximately  $5 \times 10^6 - 10^7 \text{ cm}^{-2}$  on the front surface and about  $(4-5) \times 10^6 \text{ cm}^{-2}$  in the bulk of the material. The distribution of clusters in the bulk is nearly uniform, and their size is less than  $0.5 \mu\text{m}$  (approximately 20–100 nm).

These findings confirm the results of the previous studies [16, 28, 29]. It should be noted that these results were observed at all studied diffusion temperatures within the range of annealing temperatures of  $T_{\text{ann}} = 800-900^\circ\text{C}$ . Based on the obtained data, the concentrations of clusters ( $n_k$ ) were calculated to be approximately  $10^{11}-10^{13} \text{ cm}^{-3}$  in the bulk of the sample and approximately  $10^{13}-10^{15} \text{ cm}^{-3}$  in the nearsurface region enriched with nickel.

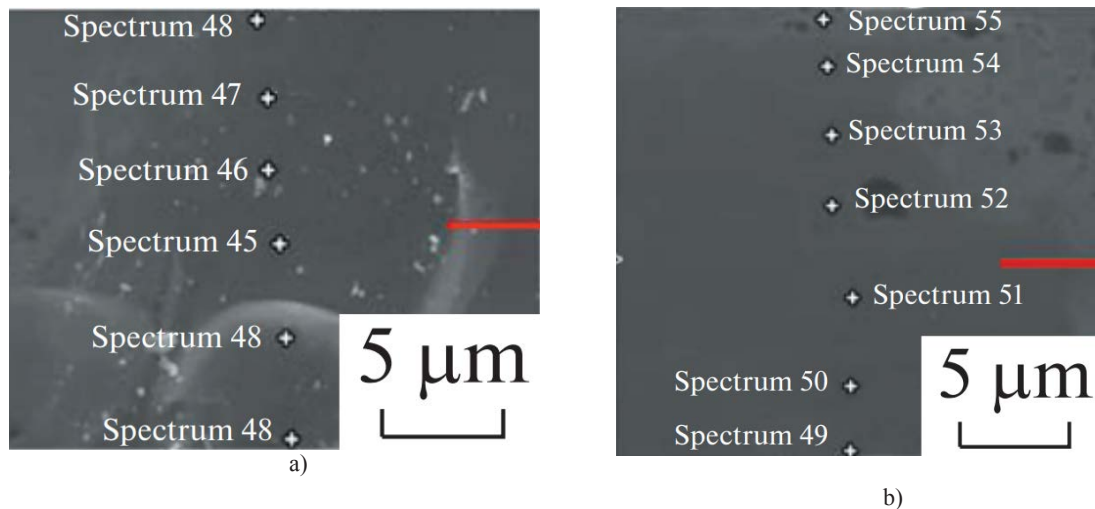


**Figure 1** - Images of the investigated points and clusters of nickel atoms in the bulk (a) and on the surface (b) of the samples after additional thermal annealing at  $T_{\text{ann}} = 800^\circ\text{C}$

Changes in the size and state of nickel atom clusters in silicon were observed after additional thermal annealing. Annealing in the temperature range of  $T_{\text{ann}} = 650-800^\circ\text{C}$  led to the coarsening of nickel clusters, while at  $T_{\text{ann}} > 900^\circ\text{C}$ , the clusters underwent decomposition.

The measurement of the cluster composition revealed that clusters (Fig. 2) on the surface of silicon primarily consist of silicon atoms (~84–86%) and nickel atoms (~13–15%). However, they also contain traces of copper (Cu), iron (Fe), chromium (Cr), and other elements [27]. This demonstrates the efficient gettering of harmful impurities by nickel clusters, which act as recombination centers in silicon. This can lead to a significant increase in the lifetime of minority charge carrier primarily due to the formation of nickel clusters in the near-surface layers.

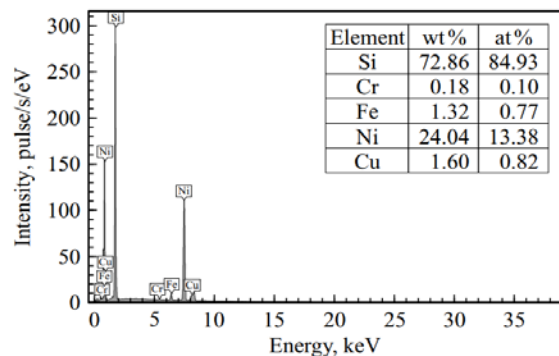


**Figure 2** - Impurity atoms clusters composition observed through probe elementary analysis using the scanning electron microscope TESCAN MIRA 3

Using the same method, we determined the composition of nickel clusters after the additional thermal treatment ( $T_{\text{ann}} = 800^\circ\text{C}$ ,  $t = 30 \text{ min}$ ). It was

found that, after the annealing, the concentration of nickel atoms increased by about 40–60%, oxygen, by approximately 30–35%, and fast-diffusing impurities (FDI), by about 30–50%, in comparison with the values before annealing. This demonstrates the efficient gettering of uncontrolled impurities by nickel clusters during the additional thermal annealing.

As the diffusion temperature increases, the solubility of nickel atoms in silicon also increases [30], leading to an increase in the concentration of clusters [20–22] and a decrease in the concentration of recombination centers (Cr) [28]. However, as a rule, with an increase in temperature and duration of diffusion, Cr increases [8, 31]; consequently, the lifetime of minority charge carriers ( $\tau$ ) decreases, which reduces the efficiency of SCs.

Furthermore, for the formation of the front-side  $p$ – $n$  junction of SCs, diffusion is typically carried out in the temperature range of  $T_{\text{diff}} = 900$ – $1050^\circ\text{C}$ , which invariably leads to an increase in  $C_r$  and a reduction in  $\tau$  by several times [3]. Therefore, it is necessary to optimize the technological conditions for gettering recombination defects by nickel atom clusters.

It was demonstrated [27] that the enhancement of the efficiency of the SC is significantly contributed by the nickel-atom-enriched near-surface region of the SC. Additionally, it was shown that doping SCs with nickel atoms increases the carrier lifetime regardless of the method of introduction, and under optimal conditions, it can extend the carrier lifetime to 30–32  $\mu\text{s}$  (up to double that of the reference SC, which has a carrier lifetime of 14–16  $\mu\text{s}$ ).

Thus [23–27], the optimal conditions for gettering with nickel atom clusters have been experimentally determined (nickel diffusion conditions –  $T_{\text{diff}} = 800$ – $850^\circ\text{C}$ , additional thermal annealing –  $T_{\text{ann}} = 750$ – $800^\circ\text{C}$ ), which can increase the efficiency of silicon SCs by 25–30%.

## 4 Discussion

### 4.1 Physical Model of the Structure of a Nickel Atom Cluster

During cooling after diffusion, nickel atoms in silicon form nuclei of clusters, and additional thermal annealing activates the processes of cluster formation and growth [16]. According to our measurements [26], nickel clusters primarily consist of silicon atoms and contain up to ~15% nickel atoms. Considering the high lability [28, 29] of nickel in clusters, it can be assumed that nickel atoms in clusters are in

interstitial states ( $\text{Ni}_i$ ) and do not form silicides. Electroneutral nickel atoms in clusters are in the nearest equivalent interstitial positions and form a cubic nickel sublattice, partially or completely filled.

The  $\text{Ni}_i$  configuration with the lowest energy is in a tetrahedral interstitial position [16] with a very small change in the lattice constant (displacement of the four nearest Si neighbor's outward). The  $\text{Ni}_i$ –Si distance is 2.438 Å, while the distance between lattice atoms in the ideal silicon crystal is 2.367 Å. The population of the overlap in Ni–Si bonds is very low [7, 16], indicating minimal covalent interactions between  $\text{Ni}_i$  and Si atoms. Therefore, the binding forces between the silicon lattice and interstitial nickel atoms are weak, and the lattice has little effect on the nickel–nickel interaction within the cluster. It is most likely that the bonds between nickel atoms in the cluster are predominantly of a metallic nature. Metallic bonding explains the optical opacity of the clusters [20, 28, 31] and their high conductivity [14, 32].

Let us estimate the distance  $R_{\text{Ni–Ni}}$  between nickel atoms in clusters (Figure 3 and Figure 4) based on the silicon lattice geometry (silicon lattice constant  $a = 5.43$  Å, distance between silicon atoms  $R_{\text{Si–Si}} = 2.34$  Å, angle  $\alpha = 109^\circ$  [33]):

$$R_{\text{Ni–Ni}} = a \cdot \frac{\sqrt{2}}{2} \quad \text{or} \\ R_{\text{Ni–Ni}} = 2R_{\text{Si–Si}} \cdot \sin\left(\frac{\alpha}{2}\right) = 3.84 \text{ \AA}, \quad (1)$$

We also determined the distance  $R_{\text{Si–Ni}}$  from the interstitial nickel atom to silicon atoms in the lattice:

$$R_{\text{Si–Ni}} = \sqrt{\left(\frac{R_{\text{Si–Si}}}{2}\right)^2 + \left(\frac{\sqrt{2} \cdot R_{\text{Ni–Ni}}}{2}\right)^2} = 3.2 \text{ \AA}. \quad (2)$$

It was found that one unit cell of silicon contains four interstitial nickel atoms ( $N_{\text{Ni}} = 4$ ) and eight silicon atoms ( $N_{\text{Si}} = 8$ ). Therefore, the maximum possible concentration  $C_{\text{lim}}$  of nickel atoms in clusters is

$$C_{\text{lim}} = C_{\text{Si}} \cdot \frac{N_{\text{Ni}}}{N_{\text{Si}}} = 2.5 \cdot 10^{22} \text{ cm}^{-3} \quad (3)$$

where  $C_{\text{Si}}$  is the concentration of silicon atoms in 1  $\text{cm}^{-3}$  ( $5 \times 10^{22} \text{ cm}^{-3}$ ) [33].

To assess the stability of the clusters formed in the silicon lattice, we calculated the binding energy  $\Delta E_k$  of Ni–Ni in clusters using different methods:



1. We used the Arrhenius equation at the temperature of cluster formation (additional annealing temperature  $T = 600\text{--}900^\circ\text{C}$ ).

The concentration (solubility) of nickel atoms in the silicon lattice [7, 30] can be estimated using the formula

$$C = C_0 \cdot \exp\left(-\frac{E_a}{kT_{ann}}\right) \quad (4)$$

For nickel in silicon,  $C_0 = 1.227 \times 10^{24} \text{ cm}^{-3}$  and  $E_a = 1.68 \text{ eV}$ .

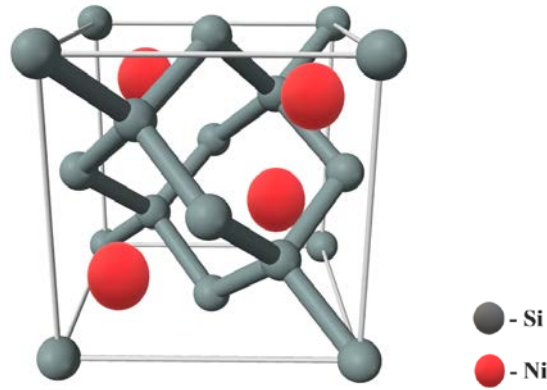


**Figure 3** - Interstitial state of nickel atoms in the unit cell of the silicon lattice

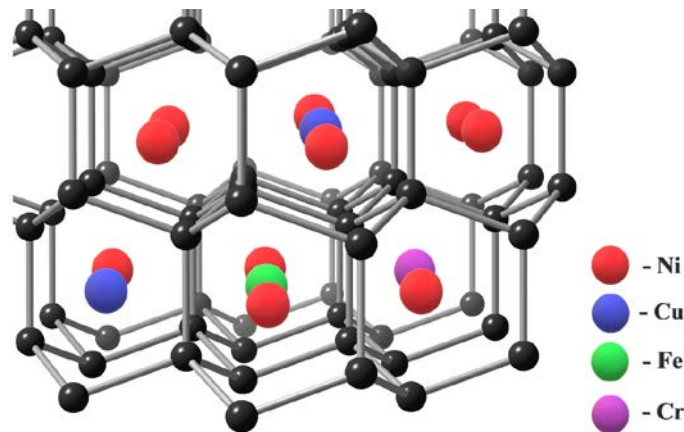


**Figure 4** - Structural model of a cluster of nickel atoms with metallic bonding in the silicon lattice

At the same time, nickel atoms in the silicon lattice are in equilibrium with clusters; therefore, the concentration (solubility) of nickel atoms in the silicon lattice can be determined by the formula [34, 35]

$$C = C_{lim} \cdot \exp\left(-\frac{\Delta E_{kl}}{kT_{ann}}\right) \quad (5)$$

From Eqs. (4) and (5), the binding energy  $\Delta E_{kl}$  of nickel atoms with the cluster can be found:

$$\Delta E_{kl} = E_a - kT_{ann} \cdot \ln\left(\frac{C_0}{C_{lim}}\right) \quad (6)$$

where  $k = 8.6 \times 10^{-5} \text{ eV/K}$  is the Boltzmann constant.

The calculation showed that the binding energy of nickel atoms with the nickel cluster at  $T_{ann} = 1073 \text{ K}$  is  $\Delta E_{kl} \approx 1.32 \text{ eV}$ . In the annealing temperature range of  $T_{ann} = 873\text{--}1173 \text{ K}$ , the binding energy takes values in the range of  $1.26\text{--}1.34 \text{ eV}$ .

2.  $\Delta E_k$  can also be estimated using the specific heat of vaporization of nickel atoms ( $\Delta E_l = 3.92 \text{ eV}$ ) [36]. To do this, we calculated the boundary energy  $\Delta E_{kl}$  of binding between nickel atoms in the cluster, taking into account the change in distance between nickel atoms in the cluster in comparison with pure metal (assuming a quadratic interaction potential):

$$\Delta E_{k2} = \Delta E_t \cdot \left( \frac{R'_{Ni-Ni}}{R_{Ni-Ni}} \right)^2 \approx 1.66 \text{ eV}, \quad (7)$$

where  $R'_{Ni-Ni}$  is the distance Ni–Ni in the nickel lattice (2.5 Å [36]) and  $R_{Ni-Ni}$  is the distance Ni–Ni in the nickel cluster (3.84 Å).

3. Another method is based on calculating the surface energy of the nickel cluster (surface energy  $\sigma = E/S$ , where  $E$  is the binding energy of the adsorbate on the surface of the material,  $S = 4\pi R^2$  is the interaction area of the atom with the surface of the material,  $R = 1.25$  Å is the radius of the nickel atom [33]), and the component  $\sigma_{Ni} = 2280 \text{ erg/cm}^2 = 1.42 \times 10^{15} \text{ eV/cm}^2$  [37]. Then, the binding energy of a single nickel atom with the nickel lattice is

$$\Delta E_{Ni} = \sigma_{Ni} \cdot S \approx 2.79 \text{ eV}. \quad (8)$$

Taking into account a similar change in interatomic distances within the cluster, we find the binding energy of a single nickel atom (adsorbate) with the nickel cluster in the silicon lattice:

$$\Delta E_{k3} = \Delta E_{Ni} \cdot \left( \frac{R'_{Ni-Ni}}{R_{Ni-Ni}} \right)^2 \approx 1.18 \text{ eV}. \quad (9)$$

Let us calculate the average binding energy of nickel atoms with the nickel cluster using data obtained by various methods:

$$\Delta E_k = \frac{\Delta E_{K1} + \Delta E_{K2} + \Delta E_{K3}}{3} \approx 1.39 \text{ eV}. \quad (10)$$

Using the obtained value of the binding energy and the Arrhenius equation, the concentration of nickel atoms in clusters can be calculated:

$$C = C_k \exp\left(-\frac{\Delta E_k}{kT_{ann}}\right) \quad (11)$$

where  $C_k$  is the concentration of nickel atoms in clusters and  $C$  is the residual concentration of nickel in the silicon lattice (outside the clusters). From here, it is easy to calculate the ratio of the concentrations of nickel atoms in clusters and in the silicon lattice:

$$\frac{C_k}{C} = \exp\left(\frac{\Delta E_k}{kT_{ann}}\right) \quad (12)$$

Depending on the annealing temperature  $T_{ann} = 873\text{--}1173$  K, the ratio  $C_k/C \approx 10^6\text{--}10^8$ . Therefore, most of the nickel atoms after additional thermal

annealing are located in clusters. Calculations showed that the maximum concentration of nickel atoms participating in cluster formation is  $C_k \approx 3 \times 10^{22} \text{ cm}^{-3}$  at  $T_{ann} = 1073$  K. This concentration is close to maximum theoretically possible solubility  $C_{lim}$  (3) of nickel atoms in the cluster, which confirms the correctness of calculating the binding energy.

Therefore, the binding energy of nickel atoms with the cluster is  $\Delta E_k \approx 1.39$  eV, and the concentration of nickel atoms in the clusters is 6–8 orders of magnitude higher than the residual concentration (solubility) of nickel in the silicon lattice.

The maximum radius of nickel clusters can be determined as follows [38]:

$$R_k = \left[ \frac{3}{4\pi n_k} \cdot \frac{C_{0(Ni)} - C}{C_{lim} - C} \right]^{1/3} \quad (13)$$

where  $C_{0(Ni)}$  is the solubility of nickel atoms ( $\sim 10^{16}\text{--}10^{18} \text{ cm}^{-3}$ ) in the bulk of monocrystalline silicon.

Taking into account the constancy of the total amount of nickel in the silicon lattice, the size of clusters varies in the range from 20 nm to 1 μm, depending on the cluster concentration in the range of  $n_k$  from  $10^{10}$  to  $10^{16} \text{ cm}^{-3}$ . This confirms the results of our experiment and the results obtained by other researchers [12, 16, 28, 29]. Importantly, the size and concentration of clusters, as well as the concentration of nickel atoms in clusters, depend on the number of defects in the crystal, mechanical stresses in it, as well as the temperature, time, and cooling rate after diffusion and additional thermal annealing. Therefore, the above estimates of cluster concentration are purely approximate.

#### 4.2 Physical Model of Gettering by Nickel Atom Clusters

The analysis of the experimental results showed [17–27] that the formation of electroneutral nickel clusters reduces the concentration  $C_r$  of recombination centers; i.e., nickel clusters getter uncontrollable recombination impurities and purify the silicon crystal lattice.

We attribute the mechanism of gettering by nickel atom clusters to the following principles:

- the gettering properties of nickel clusters are determined by the metallic bonding forces acting in them. Since the metallic bonding forces primarily depend on the concentration of electrons (metal atoms) [30, 39], all metallic uncontrollable impurity atoms have binding energies close to  $\Delta E_k \approx 1.39$  eV;

– there is always a large number of macrodefects on the surface, leading to intense nickel precipitation. The precipitates are virtually pure metal and have higher binding energies with fast-diffusing impurities (FDI) (up to  $\sim 2.7$  eV for monocrystalline nickel [32]); therefore, the precipitates have better gettering properties than clusters;

– in the near-surface region, the concentration of nickel atoms is higher than that in the bulk by 2–3 orders of magnitude [30, 26]; therefore, the gettering rate in the near-surface region is higher due to the greater amounts of formed clusters and precipitates [23–27];

– the gettering process by nickel clusters is intensified by additional thermal annealing, which accelerates the attainment of equilibrium. However, too high annealing temperatures can lead to the decomposition of nickel clusters and precipitates [27–29]. Therefore, there is an optimal temperature at which the gettering of FDI is maximum;

– the gettering properties of clusters can be enhanced if uncontrollable impurity atoms form intermetallic compounds with nickel because this increases the binding energy with FDI atoms.

To determine the effect of cluster concentration on gettering, the ratio of the concentration of FDI atoms in the clusters to that in the silicon lattice

$$\frac{C_r}{C_{rk}} = \exp\left(\frac{\Delta E_r}{kT_{ann}}\right) \quad (14)$$

where  $C_{rk}$  is the concentration of FDI such as Cu, Fe, Cr, etc., in the clusters;  $C_r$  is the residual concentration of FDI in the silicon lattice (outside the clusters); and  $T_{ann}$  is the annealing temperature. Depending on the annealing temperature in the range of  $T = 873$ – $1173$  K, the ratio  $C_r/C_{rk}$  varies from  $10^6$  to  $10^8$ , respectively.

The concentration of recombination centers in silicon doped with nickel atoms after thermal annealing is determined from the equation (15) where is the initial concentration of FDI in the silicon lattice,  $C_r$  is the residual concentration of FDI in the silicon lattice (outside the clusters), and  $\Delta C_r$  is the decrease in the FDI concentration due to gettering by nickel clusters.

From Eq. (15), it is possible to determine the change in the concentration of recombination centers:

$$C_r = C_{r0} - \Delta C_r \quad (15)$$

Depending on the initial concentration of FDI ( $\approx 10^{11}$ – $10^{13}$  cm $^{-3}$ ) and the ratio of the concentrations of FDI atoms in the clusters and in the silicon lattice ( $C_r/C_{rk} \approx 10^6$ – $10^8$  cm $^{-3}$ ) under the conditions of additional thermal annealing ( $T = 873$ – $1173$  K), the change in the concentration of recombination centers ( $C_r/C_{r0}$ ) is estimated to be within the range of 0.3–0.5.

Thus, the doping with nickel atoms and the formation of clusters in silicon reduce the concentration of uncontrolled recombination impurities by 50–70% in comparison with the initial value, which corresponds to a change in the concentration of FDI ( $C_{r0}/C_r$ ) by a factor of 2–4.

Using the change in the concentration of recombination centers, the change in the bulk lifetime  $\tau$  of minority charge carriers:

in the reference (nickel-free) solar cells

$$\tau_0 = \frac{1}{C_{r0}v_{th}\sigma} \quad (17)$$

in the SC doped with nickel atoms,

$$\tau_{Ni} = \frac{1}{C_rv_{th}\sigma} \quad (18)$$

where  $v_{th}$  is the thermal velocity of carriers and  $\sigma$  is the capture cross-section of recombination centers.

Using Eqs. (17) and (18), we determine the relationship

$$\frac{\tau_{Ni}}{\tau_0} = \frac{C_{r0}}{C_r} \quad (19)$$

Thus, the lifetime of minority charge carriers in the solar cell base after doping with nickel atoms and additional thermal annealing should increase by a factor of 2–4. These data are also supported by the results obtained in [16, 17, 22].

It was experimentally shown that the lifetime of minority charge carriers in the base of a solar cell doped with nickel atoms increases by a factor of up to 2 in comparison with the reference sample [15]. This confirms the correctness of the proposed gettering model and the calculations performed.

## 5 Conclusions

The optimal conditions for gettering by nickel clusters were experimentally determined to be within a nickel diffusion temperature range of 800–850°C and an additional thermal annealing temperature range of 750–800°C.

Based on IR microscopy, SEM, and SIMS results, the surface density of nickel clusters was found to be approximately  $10^6$ – $10^7$  cm<sup>-2</sup>, with an average cluster diameter of 20–100 nm and a cluster concentration of about  $10^{11}$ – $10^{15}$  cm<sup>-3</sup>.

A physical model for the structure of a nickel atom cluster in silicon was developed. It was shown that the binding energy of nickel atoms to a cluster is approximately  $\Delta E_k \approx 1.39$  eV, and the concentration of nickel atoms in clusters is 6–8 times higher than the residual concentration (solubility) of nickel in the silicon lattice.

Calculations indicated that nickel doping can increase the lifetime of minority charge carriers by a

factor of 2–4. Experimental results confirmed an increase in the lifetime of minority charge carriers by up to a factor of 2.

### Acknowledgments

Authors are grateful to Professor N.F. Zikrillayev for participation in the experiment and discussion of the results.

Work was performed in the framework of the AL-202102215 “Integrated Microfluidic System to Capture Circulating Tumor Cells by Ferromagnetic Nano-clusters in Si”.

### References

1. Green, M., Dunlop, E., Hohl-Ebinger, J., Yoshita, M., Kopidakis N., Hao X., Solar Cell Efficiency Tables (Version 58) // Prog Photovolt Res Appl. –2021. –Vol. 29. –P. 657–667. <https://doi.org/10.1002/pip.3444>
2. Glunz, S.W., High-Efficiency Crystalline Silicon Solar Cells // Adv. OptoElectron. – 2007. – Vol. – P. 97370(1-15). <https://doi.org/10.1155/2007/97370>
3. Schmidt, J., Lim, B., Walter, D., Bothe, K., Gatz S., Dullweber Th., Altermatt P.P., Impurity-Related Limitations of Next-Generation Industrial Silicon Solar Cells. // IEEE J. of Photovoltaics. – 2013. – Vol. 3. – No. 1. – P. 114–118. <https://doi.org/10.1109/pvsc-vol2.2013.6656779>
4. Panaiotti, I.E., Terukov, E.I., A Study of the Effect of Radiation on Recombination Loss in Heterojunction Solar Cells Based on Single-Crystal Silicon // Tech. Phys. Lett. – 2019. – Vol. 45. – No. 3. – P. 193–196. <https://doi.org/10.1134/S106378501903012X>
5. Bakhadyrkhanov, M.K., Valiev, S.A., Zikrillayev, N.F. Koveshnikov S.V., Saitov E.B., Tachilin S.A., Silicon photovoltaic cells with clusters of nickel atoms // Appl. Sol. Energy. – 2016. – Vol. 52. – P. 278–281. <https://doi.org/10.3103/S0003701X1604006X>
6. Richter, A., Müller, R., Benick, J., Feldmann, F., Steinhauser, B., Reichel, Ch., Fell, A., Bivour, M., Hermle, M., Glunz, S.W., Design rules for high-efficiency both-sides-contacted silicon solar cells with balanced charge carrier transport and recombination losses // Nature Energy. – 2021. –Vol. 6. – P. 429–438. <https://doi.org/10.1038/s41560-021-00805-w>
7. Yatsukhnenko, S., Druzhinin, A., Ostrovskii, I., Khoverko, Yu., Chernetskiy M., Nanoscale Conductive Channels in Silicon Whiskers with Nickel Impurity // Nanoscale Res Lett. – 2017. – Vol. 12. – No. 78. – P. 1–7. <https://doi.org/10.1186/s11671-017-1855-9>
8. Sh. Huang, Y., Ding, L. Zhou, K. Shi, Dan Chi, Daxin Bao, Yue He, Simulation of Silicon Solar Cells with Passivation Contact of Tunnel Oxide Layer // Surf. Engin. Appl. Electrochem. – 2021. – No. 57. – P. 607–615. <https://doi.org/10.3103/S1068375521050045>
9. Saltas, V., Chronos, A., Vallianatos, F., Thermodynamic modelling of fast dopant diffusion in Si // J. Appl. Phys. – 2018, – Vol. 123. – P. 161527. <https://doi.org/10.1063/1.5001755>
10. Lozhkina, D.A., Astrova, E.V., Sokolov, R.V., Kirilenko, D.A., Levin A.A., Parfeneva A.V., Ulin V.P., Formation of Silicon Nanoclusters in Disproportionation of Silicon Monoxide // Semiconductors. – 2021. – Vol. 55. – No. 4. – P. 423–437. <https://doi.org/10.21883/FTP.2021.04.50743.9575>
11. Zikrillayev, N.F., K ushiev, G.A.U., Koveshnikov, S.V., Abdurakhmanov B.A., Qurbonova, U.K., Sattorov, A.A., Current Status of Silicon Studies with Ge<sub>x</sub>Si<sub>1-x</sub> Binary Compounds and Possibilities of Their Applications in Electronics // East European Journal of Physics. – 2023. – Vol. 3. – P. 334–339, <https://doi.org/10.26565/2312-4334-2023-3-34>
12. Gafner, Y.Y., Gafner, S.L., Entel, P., Formation of an icosahedral structure during crystallization of nickel nanoclusters // Phys. Solid State. – 2004. – Vol. 46. –No. 7. – P. 1327–1330. <https://doi.org/10.1134/1.1778460>
13. Iliyev, X.M., Isamov, S.B., Isakov, B.O., Qurbonova, U.X., Abduraxmonov, S.A., A surface study of Si doped simultaneously with Ga and Sb // East European Journal of Physics. – 2023, – Vol. 3. – P. 303–307. <https://doi.org/10.26565/2312-4334-2023-3-29>
14. Galashev, A., Vorob'ev, A., Electronic Properties and Structure of Silicene on Cu and Ni Substrates // Materials. – 2022. – Vol. 15. – P. 3863(1–12). <https://doi.org/10.3390/ma15113863>
15. Saymbetov A.K., Muminov R.A., Japashov N.M., Toshmurodov Yo.K., Nurgaliyev M.K., Kuttybay N.B., Zholamanov B.N., Optimal regime of the double-sided drift of lithium ions into silicon monocrystal // Physical Sciences and Technology. – 2023. – Vol. 10. – No. 1-2. – P. 19-25. <https://doi.org/10.26577/phst.2023.v10.i1.03>
16. Mil'vidskii, M.G., Chaldyshev, V.V., Nanometer-size atomic clusters in semiconductors – a new approach to tailoring material properties // Semiconductors. – 1998. – Vol. 32. – No. 5. – P. 457–465. <https://doi.org/10.1134/1.1187418>
17. Zikrillayev N.F., Shoabdurahimova M.M., Kamilov T., Khusanov A.Zh., Kurbonaliev K.K., Norkulov N., Saitov E.B., Obtaining manganese silicide films on a silicon substrate by the diffusion method // Physical Sciences and Technology. – 2022. – Vol. 9. – no.3–4. – P. 89–93. <https://doi.org/10.26577/phst.2022.v9.i2.011>

18. Bakhadyrkhanov, M.K., Isamov, S.B., Zikrillaev, N.F., Tursunov, M.O., Anomalous Photoelectric Phenomena in Silicon with Nanoclusters of Manganese Atoms // *Semiconductors*. – 2021. – Vol. 55. – No. 6. – P. 542–545. <https://doi.org/10.1134/S1063782621060038>
19. Bakhadyrkhanov, M.K., Ismailov, K.A., Kosbergenov, E.Z., Thermal stability of electrical parameters of silicon crystal doped with nickel during growth // *SPQEO*. – 2022. – Vol. 25. – No. 1. – P. 006–009. <https://doi.org/10.15407/spqeo25.01.006>
20. Bakhadyrkhanov, M.K., Ismaylov, B.K., Tachilin, S.A., Ismailov, K.A., Zikrillaev, N.F., Influence of electrically neutral nickel atoms on electrical and recombination parameters of silicon // *SPQEO*. – 2020. – Vol. 23. – No. 4, pp. 361–365. [doi:10.15407/spqeo23.04.361](https://doi.org/10.15407/spqeo23.04.361)
21. Ismailov, K.A., Kenzhaev, Z.T., Koveshnikov, S.V., Kosbergenov, E.Z., Ismaylov, B.K., Radiation Stability of Nickel Doped Solar Cells // *Physics of the Solid State*. – 2022. – Vol. 64. – No. 3. – P. 154–156. <https://doi.org/10.1134/S1063783422040011>
22. Ismaylov, B.K., Zikrillayev, N.F., Ismailov, K.A., Kenzhaev, Z.T., Clusters of impurity nickel atoms and their migration in the crystal lattice of silicon // *Physical Sciences and Technology*. – 2023. – Vol. 10. – No. 1. – P. 13–18. <https://doi.org/10.26577/phst.2023.v10.i1.02>
23. Bakhadyrkhanov, M.K., Isamov, S.B., Kenzhaev, Z.T., Koveshnikov, S.V. Studying the effect of doping with nickel on silicon-based solar cells with a deep p–n-junction // *Tech. Phys. Lett.* – 2019. – Vol. 45. – No.10. – P. 959. <https://doi.org/10.1134/S1063785019100031>
24. Bakhadyrkhanov M.K., Isamov S.B., Kenzhaev Z.T., Melebaev D., Zikrillayev Kh.F., Ikhtiyarova G.A., Silicon Photovoltaic Cells with Deep p–n Junction // *Applied Solar Energy*. – 2020. – Vol. 56. – No. 1. – P. 13–17. <https://doi.org/10.3103/S0003701X2001003X>
25. Zikrillayev, N., Kenzhaev, Z., Ismailov, T., Kurbanova, U., Aliyev, B., Effect of nickel doping on the spectral sensitivity of silicon solar cells // *E3S Web of Conferences*. – 2023. – Vol. 434. – P. 01036(1-3). <https://doi.org/10.1051/e3sconf/202343401036>
26. Bakhadyrkhanov, M.K., Kenzhaev, Z.T., Optimal Conditions for Nickel Doping to Improve the Efficiency of Silicon Photoelectric Cells // *Tech. Phys.* – 2021. – Vol. 66. – No. 7. – P. 851–856. <https://doi.org/10.1134/S1063784221060049>
27. Bakhadyrkhanov M.K., Kenzhaev Z.T., Koveshnikov S.V., Ayupov K.S., Kosbergenov E.Zh., Effect of nickel on the lifetime of charge carriers in silicon solar cells // *Semiconductors*. – 2022. – Vol. 56. – No. 1. – P. 101–105. <https://doi.org/10.21883/SC.2022.01.53028.9642>
28. Astashchenkov, A.S., Brinkevich, D.I., Petrov, V.V., Properties of silicon doped with nickel impurity by diffusion method // *Dokl. BGUIR*. – 2008. – Vol. 38. – No. 8. – P. 37–43.
29. Tanaka, Sh., Ikari, T., Kitagawa, H., In-Diffusion and Annealing Processes of Substitutional Nickel Atoms in Dislocation-Free Silicon // *Jpn. J. Appl. Phys.* – 2001. – Vol. 40. – P. 3063–3068. <https://doi.org/10.1143/JJAP.40.3063>
30. Lindroos, J., Fenning, D.P., Backlund, D.J., Verlage, E., Gorgulla A., Estreicher, S.K., Savin, H., Buonassisi, T., Nickel: A very fast diffuser in silicon // *J. Appl. Phys.* – 2013. – Vol. 113. – P. 204906. <https://doi.org/10.1063/1.4807799>
31. Liu, A., Phang, S.P., Macdonald, D., Gettering in silicon photovoltaics: A review // *Solar Energy Materials and Solar Cells*. – 2022. – Vol. 234. – P.111447. <https://doi.org/10.1016/j.solmat.2021.111447>
32. Imran, M., Coskun, H., Khan, N.A., Ouyang, J., Role of annealing temperature of nickel oxide (NiO<sub>x</sub>) as hole transport layer in work function alignment with perovskite // *Applied Physics A*. – 2021. – Vol. 127. – P. 117(1–8). <https://doi.org/10.1007/s00339-021-04283-5>
33. Emsley, J., *The Elements* // Oxford University Press. – 1989. – P. 256.
34. Bakhadyrkhanov, M.K., Kenzhaev, Z.T., Koveshnikov, S.V., Usmonov, A.A., Mavlonov, G.K. Formation of Complexes of Phosphorus and Boron Impurity Atoms in Silicon // *Inorg. Mater.* – 2022. – Vol. 58. – No. 1. – P. 1–6. <https://doi.org/10.1134/S0020168522010034>
35. Zikrillaev, N.F., Isamov, S.B., Koveshnikov, S.V., Kenzhaev, Z.T., Turekeev, K.S., Codiffusion of Gallium and Phosphorus Atoms in Silicon // *Surf. Engin. Appl. Electrochem.* – 2023. – Vol. 59. No. 2. P. 210–215. <https://doi.org/10.3103/S1068375523020199>
36. Kondrateva, A.S., Alexandrov, S.E., Fundamental physicochemical regularities of the chemical vapor deposition of nickel oxide layers // *Russ. J. Appl. Chem.* – 2016. – Vol. 89. – No. 9. – P.1402–1408. <https://doi.org/10.1134/S1070427216090032>
37. Egorov, S.N., Calculation of the surface energy of metals in the solid state. // *Izv. Vyssh. Uchebn. Zaved., Sev.-Kavkaz. Reg., Tekh. Nauki*. – 2003. – No. 3. – P. 132.
38. Babich, V.M., Bletskan, N.I., Venger, E.F., Kislород v monokristallakh kremniya (Oxygen in Silicon Single Crystals) // *Kyiv: Interpress*. – 1997. – P. 240.
39. Xiaoxuan Li, Aimin Liu, Carrier Transmission Mechanism-Based Analysis of Front Surface Field Effects on Simplified Industrially Feasible Interdigitated Back Contact Solar Cells // *Energies*. – 2020. – Vol. 13. – No. 20. – P. 5303(1–13). <https://doi.org/10.3390/en13205303>
40. Dellis S., Christoulaki A., Spiliopoulos N., Anastassopoulos D.L., Vradis A.A., Electrochemical synthesis of large diameter monocrystalline nickel nanowires in porous alumina membranes // *J. Appl. Phys.* – 2013. – Vol. 114. – P. 164308. <https://doi.org/10.1063/1.4826900>

**Information about authors:**

*Kenzhaev Zoir Tohir ugli (corresponding author), PhD in physical and mathematical sciences, is an Associate professor at I.A. Karimov Tashkent State Technical University (Tashkent, Uzbekistan), e-mail: zoir1991@bk.ru;*

*Iliev Halmurat Midzhitovich, Doctor of Physical and Mathematical Sciences, is a Professor at I.A. Karimov Tashkent State Technical University (Tashkent, Uzbekistan), e-mail: iliyevx@bk.ru;*

*Ismailov Kanatbay Abdreymovich, Doctor of Physical and Mathematical Sciences, is a Professor at Berdakh Karakalpak State University (Nukus, Uzbekistan), e-mail: ismailov\_k@list.ru;*





*Mavlonov Giyosiddin Khaidarovich, Doctor of Physical and Mathematical Sciences, is a Professor at I.A. Karimov Tashkent State Technical University (Tashkent, Uzbekistan), e-mail: mavlonov@mail.ru;*

*Koveshnikov Sergey Vladimirovich is a Senior lecturer at I.A. Karimov Tashkent State Technical University (Tashkent, Uzbekistan), e-mail: koveshnikov\_s@mail.ru;*

*Ismailov Bayrambay Kanatbaevich – PhD in physical and mathematical sciences, Associate professor is a basic doctoral student at Berdakh Karakalpak State University, (Nukus, Uzbekistan), e-mail: i.bairam@bk.ru;*

*Isamov Sobirzhon Boltaevich – PhD in physical and mathematical sciences, Associate professor is a basic doctoral student at I.A. Karimov Tashkent State Technical University, (Tashkent, Uzbekistan), e-mail: sobir-i@mail.ru*

## Effect of dislocation density-associated strengthening factors on the thermal stability of composite ceramics

I.E. Kenzhina<sup>1\*</sup> , A.L. Kozlovskiy<sup>1,2</sup> ,  
P. Blynskiy<sup>1</sup>  and A.U. Tolenova<sup>1</sup> 

<sup>1</sup>Satbayev University, Almaty, Kazakhstan

<sup>2</sup>Institute of nuclear physics, Almaty, Kazakhstan

\*e-mail: kenzhina@physics.kz

(Received May 12, 2024; received in revised form May, 21, 2024; accepted May 29, 2024)

Interest in composite ceramics based on oxide and nitride compounds is due to the combination of their structural, strength and thermophysical parameters. Moreover, in the case of composites based on  $x\text{Si}_3\text{N}_4 - (1-x)\text{ZrO}_2$ , the strength parameters, as well as resistance to thermal expansion, are determined by the characteristics of zirconium dioxide, while the thermophysical parameters are determined by silicon nitride, for which the thermal conductivity values are almost an order of magnitude higher than for zirconium dioxide. The main method for production of composite  $x\text{Si}_3\text{N}_4 - (1-x)\text{ZrO}_2$  ceramics was the mechanochemical solid-phase synthesis method using high-speed grinding and thermal annealing, used to stabilize structural deformations caused by mechanical action. During the research, it was determined that a change in the ratio of ceramic components due to an increase in the contribution of  $\text{Si}_3\text{N}_4$  in the composition leads to an increase in thermophysical parameters, the change of which is due to the higher thermal conductivity of silicon nitride. In turn, a change in thermophysical parameters, and as a consequence, an alteration in the rate of heat transfer due to phonon mechanisms, causes an elevation in resistance to external influences during thermal shocks. Experiments to determine resistance to thermal influences have shown that the presence of a high density of dislocations in the near-surface layer of ceramics contributes to a rise in resistance to temperature changes, alongside external mechanical influences, which is expressed in less pronounced trends in decreasing hardness indicators during heat resistance tests.

**Key words:** composite ceramics, thermal stability, thermophysical parameters, silicon nitride, zirconium dioxide, dislocation strengthening.

**PACS number(s):** 28.41.Bm.

### 1 Introduction

Over the past few years, in the field of structural materials, the main emphasis has been placed on increasing the resistance of new types of materials to external influences, alongside their ability to operate under extreme conditions, including elevated temperatures, high doses of radiation damage, exposure to aggressive media, etc. [1,2]. Among the most promising materials in this research area are high-entropy alloys based on refractory compounds, as well as composite ceramics, which are a combination of oxide, nitride and carbide compounds of aluminum, silicon, zirconium, niobium, tantalum or tungsten [3-5].

At the same time, the key limiting factor for the widespread use of composite ceramics based on oxide

and nitride compounds is the low thermophysical parameters, in particular, thermal conductivity indicators, which in the case of ceramics are about 2-50 W/Km, while for steels and alloys these indicators are two orders of magnitude higher [6,7]. It should also be noted that in most cases, nitride ceramics have higher thermal conductivity than oxide ceramics, however, oxide ceramics have fairly high resistance to external influences, which determines their strength properties [8,9]. In this regard, one of the important areas of research in the field of creating composite ceramics is the search for new methodological approaches to improve the strength characteristics of ceramics, the main goal of which is to preserve the phase and elemental composition. In particular, one of the ways to increase resistance to external influences, including mechanical and

thermal, is the use of ceramics with nano-sized grains, interest in which is due to their unique properties, which are caused by the presence of a large number of grain boundaries, as well as dislocations. In this case, changing the grain size allows you to vary the dislocation density, as well as the packing density of grains, which eliminates the presence of a large number of voids in the volume of ceramics, which also allows you to solve a number of problems associated with the porosity of ceramic materials.

The dislocation strengthening factor associated with size effects is considered as one of the ways to increase the resistance of materials, including composite ceramics, to external influences, such as thermal effects, high-temperature aging associated with degradation and embrittlement, and radiation damage [10-12]. In this case, the variation in the density of dislocations can be carried out both by crushing grains under external mechanical loads and by changing the variation in the concentration of components in the composition of composite ceramics. If in the first case, the change in dislocations is directly dependent on the grain sizes, then in the case of variations in the components, the change in dislocation density depends on many factors, including the phase composition of the composites, the change of which directly depends on the conditions for obtaining ceramics [13, 14]. The combination of two methods of changing the dislocation density makes it possible to obtain high-strength ceramics that can withstand large mechanical loads, as well as maintain the stability of strength properties during long-term exposure to external factors, such as high temperatures or thermal shocks. Moreover, earlier, in [15], it was shown that the most effective way to change the dislocation density due to mechanical influences is high-speed grinding in planetary mills with subsequent thermal stabilization of the phase composition by removing deformation distortions in the structure of composite ceramics arising under external mechanical influences.

The main aim of the presented study is to determine the influence of dislocation strengthening caused by size effects in  $x\text{Si}_3\text{N}_4 - (1-x)\text{ZrO}_2$  on the change in resistance to thermal shocks resulting from extreme operating conditions [16-18]. At the same time, during the experiments, dependencies were obtained for changes not only in strength properties, i.e. changes in the hardness values of ceramics before and after external influences, but also in maintaining the stability of thermophysical parameters, the change of which is directly related to deformation distortions that occur during embrittlement and softening of ceramics. Interest in this type of ceramics is primarily

due to the possibility of creating high-strength ceramics due to the strength properties of zirconium dioxide, which have high thermal conductivity, which is due to the presence of silicon nitride in the composition of composite ceramics, which has fairly high thermal conductivity in comparison with oxide materials [19, 20].

## 2 Methodology

To obtain samples of composite ceramics based on  $x\text{Si}_3\text{N}_4 - (1-x)\text{ZrO}_2$  compounds, mechanochemical solid-phase synthesis combined with thermal sintering of the samples was used. The synthesis was carried out using chemical reagents of 99.95 % purity; the initial powders were purchased from Sigma Aldrich (Sigma Aldrich, USA). The grain sizes of the original powders were on the order of 5 – 10  $\mu\text{m}$ . To give them nanosizes, a high-speed grinding method was used in a planetary mill PULVERISETTE 6 classic line (Fritsch, Berlin, Germany). The grinding speed was 600 rpm, the time of mechanical action of the grinding media was about 30 minutes. Thermal sintering in a muffle furnace at a temperature of 1500°C for 5 hours was chosen to stabilize the crystal structure, initiate phase transformation processes, and also reduce mechanically induced deformation distortions in the crystal structure of ceramics during grinding. At the same time, the selection of temperature and annealing time conditions was carried out a priori to prevent the occurrence of effects of thermal fusion and agglomeration of grains into large agglomerates, eliminating the occurrence of the effect of dislocation strengthening associated with the size factor.

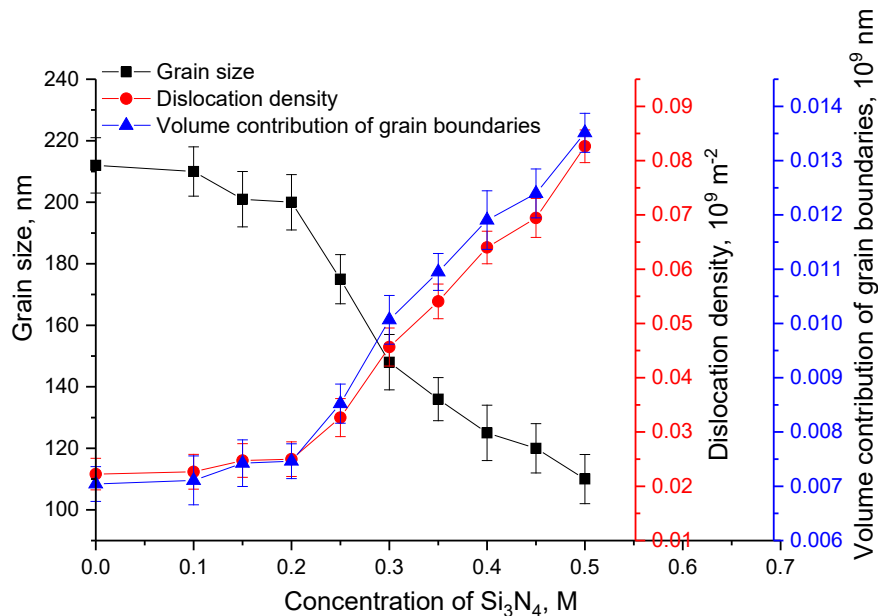
The grain sizes of the studied ceramics were determined using the optical laser diffraction method implemented on an ANALYSETTE 22 NeXT Nano particle analyzer (Fritsch, Berlin, Germany).

Figure 1 reveals data on alterations in grain sizes depending on the concentration of components in the ceramic composition, obtained by analyzing grain size distribution diagrams in the form of average values with measurement error. The formation of dislocation strengthening associated with the size factor was carried out by varying the concentration of components in the ceramic composition in the range  $x$  from 0.1 to 0.5 M, changing which during high-speed grinding results in more intensive crushing of grains and their reduction by more than 2 times. At the same time, a reduction in grain size, as is evident from the data presented in Figure 1, leads to the effect of an elevation in dislocations and the volumetric contribution of grain boundaries. This effect is most pronounced at  $\text{Si}_3\text{N}_4$  concentrations above 0.25 M in



the ceramic composition. According to the presented data, a decline in grain size by more than 2 times leads to a growth in the dislocation density of the volume fraction of grain boundaries by more than 3.5

– 4 times, which indicates that even small changes in grain size allow one to vary the dislocation density, changes in which can be used to create strengthening effects [21-23].



**Figure 1** – Results of a comparative analysis of changes in grain sizes, dislocation density and volumetric contribution of grain boundaries

Determination of the influence of variations in the ratio of components in  $x\text{Si}_3\text{N}_4 - (1-x)\text{ZrO}_2$  ceramics on changes in thermophysical parameters, in particular, on changes in the thermal conductivity coefficient, was carried out using the method of measuring longitudinal thermal flow. The measurements were carried out on ceramic samples pressed into tablets with a diameter of 10 mm and a thickness of about 1 mm, which made it possible to eliminate the effects of uneven heat transfer and also reduce heat losses in a small volume. The measurements were carried out using a thermal conductivity meter KIT-800 (KB Teplofon, Russia).

The determination of strength properties, in particular, the hardness values of ceramics, alongside their changes depending on external influences, including thermal tests for heat resistance, was carried out by the indentation method, implemented using a Duroline M1 microhardness tester (Metkon, Bursa, Turkey).

The thermal stability of the studied  $x\text{Si}_3\text{N}_4 - (1-x)\text{ZrO}_2$  ceramics, obtained by mechanochemical grinding, was assessed through experimental work,

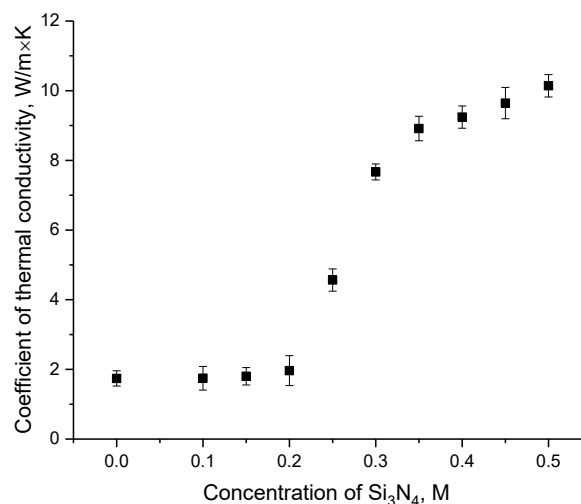
consisting of rapid thermal heating of samples to a temperature of 1000 °C, holding them at this temperature for 1 hour and subsequent rapid removal to air in order to create a sharp temperature gradient that can lead to the initiation of oxidation processes and destabilization of the strength properties of ceramics. The heating rate of the samples was about 50 °C/min. For testing, a muffle furnace was used with the ability to control the temperature inside the chamber with an accuracy of about  $\pm 5^\circ\text{C}$ , which is an acceptable error parameter for high-temperature effects. Determination of the influence of hardening factors in this case was carried out by assessment of the change in the strength and thermophysical parameters of ceramics before and after heat resistance tests. Determination of the effect of dislocation strengthening on maintaining stability after thermal tests was carried out by comparative analysis of changes in the degree of hardness degradation after 5 successive test cycles with changes in dislocation density, presented in Figure 1. Calculation of the strength degradation degree was carried out by comparing the hardness value in the initial state and

after 5 successive test cycles, which, in terms of percentage, made it possible to estimate the amount of softening caused by thermal effects.

### 3 Results and discussion

Figure 2 demonstrates the results of alterations in the thermal conductivity coefficient for  $x\text{Si}_3\text{N}_4 - (1-x)\text{ZrO}_2$  ceramics with varying component concentrations. Changes in the thermal conductivity coefficient observed in the presented dependence reflect the direct influence of the ratio of components in the composition on the increase in thermal conductivity. In the case of low concentrations of  $\text{Si}_3\text{N}_4$  (less than 0.2 M), the thermal conductivity coefficient is less than  $2 \text{ W/m}\cdot\text{K}$ , a value characteristic of  $\text{ZrO}_2$  ceramics, the thermal conductivity value of which is significantly lower than for nitride ceramics. In the case when the  $\text{Si}_3\text{N}_4$  concentration is greater than 0.25 M, an increase in the thermal conductivity

coefficient to  $4 - 10 \text{ W/m}\cdot\text{K}$  is observed, depending on the  $\text{Si}_3\text{N}_4$  concentration in the composition. Such changes in thermal conductivity are due to the effect associated with higher thermal conductivity of  $\text{Si}_3\text{N}_4$ , the contribution of which increases with increasing concentration in the ceramic composition. It should be noted that, according to the data presented in Figure 2, the mechanisms of changes in thermal conductivity at high concentrations of  $\text{Si}_3\text{N}_4$  are not significantly affected by changes in grain sizes, since in the case of thermophysical parameters, a key role in determination of the heat transfer mechanisms is played by phonon mechanisms, which are the rescattering of phonons that carry heat, and in the case of a large number of small grains, the rescattering effect can be slowed down. However, the thermophysical parameters of  $\text{Si}_3\text{N}_4$  themselves in this case suppress the size effect, which results in thermal conductivity growth when the ratio of components in the ceramic composition changes.



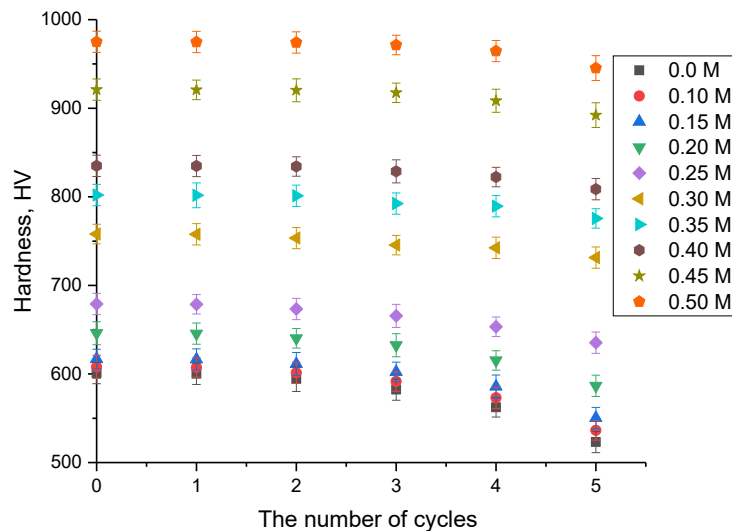
**Figure 2** – Data on changes in the thermal conductivity coefficient for  $x\text{Si}_3\text{N}_4 - (1-x)\text{ZrO}_2$  ceramics depending on variations in the concentration of components

Figure 3 illustrates the results of changes in the hardness of  $x\text{Si}_3\text{N}_4 - (1-x)\text{ZrO}_2$  ceramics during heat resistance tests, which were carried out to establish the stability of the strength properties of ceramics under external thermal influences. Assessing the data on changes in hardness values for  $x\text{Si}_3\text{N}_4 - (1-x)\text{ZrO}_2$  ceramics in the initial state, it can be concluded that a decline in grain size from 200 – 210 nm, characteristic of low  $\text{Si}_3\text{N}_4$  concentrations in ceramics up to 110 – 140 nm, characteristic of  $\text{Si}_3\text{N}_4$  concentrations of more than 0.2 M, leads to an elevation in hardness.

Such changes are due to the effect of dislocation strengthening, which manifests itself for ceramics with small grain sizes and causes strengthening, as well as an increase in stability to mechanical stress, which can be assessed by the shape and imprints of the indenter, characterized by the absence of microcracks near the tops of the imprint pyramid. Moreover, according to the data presented, an alteration in grain size, caused by a variation in the ratio of components in the composition of ceramics, results in hardness growth by more than 1.4 – 1.5 times compared to  $\text{ZrO}_2$

ceramics, without adding  $\text{Si}_3\text{N}_4$  to them. From which it can be concluded that the variation in the ratio of the components determines the processes of grain crushing when the  $\text{Si}_3\text{N}_4$  concentration in the ceramics reaches more than 0.2 M, which indicates that at low concentrations of  $\text{Si}_3\text{N}_4$  in the ceramics, the dominant

role in determining the strength parameters is played by  $\text{ZrO}_2$ . In the case when the  $\text{Si}_3\text{N}_4$  concentration is more than 0.2 M, strengthening is due to the effects of grain crushing and boundary effects, leading to the emergence of additional barriers to the propagation of microcracks that arise under mechanical stress.



**Figure 3** – Results of measurements of hardness values of the studied samples contingent upon the number of heat resistance test cycles

The overall view of the presented dependences of alterations in hardness values during heat resistance tests indicates that with a small number of thermal changes (1 – 2 consecutive tests), the decrease in hardness values is within the permissible error, and the deviation is no more than 0.1 %. In this case, a change in the ratio of components in  $x\text{Si}_3\text{N}_4 - (1-x)\text{ZrO}_2$  ceramics results in a decrease in the hardness value deviation from the initial value. The main changes in hardness values are observed after 2-3 cycles, while the trend of changes in hardness is different for the ceramics under study. The observed reduction in the hardness values of ceramics after 2-3 successive cycles of heat resistance tests is due to degradation associated with deformation processes resulting from thermal expansion of the crystal lattice and subsequent sudden cooling. In the case where  $\text{ZrO}_2$  dominates in the composition of  $x\text{Si}_3\text{N}_4 - (1-x)$

$\text{ZrO}_2$  ceramics, the trend of hardness deterioration as a result of successive tests is more pronounced, and the maximum deviation ( $\Delta\text{Hardness}$ ) is more than 12 % compared to the initial value, which indicates a fairly pronounced softening of ceramics as a result of thermal tests for heat resistance. In the case of ceramics in which the  $\text{Si}_3\text{N}_4$  concentration is more than 0.2 M, the value of  $\Delta\text{Hardness}$  is no more than 3.0 – 3.2 %, which is acceptable for such tests, and such a small change indicates a fairly high resistance of the ceramics to external influences, including thermal expansion and deformation distortion of the structure caused by a sharp change in the temperature of the sample.

Figure 4 reveals a comparison of variations in the softening value (decrease in hardness after 5 successive cycles of heat resistance tests) and dislocation density associated with changes in grain sizes in  $x\text{Si}_3\text{N}_4 - (1-x)\text{ZrO}_2$  ceramics.

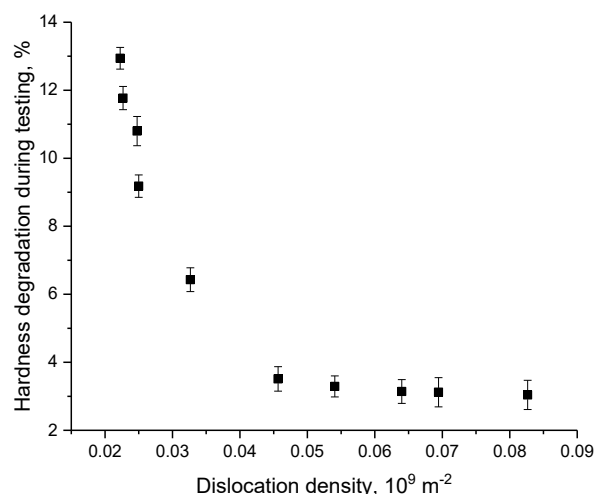


**Figure 4** – Comparison of the softening value after 5 cycles and dislocation density in  $x\text{Si}_3\text{N}_4 - (1-x)\text{ZrO}_2$  ceramics

The general view of the presented dependence of the variation in the softening value (decrease in hardness after 5 cycles of heat resistance tests) on the dislocation density indicates the positive effect of increasing the dislocation density on maintaining the stability of hardness during thermal tests. It is important to highlight that the most pronounced alterations are observed with an elevation in dislocation density from  $0.02 \times 10^9 \text{ m}^{-2}$  to  $0.04\text{--}0.05 \times 10^9 \text{ m}^{-2}$ , at which the softening resistance growth is more than fourfold (from 12 % to 3 %). In turn, a further increase in dislocation density does not lead to such a pronounced change in the resistance to degradation of strength properties, which can be explained by effects associated with dimensional factors, as well as the phase composition of ceramics. The influence of the phase composition in this case may be that with an increase in  $\text{Si}_3\text{N}_4$  composition, which results in hardness growth in the initial state, as well as a decrease in grain size, in the case of long-term thermal tests, it does not contribute to higher stability under thermal influences, as well as mechanical loads.

Figure 5 demonstrates the comparison results of changes in the thermal conductivity coefficient of the studied  $x\text{Si}_3\text{N}_4 - (1-x)\text{ZrO}_2$  ceramics after 5 successive cycles of heat resistance tests, reflecting the influence of dislocation strengthening factors on resistance to thermal influences.

The general appearance of the data presented reflects the direct influence of both the size factor, which determines dislocation strengthening, and the influence of variations in the ratio of components

in the composition of ceramics. In the case when  $\text{ZrO}_2$  dominates in the composition of ceramics, the degradation of strength and thermophysical parameters is maximum and amounts to more than 8 – 12 % after five test cycles. Such a strong decrease is due to heat transfer mechanisms, which in the case of low thermal conductivity of  $\text{ZrO}_2$  result in thermal expansion coefficient growth, which in turn plays an important role in the volumetric change of the heated material due to an increase in the vibration amplitude of atoms in the crystal lattice. In this case, a sharp change in temperature (the so-called thermal shock) and low thermal conductivity lead to the occurrence of deformation structural distortions caused by thermal expansion and slow heat transfer. As a result, not only volumetric distortion of the crystalline structure occurs, but also the formation of highly disordered inclusions in the ceramic composition, a rise in the number of which as a result of successive thermal effects results in surface layer destabilization, and as a consequence, a decrease in hardness and resistance to external mechanical influences. A change in the thermophysical parameters of  $x\text{Si}_3\text{N}_4 - (1-x)\text{ZrO}_2$  ceramics with an increase in the concentration of  $\text{Si}_3\text{N}_4$  in the composition leads to an increase in the stability of the strength and thermophysical parameters, and their decrease after five cycles of successive tests is no more than 3 – 3.3 % of the initial value. Such small alterations are due to heat transfer mechanisms due to the contribution to the thermal conductivity of  $\text{Si}_3\text{N}_4$ , which leads to the fact that with sharp temperature changes, the influence of the disorder factor caused by changes in the amplitude of thermal

vibrations is less pronounced than in the case of  $\text{ZrO}_2$  dominance. Also, in this case, the stabilization of strength properties is influenced by the dislocation strengthening factor, the influence of which is expressed in the creation of additional dissipative barriers that restrain deformation distortion resulting from thermal effects. From the analysis it follows that the formation of composite ceramics in which the ratio of components is close to equal makes it

possible to obtain high-strength ceramics with good resistance to thermal shock, as well as having fairly high thermal conductivity in comparison with  $\text{ZrO}_2$ . At the same time, the use of high-speed mechanical-chemical grinding makes it possible to obtain nano-sized composite ceramics, the grain size of which is about 100 – 120 nm, which causes the presence of dislocation strengthening associated with the size factor.

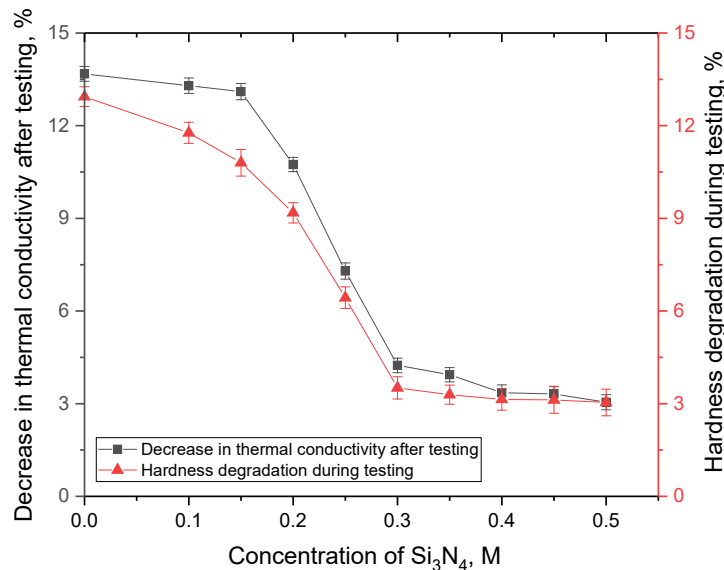


**Figure 5** – Comparison of the results of changes in thermal conductivity coefficient and hardness degradation during heat resistance tests

#### 4 Conclusions

The paper presents the assessment results of changes in the thermophysical and strength parameters of  $x\text{Si}_3\text{N}_4 - (1-x)\text{ZrO}_2$  ceramics during heat resistance tests (i.e., under a sharp temperature change). According to the studies carried out, it was found that a variation in the ratio of components in ceramics, caused by a rise in  $\text{Si}_3\text{N}_4$  in the composition, results in accelerated fragmentation of grains during mechanical grinding, which in turn determines a change in the dislocation density and volume fraction of grain boundaries in the composition of ceramics.

According to the assessment of changes in thermophysical parameters, it was determined that an increase in the composition of  $x\text{Si}_3\text{N}_4 - (1-x)\text{ZrO}_2$  ceramics  $\text{Si}_3\text{N}_4$  by more than 0.2 M leads to an increase in the thermal conductivity coefficient from 2  $\text{W/m}\times\text{K}$  to 9 – 10  $\text{W/m}\times\text{K}$ , which in turn results

in stabilization of thermophysical parameters under external influences.

During determination of the main mechanisms of softening caused by thermal effects, it was determined that the most significant alterations in hardness are associated both with the size effect, which consists in the fact that at  $\text{Si}_3\text{N}_4$  concentrations in  $x\text{Si}_3\text{N}_4 - (1-x)\text{ZrO}_2$  ceramics above 0.2 M, a sharp decrease in grain size is observed, leading to the appearance of a large number of dislocations and grain boundaries. In this case, a variation in dislocation density causes the strengthening of ceramics, both in the case of initial values and during heat resistance tests.

According to the assessment of alterations in the hardness indicators of the studied  $x\text{Si}_3\text{N}_4 - (1-x)\text{ZrO}_2$  ceramic samples after heat resistance tests, it was found that an increase in dislocation density from  $0.02 \times 10^9 \text{ m}^{-2}$  to  $0.04 - 0.08 \times 10^9 \text{ m}^{-2}$  leads to an increase in the stability of ceramics by more than 3.0 – 3.5 times. In this case, the most

significant changes in stability indicators are observed when the dislocation density changes from  $0.02 \times 10^9 \text{ m}^{-2}$  to  $0.04 \times 10^9 \text{ m}^{-2}$ , while a further increase in dislocation density does not have a significant effect on the change in degradation resistance indicators.

Further research in this direction will be related to the study of the prospects for using the dislocation strengthening factor to maintain the stability of composite ceramics under external influences, including gas swelling and radiation damage caused by exposure to both low-energy and high-energy ions. The main goal of such research will be to expand

opportunities in the search for alternative structural materials with high thermal conductivity, strength, and resistance to external influences.

### Acknowledgements

This work was carried out within the framework of program-targeted funding (program No. BR21882237 «Development and research of advanced composite materials for energy and the fuel cycle») with the support of the Science Committee of the Ministry of Science and Higher Education of the Republic of Kazakhstan.

### References

1. Belmonte M. Advanced ceramic materials for high temperature applications // *Advanced engineering materials*. – 2006. – Vol. 8, №. 8. – P. 693-703. <https://doi.org/10.1002/adem.200500269>
2. Cramer C. L., Ionescu E., Graczyk-Zajac M., Nelson A. T., Katoh Y., Haslam J. J. Minary-Jolandan M. Additive manufacturing of ceramic materials for energy applications: Road map and opportunities // *Journal of the European Ceramic Society*. – 2022. – Vol. 42. №. 7. – P. 3049-3088. <https://doi.org/10.1016/j.jeurceramsoc.2022.01.058>
3. Otitoju T. A., Okoye P. U., Chen G., Li Y., Okoye M. O., Li S. Advanced ceramic components: Materials, fabrication, and applications // *Journal of industrial and engineering chemistry*. – 2020. – Vol. 85. – P. 34-65. <https://doi.org/10.1016/j.jiec.2020.02.002>
4. George E. P., Curtin W. A., Tasan C. C. High entropy alloys: A focused review of mechanical properties and deformation mechanisms // *Acta Materialia*. – 2020. – Vol. 188. – P. 435-474. <https://doi.org/10.1016/j.actamat.2019.12.015>
5. Zhang W. Tribology of SiC ceramics under lubrication: Features, developments, and perspectives // *Current Opinion in Solid State and Materials Science*. – 2022. – Vol. 26. №. 4. – P. 101000. <https://doi.org/10.1016/j.cossms.2022.101000>
6. Zhang Z., Wu H., Zhang S., Wang Y., Zhang Y., Liu C., Qin M. The Quantitative investigation of the lattice oxygen and grain edge oxygen on the thermal conductivity of aluminum nitride ceramics // *Journal of the European Ceramic Society*. – 2023. – Vol. 43. №. 2. – P. 313-320. <https://doi.org/10.1016/j.jeurceramsoc.2022.10.023>
7. Rauchenecker J., Rabitsch J., Schwentenwein M., Konegger T. Additive manufacturing of aluminum nitride ceramics with high thermal conductivity via digital light processing // *Open Ceramics*. – 2022. – Vol. 9. – P. 100215. <https://doi.org/10.1016/j.oceram.2021.100215>
8. Luo C., Zhang Y., Deng T. Pressureless sintering of high performance silicon nitride ceramics at 1620 C // *Ceramics International*. – 2021. – Vol. 47, №. 20. – P. 29371-29378. <https://doi.org/10.1016/j.ceramint.2021.07.104>
9. Hu F., Xie Z. P., Zhang J., Hu Z. L., An D. Promising high-thermal-conductivity substrate material for high-power electronic device: Silicon nitride ceramics // *Rare Metals*. – 2020. – Vol. 39. – P. 463-478. <https://doi.org/10.1007/s12598-020-01376-7>
10. Yasnikov I. S., Kaneko Y., Uchida M., Vinogradov A. The grain size effect on strain hardening and necking instability revisited from the dislocation density evolution approach // *Materials Science and Engineering: A*. – 2022. – Vol. 831. – P. 142330. <https://doi.org/10.1016/j.msea.2021.142330>
11. Fan H., Wang Q., El-Awady J. A., Raabe D., Zaiser M. Strain rate dependency of dislocation plasticity // *Nature communications*. – 2021. – Vol. 12, №. 1. – P. 1845. <https://doi.org/10.1038/s41467-021-21939-1>
12. Li Z., Cui Y., Yan W., Zhang D., Fang Y., Chen Y., Wang Y. M. Enhanced strengthening and hardening via self-stabilized dislocation network in additively manufactured metals // *Materials Today*. – 2021. – Vol. 50. – P. 79-88. <https://doi.org/10.1016/j.mattod.2021.06.002>
13. Srivastava K., Weygand D., Caillard D., Gumbsch P. Repulsion leads to coupled dislocation motion and extended work hardening in bcc metals // *Nature Communications*. – 2020. – Vol. 11, №. 1. – P. 5098. <https://doi.org/10.1038/s41467-020-18774-1>
14. Gu L., Meng A., Chen X., Zhao Y. Simultaneously enhancing strength and ductility of HCP titanium via multi-modal grain induced extra  $c+a$  dislocation hardening // *Acta Materialia*. – 2023. – Vol. 252. – P. 118949. <https://doi.org/10.1016/j.actamat.2023.118949>
15. Kenzhina I. E., Kozlovsky A. L., Tolenova A. U. Study of the influence of size effects in  $x\text{Si}_3\text{N}_4-(1-x)\text{ZrO}_2$  ceramics obtained by the solid-phase method on the strength characteristics // *Recent Contributions to Physics (Rec.Contr.Phys.)*. – 2024. – Vol. 88, No.1. – P. 49-56. <https://doi.org/10.26577/RCPH.2024v88i1a07>
16. Yokota H., Abe H., Ibukiyama M. Effect of lattice defects on the thermal conductivity of  $\beta\text{-Si}_3\text{N}_4$  // *Journal of the European Ceramic Society*. – 2003. – Vol. 23, №. 10. – P. 1751-1759. [https://doi.org/10.1016/S0955-2219\(02\)00374-6](https://doi.org/10.1016/S0955-2219(02)00374-6)
17. Duan Y., Liu N., Zhang J., Zhang H., Li X. Cost effective preparation of  $\text{Si}_3\text{N}_4$  ceramics with improved thermal conductivity and mechanical properties // *Journal of the European Ceramic Society*. – 2020. – Vol. 40, №. 2. – P. 298-304. <https://doi.org/10.1016/j.jeurceramsoc.2019.10.003>

18. Lu T., Wang T., Jia Y., Ding M., Shi Y., Xie J., Fan L. Fabrication of high thermal conductivity silicon nitride ceramics by pressureless sintering with MgO and Y<sub>2</sub>O<sub>3</sub> as sintering additives //Ceramics International. – 2020. – Vol. 46, №. 17. – P. 27175-27183. <https://doi.org/10.1016/j.ceramint.2020.07.198>
19. Li W., Wu Y., Huang R., Ye S., Lin H. T. Effect of Si addition on the mechanical and thermal properties of sintered reaction bonded silicon nitride //Journal of the European Ceramic Society. – 2017. – Vol. 37, №. 15. – P. 4491-4496. <https://doi.org/10.1016/j.jeurceramsoc.2018.10.006>
20. Li Y., Kim H. N., Wu H., Kim M. J., Ko J. W., Park Y. J., Kim H. D. Enhanced thermal conductivity in Si<sub>3</sub>N<sub>4</sub> ceramic with the addition of Y<sub>2</sub>Si<sub>4</sub>N<sub>6</sub>C //Journal of the American Ceramic Society. – 2018. – Vol. 101, №. 9. – P. 4128-4136. <https://doi.org/10.1111/jace.15544>
21. Zhu X., Zhou Y., Hirao K. Effects of processing method and additive composition on microstructure and thermal conductivity of Si<sub>3</sub>N<sub>4</sub> ceramics //Journal of the European ceramic Society. – 2006. – Vol. 26, №. 4-5. – P. 711-718. <https://doi.org/10.1016/j.jeurceramsoc.2005.07.027>
22. Bulatov V. V., Hsiung L. L., Tang M., Arsenlis A., Bartelt M. C., Cai W., De La Rubia T. D. Dislocation multi-junctions and strain hardening //Nature. – 2006. – Vol. 440, №. 7088. – P. 1174-1178. <https://doi.org/10.1038/nature04658>
23. Huang X., Hansen N., Tsuji N. Hardening by annealing and softening by deformation in nanostructured metals //Science. – 2006. – Vol. 312, №. 5771. – P. 249-251. <https://doi.org/10.1126/science.1124268>

**Information about authors:**

*Kenzhina Inesh (corresponding author), PhD, is a Leading Researcher of Satbayev University, (Almaty, Kazakhstan) e-mail: kenzhina@physics.kz;*

*Kozlovskiy Artem, PhD, is a Leading Researcher of Satbayev University, (Almaty, Kazakhstan) e-mail: kozlovskiy.a@inp.kz;*

*Blynskiy Petr, PhD, is a Leading Researcher of Satbayev University, (Almaty, Kazakhstan) e-mail: Blynskiy@physics.kz;*

*Tolenova Aktolkyn, PhD – student, is a researcher of Satbayev University, (Almaty, Kazakhstan) e-mail: aktolkyn@tolen@gmail.com*

## Concise review of recent advances and applications of the electron linear accelerator ELU-4 in scientific and technical fields

Zh.T. Nakysbekov<sup>1\*</sup>, D. Ismailov<sup>1,2</sup>, S. Bellucci<sup>3</sup>,  
T.A. Tukhfatullin<sup>4</sup>, O.V. Bogdanov<sup>5</sup>, B.A. Tronin<sup>1</sup>,  
K.N. Turmanova<sup>1</sup>, S.G. Suyundykova<sup>1</sup>, V.F. Grichshe,  
M.I. Pshikov<sup>1</sup> and A.Ye. Alzhanova<sup>7</sup>

<sup>1</sup>Al-Farabi Kazakh National University, Almaty, Kazakhstan

<sup>2</sup>K.I. Satpayev Kazakh National Research Technical University, Almaty, Kazakhstan

<sup>3</sup>INFN-Laboratori Nazionali di Frascati, Frascati, Italy

<sup>4</sup>Almaty Branch of NRNU MEPhI, Almaty, Kazakhstan

<sup>5</sup>Tomsk Polytechnic University, Tomsk, Russia

<sup>6</sup>Ionosphere Institute LLP, Republic of Kazakhstan, Almaty, Kazakhstan

<sup>7</sup>L.N. Gumilyov Eurasian National University, Astana, Kazakhstan

\*e-mail: Zhassulan.Nakysbekov@gmail.com

(Received February 8, 2024; received in revised form April 16, 2024; accepted May 5, 2024)

The analysis presented in this concise review is directed towards evaluating the contemporary trends and practical implementations of the ELU-4 electronic linear accelerator across a broad spectrum of scientific and technological domains. The ELU-4 linear electron accelerator represents a key technological achievement in the field of accelerator technology in general and linear electronic accelerators in particular. Various aspects of the use of ELU-4 are considered, starting from its application in medicine, ecology, verification of computer models for calculating the effects of radiation, space applications, research on the effect of electronic irradiation on various materials and devices, including semiconductor devices, ending with its fundamental research of materials. Current data presented in scientific articles and reports from the last ten years are researched and analysed. This succinct review not only underscores the conventional applications of this accelerator but also underscores its potential in nascent fields of science and technology. The incorporation of ELU-4 into diverse research and engineering endeavors presents notable prospects for innovation and the advancement of scientific knowledge frontiers.

**Key words:** accelerator, electron, ELU-4, irradiation, radiation.

**PACS number(s):** 07.77.Ka.

### 1 Introduction

Electronic linear accelerators hold a distinguished position among the principal instruments in contemporary science and technology, offering unparalleled opportunities for investigating materials and processes at the molecular level [1-5]. Within this concise review, we aim to delineate the recent advancements and diverse applications of the ELU-4 electronic linear accelerator across various scientific and technical domains.

As a flagship representative of the current generation of electronic linear accelerators, ELU-4 garners attention in research domains concerned

with the ramifications of irradiation on materials. It conducts experiments geared towards scrutinizing the effects of electron irradiation on a plethora of materials, encompassing semiconductors, composites tailored for space applications, and materials integral to radiation shielding endeavors [6-19].

Moreover, ELU-4 assumes a pivotal role in validating and complementing computational models, thereby fortifying their accuracy in matters pertaining to the effects of radiation on materials [20-22]. Furthermore, the accelerator finds utility in fundamental research endeavors aimed at elucidating the impact of irradiation on materials [23, 24] and the



synthesis of novel materials endowed with distinctive properties [25, 26].

The principal objective of this article is to furnish an concise overview of the prevailing applications of ELU-4 in scientific research and engineering realms. We will delve into its contributions across a myriad of domains, encompassing materials science, radiation protection, space technology, and fundamental scientific inquiry. The outcomes and potentialities associated with ELU-4 usage signify a substantial stride towards the advancement of contemporary technologies and foundational scientific research.

## 2 Effect of irradiation at the ELU-4 electron accelerator on the electrical properties of materials

The work conducted by Mustafayev S.N. and co-authors focuses on investigating the repercussions of electron irradiation on TlGaS<sub>2</sub> single crystals, materials renowned for their responsiveness to visible and X-ray radiation. Following irradiation with varying doses of electron flux from the ELU-4 accelerator, operating at an energy of 4 MeV, ranging from  $2.1 \cdot 10^{12}$  to  $2.4 \cdot 10^{20}$  e/cm<sup>2</sup>, notable alterations in dielectric properties and conductivity are observed. These alterations manifest in a reduction of the real component of the complex dielectric constant at elevated frequencies, an augmentation in conductivity, and a shift in the mode of charge transfer through localized states proximate to the Fermi level [27].

In recent years, there has been a burgeoning utilization of low-dimensional semiconductor materials, including 2D chalcogenides, in micro- and nanoelectronics, photonics, and spintronics. Investigating the impacts of X-rays, gamma radiation, and high-energy charged particle fluxes on the physical characteristics of semiconductor materials has emerged as an imperative task. Asadov S.M. and Mustafaeva S.N., in their research, scrutinized layered single crystals of gallium-containing chalcogenide (GaS), grown utilizing the Bridgman method, exhibiting p-type conductivity. These single crystals displayed a hexagonal lattice structure characterized by lattice parameters  $a = 3.58 \text{ \AA}$  and  $c = 15.47 \text{ \AA}$ .

The authors discerned trends in alterations of dielectric properties and transverse conductivity in layered GaS single crystals contingent upon electron irradiation with an energy of 4 MeV and diverse radiation doses ( $2 \cdot 10^{12}$  and  $10^{13} \text{ cm}^{-2}$ ). It was revealed that irradiation engenders an augmentation in the real component of the complex dielectric constant, a reduction in the imaginary component, the dielectric loss tangent, and AC conductivity. Notably, at specific

irradiation doses ( $2 \cdot 10^{12} - 10^{13} \text{ cm}^{-2}$ ), conduction losses were observed in GaS. The modifications in AC conductivity in GaS, both pre- and post-irradiation, were attributed to the hopping mechanism of charge transfer along states localized proximate to the Fermi level, exhibiting a characteristic frequency dependence of AC conductivity on  $f^{0.7-0.8}$  within the frequency range  $f = 5 \cdot 10^4 - 10^7 \text{ Hz}$ .

Furthermore, it was found that at temperatures ranging from 140-238 K, layered GaS single crystals demonstrate hopping conductivity across their layers under a constant electric field, predicated on a variable hopping length along states localized in the vicinity of the Fermi level. At temperatures below 140 K, activation-free hopping conduction was discerned.

The analysis of DC- and AC-conductivity of GaS single crystals enabled the authors to estimate the density of states proximate to the Fermi level, their energy dispersion, average hopping distances, and activation energy. Additionally, the article investigated the impact of irradiation on parameters of states localized within the band gap [28].

## 3 Effect of electron irradiation on the characteristics of electronic components and devices

In their study, O. V. Dvornikov and colleagues [29] investigate the impact of a 4 MeV electron flux and gamma radiation from <sup>60</sup>Co on the characteristics of silicon complementary bipolar transistors (BT) and a broadband operational amplifier (OPA) constructed based on them.

The operational amplifier functions comprise a voltage-controlled current source, an output emitter follower, and PTAT (Proportional To Absolute Temperature) current sources. The circuit is designed with high radiation resistance mechanisms, including input current compensation, bias current stabilization, zero offset voltage minimization, and performance maintenance.

The authors conduct measurements on the current transfer coefficient, cutoff frequency, Early voltage, forward voltage drop across the emitter junction, current consumption, zero offset voltage, and open-loop voltage gain of both the BT and op-amp before and after irradiation. Notably, despite a significant reduction in the current transfer coefficient of the transistors, the op-amp parameters exhibit minimal change when subjected to ionizing radiation.

Their findings underscore that an op-amp constructed using complementary BT serves as a radiation-resistant analog device suitable

for incorporation into systems tasked with preprocessing signals from multi-element photodetectors [29].

The work of Miskevich S. A. et al. concentrates on developing semiconductor devices resilient to ionizing radiation for application in nuclear power engineering and spacecraft. The authors have proposed a physical and mathematical model delineating the radiative alteration in the lifetime of charge carriers in silicon under the influence of a

flux of 4 MeV electrons. They devised a method to calculate the change in hole lifetime and evaluated the electrical characteristics of a bipolar transistor post-irradiation. The results reveal a significant decline in the transistor characteristics upon irradiation with fast electrons. As depicted in Figure 1 and Figure 2, the developed model concurs with experimental observations, facilitating its utilization in software for modeling radiation-induced changes in semiconductor devices [30].

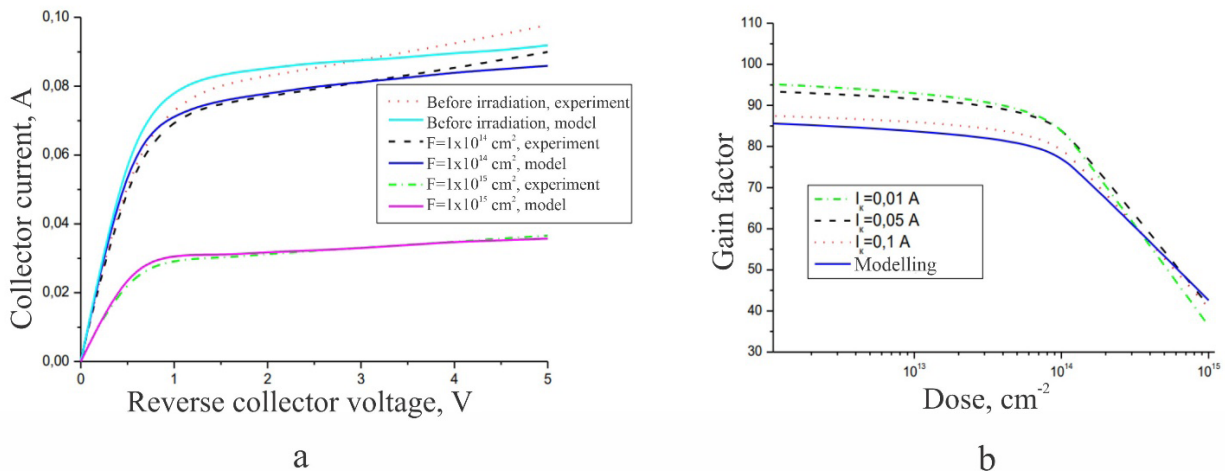


**Figure 1** – Electrical characteristics of the transistor before and after irradiation with 4 MeV electrons [30]

In another paper, Miskevich S.A. et al. [31] investigated the spatial distribution of nonequilibrium minority charge carriers in bipolar transistors before and during radiation exposure. The analysis focused on the p-p-p bipolar transistor KT3107A manufactured by INTEGRAL JSC. The device irradiation was conducted using the linear accelerator ELU-4 with electron energy  $E_e = 4 \text{ MeV}$ . The pulse duration was  $5 \mu\text{s}$ , and the pulse repetition rate was 200 Hz. The electron flux density varied within the range of  $(5-10)10^{11} \text{ cm}^{-2}\text{c}^{-1}$ , while the electron fluence ranged from  $5 \cdot 10^{13}$  to  $2 \cdot 10^{15} \text{ cm}^{-2}$  [32].

Both modeling and experimental investigations revealed consistent results: a notable deterioration in the electrical characteristics of bipolar transistors upon irradiation with fast electrons of 4 MeV energy. This deterioration was evident in the decrease of output current and gain, along with an increase in base current (refer to Fig. 1b) [32].

Strelchuk A. M. et al. [33] conducted a study on the radiation resistance of commercial Schottky

diodes based on silicon carbide (4H-SiC) with varying doping levels. Three types of diodes with differing levels of n-type conductivity doping were investigated. These diodes underwent irradiation with electrons and protons of different energies: 0.9 MeV electron irradiation was conducted at the RTE-1V accelerator, 3.5 MeV at the ELU-4 accelerator, and 15 MeV proton irradiation was carried out at the MHz-20 cyclotron.

Through analysis of current and voltage under forward and reverse bias conditions, the researchers identified several effects associated with the impact of irradiation on diode characteristics. Notably, they observed that the series resistance emerged as the most radiation-sensitive parameter across all diode types (refer to Fig. 3).

The researchers also observed a threshold dose of irradiation, below which the resistance practically remains unchanged. However, upon surpassing this threshold, the series resistance of the diodes exhibited a sharp increase, demonstrating a step

dependence with an exponent ranging from 10 to 17, and reaching values of about  $10^9$  Ohm without signs of saturation. In contrast, the breakdown voltage and pre-breakdown current were less sensitive to irradiation and began to exhibit significant changes only at higher irradiation doses [33].

The study conducted by Bumai Yu. A. *et al.* [34] investigates the impact of high-energy charged particles on light-emitting diodes (LEDs) based on heterostructures. It demonstrates that irradiation with fast electrons (4 MeV) can induce defects in the diode structure, consequently affecting their optical and electrical characteristics.

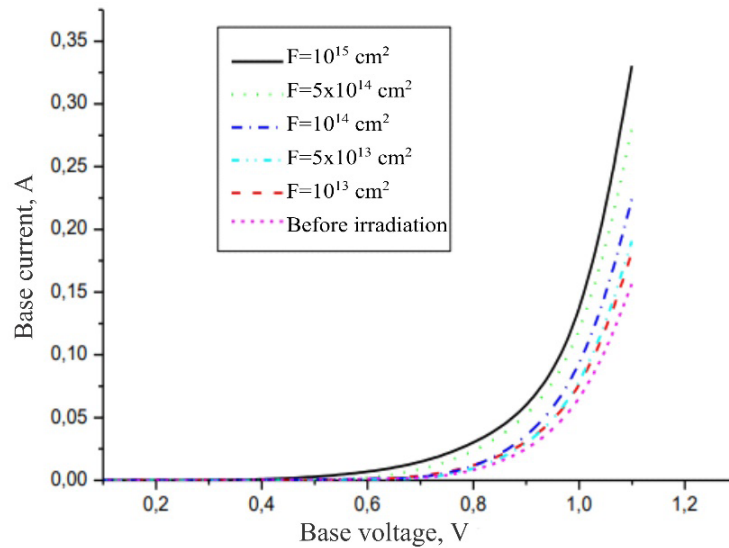


**Figure 2** – Input characteristics of BT before and after electron irradiation [30]

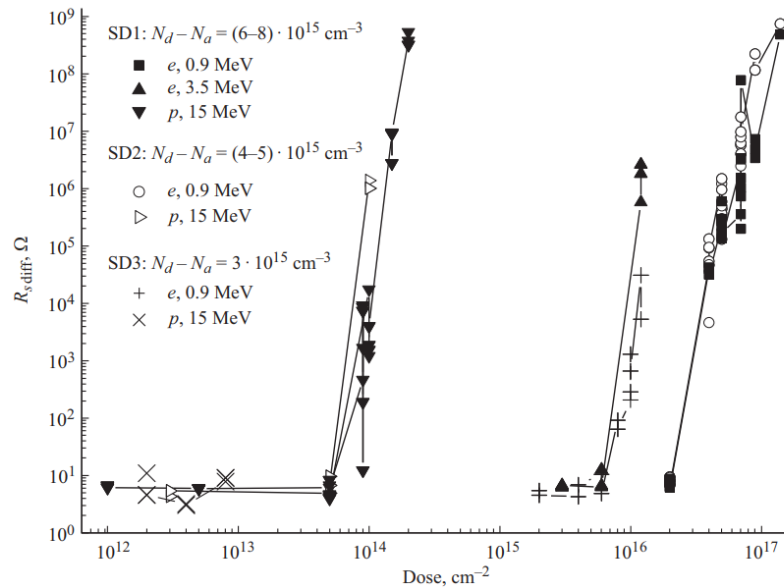


**Figure 3** – Dependences of the series differential resistance of Schottky diodes of the first (SD1), second (SD2) and third (SD3) types on the irradiation dose by electrons (e) with energies of 0.9, 3.5 MeV and protons (p) with energy of 15 MeV [33]

Various Helio LEDs (1 W) with differing luminescence and low-power Nichia LEDs (90 mV) were employed in the experiment. Irradiation of all diodes was carried out using an ELU-4 accelerator with varying parameters of electron energy and fluence.

The findings of the paper reveal that nitride-based LEDs exhibit greater resilience to degradation under irradiation compared to phosphide-based LEDs, particularly in the red color range. Alterations in the light emission spectra and Urbach energy suggest a potential increase in defects at the interfaces.

Furthermore, the authors observed that with increasing fluence of fast electrons, the temperature of the electronic subsystem decreases for nitride LEDs but increases for red diodes, thereby influencing their luminous characteristics.

In conclusion, the study underscores the influence of irradiation on the electrical and optical properties of diverse types of light-emitting diodes. It delineates patterns of changes under irradiation and speculates on the feasibility of restoring the optical power of irradiated nitride-based diodes [34].

#### **4 Application of ELU-4 for space applications and radiation protection**

Materials employed in space applications are subject to electron fluxes spanning a broad energy spectrum. These particles can induce thermal ionization within dielectric materials, leading to the accumulation of uncompensated electric charge, thus engendering radiation electrification and substantial alterations in dielectric electrical properties. Consequently, the electrical breakdown of dielectrics stands as a primary cause for the malfunction of electronic and electrical spacecraft equipment. N. I. Cherkashin's study [35] is dedicated to investigating the impact of a beam of fast electrons on a polymer composite utilized for cosmic radiation shielding.

Utilizing the Monte Carlo method and conducting experimental irradiation of composite samples at the ELU-4 electron accelerator, the author reveals that the depth of maximum accumulated energy concentration within the composite varies: 1.5 mm for electrons with an energy of 1 MeV, 2.7 mm for 1.5 MeV, and 4.6 mm for 2 MeV. Relative to protective materials comprising heavy metals like lead or bismuth, the effective range within the considered composite is several times greater. Additionally, the intensity of bremsstrahlung radiation is notably reduced, representing an advantageous characteristic compared to heavy metal-based materials.

The study demonstrates that a polymer composite consisting of fluoroplastic filled with modified bismuth oxide exhibits high radiation resistance and protective efficacy attributable to the presence of a space charge [35].

In the work by Panyushkin N.N. [36], the feasibility of calculating and experimentally predicting radiation dose effects and the radiation resistance of CMOS integrated circuits (ICs) is explored. The approach centers on utilizing predetermined parameters – specifically, the initial switching voltage and the absolute increase in power source current post-radiation testing.

The article highlights that prevailing methods for predicting product durability necessitate sample irradiation and prolonged annealing at elevated temperatures. In contrast, the author's method obviates these processes, relying instead on initial values of select electrical parameters controlled during product fabrication. This methodology enables the determination of product durability via test exposure to ionizing radiation both before and after irradiation. The resultant measurement data facilitate the development of models ensuring product radiation resistance aligns with technical specifications. Two parameters – threshold switching voltage and current consumption – are utilized for prediction due to variations in production lots and sample sensitivity to radiation effects. The method hinges on theoretically and experimentally ascertaining the radiation resistance of CMOS integrated circuits utilizing initial values of predicted electrical parameters controlled during production.

Experimental data concerning the CMOS IC 564 LE5, comprising five samples of 2 NOR gates, were employed. Irradiation was conducted using the ELU-4 linear electron accelerator with an energy of 4 MeV within a fluence range spanning 0.1 to 3.0 times the critical electron flux for this IC type. The study yielded the following outcomes: a predicted error of approximately 7% for the threshold switching voltage and about 4% for current consumption. These values closely align with measurement error, affirming the method's efficacy in selecting more resilient samples and ensuring requisite radiation resistance [36].

Bogatyrev Yu.V. and colleagues [37] present findings from studies on radiation protection utilizing tungsten-copper composites. The efficacy of these shields is evaluated based on transistor parameter changes under electron irradiation, with absorbed dose in the IMO crystal being calculated. Experimental evidence demonstrates that these screens reduce radiation by factors ranging from

10 to  $10^4$  in the energy range of 0.5-6 MeV. The experimental methodology encompasses screen fabrication, morphological and chemical composition analysis, and irradiation using the ELU-4 linear electron accelerator (refer to Figure 4).

The authors have successfully developed W77.5Cu22.5 composite materials through solid-phase synthesis for application as radiation shields

in metal-ceramic integrated circuits (ICs). These materials exhibit excellent solderability using inert fluxes and comply with contemporary technological requirements. Experimental investigations in the study demonstrated that shields ranging in thickness from 1.21 to 1.49 mm yield maximum shielding efficiency ( $K_s = 143-155$ ) for p-MOS transistors like IN74AC04.

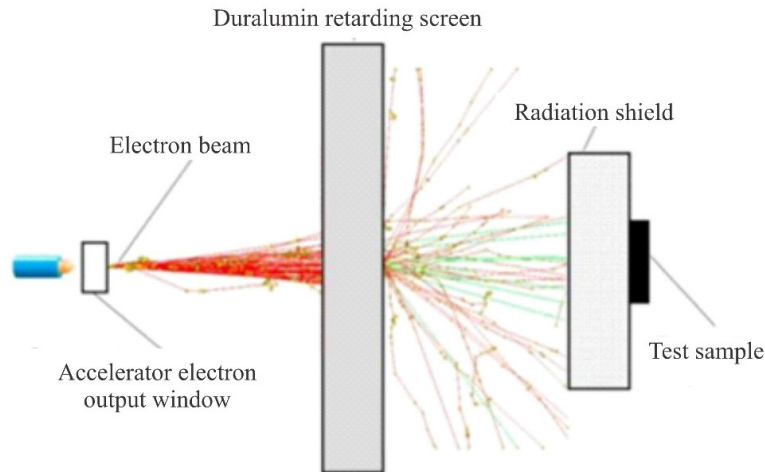


**Figure 4** – Schematic of radiation shield testing [37]

Modelling efforts conducted by the authors illustrate that the developed  $W_{77.5}Cu_{22.5}$  screens effectively attenuate electron radiation within the energy range of 0.5 to 6 MeV ( $K_s, 4040$ ). Regarding protons of cosmic origin (with energies spanning from 0.04 to 500 MeV for a  $60^\circ$  orbital inclination and a circular orbit at an altitude of 300 km), these screens provide up to a 6-fold reduction in absorbed dose.

Furthermore, the study reveals that the effectiveness of radiation shields may vary depending on the orbit type. Optimal results were attained in orbits characterized by high electron contribution, such as GEO, GLONASS, and VEO. Conversely, for orbits with a predominant proton contribution, like ISS and circular polar orbits, the screens exhibited reduced efficacy.

Overall, the research findings underscore the promising potential of the developed material and technology for fabricating more radiation-resistant enclosures for the next generation of electronic components utilized in rocket and space technology [37].

In their work, D. I. Tishkevich *et al.* [38] underscore the significance of bismuth as a promising material for safeguarding microelectronics products from ionizing radiation. Studies reveal that bismuth coatings exhibit distinct crystalline structures that

evolve with increasing thickness and the introduction of various additives. Experimental investigations demonstrate the high efficacy of bismuth shields at specific thickness values (around  $2 \text{ g/cm}^2$ ) and attenuation coefficients (equal to 156).

Particular emphasis is placed on the potential of bismuth for radiation shielding, considering its intrinsic properties and optimal exposure parameters. The fabrication technique for these coatings involves electrochemical deposition, supplemented by Ni-P chemical deposition to enhance adhesion. Experiments investigating the radiation-protective properties of bismuth-based shields on test structures of p-channel MOPTs (CMOS IC elements) subjected to electron irradiation with energies ranging from 1.6 to 1.8 MeV and exposure doses up to  $5 \cdot 10^{14} \text{ cm}^2$  indicate that as the reduced shield thickness increases from 1.1 to  $2.7 \text{ g/cm}^2$ , the shielding efficiency coefficient  $K_s$  rises from 95 to 165. The relationship between  $K_s$  and reduced thickness can be modeled by a second-degree polynomial. Optimal values of reduced thickness, considering mass and dimensional parameters, lie approximately within the range of  $1.7-2.0 \text{ g/cm}^2$ . Beyond a thickness of  $2 \text{ g/cm}^2$ , increasing shield thickness does not significantly enhance  $K_s$ , primarily due to the

prevalence of absorbed dose from braking radiation by the protected samples.

The paper concludes by accentuating the potential efficacy of bismuth as an efficient material for radiation protection in microelectronics [38].

It is noteworthy that contemporary space exploration is poised on the brink of pioneering new spacefaring technologies. Nations such as the United States of America, Russia, Europe, China, and Japan are vigorously pursuing the discovery and development of novel structural and functional materials to enhance space technology systems. Both fundamental and applied research endeavors are underway, spanning the realms of near and deep space, to facilitate the study and peaceful exploration of outer space. Concurrently, ground and space infrastructure is being established and refined, while innovative technologies are being forged in diverse domains including space materials science and instrumentation, natural resource and geophysical monitoring, and space biotechnology and medicine, with the aim of addressing the socio-economic challenges facing spacefaring nations.

The involvement of Kazakhstani cosmonauts in space experiments aboard manned complexes has yielded invaluable findings, laying the groundwork for the emergence of a novel scientific discipline in Kazakhstan: space materials science and instrumentation.

Therefore, in the study by Musabayev et al. [39], the findings regarding the comprehensive effects of outer space factors, including radiation, on materials and the devices derived from them are presented. The paper delineates a model illustrating the effects of single heavy cosmic ray nuclei (CRN) on components of onboard electronic equipment. Typically, extensive groundwork is conducted under terrestrial conditions to simulate the radiation effects on materials employed in space equipment before embarking on space experiments aboard manned complexes.

Given the aforementioned context, it is imperative to investigate the influence of space radiation, including its electronic component, on materials and associated devices under terrestrial simulation conditions. Linear accelerators, cyclotrons, synchrotrons, and other radiation sources are commonly employed for this purpose.

### **5 Effects of irradiation on materials, defect formation and synthesis of new materials**

The paper by Voitovich A. P. et al. [40] delves into the characteristics of radiation-induced defects in crystals, their utility in the detection and measurement

of ionizing radiation in electronics, and the potential application of nanocrystals harboring such defects as biological sensors. The researchers irradiated wafers with a robust stream of high-energy electrons, possessing an energy of 4 MeV and a fluence of  $10^{13}$  electrons/cm<sup>2</sup>, at room temperature utilizing an Electronica ELU-4 linear electron accelerator for several seconds. This irradiation induced defects in the material; however, these defects did not propagate far enough to interact with other parts of the material and elicit reactions. The authors demonstrated that the fragmentation of irradiated LiF crystals engendered new defects, with the concentrations of these defects remaining stable at room temperature for prolonged periods. Furthermore, UV irradiation on nanocrystals subsequent to the completion of center formation processes significantly amplifies the defect concentration. Additionally, various radiation defects were observed in unirradiated nanocrystals, underscoring the significance of processes occurring during crystal fragmentation [40].

Naumova O. V. et al. [41] conducted a study to investigate the impact of ionizing radiation on mineral raw materials used in silicon production, a crucial material in solar energy applications. The experiment involved irradiating chalcedony powder with braking gamma-rays using an accelerator. The duration of irradiation was determined by the accelerator parameters, including beam current, power, and distance to the irradiated object.

This nano-exposure technique facilitated the intensification of production processes, leading to alterations in the material's microstructure and the formation of structures characterized by high homogeneity, density, and uniform distribution of impurities. The mechanism underlying the effect of braking gamma-rays on powder raw materials lies in their potent and diverse impact.

The authors assert that the developed methodology, based on irradiating raw components with braking gamma-rays, has demonstrated the possibility of controlled alteration of material properties, which holds significant scientific and practical importance. This approach enables the production of materials with unique properties inaccessible by existing methods.

Moreover, the authors suggest that utilizing accelerator technology as a "tool" for controlling complex processes in manufacturing presents novel opportunities for addressing important challenges, including enhancing the parameters of semiconductor structures.

The article presents an experiment that, for the first time, enables the examination of structural

changes occurring in mineral raw materials during the production of polycrystalline silicon under the influence of ionizing radiation. The findings of the study are expected to enhance the technologies for deep processing of rock-forming minerals based on chalcedony, leading to more effective enrichment and purification of raw materials during silicon production.

These results highlight remarkable changes in the structure of technical silicon products achieved using radiation technology. With the high homogeneity of the obtained materials, it becomes feasible to fabricate solar cells with reproducible parameters for new light-emitting devices.

Furthermore, the study revealed the potential of obtaining nanostructured materials in the creation of complex silicon structures incorporating alloying additives. This advancement could lead to the production of photovoltaic cells capable of efficiently harnessing the entire spectrum of solar energy [41].

## **6 Application of the ELU4 accelerator in the verification of computer models to assess the effects of electron irradiation on materials**

The scientific team led by Prof. Pivovarov Y.L. at Tomsk Polytechnic University has undertaken several studies in recent years focusing on various aspects of the interaction between relativistic electrons and ions with oriented crystals.

In theoretical studies and computer simulations reported in [42-45], investigations were conducted on the scattering of 255 MeV electrons by axial and in-plane channeling in silicon crystals. Experiments were conducted at the linear accelerator of the synchrotron SAGA-LS (Japan). The simulation outcomes exhibit good agreement with experimental data, indicating the applicability of the utilized models in the computer code developed by the authors [46].

Another series of works explored the generation of photons possessing orbital angular momentum, known as twisted photons, using different emission schemes. These twisted photons offer additional degrees of freedom and can potentially overcome the diffraction limit, increase the bandwidth of telecommunication channels, and facilitate quantum cryptography. Calculations presented in [47] evaluated the probability of emission of twisted photons by axially symmetric particle clots, while [48] demonstrated that transient radiation and Vavilov-Cherenkov radiation possess orbital angular momentum for narrow relativistic Gaussian beams of electrons and ions. Additionally, investigations

in [49, 50] examined the generation of twisted photons in axial and in-plane channeling of 255 MeV electrons in thin silicon crystals. The periodicity of the projection of the total angular momentum of a photon as a function of photon energy was also uncovered in [50].

In a separate line of inquiry, theoretical studies were conducted on positron generation utilizing a hybrid scheme [51]. In this scheme, electrons pass through an oriented crystal (silicon or tungsten) to generate radiation, which is then fed into an amorphous converter where electron-positron pairs are generated. These studies, detailed in [52], encompassed computer modeling for both coherent and incoherent braking radiation in crystalline targets of silicon and germanium. Calculations were performed to determine the optimal thickness of the converter for maximal positron yield, and the energy spectrum of emitted positron beams was calculated for the optimal converter thickness.

These research endeavors hold relevance for the ELU-4 accelerator. Conducting similar investigations with the ELU-4 accelerator could unveil novel characteristics of relativistic electron treatment and enable the production of radiation with unique properties.

## **7 Conclusions**

In conclusion, electron linear accelerators, notably the ELU-4, stand as indispensable assets in contemporary scientific and technical exploration. The comprehensive review and analysis of data underscore the broad spectrum of applications afforded by the ELU-4 across diverse fields of science and technology.

Foremost among its applications is the probing of material responses to electron irradiation. This facet finds utility in investigations spanning semiconductors, space-grade composites, and the characterization of radiation shielding materials. The ELU-4 furnishes an optimal environment for such studies, facilitating nuanced examinations of material behaviors under varying irradiation levels.

Moreover, electron linear accelerators have proven instrumental in tasks ranging from validating computational models and assessing radiation shielding materials to fundamental inquiries into irradiation effects and materials synthesis. These endeavors constitute pivotal pillars supporting the advancement of contemporary technology and the frontiers of scientific inquiry.

In light of these findings, the ELU-4 emerges as a versatile and potent tool across scientific research

and engineering domains. Its exceptional capabilities in electron irradiation, coupled with cutting-edge analytical and modeling methodologies, position it as an indispensable resource for the scientific and

engineering community. It remains at the forefront of innovative research and development endeavors, driving progress and fostering breakthroughs in knowledge and technology.

## References

1. Mehnert R. Review of industrial applications of electron accelerators // *Nuclear Instruments and Methods in Physics Research Section B: Beam Interactions with Materials and Atoms*. – 1996. – Vol. 113. – P. 81-87. [https://doi.org/10.1016/0168-583X\(95\)01344-X](https://doi.org/10.1016/0168-583X(95)01344-X)
2. Martins M.N., Tiago F.S. Electron accelerators: History, applications, and perspectives // *Radiation Physics and Chemistry*. – 2014. – Vol. 95. – P. 78-85. <https://doi.org/10.1016/j.radphyschem.2012.12.008>
3. Rodríguez-Fernández L. Particle accelerator applications: ion and electron irradiation in materials science, biology and medicine // *AIP Conference Proceedings*. American Institute of Physics. – 2010. – Vol. 1271. – P. 159-179. <https://doi.org/10.1063/1.3495646>
4. Kutsaev S. V. Advanced technologies for applied particle accelerators and examples of their use // *Technical Physics* 66. – 2021. – Vol. 66. – P. 161-195. <https://doi.org/10.1007/s13201-018-0645-6>
5. Korolkov I.V., Mashentseva A.A., Güven O., Gorin Y.G., Kozlovskiy A.L., Zdorovets M.Z., Zhidkov I.S., Cholach S.O. Electron/gamma radiation-induced synthesis and catalytic activity of gold nanoparticles supported on track-etched poly (ethylene terephthalate) membranes // *Materials Chemistry and Physics*. – 2018. – Vol. 217. – P. 31-39. <https://doi.org/10.1016/j.matchemphys.2018.06.039>
6. Lepukhov E. Protection of read-out electronics from ionizing radiation // *Lappeenranta–Lahti University of Technology LUT School of Engineering Science*. Master's thesis. – 2022. – P. 54.
7. Romanova M., Avotina L., Andrulevicius M., Dekhtyar Y., Enichek G., Kizane G., Novotný M., Pajuste E., Pokorný P., Yager T., Zaslavski A. Radiation resistance of nanolayered silicon nitride capacitors // *Nuclear Instruments and Methods in Physics Research Section B: Beam Interactions with Materials and Atoms*. – 2020. – Vol. 471. – P. 17-23. <https://doi.org/10.1016/j.nimb.2020.03.010>
8. Zajkin Yu A., Shirokaya N. A. Nanostructures formation in carbon-filled polymer composites at electron irradiation [Образование наноструктур у полимерных композитов при электронном облучении] // *International conference 'Solid State Physics' Almaty (Kazakhstan)*. – 2004. – Vol. 8. – P. 391. (In Russian)
9. Zaikin Yu. A., Zaikina R.F., Silverman J. Mechanisms of radiation-chemical conversion of high-paraffinic crude oil // *Hungarian Academy of Sciences, Institute of Isotope and Surface Chemistry (Hungary)*. – 2002. – Vol. 34. – P. 21.
10. Mustafayev I. Sub-thermal effects at the radiation-thermal transformations of organic fuels // *Nu ve enerjisinin dinc megsedlerle istifadesi perspektivleri // Nuclear science and its application*. Institute of Radiation Problems, Baku (Azerbaijan). – 2010. – Vol. 43. – P. 42.
11. Kozlovski V. V., Lebedev A. A., Strel'chuk A. M., Davydovskaja K. S., Vasil'ev A. È., Makarenko L. F. Effect of the energy of bombarding electrons on the conductivity of n-4 H-SiC (CVD) epitaxial layers // *Semiconductors*. – 2017. – Vol. 51. – P. 299-304. <https://doi.org/10.21883/FTP.2017.03.44199.8399>
12. Strel'chuk A., Kozlovski V., Lebedev A. Radiation-induced damage of silicon-carbide diodes by high-energy particles // *Semiconductors*. – 2018. – Vol. 52. – P. 1758-1762. <https://doi.org/10.1134/S1063782618130171>
13. Brudnyi V. N., Grinyaev S. N., Kolin N. G. The electrical and optical properties of InAs irradiated with electrons ( $\square$  2 MeV): The energy structure of intrinsic point defects // *Semiconductors*. – 2005. – Vol. 39. – P. 385-394. <https://doi.org/10.1134/1.1900249>
14. Vikulin I.M., Gorbachev V.E., Kurmashev S.D. Degradation of the parameters of transistor temperature sensors under the effect of ionizing radiation // *Semiconductors*. – 2017. – Vol. 51. – P. 1354–1359 (2017). <https://doi.org/10.1134/S1063782617100190>
15. Visakh P. M., Nazarenko O.B., Chandran C. S., Melnikova T.V., Nazarenko S.Yu., Kim J.-C. Effect of electron beam irradiation on thermal and mechanical properties of aluminum based epoxy composites // *Radiation Physics and Chemistry*. – 2017. – Vol. 136. – P. 17-22. <https://doi.org/10.1016/j.radphyschem.2017.03.032>
16. Reinholds, I., Kalkis, V., Zicans, J., Meri, R.M., Bockovs I. New thermoshrinkable materials of radiation modified polypropylene-elastomer composites with cross-linking agents // *Key Engineering Materials*. – 2014. – Vol. 604. – P. 134-137. <https://doi.org/10.4028/www.scientific.net/KEM.604.134>
17. Reinholds I., Kalkis V., Maksimovs R.D. Zicans J., Meri R. M. The effect of radiation modification and of a uniform magnetic field on the deformation properties of polymer composite blends // *Mechanics of Composite Materials*. – 2011. – Vol. 47. – P. 497-504. <https://doi.org/10.1007/s11029-011-9227-5>
18. Zaikin Yu. A., Aimuratov D. B., Al-Sheikhly M. Dose rate effect on internal friction and structural transformations in electron-irradiated carbon-armored composites // *Radiation Physics and Chemistry*. – 2007. – Vol. 76. – P. 1399-1403. <https://doi.org/10.1016/j.radphyschem.2007.02.041>
19. Avotina L., Pajuste E., Romanova M., Zaslavskis A., Enichek G., Kinerte V., Zariņš A., Lescinskis B., Dekhtyar Y., Kizane G. FTIR analysis of electron irradiated single and multilayer Si3N4 coatings // *Key Engineering Materials*. – 2018. – Vol. 788. – P. 96-101. <https://doi.org/10.4028/www.scientific.net/KEM.788.96>
20. Nordlund K. Historical review of computer simulation of radiation effects in materials // *Journal of Nuclear Materials*. – 2019. – Vol. 520. – P. 273-295. <https://doi.org/10.1016/j.jnucmat.2019.04.028>



21. Beeler J.R. Radiation effects computer experiments. New York: Oxford, 2012.
22. Barnaby H. J., McLain M. L., Esqueda I. S., Chen X. J. Modeling ionizing radiation effects in solid state materials and CMOS devices // *IEEE Transactions on Circuits and Systems I: Regular Papers*. – 2009. – Vol. 56. – P. 1870-1883. <https://doi.org/10.1109/TCSI.2009.2028411>
23. Il'in A. R., Mostovshchikov A.V., Root L.O., Zmanovskiy S.V., Smirnova V.V., Ismailov D.V., Guzel U.R. Deystviye gamma-oblucheniya na parametry aktivnosti mikroporoshkov alyuminiya [The effect of gamma irradiation on the activity parameters of aluminum micropowders] // *Izvestiya Tomskogo politekhnicheskogo universiteta. Inzhiniring georesursov*. – 2007. – Vol. 331. – P. 201-207. (In Russian)
24. Nakysbekov Zh., Buranbayev M., Aitzhanov M., Gabdullin M. T. The change in the lattice parameter of Cu nanopowders under the action of a pulsed electron beam // *International Journal of Nanotechnology*. – 2019. – Vol. 16. – P. 115-121. <https://doi.org/10.1504/IJNT.2019.102398>
25. Asadov S. M., Mustafaeva S. N., Lukichev V. F. Modifying the dielectric properties of the TiGaS<sub>2</sub> single crystal by electron irradiation // *Russian Microelectronics*. – 2020. – Vol. 49. – P. 263-268.
26. Reinholds I., Kalkis V., Maksimovs R. D. The effect of ionizing radiation and magnetic field on deformation properties of high-density polyethylene/acrylonitrile-butadiene composites // *Journal of Chemistry and Chemical Engineering*. – 2012. – Vol. 6. – P. 242-249.
27. Mustafayeva S. N., Asadov M.M., Ismailov A. A. Vliyaniye elektronogo oblucheniya na dielektricheskiye svoystva monokristalla TiGaS<sub>2</sub> v peremennykh elektricheskikh polyakh [The influence of electron irradiation on the dielectric properties of a TiGaS<sub>2</sub> single crystal in alternating electric fields] // *In Trudy XXIII Mezhdunarodnoy nauchno-tekhnicheskoy konferentsii po fotoelektronike i priboram nochnogo videniya*. – 2014. – Vol. 76. – P. 401-402. (In Russian)
28. Asadov S. M., Mustafayeva S.N. Vliyaniye elektronogo oblucheniya na perenos zaryada v 2D monosul'fide galliya [Effect of electron irradiation on charge transfer in 2D gallium monosulfide] // *Elektronnaya obrabotka materialov*. – 2018. – Vol. 54. – P. 51-57. (In Russian)
29. Dvornikov O. V., Chekhovskiy V. A., Dyatlov V. L., Prokopenko N. N. Vliyaniye ioniziruyushchikh izlucheniya na parametry operatsionnogo usilitelya na komplementarnykh bipolyarnykh tranzistorakh [The influence of ionizing radiation on the parameters of an operational amplifier based on complementary bipolar transistors] // *Mikroelektronika*. – 2016. – Vol. 45. – P. 57-65. (In Russian) DOI: <https://doi.org/10.7868/S0544126916010038>
30. Miskevich S. A., Komarov A. F., Yuvchenko V. N., Yermolayev A. P., Shpakovskiy S. V., Bogatyrov Yu.V., Zayats G. M. Vliyaniye oblucheniya elektronami s energiyey 4 MeV na rabochiye kharakteristiki kremniyevykh bipolyarnykh tranzistorov [Effect of irradiation with 4 MeV electrons on the performance of silicon bipolar transistors] // *15th International Conference "Interaction of Radiation with Solids"*. – 2023. – Vol. 15. – P. 180-182. (In Russian)
31. Miskiewicz S. A., Komarov A. F., Komarov F. F., Zayats G. M., Soroka S. A. Radiation degradation of bipolar transistor current gain // *Proc. of the XI Int. Conf. — Ion Implantation and other Applications of Ions and Electrons, Kazimierz Dolny 2016*. – 2017. – Vol. 132. – P. 288-290. <https://10.12693/APhysPolA.132.288>
32. Miskevich S. A., Komarov A. F., Komarov F. F., Yuvchenko V. N., Yermolayev A. P., Bogatyrov Yu. V., Zayats G. M. Raschot izmeneniya elektricheskikh kharakteristik bipolyarnogo tranzistora pri obluchanii bystryimi elektronami [Calculation of changes in the electrical characteristics of a bipolar transistor when irradiated with fast electrons] // *Prikladnyye problemy fiziki kondensirovannogo sostoyaniya*. – 2023. – Vol. 4. – P. 348-350. (In Russian)
33. Strel'chuk A. M., Kozlovskiy V.V., Lebedev A.A. Radiatsionnoye povrezhdeniye karbid-kremniyevykh diodov zaryazhennymi chastitsami vysokikh energiy [Radiation damage to silicon carbide diodes by high-energy charged particles] // *Fizika i tekhnika poluprovodnikov*. – 2018. – Vol. 52. – P. 1651-1655. (In Russian) <https://doi.org/10.21883/FTP.2018.13.46882.8952>
34. Bumay Yu. A., Bobuchenko D. S., Vas'kov O. S., Vabishchevich S. A., Lastovskiy S. B., Trofimov Yu.V., Tsvirko V. I. Opticheskiye i elektricheskiye svoystva obluchennykh bystryimi elektronami svetodiodov na osnove geterostruktur [Optical and electrical properties of LEDs based on heterostructures irradiated with fast electrons] // *Vestnik Polotskogo gosudarstvennogo universiteta. Seriya C, Fundamental'nyye nauki*. – 2015. – Vol. 12. – P. 82-89 (In Russian)
35. Cherkashina N.I. Modelirovaniye vzaimodeystviya puchka elektronov s polimernym kompozitom v usloviyakh kosmicheskogo prostranstva [Modeling the interaction of an electron beam with a polymer composite in outer space conditions] // *In XII Konferentsiya molodykh uchonykh Fundamental'nyye i prikladnyye kosmicheskkiye issledovaniya*. – 2015. – Vol. 1. – P. 162-165. (In Russian)
36. Panyushkin N. N. Zavisimost dozovykh effektov v KMOP is ot iskhodnykh znacheniy elektroparametrov [Dependence of dose effects in CMOS ics on the initial values of electrical parameters] // *Aktual'nyye napravleniya nauchnykh issledovaniy XXI veka: teoriya i praktika*. – 2017. – Vol. 5. – P. 109-112. (In Russian)
37. Bogatyrev Yu.V., Vasilenkov N. A., Grabchikov S., Lastovskiy S. B., Solodukha V. A., Tishkevich D. I., Trukhanov A. V., Shvedov S. V., Yakushevich A. S. Ekrany lokal'noy radiatsionnoy zashchity izdeliy elektronnoy tekhniki na osnove kompozitov vol'fram-med' [Local radiation protection screens for electronic products based on tungsten-copper composites] // *Kry Mi Ko'2017*. – 2017. – Vol. 27. – P. 1247-1259. (In Russian)
38. Tishkevich D. I., Bogatyrev Yu. V., Grabchikov S. S., Lastovskiy S. B., Tsybul'skaya L. S., Shendyukov V. S., Perevoznikov S. S., Poznyak S. K., Trukhanov A. V. Elektrokhimicheski osazhdennyye pokrytiya na osnove vismuta i effektivnost' ikh zashchity ot elektronogo izlucheniya [Electrochemically deposited bismuth-based coatings and the effectiveness of their protection from electronic radiation] // *Izvestiya Natsional'noy akademii nauk Belarusi. Seriya fiziko-tekhnicheskikh nauk*. – 2017. – Vol. 3. – P. 19-29. (In Russian)
39. Musabayev T., Zhantayev Zh., Grichshenko V. Complex influence of space environment on materials and electronic devices in the conditions of microgravity // *Advances in space research*. – 2016. – Vol. 58. – P. 1138-1145. <https://doi.org/10.1016/j.asr.2016.05.030>

40. Voytovich A. P., Kalinov V. S., Mashko V. V., Novikov A. N., Runets L. P., Stupak A. P. Transformatsiya i formirovaniye radiatsionnykh tochechnykh defektov v obluchennykh kristallakh florida litiya posle ikh mekhanicheskoy fragmentatsii [Transformation and formation of radiation point defects in irradiated lithium fluoride crystals after their mechanical fragmentation] // Zhurnal prikladnoy spektroskopii. – 2019. – Vol. 86. – P. 71-77. (In Russian)
41. Naumova O. V., Chesnokov B. P., Mavzovin V. M., Sheshukova M. D., Tronin B. A. Poluchenije kremniya dlya solnechnykh elementov iz mineral'nogo syr'ya [Obtaining silicon for solar cells from mineral raw materials] // Tekhnicheskoye regulirovaniye v transportnom stroitel'stve. – 2020. – Vol. 4. – P. 320-332. (In Russian)
42. Takabayashi Y., Pivovarov Yu L., Tukhfatullin T. A. Studies of relativistic electron scattering at planar alignment in a thin Si crystal // Physics Letters A. – 2014. – Vol. 378. – P. 1520-1525. <https://doi.org/10.1016/j.physleta.2014.03.041>
43. Takabayashi Y., Pivovarov Yu L., Tukhfatullin T. A. Observation of sub-GeV electrons mirrored by ultrathin crystalline Si // Physics Letters B. – 2015. – Vol. 751. – P. 453-457. <https://doi.org/10.1016/j.physletb.2015.10.079>
44. Takabayashi Y., Bagrov V.G., Bogdanov O.V., Pivovarov Yu L. Tukhfatullin T.A. Planar channelling of relativistic electrons in half-wave silicon crystal and corresponding radiation // In Journal of Physics: Conference Series. – 2016. – Vol. 732. – P. 012036. <https://doi.org/10.1088/1742-6596/732/1/012036>
45. Takabayashi Y., Pivovarov Yu L. Tukhfatullin T.A. First observation of scattering of sub-GeV electrons in ultrathin Si crystal at planar alignment and its relevance to crystal-assisted 1D rainbow scattering // Physics Letters B. – 2018. – Vol. 785. – P. 347-353. <https://doi.org/10.1016/j.physletb.2018.08.063>
46. Abdrashitov S. V., Bogdanov O. V., Korotchenko K. B., Pivovarov Yu L., Rozhkova E. I., Tukhfatullin T. A., Eikhorn Yu. L. BCM-2.0–The new version of computer code Basic Channeling with Mathematica© // Nuclear Instruments and Methods in Physics Research Section B: Beam Interactions with Materials and Atoms. – 2017. – Vol. 402. – P. 106-111. <https://doi.org/10.1016/j.nimb.2017.03.132>
47. Bogdanov O. V., Kazinski P. O. Probability of radiation of twisted photons by axially symmetric bunches of particles // The European Physical Journal Plus. – 2019. – Vol. 134. – P. 1-13. <https://doi.org/10.1140/epjp/i2019-13038-8>
48. Bogdanov O. V., Kazinski P. O., Lazarenko G. Yu. Proposal for experimental observation of the twisted photons in transition and Vavilov-Cherenkov radiations // Journal of Instrumentation. – 2018. – Vol. 15. – P. 4052. <https://doi.org/10.1088/1748-0221/15/04/C04052>
49. Abdrashitov S.V., Bogdanov O.V., Kazinski P.O., Tukhfatullin T.A. Orbital angular momentum of channeling radiation from relativistic electrons in thin Si crystal // Physics Letters A. – 2018. – Vol. 382. – P. 3141-3145. <https://doi.org/10.1016/j.physleta.2018.07.044>
50. Bogdanov O.V., Kazinski P.O., Tukhfatullin T.A. Orbital angular momentum of radiation from relativistic planar channeled in Si crystal electrons // Physics Letters A. – 2022. – Vol. 451. – P. 128431. <https://doi.org/10.1016/j.physleta.2022.128431>
51. Abdrashitov S. V., Bogdanov O. V., Dabagov S. B., Pivovarov Yu L., Tukhfatullin T. A. Hybrid scheme of positron source at SPARC\_LAB LNF facility // Nuclear Instruments and Methods in Physics Research Section B: Beam Interactions with Materials and Atoms. – 2015. – Vol. 355. – P. 65-68. <https://doi.org/10.1016/j.nimb.2015.03.091>
52. Abdrashitov S.V., Kunashenko Yu.P., Pivovarov Yu. L., Dabagov S.B. On a crystal assisted positron source by  $10 \div 50$  MeV electrons // Journal of Instrumentation. – 2020. – Vol. 15. – P. 10011. <https://doi.org/10.1088/1748-0221/15/10/C10011>

**Information about authors:**

Zhassulan Nakysbekov (corresponding author, PhD, is a Senior Lecturer at Al-Farabi Kazakh National University (Almaty, Kazakhstan), e-mail: [Zhassulan.Nakysbekov@gmail.com](mailto:Zhassulan.Nakysbekov@gmail.com);

Daniyar Ismailov, PhD, is a Head of the Laboratory of Radiation Physics and Functional Materials at the Faculty of Physics of al-Farabi Kazakh National University, Head of National scientific laboratory for collective use of Information and space technologies at Satpayev University (Almaty, Kazakhstan), e-mail: [ismailov\\_daniyar\\_v@bk.ru](mailto:ismailov_daniyar_v@bk.ru);

Stefano Bellucci, PhD, is a First Researcher, Head of NEXT Nanotechnology Lab. INFN-Laboratori Nazionali di Frascati (Frascati, Italy), e-mail: [bellucci@lnf.infn.it](mailto:bellucci@lnf.infn.it);

Timur Tukhfatullin, PhD (candidate of sciences), is an associate professor at Almaty Branch of NRNU MEPhI (Almaty, Kazakhstan), e-mail: [tta@tpu.ru](mailto:tta@tpu.ru);

Oleg Bogdanov PhD (candidate of sciences), is an associate professor at Tomsk Polytechnic University (Tomsk, Russia), e-mail: [bov@tpu.ru](mailto:bov@tpu.ru);

Boris Tronin is a Senior Researcher at the Laboratory of Radiation Physics and Functional Materials FTP, Al-Farabi Kazakh National University, (Almaty, Kazakhstan), e-mail: [troninboris@mail.ru](mailto:troninboris@mail.ru);

Kundyz Turmanova is a Senior Researcher at the Laboratory of Radiation Physics and Functional Materials FTP, Al-Farabi Kazakh National University, (Almaty, Kazakhstan), e-mail: [turmanova.kundyz@mail.ru](mailto:turmanova.kundyz@mail.ru);







Gulnur Suyundykova is Senior Lecturer at Al-Farabi Kazakh National University (Almaty, Kazakhstan), e-mail: [sgserikkalieвна@gmail.com](mailto:sgserikkalieвна@gmail.com);

Valentina Grichshenko, PhD (candidate of sciences), is a professor, Head of Ionosphere Institute LLP (Almaty, Kazakhstan), e-mail: [labreab@mail.ru](mailto:labreab@mail.ru);

Mustakhim Pshikov, candidate of science, act PhD (candidate of sciences), is an associate professor at Al-Farabi Kazakh National University (Almaty, Kazakhstan), e-mail: [mustahim64@mail.ru](mailto:mustahim64@mail.ru);

Assem Alzhanova, PhD student at L.N. Gumilyov Eurasian National University (Astana, Kazakhstan), e-mail: [aliya.alzhan@yandex.kz](mailto:aliya.alzhan@yandex.kz)

## Single gateway placement in wireless mesh networks

D.A. Turlykozhayeva\* , W. Waldemar , A.B. Akhmetali ,  
N.M. Ussipov , S.A. Temesheva , and S.N. Akhtanov 

Lublin University of Technology, Lublin, Poland

\*e-mail:symbat.temesheva@gmail.com

(Received March 26, 2024; received in revised form May 13, 2024; accepted May 23, 2024)

Wireless Mesh Networks (WMNs) remain integral to various sectors due to their adaptability and scalability, providing robust connectivity where traditional wired networks are impractical. From facilitating smart city initiatives to enabling disaster recovery efforts and supporting industrial automation, WMNs play a pivotal role in modern networking applications. Their versatility extends to rural connectivity, underscoring their relevance across diverse scenarios. Recent research in WMNs has honed in on optimizing gateway placement and selection to bolster network performance and ensure efficient data transmission. This paper introduces a novel approach to maximize average throughput by strategically positioning gateways within the mesh topology. Inspired by Coulomb's law, which has been previously employed in network analysis, this approach aims to improve network performance by strategically positioning gateways for optimization. Comprehensive simulations and analyses carried out in this research demonstrate the effectiveness of the proposed method in enhancing both throughput and network efficiency. By leveraging physics-based models such as Coulomb's law, the study offers an objective means to optimize gateway placement—a critical component in WMN design. These findings provide invaluable insights for network designers and operators, guiding informed decision-making processes for gateway deployment across a spectrum of WMN deployments. As such, this research contributes significantly to the ongoing evolution of WMN optimization strategies, reaffirming the indispensable role of gateway placement in establishing resilient and efficient wireless communication infrastructures.

**Key words:** WMN, Coulomb's law, network analysis, gateway placement.

**PACS number(s):** 01.30.-y; 07.05.Tp; 07.50.Qx.

### 1 Introduction

WMN continue to hold significance and offer potential in contemporary networking landscapes due to their flexibility, scalability, and capacity for self-organization. They find applicability across a broad spectrum of uses, spanning from household networking to expansive urban installations and industrial environments [1]. WMNs prove especially adept at expanding network reach and capability in a resource-efficient manner. Their adaptability makes them particularly well-suited for scenarios where the installation of conventional wired networks is either economically impractical or logistically challenging [2]. WMNs can dynamically respond to alterations

in network structure, environmental factors, and user requirements.

The structure of a Wireless Mesh Network (WMN) involves mesh clients (MCs), gateways (GWs), and mesh routers (MRs). MRs with low mobility form a wireless backbone network within their designated service areas, serving as both traffic relays and access points for MCs [3]. This dual functionality renders them suitable for diverse usage scenarios. GWs hold pivotal roles in network architecture, bridging connectivity between the wireless backbone (comprising MRs) and external networks such as the Internet. They act as ingress and egress points for data traffic entering or exiting the WMN, facilitating essential communication pathways. Previous studies have highlighted the importance of strategically

positioning gateways, with a focus on addressing challenges such as identifying the most effective locations and quantities of gateways. Researchers have extensively investigated this aspect [7-11]. For instance, in [12], authors propose heuristic methods utilizing various wireless link models to iteratively select the best gateway positions in order to fulfill Quality of Service (QoS) requirements for associated nodes. In another study [13], an algorithm is introduced to recursively compute the minimum weighted dominating set, aiding in optimal gateway placements while upholding user QoS expectations. It's noteworthy that determining the most suitable gateway placements necessitates intricate computations, thus inviting further exploration [14].

This research proposes enhancing throughput and efficiency in Wireless Mesh Networks by optimizing the placement of a single gateway, leveraging Coulomb's law. This approach draws from a method previously employed by Zhang et al. in the analysis of fractal networks [15].

This article is structured as follows: Section 2 discusses the issue of gateway node placement. Section 3 presents our approach for calculating gateway placement. Finally, Section 4 outlines the key findings and conclusions derived from our investigation.

## 2 Gateway node placement

The Generalized Network Design Problem (GNP) is categorized as NP-hard [16]. Past studies have concentrated on developing efficient heuristic algorithms to achieve near-optimal solutions. Typically, the GNP is formulated as an Integer Linear Program (ILP) to ascertain the minimum number of gateway nodes needed for a given WMN backbone network, while adhering to specific Quality of Service (QoS) constraints. These constraints usually encompass communication delay, relay load, and gateway throughput, all of which significantly influence network performance.

Numerous heuristic algorithms have been proposed to tackle the GNP, aiming to minimize the number of gateway nodes while satisfying the mentioned QoS constraints [16-19]. Additionally, some research has integrated a secondary objective of reducing the number of hops between a mesh router (RN) and its designated gateway [20, 21]. One method suggested for addressing the combined RNP-GNP problem involves employing the heuristic graph clustering technique delineated in [22] among these algorithms.

## 3 Model description

The box-covering method used in fractal network algorithms by Zhang et al. was adopted to calculate the single gateway placement of the network [23]. Two nodes within the network, designated as node 1 and node 2, each characterized by a specific electric charge  $q_1$  and  $q_2$  and separated by a distance  $r$ , were considered. The electrostatic interaction force between these nodes was determined by formula (1):

$$F = k \frac{|q_1 q_2|}{r^2}, \quad (1)$$

The interaction strength between nodes is directly proportional to the multiplication of their attributes and inversely proportional to the square of the distance between them. Our research methodology involves modelling interactions within complex networks using a node degree-based repulsion algorithm. In this algorithm, we consider each node's degree as its 'charge' in the network and compute repulsive forces based on node connectivity. The first step is to calculate the Euclidean distances between nodes to measure their straight-line distance in a two-dimensional space. Then, we systematically evaluated the interactions between network nodes, including quantifying the cumulative force exerted by neighbouring nodes for each node. Then, we systematically evaluated the interactions between network nodes, including quantifying the cumulative force exerted by neighbouring nodes for each node. This is essential for gauging its overall influence within the network. By using Coulomb's law, we calculated the electrostatic interaction force between nodes within a specific coverage radius. We then accumulated the resulting forces to represent the combined impact of neighbouring nodes on each individual node. The calculated forces were stored for further analysis, which allowed us to identify influential nodes by sorting them based on their computed forces.

The analysis concluded by measuring the average network throughput in NS3, which provided crucial insights into the network's performance. To simulate real-world data flow scenarios, each node was treated as a gateway and linked to a server (NS3) responsible for packet transmission. By systematically connecting a server to each gateway node and calculating the average throughput, we gained a comprehensive

understanding of how data transmission efficiency varied across different nodes within the network.

#### 4 Results

This section presents the results that demonstrate the impact of gateway location on force and throughput for two types of topologies: grid and random. To construct the networks, we used the NS-3 simulation program with the parameters outlined in Table 1. To determine the throughput between nodes in these networks, we used the existing OLSR routing algorithm.

In Figure 1(a), an example of a deployed grid network configuration of 5x5, consisting of 25 nodes, is shown. In this network, four mesh routers are highlighted with their respective coverage depicted by a yellow circle, and in the middle, a gateway node is specially chosen as a yellow node. Figure 1(b) illustrates the calculated force per throughput ratios in a grid network.

**Table 1** – Parameters used for NS-3 simulation program

Network simulator	NS-3.40
Channel type	Wireless channel
Propagation model	Friis Propagation Loss Model
Network interface type	Phy/Wireless Phy
Mac type	Mac/802.11ac
Interface Queue type	Drop Tail/PriQueue
Link layer type	LL
Antenna Model	Single Antenna
Traffic type	CBR
Transport protocol	UDP
Simulation time	50 s
Packet size	1024
Simulation area	1000m*1000m
Mobility model	Constant
Protocol	OLSR

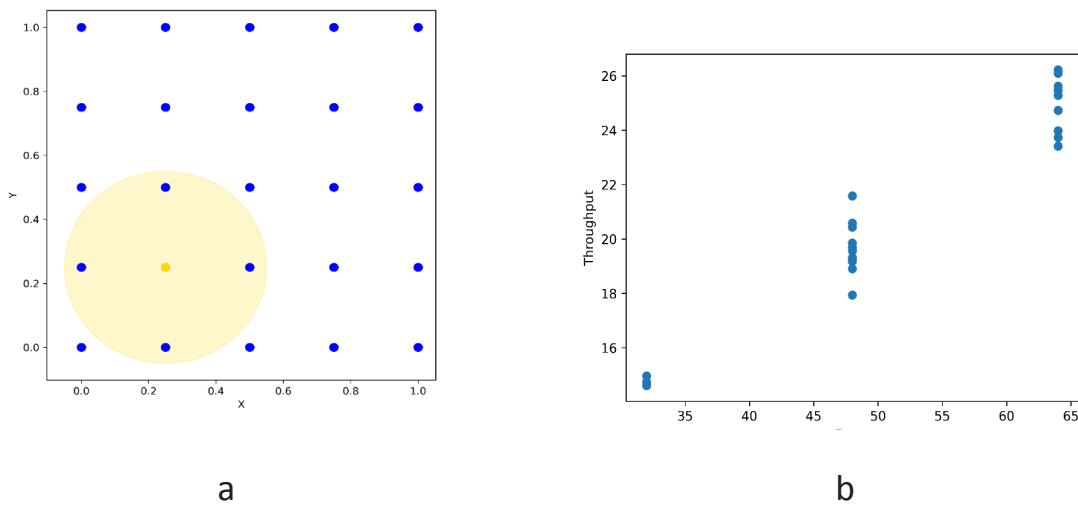


**Figure 1** (a) – Illustration of a Grid network with a Gateway placed at the Center; (b) – Force-to-Throughput Ratio

Figure 1(b) illustrates a direct positive correlation between force and throughput, suggesting that higher force values correspond to increased throughput. Selecting a node with the highest force could serve as an effective strategy for gateway placement. In Figure 2 (a), a random network comprising 25 nodes

is depicted, where 9 mesh routers along with their respective coverage highlighted by a yellow circle and a centrally located gateway node is specially chosen as a yellow node. Figure 2 (b) illustrates the calculated force per throughput ratios in a random network.

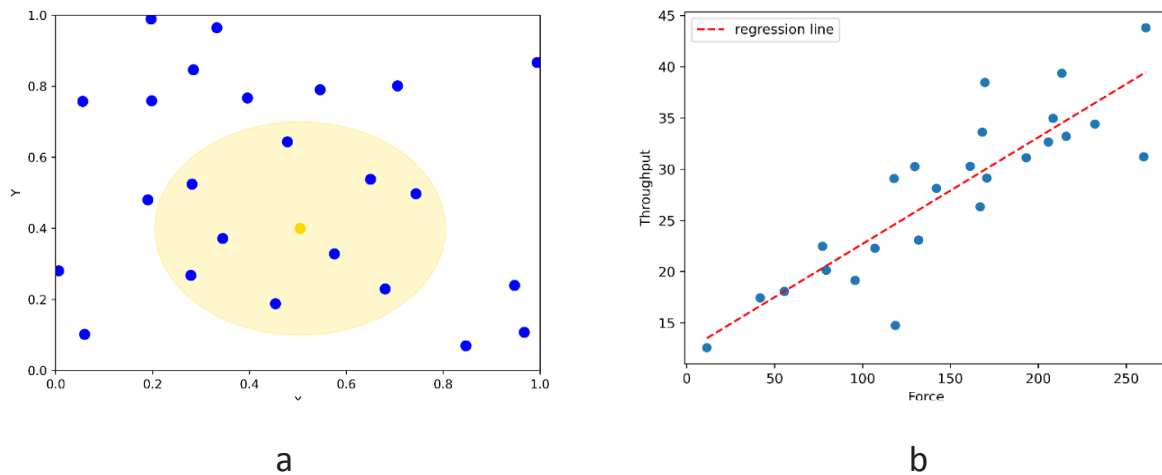


**Figure 2** (a) – Illustration of a random network with a Gateway placed at the Center; (b) – Force-to-Throughput Ratio

Figure 2 (b) demonstrates a clear direct correlation between force and throughput, indicating that higher force values are associated with increased throughput. Opting for a node with the highest force might prove to be an efficient strategy for selecting gateway placement. These results underscore the critical role of gateway placement in determining network throughput and emphasize the importance of strategic decision-making in network design and optimisation efforts.

## 5 Conclusions

Our study investigated the impact of gateway placement on two common network topologies: random and grid. Our analysis revealed distinct behaviours in each topology.

In the random network topology, which is characterized by a decentralized and irregular node arrangement, strategic gateway placement remained crucial. Although the network is inherently unpredictable, our findings suggest a clear correlation between force and throughput, indicating that optimal gateway positioning can significantly enhance network performance.

In contrast, in the grid network topology, where nodes are organized in a structured and uniform manner, the impact of gateway placement was more

pronounced. By strategically placing gateways within the grid, we observed a direct positive correlation between force and throughput. This study emphasizes the significance of taking network topology into account when devising gateway placement strategies. Structured layouts may provide more predictable outcomes.

Our research contributes to the ongoing efforts in optimizing wireless mesh networks and highlights the importance of gateway placement as a key factor in achieving robust and efficient wireless communication networks. Further research could investigate additional factors and algorithms to enhance WMN performance in various deployment scenarios by improving gateway placement strategies.

## Acknowledgments

We would like to express our sincerest gratitude to the Research Institute of Experimental and Theoretical Physics of the Al-Farabi Kazakh National University for supporting this work by providing computing resources (Department of Physics and Technology). This research was funded by the Ministry of Science and Higher Education of the Republic of Kazakhstan, grant AP19674715 ('Routing of wireless mesh networks based on box-covering algorithms').

## References

1. Kaur J., Singh H. Several Routing Protocols, "Features and Limitations for Wireless Mesh Network (WMN): A Review." ICDSMLA 2021: Proceedings of the 3rd International Conference on Data Science, Machine Learning and Applications. – Singapore // Springer Nature Singapore, 2023. – P. 187-200. [https://doi.org/10.1007/978-981-19-5936-3\\_18](https://doi.org/10.1007/978-981-19-5936-3_18)
2. Turlykozhasheva D., Ussipov N., Baigaliyeva A., Temesheva S., Bolysbay A., Abrakhmatova G., Akhtanov S. Routing metric and protocol for wireless mesh network based on information entropy theory // Eurasian Physical Technical Journal. – 2023. – Vol. 20. – №. 4 (46). – P. 90-98. <https://doi.org/10.31489/2023No4/90-98>
3. Zhanabaev Z., Akhtanov S., Turlykozhasheva D., Ussipov N., Ibraimov M. Cluster router based on eccentricity // Eurasian phys. tech. j. – 2022. – Vol. 19. – №. 3. – P. 41. <https://doi.org/10.31489/2022No3/84-90>
4. Taleb S. M., Meraihi Y., Gabis A. B., Mirjalili S., Ramdane-Cherif A. Nodes placement in wireless mesh networks using optimization approaches: a survey // Neural Computing and Applications. – 2022. – Vol. 34. – №. 7. – P. 5283-5319. <https://doi.org/10.1007/s00521-022-06941-y>
5. Wzorek M., Berger C., Doherty P. Router and gateway node placement in wireless mesh networks for emergency rescue scenarios // Autonomous Intelligent Systems. – 2021. – Vol. 1. – P. 1-30. <https://doi.org/10.1007/s43684-021-00012-0>
6. Binh L. H., Truong T. K. An efficient method for solving router placement problem in wireless mesh networks using multi-verse optimizer algorithm // Sensors. – 2022. – T. 22. – №. 15. – C. 5494. <https://doi.org/10.3390/s22155494>
7. Akhtanov S. et al. Centre including eccentricity algorithm for complex networks // Electronics Letters. – 2022. – Vol. 58. – №. 7. – P. 283-285. <https://doi.org/10.1049/ell2.12424>
8. Patil S., Gokhale P. Throughput optimization-based gateways placement methods in wireless networks // International Journal of Computer Networks and Applications. – 2021. – Vol. 8. – №. 4. – P. 346-357. <https://doi.org/10.22247/ijcna/2021/209701>
9. Seetha S., Anand John Francis S., Grace Mary Kanaga E. Optimal placement techniques of mesh router nodes in wireless mesh networks // 2nd EAI International Conference on Big Data Innovation for Sustainable Cognitive Computing: BDCC 2019. – Springer International Publishing, 2021. – P. 217-226. [https://doi.org/10.1007/978-3-030-47560-4\\_17](https://doi.org/10.1007/978-3-030-47560-4_17)
10. Kushwah R. A novel traffic aware reliable gateway selection in wireless mesh network // Cluster Computing. – 2024. – Vol. 27. – №. 1. – P. 673-687. <https://doi.org/10.1007/s10586-023-03971-6>
11. Patil S., Gokhale P., Bhende M. Analysis of internet gateway placement problem in heterogeneous wireless networks for machine to machine communication // 2019 International Conference on Smart Systems and Inventive Technology (ICSSIT). – IEEE, 2019. – P. 979-982. <https://doi.org/10.1109/ICSSIT46314.2019.8987918>
12. Hussain M. I. et al. QoS provisioning in wireless mesh networks: A survey // Wireless Personal Communications. – 2022. – Vol. 122. – №. 1. – P. 157-195. <https://doi.org/10.1007/s11277-021-08893-3>
13. Coelho A., Campos R., Ricardo M. Traffic-aware gateway placement and queue management in flying networks // Ad Hoc Networks. – 2023. – Vol. 138. – P. 103000. <https://doi.org/10.1016/j.adhoc.2022.103000>
14. Wang W. Deployment and optimization of wireless network node deployment and optimization in smart cities // Computer Communications. – 2020. – Vol. 155. – P. 117-124. <https://doi.org/10.1016/j.comcom.2020.03.022>
15. Zhang H. et al. Modeling the self-similarity in complex networks based on Coulomb's law // Communications in Nonlinear Science and Numerical Simulation. – 2016. – Vol. 35. – P. 97-104. <https://doi.org/10.1016/j.cnsns.2015.10.017>
16. Drabu Y., Peyravi H. Gateway placement with QoS constraints in wireless mesh networks // Seventh International Conference on Networking (Icn 2008). – IEEE, 2008. – P. 46-51. <https://doi.org/10.1109/ICN.2008.89>
17. Bejerano Y. Efficient integration of multi-hop wireless and wired networks with QoS constraints // Proceedings of the 8th annual international conference on Mobile computing and networking. – 2002. – P. 215-226. <https://doi.org/10.1145/570645.570672>
18. Aoun B. et al. Gateway placement optimization in wireless mesh networks with QoS constraints // IEEE Journal on Selected Areas in Communications. – 2006. – Vol. 24. – №. 11. – P. 2127-2136. <https://doi.org/10.1109/JSAC.2006.881606>
19. Maolin T. et al. Gateways placement in backbone wireless mesh networks // Int'l J. of Communications, Network and System Sciences. – 2009. – Vol. 2. – №. 01. – P. 44. <https://doi.org/10.4236/ijcns.2009.21005>
20. He B., Xie B., Agrawal D. P. Optimizing deployment of internet gateway in wireless mesh networks // Computer Communications. – 2008. – Vol. 31. – №. 7. – P. 1259-1275. <https://doi.org/10.1016/j.comcom.2008.01.061>
21. Seyedzadegan M. et al. Zero-degree algorithm for internet gateway placement in backbone wireless mesh networks // Journal of Network and Computer Applications. – 2013. – Vol. 36. – №. 6. – P. 1705-1723. <https://doi.org/10.1016/j.jnca.2013.02.031>
22. Drabu Y., Peyravi H. Gateway placement with QoS constraints in wireless mesh networks // Seventh International Conference on Networking (Icn 2008). – IEEE, 2008. – P. 46-51. <https://doi.org/10.1109/ICN.2008.89>
23. Turlykozhasheva, D., Akhtanov, S., Ussipov, N., Akhmetali, A., Bolysbay, A., & Shabdan, Y. Routing Algorithm for Software Defined Network Based on Boxcovering Algorithm // 2023 10th International Conference on Wireless Networks and Mobile Communications (WINCOM). – IEEE, 2023. – P. 1-5. <https://doi.org/10.1109/WINCOM59760.2023.10322960>

**Information about authors:**

*Turlykozhayeva D. A., Master of Physical Sciences. Senior researcher at the Institute of Electronics and Information Technology, Lublin University of Technology (Lublin, Poland) e-mail: turlykozhayeva.dana@kaznu.kz;*

*Waldemar W. is a Professor of Technical Sciences, Director of Institute of Electronics and Information Technology, Lublin University of Technology (Lublin, Poland) e-mail: waldemar.wojcik@pollub.pl;*

*Akhmetali A.B., BS in Physics, is a Junior researcher at the Institute of Electronics and Information Technology, Lublin University of Technology (Lublin, Poland) e-mail: akhmetali\_almat@kaznu.edu.kz;*







*Ussipov N.M., Master of Physical Sciences, is a Senior researcher at the Institute of Electronics and Information Technology, Lublin University of Technology (Lublin, Poland) e-mail: nurzhan.ussipov@kaznu.edu.kz;*

*Temeshova S.A. (corresponding author), Master of Physical Sciences, is Senior researcher at the Institute of Electronics and Information Technology, Lublin University of Technology (Lublin, Poland) e-mail: symbat.temesheva@gmail.com;*

*Akhtanov S.A., PhD in Physics, is Senior researcher with the Institute of Electronics and Information Technology, Lublin University of Technology (Lublin, Poland) e-mail: saiyat.ahtanov@kaznu.edu.kz*



## The influence of synthesis parameters and thermal treatment on the optical and structural properties of zinc oxide-based nanomaterials

Zh.U. Paltusheva<sup>1</sup> , Y.Y. Kedruk<sup>2\*</sup> , L.V. Gritsenko<sup>1,3\*</sup> ,  
M.A. Tulegenova<sup>3</sup> , V. Syritski<sup>4</sup>  and Kh.A. Abdullin<sup>3</sup> 

<sup>1</sup>Satbayev University, Almaty, Kazakhstan

<sup>2</sup>Kazakh-British Technical University, Almaty, Kazakhstan

<sup>3</sup>Al-Farabi Kazakh National University, Almaty, Kazakhstan

<sup>4</sup>Tallinn University of Technology, Tallinn, Estonia

\*e-mail: y.kedruk@kbtu.kz, l.gritsenko@satbayev.university

(Received October 10, 2023; received in revised form November 28, 2023; accepted January 9, 2024)

In this paper, the synthesis of high-quality nanostructured zinc oxide (ZnO) and zinc oxide-graphene oxide (ZnO-GO) nanocomposites was carried out by a simple and efficient cost-effective chemical bath deposition method. The effect of different GO concentrations as well as thermal treatment on the structural, optical and photoluminescent properties of ZnO-GO semiconductor composites was investigated. All the synthesised samples were studied by electron microscopy, energy dispersive X-ray and Raman spectroscopy. ZnO usually exhibits luminescence in the visible region of the spectrum due to various intrinsic defects. This emission can be controlled by surface modification, doping and various treatments of the synthesised materials after synthesis. The considered ZnO-GO composites were subjected to thermal treatment in air at 375°C for one hour. The study of photoluminescence spectra showed that the heat treatment affects different types of optical recombination in the considered samples of zinc oxide – graphene oxide composites. The improved photoluminescence properties of ZnO-GO nanocomposites make them promising for application in various optical devices of nano- and microelectronics.

**Key words:** zinc oxide, chemical bath deposition, optical properties, photoluminescence, raman spectra, heat treatment.

**PACS number(s):** 78.67.Bf, 87.64.– t, 81.10.Dn, 78.55.Et.

### 1 Introduction

Zinc oxide based nanostructures are very interesting for scientist materials due to its wide range of applications [1, 2]. In addition, nanostructured ZnO is an inexpensive, safe and relatively simple semiconductor material to fabricate [3]. The chemical and physical properties of zinc oxide nanoparticles can be easily modified by controlling the morphology, using different synthesis methods or different precursors [4]. ZnO belongs to inorganic compounds of semiconductor group II-IV. Zinc oxide nanoparticles are white powder, insoluble in water. The bandgap width is 3.37 eV and binding energy is 60 MeV, which provides high chemical, electrical and thermal stability [5, 6]. Due to their optical, electrical and photocatalytic properties, zinc oxide nanoparticles are used in solar cells, as

photocatalysts, in chemical sensors, piezoelectric nanogenerators, light-emitting diodes and many other electronic devices [7 – 11].

Currently, many studies are devoted to graphene, graphene oxide and composites based on it. The interest in these materials is due to the fact that they have unique electronic and crystalline properties arising from the nature of charge carriers that behave like relativistic particles [12]. Graphene consists of only carbon atoms, connected by  $sp^2$  – hybrid orbitals forming a honeycomb lattice [13]. In turn, graphene oxide is a two-dimensional material with such peculiarities as large specific surface area, high optical transparency and electron transfer capabilities [14]. The above properties allow to consider one as a promising material for bio-application. Commercially produced graphene oxide can be used in solar cells, hydrogen storage, transparent conductive films,

polymer composites, in biomedicine, nanoelectronic devices and in biosensors [15 – 17].

An analysis of literature data showed that modification of nanostructured zinc oxide by adding graphene oxide to the solution effectively prevents aggregation of ZnO particles and provides high stability in the environment [18]. The large specific surface area of graphene oxide and wide forbidden zone of ZnO particles can significantly improve the electrochemical properties of ZnO-GO composites compared to pure zinc oxide or graphene oxide.

One of the most urgent issues is the synthesis of nanostructures with specified, i.e. necessary for this or that application, properties. For this purpose, it is necessary to develop controlled methods for obtaining nanoparticles and determine the optimal parameters [19]. In order to obtain active ZnO-GO composites with the required properties, various treatments are used. Air annealing, hydrogen atmosphere annealing, hydrogen plasma treatment, etc. are often applied. The thermal treatment is one of the most valuable techniques that can significantly affect the properties of nanostructured materials. Many researchers reported that treatment affects the physicochemical properties of zinc oxide and zinc oxide based composites [20-22]. Annealing as a surface treatment process can not only remove surface impurities or defects, but also it can change the surface desorption and absorption of oxygen molecules, leading to the surface states improvement of nanocomposites [23]. It is commonly known that photoconductivity in nanostructures is controlled by the desorption or adsorption of oxygen on the surface, hence the thermal treatment leads to the improves the photosensitivity as well as photoresponse of ZnO by modifying the surface and improving the structure [24]. In turn, annealing in hydrogen atmosphere is often used to improvement of the optical and electrical characteristics of nanoparticles, because hydrogen atoms can passivate broken bonds on the surface and energy band gap states [25].

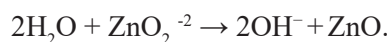
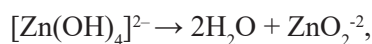
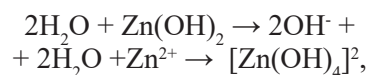
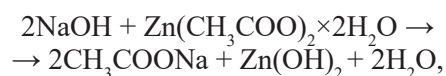
In this work, the optical, structural, as well as photocatalytic properties of ZnO, ZnO-GO semiconductor materials synthesised by a simple, economical and low temperature chemical solution deposition method subjected to heat treatment in air were studied.

## 2 Materials and methods

Zinc oxide (ZnO) and zinc oxide-graphene oxide (ZnO-GO) nanostructured semiconductor materials were synthesized at room temperature by chemical bath deposition [2]. An aqueous solution of 50mM

zinc acetate dihydrate ( $(\text{CH}_3\text{COO})_2\text{Zn}\times 2\text{H}_2\text{O}$ , 98% purity) was used for the synthesis of zinc oxide. The beaker containing this solution was placed on a magnetic stirrer. 0.7M aqueous solution of sodium hydroxide (NaOH, 98% purity, Component-Reaktiv, Russia) was added gradually to the zinc acetate solution while stirring thoroughly. Subsequently, the precipitated zinc oxide was thoroughly washed with distilled water during centrifugation and dried in atmosphere at 115°C for half a day. Sample #1 was synthesised in this way.

According to the literature [26], the following chemical reactions occur during low temperature chemical bath deposition of zinc oxide:



During zinc oxide-graphene oxide composites synthesis the difference was only that an aqueous solution of zinc acetate dihydrate was mixed with an aqueous solution of prepared graphene oxide synthesised by Hammer's method [27], and then a solution with alkali was added dropwise. The GO concentration was 0.1 wt.% (sample #2) and 0.2 wt.% (sample #3). Samples #4 and #5 were synthesised by thermal annealing a portion of samples #2 and #3, respectively, in an atmosphere at 375°C for one hour. The temperature of 375°C is the minimum at which significant changes in the photoluminescence spectra and Raman spectroscopy spectra of ZnO-GO samples are observed.

## 3 Results and discussion

An electron scanning microscope (JEOL, JSM-6490 LA) was used to study the morphology of ZnO and ZnO-GO synthesised samples. The analysis of the morphology of ZnO and ZnO-GO samples by SEM showed that zinc oxide and zinc oxide – graphene oxide composites at low-temperature synthesis by chemical bath deposition grow as two-dimensional thin plates with length and height of the order of several hundred nanometres. The thickness of the plates was of the order of a few tens of nanometres (Figures 1, 2). No significant difference in the structure of ZnO-GO and ZnO samples was observed.

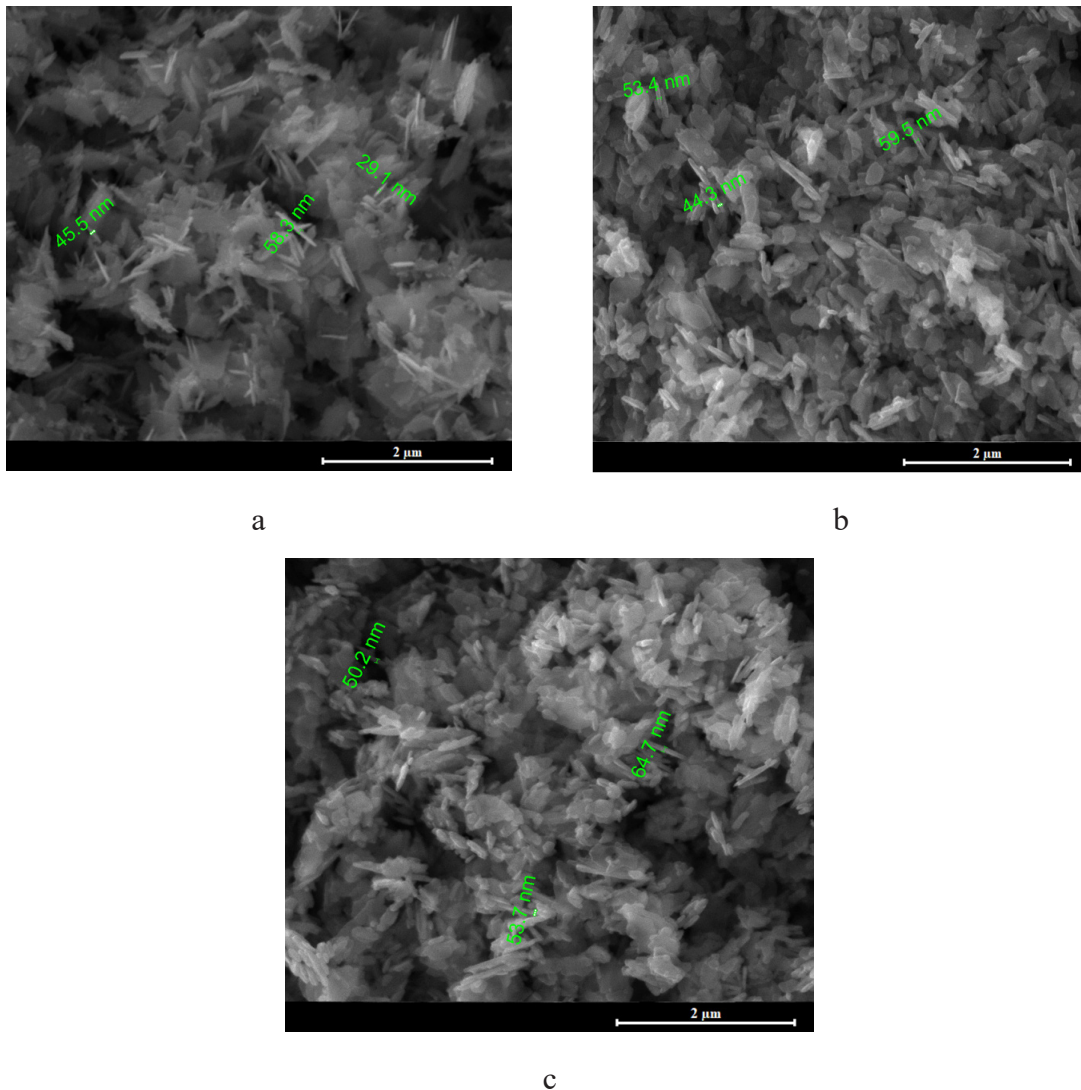


**Figure 1** – SEM of samples: a – ZnO (sample #1), b – ZnO-GO (sample #2), c – ZnO-GO (sample #3)

Elemental analysis (EDAX) was carried out for samples #2, #3, #4 and #5 by energy dispersive X-ray spectroscopy, which showed that all the samples considered contain carbon (C), oxygen (O) and zinc (Zn) atoms (Figure 3).

It is noticed that in sample #3 there is more carbon than in sample #2, which is explained by the large content of GO in the growth solution. After thermal annealing of ZnO-GO samples #2 and #3 at 375°C in air, the content of carbon atoms in these samples decreased, which is apparently due to the release of carbon dioxide during thermal air treatment of the samples.

Optical density spectra of the synthesised nanostructured samples were studied on a PerkinElmer, UV/Vis Lambda35 spectrophotometer. The optical properties of ZnO and ZnO-GO samples

were studied by spectroscopy in the UV and visible region. Optical density spectra of ZnO and ZnO-GO samples are presented in Figure 4a. The spectra demonstrate significant UV-absorption and negligible absorption in the visible region. ZnO possesses by a broad UV-absorption peak (360-400 nm), characterized hexagonal wurtzite phase of ZnO. The band gap of a pure ZnO sample and ZnO-GO composites was estimated using the Tauc's ratio for allowed direct transitions:

$$(\alpha h\nu) = A (h\nu - E_g)^n,$$

where  $h\nu$  is the photon energy,  $\alpha$  is the coefficient of absorption,  $A$  is the proportionality factor,  $n = 0.5$ , since zinc oxide is a direct-gap semiconductor material [28].

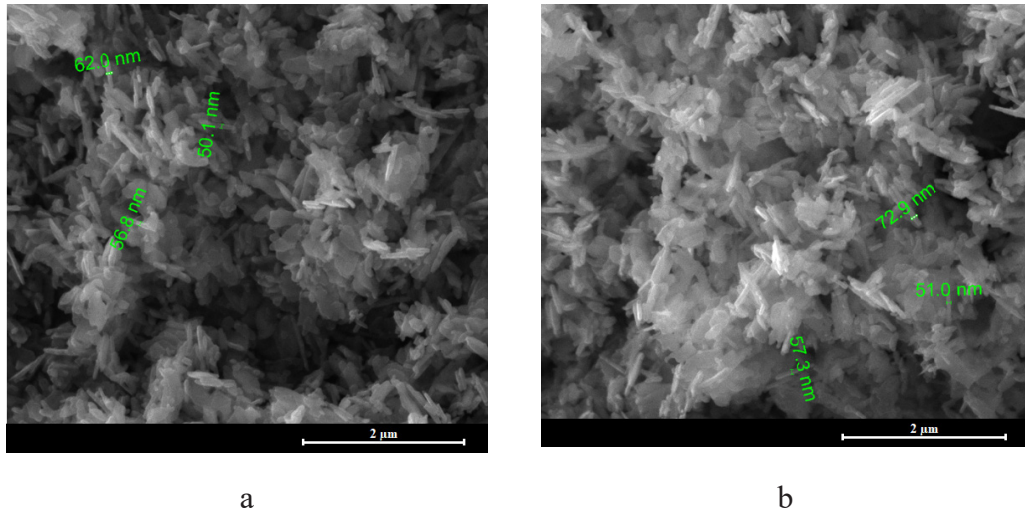


Figure 2 – SEM of samples: a – ZnO-GO (sample #4), b – ZnO-GO (sample #5)

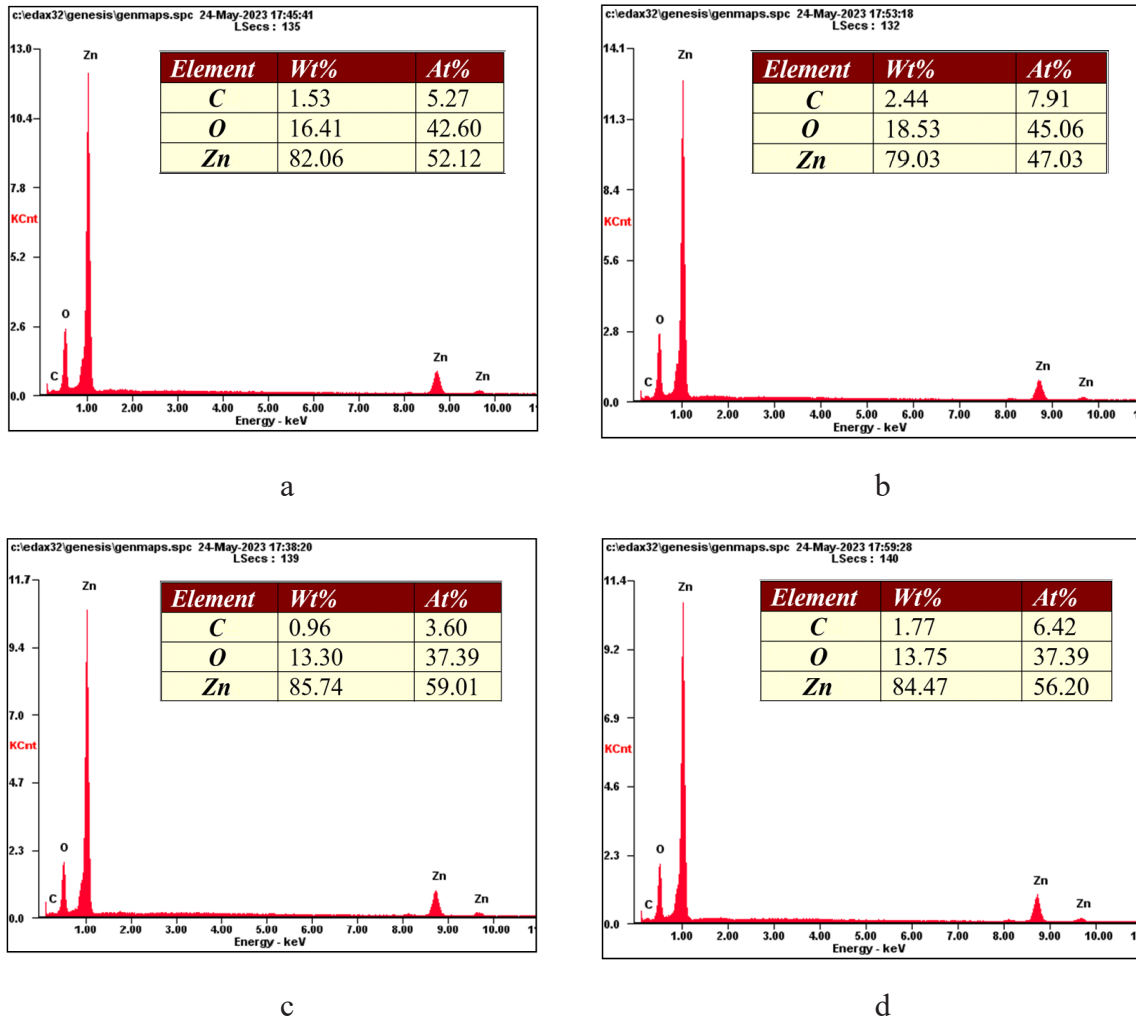
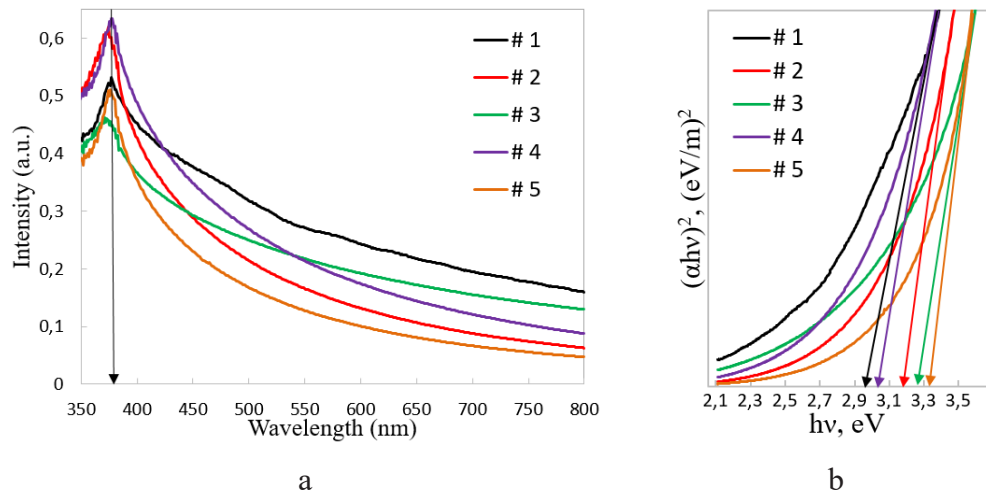


Figure 3 – EDAX ZnO-GO samples: a – sample #2, b – sample #3, c – sample #4, d – sample #5



**Figure 4** – Optical properties of ZnO and ZnO-GO samples:  
(a) absorption spectra, (b) Tauc Plot diagrams

The extrapolation the linear part of the dependence of  $(\alpha h\nu)^2$  on  $h\nu$  allow estimate band gap energy in the optical range  $E_g$  (Figure 4b). The  $E_g$  value of all samples is on the order of  $(3.2 \pm 0.15)$  eV.

Photoluminescence (PL) spectra were measured at room temperature using a Cary-Eclipse spectrophotometer. A xenon lamp emitting at a wavelength of 300 nm provided optical excitation.

Photoluminescent properties of semiconductor nanostructures are actively investigated with the prospect of subsequent application in biological markers, lasers, organic light-emitting diodes, quantum electronics, etc. Photoluminescence spectra were measured and studied for all ZnO and ZnO-GO samples. Figure 5 shows the photoluminescence spectra measured at room temperature. The excitation energy used (4.1 eV) is higher than  $E_g$  of ZnO (3.37 eV), so the electron from the valence band due to excitation can both move to the conduction band and to deep levels inside the forbidden band [29]. In the FL spectra of the considered ZnO and ZnO-GO samples, two emission bands are observed: one in the UV region (385 nm) and the other in the visible region (450-650 nm). The UV emission peak at 385 nm corresponds to the near-band emission (NBE) of ZnO and is due to the radiative recombination of free excitons [30]. When the size of nanocrystals decreases, sample impurities and various defects come to the surface as a result an increasing in the fraction of surface atoms providing impurity photoluminescence (DLE). The ratio of NBE and DLE intensities is often related to the crystal quality and the state of trapped defects.

The photoluminescence spectra show that samples #2 and #3 exhibit visible emission in the

yellow and yellow-orange regions with a peak at wavelengths of 565 nm and 581 nm, respectively. The radiative recombination of localised electrons with deeply trapped holes in oxygen interstitials located at 2.2 and 2.14 eV below the conduction band results in yellow and yellow-orange luminescence (DLE) bands, respectively [31]. It was observed that after atmospheric heat treatment at 375°C in ZnO-GO samples #4 and #5, the DLE band shifts from yellow to green region. The nature of green luminescence in ZnO is the most controversial; there are many hypotheses to explain this luminescence [30-33]. According to some of them, the green luminescence band observed at 505 nm can be associated with recombination of electrons in singly ionised oxygen vacancies with photoexcited holes in the valence band [30, 32]. In this case, samples # 4 and # 5 showed typical edge emission of the band at 383 nm. It was noted that the PL intensity of the UV-band decreased after heat treatment, which may be explained by the partial dissociation of the exciton bound to the donor [32]. Thus, it is obvious from the photoluminescence spectra that annealing of the synthesised nanoparticles clears the samples of moisture and affects various types of optical recombination [33].

Raman scattering for all synthesised samples was examined by a Solver Spectrum spectrometer. The excitation was carried out by means of a blue laser at 473 nm. The Raman spectra of the synthesised samples are shown in Figure 6. The spectrum of ZnO sample #1 (Figure 6a) shows the presence of peaks at  $100 \text{ cm}^{-1}$ ,  $330 \text{ cm}^{-1}$ ,  $437 \text{ cm}^{-1}$ ,  $575 \text{ cm}^{-1}$  and  $1150 \text{ cm}^{-1}$ . The peak at  $330 \text{ cm}^{-1}$  corresponds to zone-boundary phonons of hexagonal ZnO, while the peak at  $437 \text{ cm}^{-1}$ , belongs to the characteristic E2 (High) mode of the wurtzite

phase of ZnO [35]. The peak present at  $575\text{ cm}^{-1}$ , belong to transverse optical modes with A1 symmetry and longitudinal optical (Low) modes characteristic of defects (oxygen deficiency) present in ZnO [36]. The observed peak at  $1150\text{ cm}^{-1}$  corresponds to the phonon scattering phenomenon [37].

The spectra of ZnO-GO samples (Figure 6b) show two main peaks at  $1350\text{ cm}^{-1}$  and  $1588\text{ cm}^{-1}$ , characterised by the D and G bands, respectively. The D band arises due to defects  $sp^3$ , and the G band due to the planar vibrations of carbon atoms  $sp^2$  and the twice degenerate phonon mode [38].

After thermal treatment of the ZnO-GO samples, the peaks characteristic of the presence of GO in the samples do not appear (Figure 6c), which seems to be due to the reduction of carbon atoms (Figure 3) and also as a result of the green DLE luminescence increasing after thermal treatment (Figure 5).

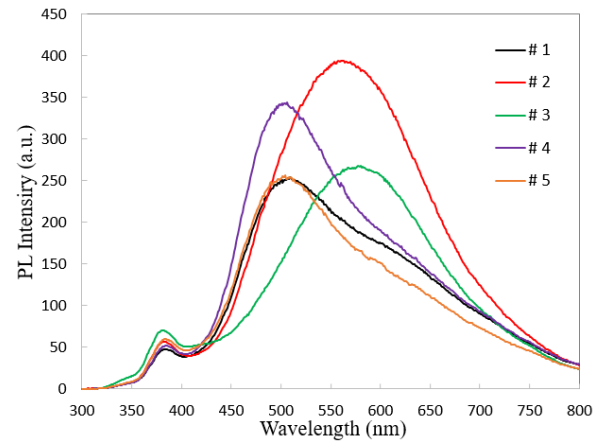


**Figure 5** – Photoluminescence (PL) spectra of ZnO-GO and ZnO samples

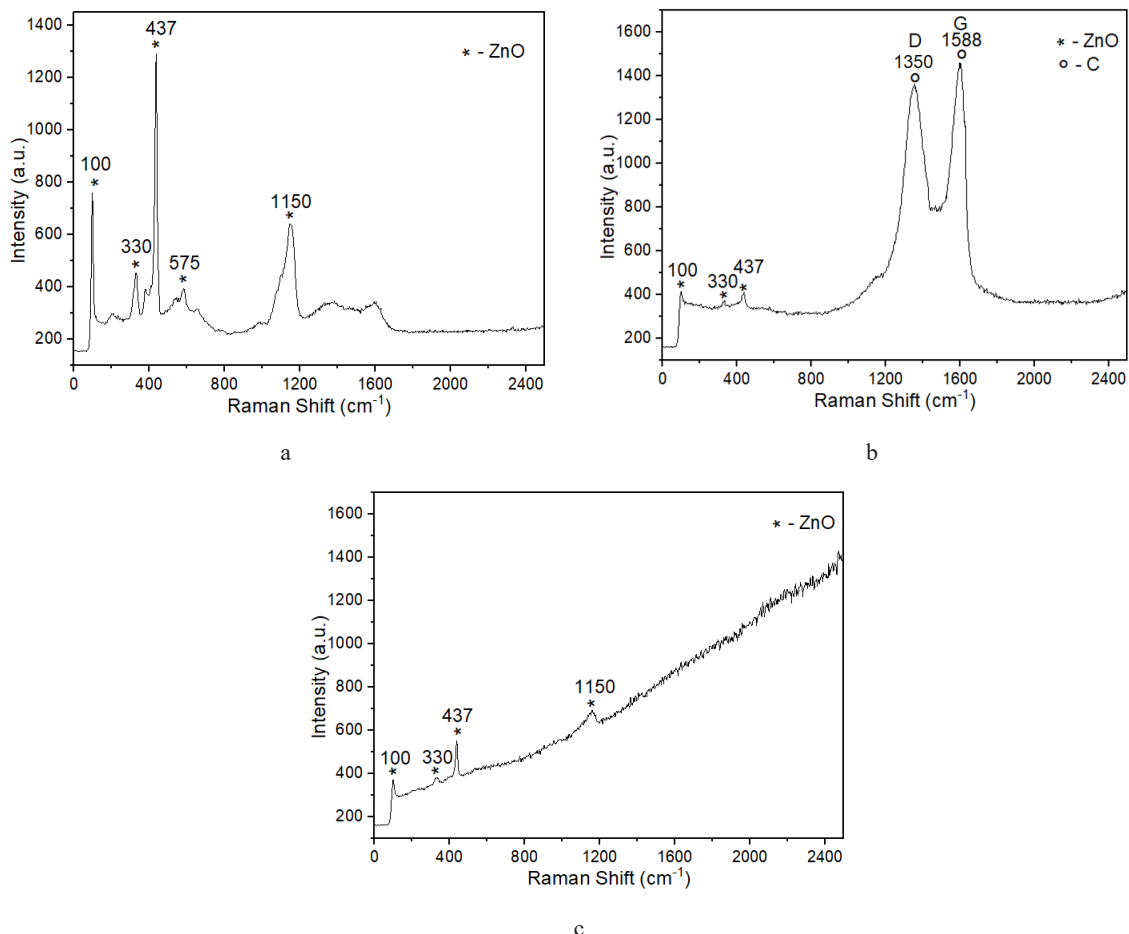


**Figure 6** – Raman spectra: a – ZnO (sample #1), b – ZnO-GO (sample #3), c – ZnO-GO (sample #5)

## 4 Conclusions

Nanostructured ZnO and ZnO-GO samples were synthesised by a simple low-cost method of chemical bath deposition. The morphology, as well as electrochemical and structural characteristics of the synthesised ZnO and ZnO-GO samples were studied. The results of the study of the synthesised samples by SEM showed that the synthesised samples grow as two-dimensional thin plates with length and height of the order of a few hundred nanometres and thickness of the order of a few tens of nanometres. It was demonstrated that the thermal treatment of the synthesised ZnO-GO nanoparticles in air at 375°C is not only able to

affect various types of optical recombination. Thus, the proposed method of synthesis of ZnO-GO and ZnO nanoparticles with subsequent heat treatment allows controlling their luminescent and structural properties, which makes these materials promising for application in the production of white light-emitting diodes, display devices, biological labelling and other optical devices of nanoelectronics.

## Acknowledgments

This research was funded by the Ministry of Science and Higher Education of the Republic of Kazakhstan, grant no. AP19676535.

## References

1. Krishna K.G., Umadevi G., Parne S., Pothukanuri N. Zinc oxide-based gas sensors and their derivatives: a critical review // *J. Mater. Chem. C*. – 2023. – Vol. 11. – P. 3906–3925. <https://doi.org/10.1039/D2TC04690C>
2. Kedruk Y.Y., Baigarinova G.A., Gritsenko L.V., Cicero G. Facile Low-Cost Synthesis of Highly Photocatalytically Active Zinc Oxide Powders // *Frontiers in Materials*. – 2022. – Vol. 9. – P. 869493. <https://doi.org/10.3389/fmats.2022.869493>
3. Rahaa S., Ahmaruzzaman Md. ZnO nanostructured materials and their potential applications: progress, challenges and perspectives // *Nanoscale Adv.* – 2022. – Vol. 4. – P. 1868–1925. <https://doi.org/10.1039/D1NA00880C>
4. Erazo A., Mosquera S. A., Rodríguez-Paéz J.E. Synthesis of ZnO nanoparticles with different morphology: Study of their anti-fungal effect on strains of *Aspergillus niger* and *Botrytis cinerea* // *Materials Chemistry and Physics*. – 2019. – Vol. 234. – P. 172–184. <https://doi.org/10.1016/j.matchemphys.2019.05.075>
5. Ayyasamy A., Thanapathi Dr. G. Structural and optical studies of zno nanorods prepared of nanorods prepared by hydrothermal method // *International Journal of Development Research*. – 2015. – Vol. 5 (10). – P. 5715–5720. <https://doi.org/10.1016/j.optmat.2022.112295>
6. Abdullin Kh. A., Gabdullin M. T., Gritsenko L.V., Ismailov D.V., Kalkozova Zh. K., Kumekov S.E., Mukash Zh. O., Sazonov A. Yu., Terukov E.I. Electrical, optical, and photoluminescence properties of ZnO films subjected to thermal annealing and treatment in hydrogen plasma // *Semiconductors*. – 2016. – Vol. 50 (8). – P. 1010–1014. <https://doi.org/10.26577/phst.2022.v9.i2.02>
7. Qiu C., Wu Y., Song J., Wang W., Li Z. Efficient Planar Perovskite Solar Cells with ZnO Electron Transport Layer // *Coatings*. – 2022. – Vol. 12. – P. 1981. <https://doi.org/10.3390/coatings12121981>
8. Wijaya Th. J., Yokota T., Lee S., Okano R., Kobayashi M., Someya T. Photostability Improvement of Organic Photodiodes with ZnO Electron Transport Layer // *Advanced Photonics Research*. – 2023. – Vol. 4 (3). – P. 2200355. <https://doi.org/10.1002/adpr.202200355>
9. Bhadwal N., Ben Mrad R., Behdinin K. Review of Zinc Oxide Piezoelectric Nanogenerators: Piezoelectric Properties, Composite Structures and Power Output // *Sensors*. – 2023. – Vol. 23. – P. 3859. <https://doi.org/10.3390/s23083859>
10. Maraeva E.V., Permiakov N.V., Kedruk Y.Y., Gritsenko L.V., Abdullin Kh.A. Creating a virtual device for processing the results of sorption measurements in the study of zinc oxide nanorods // *Chimica Techno Acta*. – 2020. – Vol. 7 (4). – P. 154–158. <https://doi.org/10.15826/chimtech.2020.7.4.03>
11. Seitov B., Kurbanbekov S., Bakranova D., Abdyldayeva N., Bakranov N. Study of the photoelectrochemical properties of 1D ZnO based nanocomposites // *Catalysts*. – 2021. – Vol. 11 (10). – P. 1235. <https://doi.org/10.3390/catal11101235>
12. Tiwari S. K., Sahoo S., Wang N., Huczko A. Graphene research and their outputs: Status and prospect // *Journal of Science: Advanced Materials and Devices*. – Vol. 5 (1). – 2020. – P. 10–29. <https://doi.org/10.1016/j.jsamd.2020.01.006>
13. Pérez M., Elías J., Sosa M., Vallejo M. Hybridization bond states and band structure of graphene: a simple approach // *European Journal of Physics*. – 2022. – Vol. 43 (4). – P. 045401. <https://doi.org/10.1088/1361-6404/ac654e>
14. Asghar F., Shakoor B., Fatima S., Munir Sh., Razaq H., Naheeda Sh., Butler I. S. Fabrication and prospective applications of graphene oxide-modified nanocomposites for wastewater remediation // *RSC Adv.* – 2022. – Vol. 12. – P. 11750–11768. <https://doi.org/10.1039/D2RA00271J>
15. Paltusheva Z.U., Ashikbayeva Z., Tosi D., Gritsenko L.V. Highly sensitive zinc oxide fiber-optic biosensor for the detection of CD44 protein // *Biosensors*. – 2022. – Vol. 12. – P. 1015. <https://doi.org/10.3390/bios12111015>
16. Jiříčková A., Jankovský O., Sofer Z., Sedmidubský D. Synthesis and applications of graphene oxide // *Materials*. – 2022. – Vol. 15(3). – P. 920. <https://doi.org/10.3390/ma15030920>

17. Tolubayeva D.B., Gritsenko L.V., Kedruk Y.Y., Aitzhanov M.B., Nemkayeva R.R., Abdullin K.A. Effect of hydrogen plasma treatment on the sensitivity of ZnO based electrochemical non-enzymatic biosensor // *Biosensors*. – 2023. – Vol. 13. – P. 793. <https://doi.org/10.3390/bios13080793>
18. Jin C., Cheng Y., Liu W., Lv Y. Preparation of ZnO–GO nanocomposites and their properties // *E3S Web of Conferences*. – 2022. – Vol. 341. – P. 01001. <https://doi.org/10.1051/e3sconf/202234101001>
19. Tyagi S., Singh P. K., Tiwari A. K., Pain P. Optimization and comparison of photovoltaic parameters of zinc oxide (ZnO)/graphene oxide (GO) and zinc oxide (ZnO)/carbon quantum dots (CQDs) hybrid solar cell using firefly algorithm for application in solar trigeneration system in commercial buildings // *Sustainable Energy Technologies and Assessments*. – 2021. – Vol. 47. – P. 101357. <https://doi.org/10.1016/j.seta.2021.101357>
20. Kumar P. S., Padmalaya G., Elavarasan N., Sreeja B.S. GO/ZnO nanocomposite – as transducer platform for electrochemical sensing towards environmental applications // *Chemosphere*. – 2023. – Vol. 313. – P. 137345. <https://doi.org/10.1016/j.chemosphere.2022.137345>
21. Kedruk Y.Y., Contestabile A., Zeng J., Fontana M., Laurenti M., Gritsenko L.V., Cicero G., Pirri C.F., Abdullin K.A. Morphology effects on electro- and photo-catalytic properties of zinc oxide nanostructures // *Nanomaterials*. – 2023. – Vol. 13 (18). – P. 2527. <https://doi.org/10.3390/nano13182527>
22. Abdullin Kh.A., Gritsenko L.V., Kumekov S.E., Markhabaeva A.A., Terukov E.I., Effect of heat and plasma treatments on the photoluminescence of zinc-oxide films // *Semiconductors*. – 2018. – Vol. 52 (2). – P.177–183 <https://doi.org/10.1134/S1063782618020021>
23. Il'ves V.G., Sokovnin S.Y., Zuev M.G., Uimin M.A., Rähn M., Kozlova J., Sammelselg V. Effect of annealing on structural, textural, thermal, magnetic, and luminescence properties of calcium fluoride nanoparticles // *Physics of the Solid State*. – 2019. – Vol. 61 (11). – P. 2200–2217. <https://doi.org/10.1134/S1063783419110179>
24. Crapanzano R., Villa I., Mostoni S., D'Arienzo M., Di Credico B., Fasoli M., Scotti R., Vedda A. Morphology related defectiveness in ZnO luminescence: from bulk to nano-size // *J. Nanomaterials*. – 2020. – Vol. 10. – P. 1983. <https://doi.org/10.3390/nano10101983>
25. Rodrigues J., Holz T., Allah R. F., Gonzalez D., Ben T., Correia M. R., Monteiro T., Costa F. Effect of N<sub>2</sub> and H<sub>2</sub> plasma treatments on band edge emission of ZnO microrods // *J. Sci. Rep.* – 2015. –Vol. 5. – P. 10783. <https://doi.org/10.1038/srep10783>
26. Dalia A.M.O., Mustafa A.M. Synthesis and characterization of zinc oxide nanoparticles using zinc acetate dihydrate and sodium hydroxide // *Journal of Nanoscience and Nanoengineering*. – 2015. – Vol.1 (4). – P.248–251. <http://www.aiscience.org/journal/jnn>
27. Yu H., Zhang B., Bulin C., Li R., Xing R. High-efficient Synthesis of graphene oxide based on improved hummers method // *Scientific Reports*. – 2016. – Vol.6. – P.24–26. <https://doi.org/10.1038/srep36143>
28. Rusdi R., Rahman A. A., Mohamed N. S., Kamarudin N., Kamarulzaman N. Preparation and band gap energies of ZnO nanotubes, nanorods and spherical nanostructures // *Powder Technol.* –2011. – Vol. 210. – P. 18–22. <https://doi.org/10.1016/j.powtec.2011.02.005>
29. Kumar R.G.A., Hata S., Gopchandran K.G. Diethylene glycol mediated synthesis of Gd<sub>2</sub>O<sub>3</sub>:Eu<sub>3</sub> nanophosphor and its analysis // *Ceram. Int.* –2013. – Vol. 39. – P. 9125–9136. <https://doi.org/10.1016/j.ceramint.2013.05.010>
30. Ozgur U., Alivov I. Ya., Liu C., Teke A., Reshchikov M.A., Dogan S., Avrutin V., Cho S.J., Morkoc H. A comprehensive review of ZnO materials and devices // *J. Appl. Phys.* – 2005. –Vol. 98. – P. 041301. <https://doi.org/10.1063/1.1992666>
31. Studenikin S.A., Golego N., Cocivera M. Fabrication of green and orange photoluminescent, undoped ZnO films using spray pyrolysis // *J. Appl. Phys.* – 2021. – Vol. 84. – P.2287–2294. <https://doi.org/10.1063/1.368295>
32. Zeng B.H., Duan G., Li Y., Yang S., Xu X., Cai W. Blue Luminescence of ZnO nanoparticles based on non-equilibrium processes: defect origins and emission controls // *Adv. Funct. Mater.* –2010. – Vol. 20. – P. 561–572. <https://doi.org/10.1002/adfm.200901884>
33. Chand P., Gaur A., Kumar A. Structural optical and ferroelectric behavior of hydrothermally grown ZnO nanostructures // *Superlattices Microstruct.* – 2013. – Vol. 64. – P. 331–342. <https://doi.org/10.1016/j.spmi.2013.09.038>
34. Bhaskar R., Lakshmanan A.R., Sundarajan M., Ravishankar T., Jose M.T., Lakshminarayan N. Mechanism of green luminescence in ZnO // *Ind. J. Pure Appl. Phys.* – 2009. – Vol. 47. – P. 772–774. <https://doi.org/10.1063/1.362349>
35. Omar F.S., Ming H. N., Hafiz S.M., Ngee L.H. Microwave synthesis of zinc oxide/reduced graphene oxide hybrid for adsorption- photocatalysis application // *Int. J. Photoenergy*. – 2014. – P.1–8. <https://doi.org/10.1155/2014/176835>
36. Li J.Y., Li H. Physical and electrical performance of vapor-solid grown ZnO straight nanowires // *Nanoscale Res. Lett.* – 2009. – Vol. 4. – P. 165–168. <https://doi.org/10.1007/s11671-008-9218-1>
37. Ye X., Zhou Y., Sun Y., Chen J., Wang Z. Preparation and characterization of Ag/ZnO composites via a simple hydrothermal route // *J. Nanopart. Res.* – 2009. – Vol. 11. – P.1159–1166. <https://doi.org/10.1007/s11051-008-9511-z>
38. How G.T.S., Pandikumar A., Ming H.N., Ngee L.H. Highly exposed {001} facets of titanium dioxide modified with reduced graphene oxide for dopamine sensing // *Sci. Rep.* – 2014. – Vol. 4. – P. 2–9. <https://doi.org/10.1038/srep05044>



**Information about authors:**

*Paltusheva Zhaniya Urazgalievna is a PhD student at the Satbayev University (Almaty, Kazakhstan), e-mail: zhaniya.paltusheva@gmail.com;*

*Kedruk Yevgeniya Yuryevna (corresponding author), PhD, is an Assistant Professor at the School of Natural and Social Sciences of the Kazakh-British Technical University (Almaty, Kazakhstan), e-mail: y.kedruk@kbtu.kz;*










*Gritsenko Lesya Vladimirovna (corresponding author) – PhD, is a professor at the Satbayev University (Almaty, Kazakhstan), e-mail: l.gritsenko@satbayev.university;*

*Tulegenova Malika, PhD, senior lecturer at al-Farabi Kazakh National University (Almaty, Kazakhstan), e-mail: malika.tulegenova@bk.ru;*

*Vitali Siritski, PhD, is a head of laboratory at Tallinn Technical University (Tallinn, Estonia), e-mail: vitali.syritski@taltech.ee;*

*Abdullin Khabibulla Abdullaevich, Doctor of Physical and Mathematical Sciences, is a professor at al-Farabi Kazakh National University (Almaty, Kazakhstan), e-mail: kh.abdullin@physics.kz*

## Oxidized starch/CMC based biofilm: Synthesis and characterization

K. Akatan<sup>1,2</sup> , A.K. Battalova<sup>1,2</sup> , N.N. Sagiyeva<sup>1,2</sup> ,  
S.K. Kabdrakhmanova<sup>3</sup> , N. Kaiyrbekov<sup>2\*</sup> , A. Tursyngazykyzy<sup>2</sup> ,  
E. Shaimardan<sup>1</sup> , M.M. Beisebekov<sup>1,3</sup> , and G.A. Kampitova<sup>4</sup> 

<sup>1</sup>Scientific center of composite materials, Almaty, Kazakhstan

<sup>2</sup>Sarsen Amanzholov East Kazakhstan University, Oskemen, Kazakhstan

<sup>3</sup>Satpaev University, Almaty, Kazakhstan

<sup>4</sup>Kazakh National Agrarian Research University, Almaty, Kazakhstan

\*e-mail: narimankayrbekov@gamil.com

(Received May 3, 2024; received in revised form May 24, 2024; accepted May 29, 2024)

Starch-based biopolymers derived from renewable resources offer a sustainable alternative to plastic packaging. One of the main advantages of starch-based biopolymers is their ability to biodegrade, as well as being economical due to the availability and low cost of starch. This makes them more economically attractive for producers and consumers. Although there are still problems with improving their properties. This research centered on developing a biodegradable biofilm from oxidized corn starch and carboxymethylcellulose, using succinic anhydride as a crosslinker. The biofilm's mechanical strength, water absorption, and biodegradability were evaluated and compared to a commercial biopolymer. The biofilm exhibited a strength of 0.78 MPa, absorbed 0.21% water, and had a biodegradability rate of 0.008%. These findings suggest that the biofilm has significant potential for industrial applications, particularly in the biofilms and bioplastics sector. This study contributes to the ongoing global efforts to create sustainable alternatives to conventional plastic packaging, a critical aspect of environmental preservation. The promising characteristics of the synthesized biofilm indicate its potential to significantly influence the future of packaging materials. This research marks a progressive step in the pursuit of sustainable packaging solutions.

**Key words:** starch, biofilm, cellulose, biodegradable, composite film.

**PACS number(s):** 82.35.Lr.

### 1 Introduction

Plastic is a product with wide potential, which is obtained from petroleum raw materials. Currently, due to the low mechanical properties and moisture permeability of plastic products, the largest area of consumption is the production of packaging materials. In addition, more than 42% of all plastic materials are used in this industry [1-3]. This has led to the excessive accumulation of household plastic waste and the creation of an island of plastic waste. Because of plastic is chemically and mechanically stable, the process of its decomposition in the environment is very slow. As a result, the soil layer, atmosphere and hydrosphere are in great danger [4, 5]. In this regard, the last ten years, the development and production of biodegradable films based on

biopolymers: starch, cellulose, pectin and chitosan has started to develop rapidly. In particular, the scope of starch-based biofilms is increasing everyday [6, 7]. However, due to the special hydrophilicity and mechanical properties of starch, it becomes brittle and therefore requires starch modification. [8, 9].

In the study [10], a starch-chitosan-based packaging for food products with antibacterial properties was developed, which can reduce the amount of *Escherichia coli* up to 23.8%, and *Staphylococcus aureus* up to 25.6%. Also, in research [11], a package for storing lamb was developed by modifying the starch-pectin composite with broccoli leaf polyphenols. In addition, by oxidizing starch with a strong oxidation agent, increasing the carboxyl and carbonyl groups in its molecule, it is possible to obtain thermoplastic starch for film production

which was reported by researchers [12]. This, in turn, proves that it is possible to modify starch with other monomers.

Based on the research of scientists related to biofilms, it can be seen that the biodegradation, physical and chemical properties of materials obtained by modifying oxidized starch with biomonomers are effective.

In this regard, current study investigated the possibility of obtaining biodegradable biofilm by modifying oxidized corn starch with a cellulose ester derivative in the presence of a crosslinking agent.

## 2 Materials and methods

### 2.1 Materials

H<sub>2</sub>O<sub>2</sub> (STST 177-88, 30%), starch (STST 32159-2013), carboxyl methylcellulose (STST 5.588-70), succinic anhydride (Sigma Aldrich), glycerin (STST 6259-75) and distilled water. All reagents were used without preliminary purification.

### 2.2 Oxidation of starch

A suspension of corn starch and distilled water in a ratio of 1:10 g/ml was intensively stirred continuously in a flask with a rotary cooler at a temperature of 80±2°C for 1 hour until a stable solution was formed. The resulting thick solution was cooled to a temperature of 25±2°C. Then, 100 ml of 8% hydrogen peroxide solution was added dropwise to the prepared starch thick solution. The resulting mixture was continuously stirred at room temperature for 24 hours, and the prepared suspension was neutralized with distilled water until pH=7 using a centrifuge. The neutralized suspension was dried to a constant mass in a vacuum cabinet (Grodtorgmash DC-80, Belarus) at a temperature of 50±2°C. The dried mass was ground to obtain a film.

### 2.3 Starch/carboxyl methylcellulose (CMC) biofilm preparation

In order to develop a biodegradable film, 0.875 g of oxidized starch was weighed into 50 ml of a pre-prepared 5% carboxymethyl cellulose (CMC) solution and continuously stirred in a magnetic stirrer until a homogeneous solution was formed. Further, 0.75 g of succinic anhydride and 7.5 ml of glycerol were added to the prepared solution and stirred for another 30 minutes until a homogeneous mixture was formed. The resulting mixture was poured into a disk-shaped plate and placed in a vacuum cabinet at a temperature of 60±2°C for 16 hours. As a result, a film was obtained Figure 1.

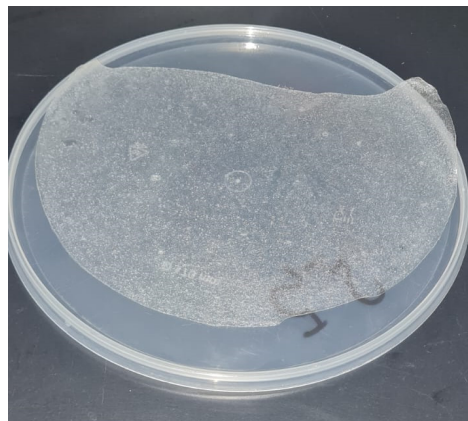


**Figure 1** – Obtained biofilm from Starch<sub>oxd</sub>/CMC

### 2.4 FTIR analysis

The analysis was performed using an FT-801 FTIR spectrometer (Simex, Russia), with a resolution of 1 cm<sup>-1</sup> at a range of 300–4700 cm<sup>-1</sup>, at a temperature of 25±10°C, in accordance with the standard method. An accessory was used to measure attenuated total reflection (ATR) and specular-diffuse reflection (SDR).

### 2.5 Mechanical Characterization

The mechanical characteristics of the biofilm was studied using a texture analyzer (TA-3000, LabSol, China) with a measured load range of 0.01–60N and a loading speed range of 0.0005–500 mm/min. The data registration was performed automatically using a computer. During the testing of the samples under a load of 0.01 N, the movement speed was 0.1 mm/min. The samples were tested until the maximum tensile force was reached or before the sample became deformed.

### 2.6 Water absorption and biodegradation properties

The film sample was prepared and dried at 50°C for 24 hours. The dried film was placed in a buffer solution with a pH of 5.5 for 3 days, removed from the water and dried using a filter paper, and its weight was measured with an accuracy of 0.0001 g.

## 3 Results and discussion

### 3.1 FTIR analysis of oxidized starch

Figure 2 shows the result of FTIR analysis of oxidized starch compared to the original starch. In the figure 2a represented spectra region between 3500-

3000  $\text{cm}^{-1}$  indicates the presence of OH groups and signal on 1653  $\text{cm}^{-1}$  is characterized by the absorption of the C-O bond [13,14]. Corresponding absorption of all  $\text{CH}_2$  groups was identified on 2868  $\text{cm}^{-1}$ . The absorption at 1147  $\text{cm}^{-1}$ , 1078  $\text{cm}^{-1}$  and 990  $\text{cm}^{-1}$ , respectively, reflects the valence oscillations of the C-O bond, C-O-H and C-O-C groups in the glucose ring. The absorption signals 855  $\text{cm}^{-1}$ , 856  $\text{cm}^{-1}$  and 867  $\text{cm}^{-1}$  indicate a  $\beta$ -glycosidic bond [15,16]. In Figure 2b, absorption of C=O bond in carboxyl and carbonyl groups formed in oxidized starch was observed in the range of 2100-2150  $\text{cm}^{-1}$  [17].

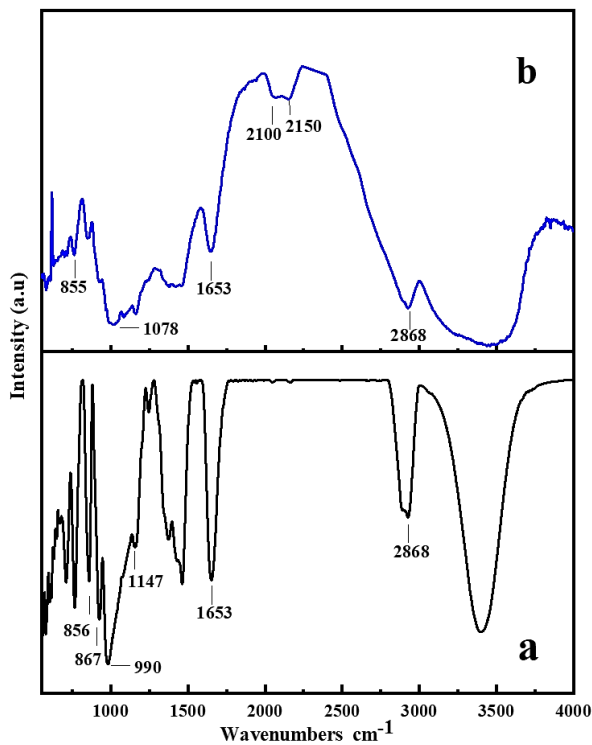


**Figure 2** – FTIR spectrum of a-initial starch; b- oxidized starch

### 3.2 FTIR analysis of biofilm

Figure 3 shows the relative FTIR spectrum of the starch/CMC biofilm with the original monomers. The intensity of the signal can be noticed in the absorption region of 1710  $\text{cm}^{-1}$ , characteristic of the carboxyl groups in the molecule of oxidized starch and CMC, is maximally reduced in the spectrum of the biofilm. This may be due to the fact that during the synthesis, the bonding agent succinic anhydride leads to low

intensity by cross-linking the carboxyl groups in the monomer molecule [18-20].

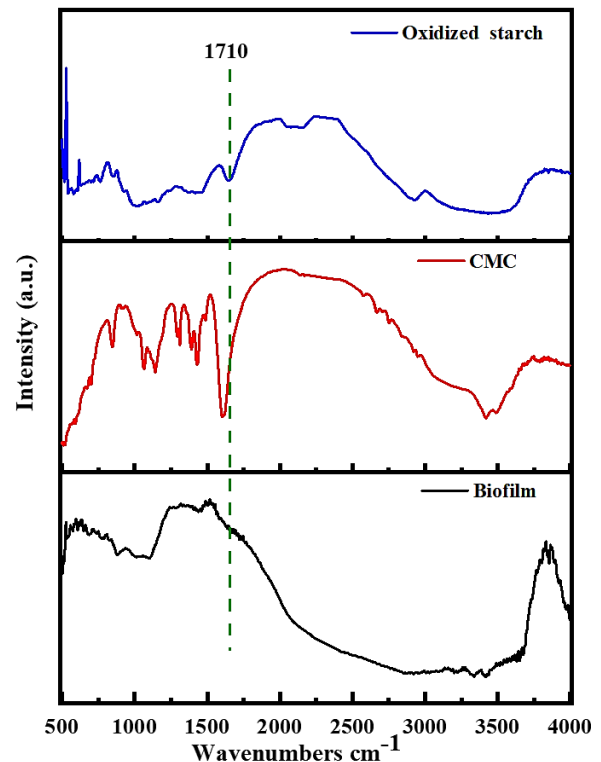


**Figure 3** – FTIR spectrum of biofilm  $\text{Starch}_{\text{oxd}}/\text{CMC}$

### 3.3 Mechanical Characterization

During the study, the mechanical properties and water absorption properties of the biofilm were compared with the polyester-based biodegradable commercial product TAPIOPLAST (SMS Corporation, Thailand). The result of studying the mechanical properties of the biofilm is shown in Figure 4. The commercial product TAPIOPLAST has been found to have a mechanical strength of 2.5 MPa. The mechanical strength limit was to be found, of starch/CMC biofilm is equal to 0.78 MPa, that is, 3 times smaller than that of TAPIOPLAST. This is because the main composition of the TAPIOPLAST film can be synthetic polyester in addition to the biodegradable component.

In the studies [21, 22], it was determined that the mechanical strength limits of films based on oat starch and topaca starch are equal to 0.36 and 0.78 MPa. It shows that the result obtained in this study corresponds to the indicators of the previous study.

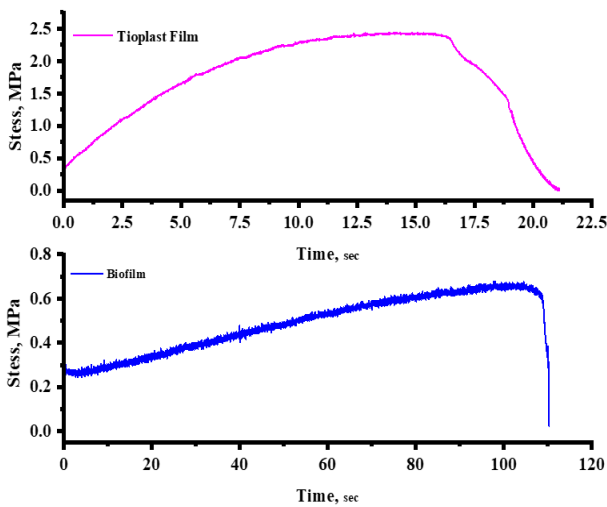


**Figure 4** – Plot of mechanical strength of Starch<sub>oxd</sub>/CMC biofilm compared to commercial film

### 3.4 Water absorption and biodegradation properties

Short-term biodegradability of Starch<sub>oxd</sub>/CMC-based biofilm compared with commercial product TAPIOPLAST (Table 1). Since the pH of the surface layer of the soil is between 5.5 and 6.5, the biodegradation properties of biofilms were studied over a period of 3 days using a weak acid buffer solution with a pH of 5.5 as a soil model. In addition, the property of water absorption in this environment was also determined. According to the obtained results, the degree of water absorption of polyester-based biodegradable commercial product TAPIOPLAST was 0.19%, and the degree of biodegradation was 0.0001%. Starch<sub>oxd</sub>/CMC biofilm had a water absorption degree of 0.21% and a biodegradation degree of 0.008%. The values of the degree of water absorption of both obtained samples

were insignificant and showed that the Starch<sub>oxd</sub>/CMC film was exposed to biodegradation for a longer time [23,24].

**Table 1** – Starch<sub>oxd</sub>/CMC comparative values of the short-term biodegradation rate of the biofilm based on the commercial product TAPIOPLAST

Sample	Water absorption degree, %	Biodegradability, %
TAPIOPLAST	0,19%	0,0001
Biofilm	0,21%	0,008

## 4 Conclusions

The chemical structure of the Starch<sub>oxd</sub>/CMC biofilm obtained during the study revealed that the cross-linking agent succinic anhydride binds the carboxyl groups in the starch and CMC molecules. In addition, the biodegradation, mechanical and water-swelling properties of the obtained biofilm were compared with the commercial film TAPIOPLAST. As a result, the mechanical strength limit of Starch<sub>oxd</sub>/CMC biofilm was 0.78 MPa. The degree of water absorption was to be determined in a short period of time was 0.21%, and the degree of biodegradation was equal to 0.008%. The Starch<sub>oxd</sub>/CMC biofilm obtained within the framework of this study has the potential to be used in the development of food packaging, mulching coatings in agriculture, and drug-carrying capsules in pharmaceuticals.

### Acknowledgement:

This research has been funded by the Science Committee of the Ministry of Science and Higher Education of the Republic of Kazakhstan (Grant No. AP19579302).

## References

- Hosseini S.N., Pirsá S., & Farzi J. Biodegradable nano composite film based on modified starch-albumin/MgO; antibacterial, antioxidant and structural properties // *Polymer Testing*. – 2021. – Vol. 97. – P. 107182. <https://doi.org/10.1016/j.polymertesting.2021.107182>
- Sganzerla W.G., Rosa G.B., Ferreira A.L.A., et al. Bioactive food packaging based on starch, citric pectin and functionalized with *Acca sellowiana* waste by-product: Characterization and application in the postharvest conservation of apple//*International Journal of Biological Macromolecules*. – 2020. – Vol. 147. – P. 295-303. <https://doi.org/10.1016/j.ijbiomac.2020.01.074>
- Resano-Goizueta B.K., Ashokan T.A., & Trezza Padua, G.W. Effect of nano-fillers on tensile properties of biopolymer films // *Journal of Polymer Environment*. – 2018. – Vol. 26. – P. 3817–3823.
- Shankar S., & Rhim J-W. Bionanocomposite films for food packaging applications. Reference module in food science. – 2018 <https://doi.org/10.1016/B978-0-08-100596-5.21875-1>

5. Biduski B., do Evangelho J.A., da Silva F.T., de Mello S.L., Halal E., Takimi A.S., Carreno N.L.V., Dias A.R.G., & da Rossa E. Physicochemical properties of nanocomposite films made from sorghum-oxidized starch and nanoclay. *Starch Biosynthesis, Nutrition, and Biomedicine*. – 2017. – Vol. 69. – P. 1700079.
6. Bandopadhyay S., Martin-Closas L., Pelacho A. M., & DeBruyn J. M. Biodegradable Plastic Mulch Films: Impacts on Soil Microbial Communities and Ecosystem Functions // *Frontiers in Microbiology*. – 2018. – Vol. 9. – P. 819. <https://doi.org/10.3389/fmicb.2018.00819>
7. Wang B., Sui J., Yu B., Yuan C., Guo L., Abd El-Aty A. M., & Cui B. Physicochemical properties and antibacterial activity of corn starch-based films incorporated with *Zanthoxylum bungeanum* essential oil // *Carbohydrate Polymers*. – 2021. – Vol. 254. – P. 117314. <https://doi.org/10.1016/j.carbpol.2020.117314>
8. Kaur P., Alam T., Singh H., Jain J., Singh G., & Broadway A. A. Organic acids modified starch–CMC based biodegradable film: antibacterial activity, morphological, structural, thermal, and crystalline properties // *Journal of Pure and Applied Microbiology*. – 2023. – Vol. 17(1). – P. 241-257. <https://doi.org/10.22207/JPAM.17.1.14>
9. Vu H.P.N., & Lumdubwong N. Starch behaviors and mechanical properties of starch blend films with different plasticizers // *Carbohydrate Polymers*. – 2016. – Vol. 154. – P. 112–120. <http://dx.doi.org/10.1016/j.carbpol.2016.08.034>
10. Wu L., Lev S., Wei D., Zhang S., Zhang S., Li Z., Liu L., & He T. Structure and properties of starch/chitosan food packaging film containing ultra-low dosage GO with barrier and antibacterial // *Food Hydrocolloids*. – 2023. – Vol. 137. – P. 108329. <https://doi.org/10.1016/j.foodhyd.2022.108329>
11. El Halal S.L.M., Colussi R., Deon V.G., Pinto V.Z., Villanova F.A., Carreño, N.L.V., Dias A.R.G., & da Rosa Zavareze E. Films based on oxidized starch and cellulose from barley // *Carbohydrate Polymers*. – 2015. – Vol. 133. – P. 644–653. <http://dx.doi.org/10.1016/j.carbpol.2015.07.024>
12. Kaiyrbekov N., Akatan, K., Kabdrakhmanova S., Kuanyshbekov T., Imasheva A., & Battalova A. Modification of nanostarch by citric acid // *Physical Sciences and Technology*. – 2021. – Vol. 8(1-2). – P. 66-70. <https://doi.org/10.26577/phst.2021.v8.i1.09>
13. Da Rosa Zavareze E., Pinto V.Z., Klein B., El Halal S.L.M., Elias M.C., Prentice-Hernández C., & Dias A.R.G. Development of oxidised and heat–moisture treated potato starch film // *Food Chemistry*. – 2012. – Vol. 132. – P. 344–350.
14. Liewchirakorn P., Ngamchuea K. Benign electrolytic modifications of starch: effects on functional groups and physical properties // *RSC Advances*. – 2023. – Vol. 13. – P. 30040-30051. <https://doi.org/10.1039/D3RA06382H>
15. Prabhu S.V., Hemalatha P., Tizazu B.Z., & Gosu A. Development of teff-starch based edible film: mechanical and optical properties // *IOP Conference Series: Materials Science and Engineering*. – 2021. – Vol. 1091. – P. 012050.
16. Subramanian S., Natarajan K. A., & Sathyanarayana D. N. FTIR spectroscopic studies on the adsorption of an oxidized starch on some oxide minerals // *Mining, Metallurgy & Exploration*. – 1989. – Vol. 6. – P. 152–158. <https://doi.org/10.1007/BF03402707>
17. Wilpiszewska K. Hydrophilic films based on starch and carboxymethyl starch // *Polish Journal of Chemical Technology*. – 2019. – Vol. 21(2). – P. 26-30. <https://doi.org/10.2478/pjct-2019-0016>
18. Vu H. P. N., & Lumdubwong N. Starch behaviors and mechanical properties of starch blend films with different plasticizers // *Carbohydrate Polymers*. – 2016. – Vol. 154. – P. 112–120.
19. Wang Y., Liu H., Geng F., Yang P., Lü J., Li X. Label-free analysis of biofilm phenotypes by infrared micro- and correlation spectroscopy // *Analytical and Bioanalytical Chemistry*. – 2023. – Vol. 415. – P. 3515–3523. <https://doi.org/10.1007/s00216-023-04741-4>
20. Ortega-Toro R., Jimenez A., Talens P., & Chiralt A. Properties of starch-hydroxypropyl methylcellulose based films obtained by compression molding // *Carbohydrate Polymers*. – 2014. – Vol. 109. – P. 155–165.
21. Saberi B., Thakur R., Vuong Q.V., Chockchaisawasdee S., Golding J.B., Scarlett C. J., & Stathopoulos C.E. Optimization of physical and optical properties of biodegradable edible films based on pea starch and guar gum // *Industrial Crops and Products*. – 2016. – Vol. 86. – P. 342–352.
22. Żołek-Tryznowska Z., & Kałuża A. The influence of starch origin on the properties of starch films: Packaging Performance // *Materials*. – 2021. – Vol. 14. – P. 1146.
23. Zainuddin, S., Hasan, S. M. K., Loeven, D., Hosur, M. Mechanical, fire retardant, water absorption and soil biodegradation properties of poly (3-hydroxy-butyrates-co-3-valerate) nanofilms // *Journal of Polymers and the Environment*. – 2019. – Vol. 27. – P. 2292–2304. <https://doi.org/10.1007/s10924-019-01517-9>
24. Santos Cotta A. A. R., Ferreira L. F., Borges S. V., Nascimento B. D. S., Dias M. V. Biodegradation, water sorption isotherms and thermodynamic properties of extruded packaging composed of cassava starch with tomato peel // *Journal of Polymers and the Environment*. – 2023. <https://doi.org/10.1007/s10924-023-03094-4>

**Information about the authors:**

Akatan Kydyrmolla, PhD in Chemistry, Sarsen Amanzholov East Kazakhstan University (Ust-Kamenogorsk, Kazakhstan), e-mail: ahnur.hj@mail.ru;

Battalova Ainur, Master of Chemistry, Sarsen Amanzholov East Kazakhstan University (Ust-Kamenogorsk, Kazakhstan), e-mail: 2012kausar@mail.ru;

Sagiyeva Nazym, Master of Chemistry, Sarsen Amanzholov East Kazakhstan University (Ust-Kamenogorsk, Kazakhstan), e-mail: sagieva\_n@ukk.nis.edu.kz;

Kabdrakhmanova Sana, Sarsen Amanzholov East Kazakhstan University (Almaty, Kazakhstan), e-mail: sanaly33@mail.ru;

Kaiyrbekov Nariman (Corresponding Author) – Sarsen Amanzholov East Kazakhstan University (Ust-Kamenogorsk, Kazakhstan), e-mail: narimankayrbekov@gmail.com;









Shaimardan Esbol, PhD in Chemistry, Satbaev University (Almaty, Kazakhstan), e-mail: esbol\_shay@mail.ru;

Tursyngazykyzy Altynai, Sarsen Amanzholov East Kazakhstan University (Ust-Kamenogorsk, Kazakhstan), e-mail: altynaitursyngazy@mail.ru;

Beisebekov Madiyar, PhD in Chemistry, Associate Professor at the Satbaev University (Almaty, Kazakhstan), e-mail: make1987@mail.ru;

Kampitova Gulfaridat, candidate in Agriculture, Kazakh National Agrarian Research University (Almaty, Kazakhstan), e-mail: kampitova@gmail.com

## Technology of reducing greenhouse gas emissions for decarbonization and decreasing anthropogenic pressure on the environment

S. Bolegenova , A. Askarova , Sh. Ospanova\* ,  
S. Zhumagaliyeva , A. Makanova ,  
A. Aldiyarova , A. Nurmukhanova  and G. Idrissova 

Physics and Technology Department, Al-Farabi Kazakh National University, Almaty, Kazakhstan

\*e-mail: [Shynar.Ospanova@kaznu.edu.kz](mailto:Shynar.Ospanova@kaznu.edu.kz)

(Received April 28, 2024; received in revised form May 13, 2024; accepted May 17, 2024)

The focus of this article is to research technology for reducing greenhouse gas emissions, such as carbon dioxide and nitrogen, produced by internal combustion engines when liquid fuels are burned in them to minimize humans' negative impact on the environment. Based on statistical data, the work presents an analysis of the dynamics of local and global emissions into the atmosphere in recent years and preventive measures to reduce them for decarbonization. The mathematical model is based on basic conservation equations that explain the liquid fuels combustion process in high turbulence. The paper outlines the outcomes of computational experiments that were carried out to determine the best conditions for the combustion of liquid fuels (petrol and heptane). The droplet injection rate in the combustion chamber at high turbulence was analyzed to determine the atomization and combustion processes. Optimum combustion parameters for petrol and heptane were identified. The temperature and dispersion characteristics of the fuel-air mixture, along with the concentration fields of combustion products such as CO<sub>2</sub> and N<sub>2</sub>, and the aerodynamics of multiphase flow for two types of liquid fuels were determined through computational experiments. The optimum combustion modes for petrol and heptane were determined based on the attained results, which can facilitate rational fuel combustion, reduce the number of released harmful emissions, and enhance engine efficiency. Implementing the optimum parameters that were achieved for the combustion of hydrocarbon liquid fuels in the combustion chambers of actual heat engines will minimize the anthropogenic load on the surrounding atmosphere with the release of greenhouse gases, promote decarbonization in the energy sector, and reduce the carbon footprint.

**Key words:** combustion, liquid fuels, decarbonization, greenhouse gases, harmful emissions.

**PACS number(s):** -47.70.Fw.

### 1 Introduction

Global environmental threats are greatly exacerbated by air pollution. The International Labour Organization defines air pollution as the presence of dangerous or harmful substances in the air without specifying their physical form. Fossil fuel combustion, agriculture, and mining are just some of the factors that contribute to air pollution. The air pollutants that are most prevalent and substantial include carbon dioxide, sulfur dioxide, nitrogen oxides, and dust.

Most countries around the world have always been concerned about carbon dioxide emissions. This is because the increase in the amount of gas

produced has serious consequences for the climate and the environment. The effects are so severe and broad that they involve modifications to climate conditions, increases in ocean levels, melting glaciers, unpredictability of precipitation, and even depletion of the ozone layer.

The complex global picture of carbon dioxide emissions in 2023 reflects the ongoing struggle between economic development and environmental sustainability. The entire global community will still be affected by global CO<sub>2</sub> emissions even as awareness increases and efforts are made to transition to cleaner energy sources in 2023. Emissions trends indicate a need for urgent action to address climate change, with both setbacks and



progress seen this year. The greenhouse effect is amplified by the accumulation of CO<sub>2</sub> and other greenhouse gas emissions in the atmosphere, which traps heat and causes global temperatures to rise. This warming contributes to climate change by affecting ecosystems, weather patterns, sea levels, and overall environmental sustainability [1-3].

According to the International Energy Agency, global energy CO<sub>2</sub> emissions rose by 1.1% in 2023 to reach a new record high of 37.4 billion tonnes. The electricity and heat generation sector recorded the largest increase in emissions. Emissions from the electricity and heat sector increased by 1.8% to a historic high of 14.7 billion tonnes. The main reason for this increase was the switch from gas to coal in many regions, which led to a 2.1 percent increase in CO<sub>2</sub> emissions from coal-fired power generation [4].

A complex global scenario with record high levels and regional differences is evident in the analysis of carbon dioxide emissions in 2023, resulting in urgent action to combat climate change. To keep global temperatures under control, the EU has pledged to achieve a 55 percent reduction in

greenhouse gas emissions by the decade apex compared to 1990 levels and to reach "net zero" by 2050. According to the report of the European Scientific Advisory Council on Climate Change, the 27 Member States need to reduce emissions about twice as fast as they have been doing so on average over the past 17 years.

Kazakhstan's atmosphere in 2023 is heavily polluted by sulfur dioxide, nitrogen oxides, carbon oxides, ammonia, and hydrogen sulfide. From the total volume of pollutants emitted into the atmospheric air, 80.7 percent were gaseous and liquid substances and 19.3 percent were solid substances (Fig.1) [5, 6].

Decarbonization is the process of replacing fossil fuel-based systems with electricity that is produced using low-carbon resources such as renewable energy. Traditional energy sources such as coal, oil, and natural gas cannot be abandoned due to our current level of technology. Nonetheless, it is already possible to boost the effectiveness of their utilization to decrease emissions. Climate stabilization cannot be achieved without the energy system's complete decarbonization.

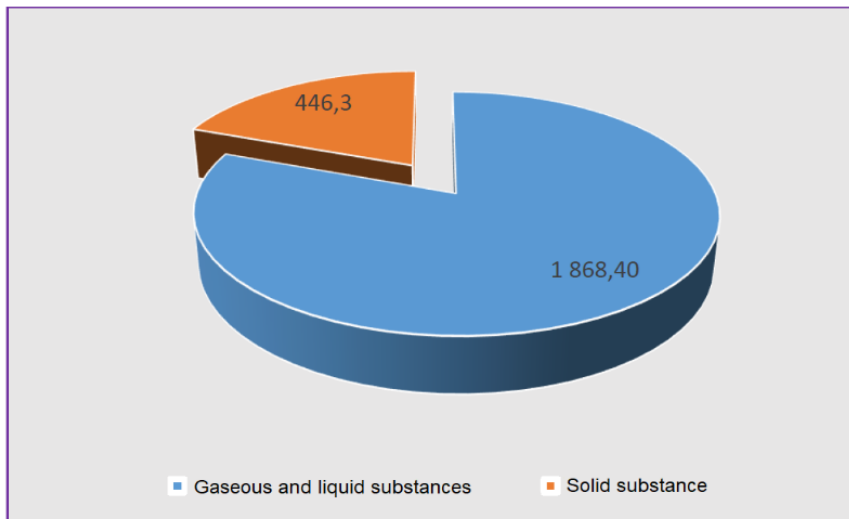


**Figure 1** – Emissions of pollutants into the air by consistency for 2023, thousand tons

Low-carbon energy sources are used to reduce carbon dioxide emissions by decarbonization, which results in reducing greenhouse gas emissions. The global economy should be completely decarbonized by 2050, carbon taxes must be introduced, and adaptation to climate change must be stepped up by

the international community [7, 8]. Despite this, carbon dioxide emissions are still on a plateau and are rapidly rising. The idea of carbon neutrality and zero emissions means that the number of emissions produced is not greater than the carbon engrossed by forests and oceans.

Scientific and technological progress is accompanied by an increase in environmental pollution, which can change its indicators and parameters. Under these conditions, it is necessary to study the impact of various pollutants on the environment, assess possible negative environmental consequences, and relying on the outcomes of the assessment, if necessary, implement local or global measures to prevent them promptly [9].

The increase in carbon dioxide emissions and its concentration in the air changes the functioning of the carbon cycle that has developed over the centuries and, together with other gases, the greenhouse effect on the Earth, which has a general tendency to increase, causing climate warming.

It is very important to establish the scientific basis for an intensive technological process that integrates the use of fuels and their wastes and eliminates the detrimental effects of their production on the biosphere. The present-day methodology of nature security and energy sparing infers the choice of the foremost successful accomplishments of scientific and innovative advance, among which three fundamental bunches of measures are highlighted: utilization, energy modernization, and accelerated energy sparing. In this respect, and the light of the Euro natural benchmarks rules, it is essential to move forward the quality of internal combustion motors, which in turn are controlled by the liquid fuel injection framework.

## 2 Mathematical model of liquid particles spray and combustion in a reacting flow

Equations of fluid phase motion, droplet evaporation, energy, and mass transfer with appropriate initial and boundary conditions determine the mathematical representation of liquid fuel atomization and combustion [10-16].

The  $m$  component's continuity equation is written in the following manner [10-13]:

$$\begin{aligned} \frac{\partial \rho_m}{\partial t} + \bar{\nabla}(\rho_m \bar{u}) = \\ = \bar{\nabla} \left[ \rho D \bar{\nabla} \left( \frac{\rho_m}{\rho} \right) \right] + \dot{\rho}_m^c + \dot{\rho}^s \delta_{m1}, \end{aligned} \quad (1)$$

where  $\rho_m$  is the  $m$  component's mass density,  $\rho$  is the full mass density, and  $u$  is fluid velocity. The

liquid's continuity equation (1) can be obtained by summing the equation of the overall phases.:

$$\frac{\partial \rho}{\partial t} + \bar{\nabla}(\rho \bar{u}) = \dot{\rho}^s. \quad (2)$$

The liquid phase's momentum transfer equation is expressed in this way [11, 12]:

$$\begin{aligned} \frac{\partial(\rho \bar{u})}{\partial t} + \bar{\nabla}(\rho \bar{u} \bar{u}) = \\ = -\frac{1}{a} \bar{\nabla} p - A_0 \bar{\nabla} \left( \frac{2}{3} \rho k \right) + \bar{\nabla} \bar{\sigma} + \bar{F}^s + \rho \bar{g}, \end{aligned} \quad (3)$$

where the laminar flows have a zero value of  $A_0$ , and turbulent flows have a unity value of  $A_0$ .

The following formula describes the viscous stress tensor [11]:

$$\sigma = \mu \left[ \bar{\nabla} \bar{u} + (\bar{\nabla} \bar{u})^T \right] + \lambda \bar{\nabla} \bar{u}. \quad (4)$$

Droplet spraying requires phase transformations to maintain the law of conservation of internal energy [13]:

$$\begin{aligned} \frac{\partial(\rho \bar{I})}{\partial t} + \bar{\nabla}(\rho \bar{u} \bar{I}) = -\rho \bar{\nabla} \bar{u} + \\ + (1 - A_0) \bar{\sigma} \bar{\nabla} \bar{u} - \bar{\nabla} \bar{J} + A_0 \rho \varepsilon + \dot{Q}^c + \dot{Q}^s. \end{aligned} \quad (5)$$

The relation is responsible for determining the heat flux vector  $J$  [9, 14]:

$$\bar{J} = -k \bar{\nabla} T - \rho D \sum_m h_m \bar{\nabla}(\rho_m / \rho), \quad (6)$$

where  $T$  is liquid temperature,  $h_m$  is the  $m$  component's enthalpy,  $\dot{Q}^c$  is used to describe the heat produced by a chemical reaction,  $\dot{Q}^s$  is the amount of heat that fuel injection brings.

Models with two differential equations are more flexible in engineering calculations of turbulent flows. The model with two differential equations is the most frequently used one in technical flows. In this  $k - \varepsilon$  model, the kinetic energy of turbulence and its dissipation rate are solved through the use of two equations. [15, 16]:

$$\rho \frac{\partial k}{\partial t} + \rho \frac{\partial \bar{u}_j k}{\partial x_j} = \frac{\partial}{\partial x_j} \left[ \left( \mu + \frac{\mu_t}{\sigma_k} \right) \frac{\partial k}{\partial x_j} \right] \frac{\partial \bar{u}_i}{\partial x_j} +$$

$$+ G - \frac{2}{3} \rho k \delta_{ij} \frac{\partial \bar{u}_i}{\partial x_j} - \rho \varepsilon \quad (7)$$

$$\rho \frac{\partial \varepsilon}{\partial t} + \rho \frac{\partial \bar{u}_j \varepsilon}{\partial x_j} - \frac{\partial}{\partial x_j} \left[ \left( \mu + \frac{\mu_t}{\sigma_\varepsilon} \right) \frac{\partial \varepsilon}{\partial x_j} \right] =$$

$$= c_{\varepsilon_1} \frac{\varepsilon}{k} G - \left[ \left( \frac{2}{3} c_{\varepsilon_2} - c_{\varepsilon_3} \right) \rho \varepsilon \delta_{ij} \frac{\partial \bar{u}_i}{\partial x_j} \right] - c_{\varepsilon_2} \rho \frac{\varepsilon^2}{k} \quad (8)$$

These are standard  $k - \varepsilon$  equations. The model's simplicity, good convergence, and accuracy make it the most used model for modeling a wide range of turbulent flows. The popularity of this turbulence model is due to its simplicity, cost-effectiveness, and accurate prediction of the properties of both non-reacting and burning flows. The model can be successfully used to calculate the characteristics of a reacting flow with chemical transformations due to its ability to work well at high Reynolds numbers and high flow turbulence. The experiment has led to the determination of model constants  $c_{\varepsilon_1}$ ,  $c_{\varepsilon_2}$ ,  $c_{\varepsilon_3}$ ,  $\sigma_k$ ,  $\sigma_\varepsilon$  [17]. The empirical determination of standard values for these constants is commonly used in engineering calculations.

### 3 Physical statement of the problem and computing mesh

A quantitative assessment of harmful anthropogenic gaseous emissions emitted during heat engine operation has been conducted by computer studies of the combustion processes of two kinds of liquid hydrocarbon fuels in combustion chambers. The following fuels were used in this work: petrol and heptane. Carbon dioxide and water are produced by the combustion of these fuels in the combustion chamber.

Petrol is the fuel used most frequently in cars. Automobile and motorcycle engines use automotive petrol as fuel, and it can also be used to make engine components for other purposes. The colorless liquid known as petrol is a mixture of hydrocarbons of different structures and can boil at a temperature of 33-205°C. It is employed in vehicles designed for

both cargo and passengers, as well as individual motor vehicles.

The liquid heptane, which is colorless and flammable, is used as rocket fuel and has a low flash point of around 4°C and a high auto-ignition temperature of 223°C. Heptane vapors in air have an area of ignition that is 1.1-6.7 % (by volume). Heptane is a hydrocarbon from the paraffin series and is categorized as a hazardous substance [18].

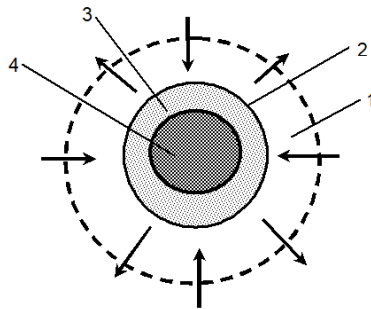
Burning liquid fuel is only possible due to the flame, which is then pre-sprayed into small droplets. Several factors can affect the combustion process, including the combustion chamber design, the oxygen concentration of the supplied air, and the injection pressure. The combustion of liquid fuel involves multiple stages.

The first stage involves heating the liquid fuel to boiling point and vaporizing it, followed by combustion in the second stage. Figure 2 illustrates how liquid fuel droplets burn. The fuel's combustion process occurs first after the droplets start vaporizing since their boiling point is lower than the ignition temperature. The combustion surface is penetrated by air through the resulting combustion products. The combustion rate is dependent on the size of the combustion surface, which is dependent on the degree of atomization of the liquid fuel. The greater the degree of atomization, the faster and more complete the combustion process.

A combustion zone is created near the droplet by the spherical surface, which has a diameter that is 1-5 times larger than the droplet's size. The droplet evaporates as a result of radiation heat from the combustion zone. Liquid fuel vapors and combustion products exist in the space between the droplet and the combustion zone. Air and combustion products can be found outside of the combustion zone. Fuel vapors are diffused into the combustion zone from the interior, and oxygen from the exterior. The chemical reaction is initiated by these components, which is followed by the release of heat and the formation of combustion products [19].

The cylindrical combustion chamber is 15 cm high and 4 cm in diameter (Fig.3). As depicted in Figure 4, the combustion chamber's general form is shown. The calculation space comprises of 600 cells. The fuel burns at 4 ms. The combustion chamber is filled with liquid fuel through a circular nozzle embedded in the middle of the chamber's lower part. The fuel droplet injection takes 1.4 ms to complete. Fuel injection speed is 250 m/s. Rapid

vaporization of the fuel after injection leads to combustion in the gas phase.



1 – oxidant and combustion products dissemination zone,  
2 – liquid, 3 – fuel vapor, 4 – liquid droplet  
**Figure 2** – Liquid fuel's single droplet combustion plot

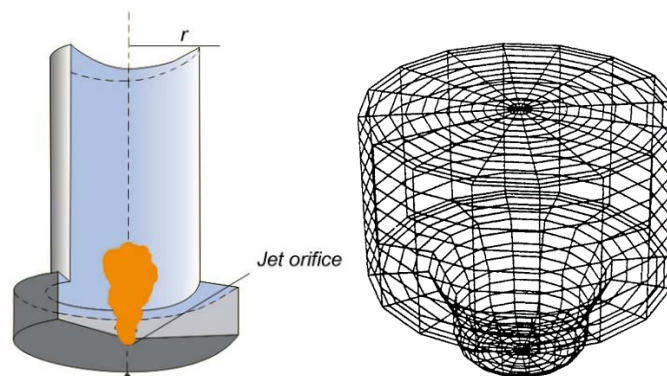


**Figure 3** – The combustion chamber's computer model and the prospect of the computing mesh created from the OFFSET option

#### 4 Modeling results

The work's objective is to investigate the liquid fuel injection speed impact on combustion by applying computer modeling techniques that solve for the differential equations of complex turbulent flows. The speed of how the liquid fuels were put into the chamber went from 150 to 350 m/s. Figure 4 displays how the flame temperature changes when the injecting liquid fuel droplets' speed is increased. The research focused on the fuel's injection rate and its influence on the maximum temperature achieved during the burning process. At speeds below 150 m/s, liquid fuels fail to ignite due to insufficient injection speed.

The most efficient combustion process of petrol occurs at the fuel injection speed of 200 m/s; at this time the temperature in the chamber takes the value of 2417 K. The effective speed of heptane is 250

The wall's temperature in the combustion chamber is 353 K. The chamber's initial gas temperature is approximately 900 K. 300 K is the injected fuel's temperature. The injected droplets' initial radius is 3  $\mu\text{m}$ . The angle for droplet injection is 10 degrees.

Figure 3 also shows an axisymmetric structured computational grid used when conducting a numerical experiment in 3D modeling. The chamber's three-dimensional geometry is implemented by the SETUP subroutine by reading the initial design data using the OFFSET input option, considering the actual dimensions of the combustion chamber [10, 14, 20].

m/s. The maximum temperature at a given heptane droplet injection rate is 2177 K. Heptane's maximum gas temperature in the combustion chamber and the amount of carbon dioxide produced from burning the fuel depending on how fast the droplets are injected. At these injection rates, the fuel burns without residue, the concentration of produced  $\text{CO}_2$  is the lowest (Fig.5), and the chamber becomes extremely heated.

The graph in Figure 5 illustrates the correlation between the injection speed of petrol and heptane and the amount of carbon dioxide released in the combustion chamber. For petrol, at the optimum injection speed of 200 m/s, the concentration of  $\text{CO}_2$  produced is minimal, its value was 0.182 g/g. And at the combustion of heptane much less greenhouse gas is emitted (0.127 g/g) in comparison with petrol, which is an indicator of good calorific value of fuel, high mobility of its droplets, and active reacting chemical medium.

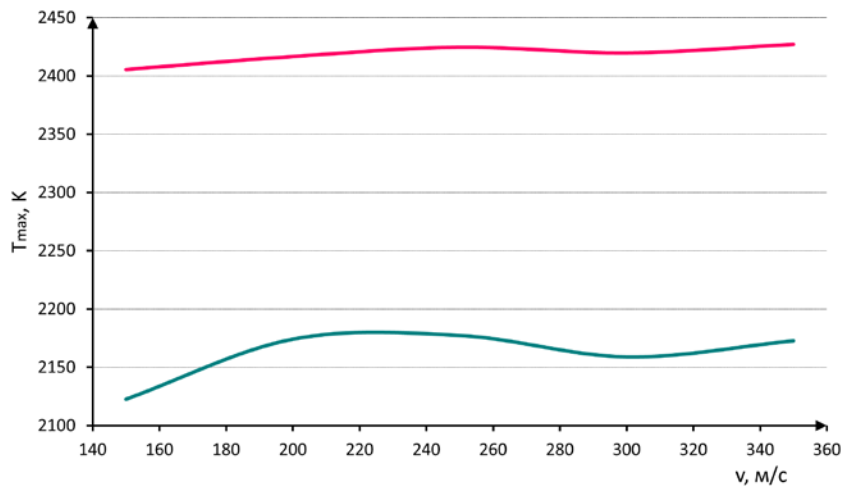


**Figure 4** – Change in the maximum combustion temperature of liquid fuel droplets with an increase in their injection rate: red line – petrol, green line – heptane

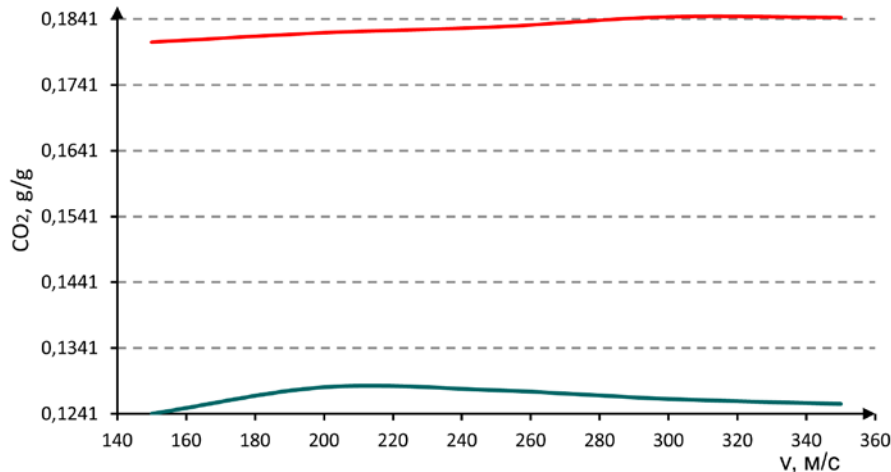


**Figure 5** – Effect of liquid fuel droplet injection rate on carbon dioxide  $CO_2$  distribution: red line – petrol, green line – heptane

Figures 6-14 exhibit the computer simulation results showing how liquid fuel burns in the chamber with droplets moving at an optimum speed.

Figures 6 and 7 demonstrate the liquid fuel droplets spread in the combustion chamber when it's injected at the proper speed. Flow visualization is presented at different time moments.

Analyzing the particle dispersion in Figures 6 and 7, during the combustion process, petrol droplets are concentrated at a 2 cm height in the combustion chamber, and heptane droplets up to 1 cm. Since heptane has a high surface tension, this affects the mobility and active reaction of its droplets with the oxidizing medium. In this regard,

it's safe to say that petrol droplets occupy a larger chamber area compared to heptane.

Similar distribution patterns of liquid fuel droplets (octane and dodecane) were observed by the authors in their studies [21-23]. Small fuel droplets and high levels of turbulence were determined to result in improved mixing with the oxidizer. This leads to plasma-chemical reactions taking place throughout the interior of the combustion chamber. These high-temperature energy processes are associated with the creation of environmentally friendly, energy-efficient, and energy-saving fuel technologies with minimal anthropogenic influence.

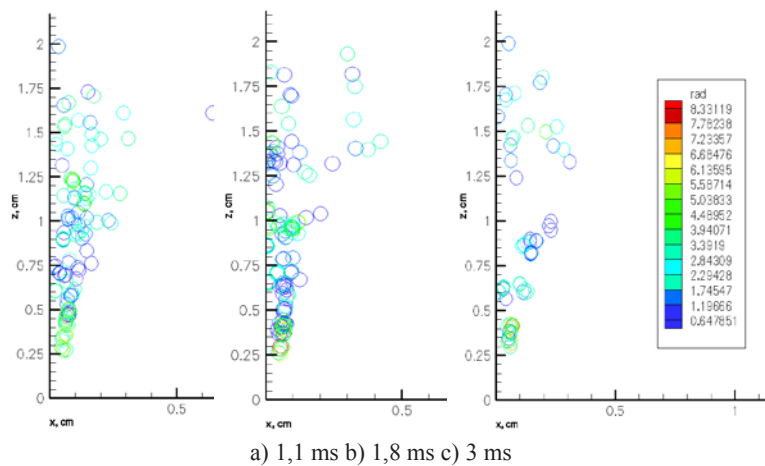


**Figure 6** –The petrol droplets dispersion by size at optimum injection speed 200 m/s

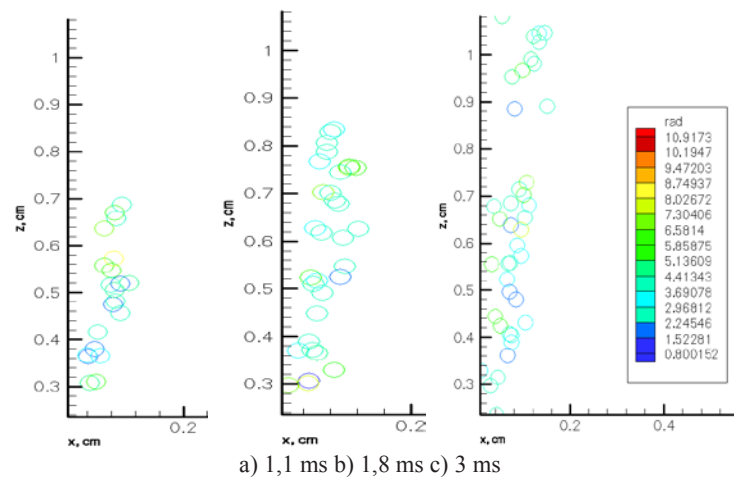


**Figure 7** – The heptane droplets dispersion by size at optimum injection speed 250 m/s

Figures 8 and 9 illustrate the fluctuation in peak temperatures for petrol and heptane in the combustion chamber at various time intervals. The graph in Figure 8 demonstrates the fluctuations in temperature within the fuel chamber for petrol. The hottest spot in the flame, which is at the center, reaches 3.6 cm high in the combustion chamber. The temperature in the remaining part of the chamber rises to 1133 K. Petrol can withstand temperatures of up to 2427 K while heptane can tolerate temperatures of up to 2177 K. Since the core of the heptane flare is at a chamber height of 4.2 cm.

Thus, with optimal temperature and speed of injected droplets, as well as rational combustion and proper organization of this process, it is conceivable to reduce the formation of such intermediate

reaction products as carbon monoxide and soot, which greatly harm the operation of the thermal engine [24].

Graphs 10 and 11 illustrate the fluctuations in carbon dioxide concentration at different altitudes within a combustion chamber while burning petrol and heptane. Up to 1.8 ms, no carbon dioxide is formed and the combustion process does not occur. While the  $\text{CO}_2$  concentration for petrol is 0.012 g/g at the initial time of 1.8 ms, during the last 4 ms of combustion time its value reaches up to 0.182 g/g. The combustion products reach their maximum values in the central part of the flare, also the maximum temperature values are observed here. The quantity of carbon dioxide formed during heptane combustion was 0.127 g/g.

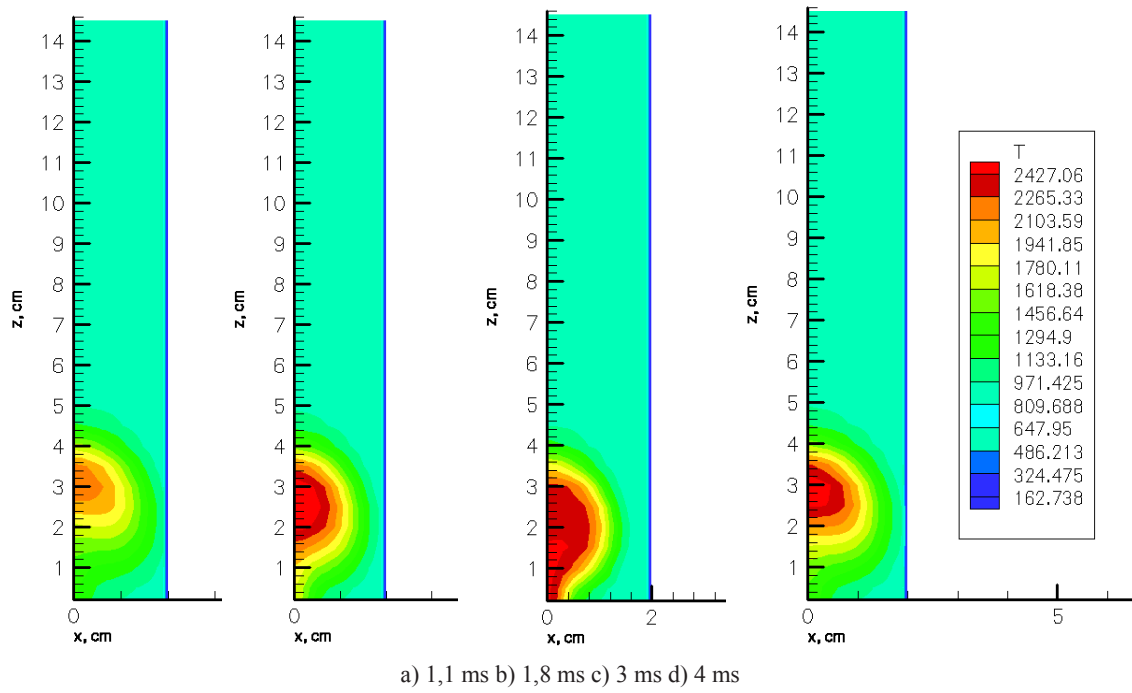


Figure 8 – Temperature profile during petrol combustion at different moments of time

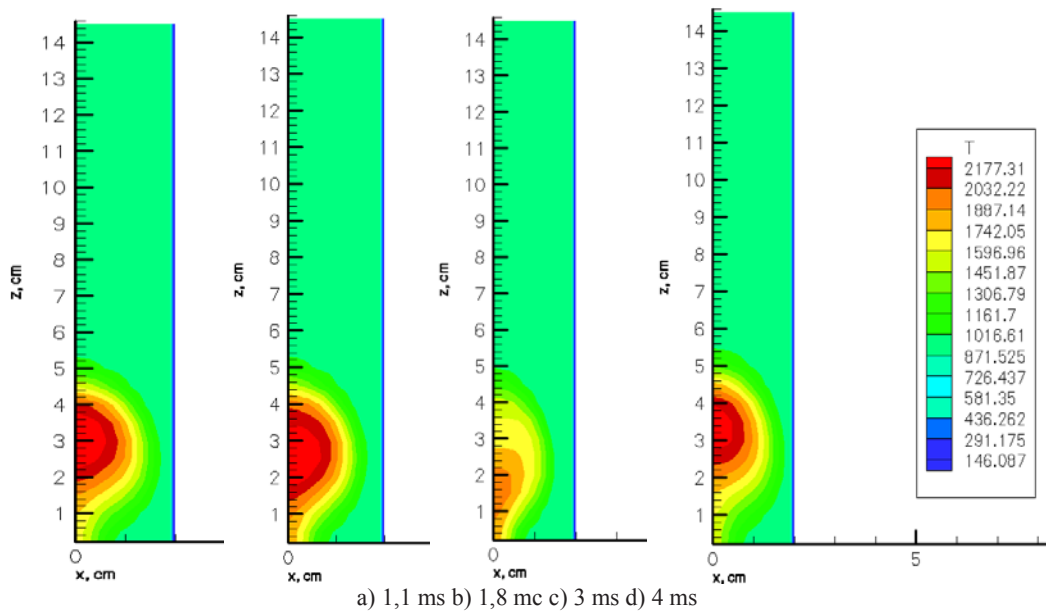


Figure 9 – Temperature profile during heptane combustion at different moments of time

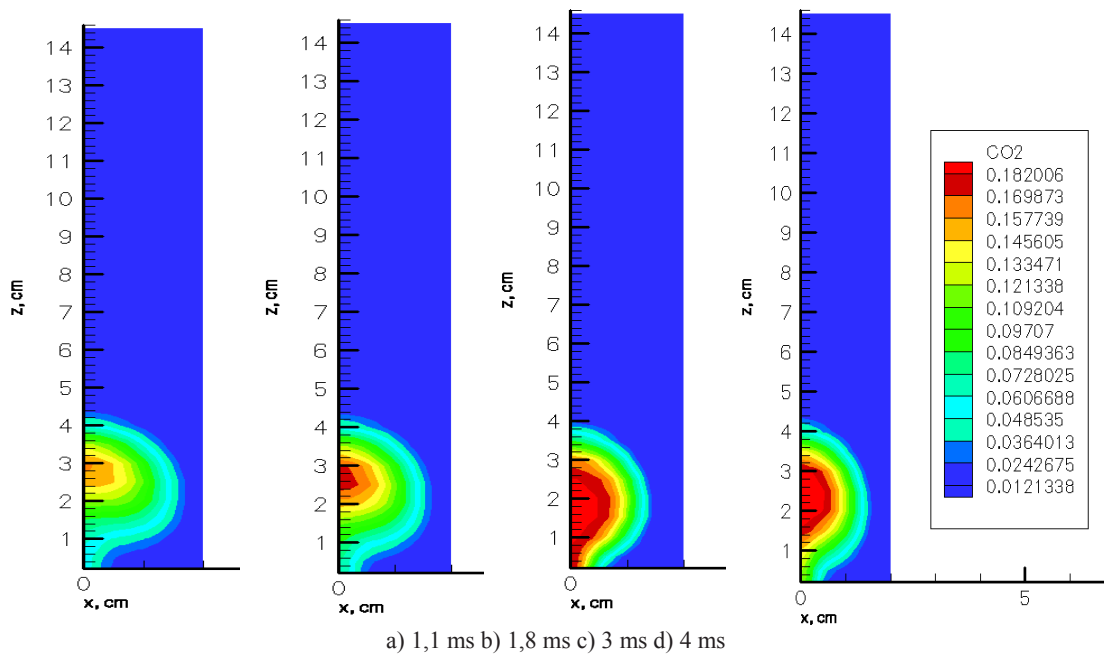


Figure 10 – Changes in CO<sub>2</sub> concentration fields during petrol combustion at different moments of time

Figures 12-13 show the change in nitrogen concentration with time. The highest amount of CO<sub>2</sub> changes at 1.5 ms. This time, the fuel is fully put into the combustion chamber, turned into vapor, and the chemical reaction starts.

In Figure 14, the rate at which the gas is moving in the combustion chamber is shown after 0.5 ms

during two different types of fuel (petrol and heptane) combustion. Petrol droplets are injected into the chamber at a speed of 200 m/s, and the gas inside the chamber is stationary, after injection liquid particles entrain the gas and acquire some speed, the graph of which is shown in Figure 14, a.

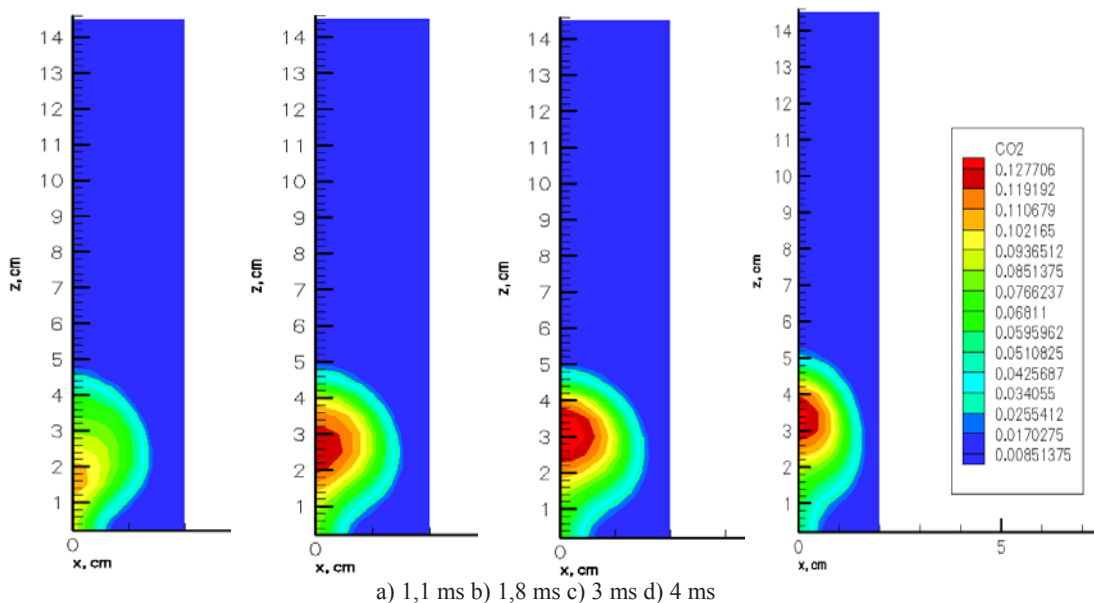


Figure 11 – Changes in CO<sub>2</sub> concentration fields during heptane combustion at different time moments



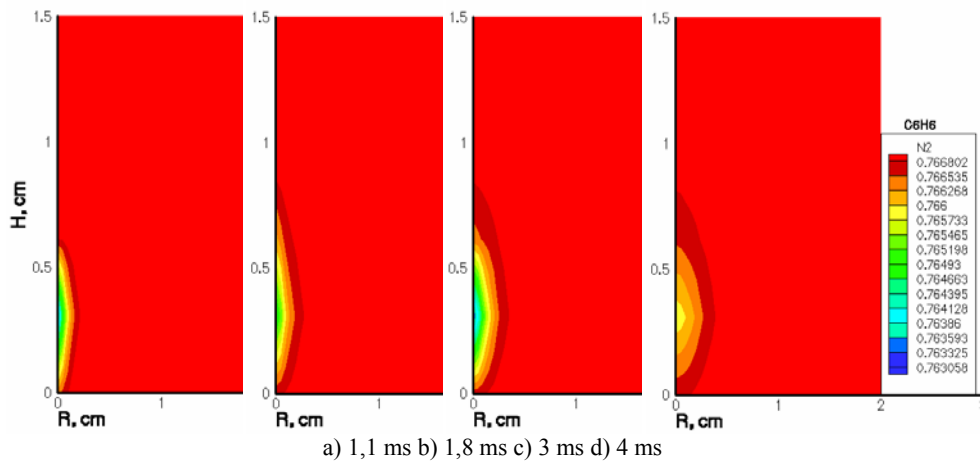


Figure 12 – Nitrogen concentration distribution during petrol combustion at different time moments

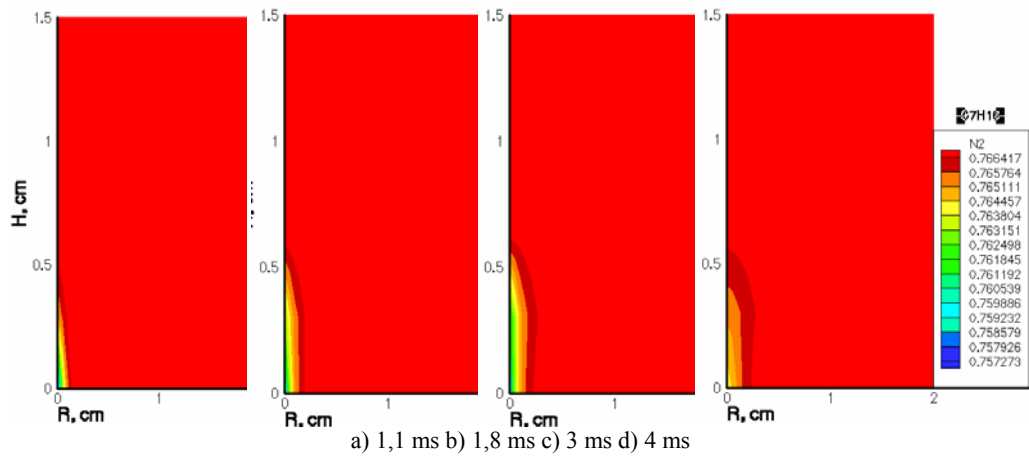


Figure 13 – Nitrogen concentration distribution during heptane combustion at different time moments

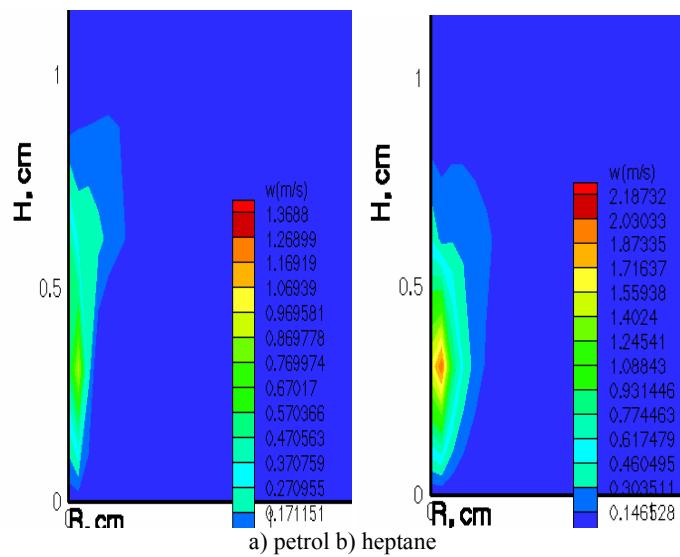


Figure 14 – Speed distribution in the combustion chamber during petrol and heptane combustion

The highest speed is observed in the middle of the combustion chamber, at a distance of about 1 cm from the center. Figure 14, b presents the results of speed calculations of heptane droplets in the combustion chamber at the same moment as for petrol. The optimum heptane droplet rate was 250 m/s.

## 5 Conclusions

This research focuses on understanding the combustion mechanisms of two different types of liquid fuel. It endeavors to find the most favorable air dynamics during turbulence and utilizes mathematical analysis to assess carbon dioxide generation in the combustion chamber.

When the injection speed is less than 200 m/s, there is no combustion because the speed is not fast enough to start and maintain the burning process. The optimum injection speed for liquid petrol is 200 m/s, while heptane is 250 m/s. As the fuel is ignited, the temperature inside the combustion chamber increases due to the accelerated spraying of fuel droplets.

How the distribution of specific chemicals and the temperature in the combustion chamber varies for two different fuels were determined. The liquid fuels combustion results in the creation of carbon

dioxide, leading to a rise in temperature within the combustion chamber and a faster burning of the fuel.

The use of computer models in studying the impact of turbulence on the dispersion of liquid particles in fuel combustion reveals an increased spread of fuel droplets. The combustion process is enhanced by the increased mixing area for fuel and air.

Our research findings can contribute to enhancing the efficiency of internal combustion engines. This will assist in increasing fuel efficiency and reducing detrimental emissions.

The application of the obtained optimal parameters in real thermal and technological installations will reduce the anthropogenic load on the surrounding atmosphere, which grows with the intensity of greenhouse gas emissions. Such methods of decarbonization in the energy sector contribute to the full implementation of sustainable global development goals.

## Acknowledgments

The Ministry of Science and Higher Education of Kazakhstan of the Republic of Kazakhstan No. AP14870834 has supported financially this work.

## References

1. Karaşan A., Gündoğdu F.K., Işık G., Kaya I., İlbarhar E. Assessment of governmental strategies for sustainable environment regarding greenhouse gas emission reduction under uncertainty // *Journal of Environmental Management*. – 2024. – Vol. 349, No. 119577. <https://doi.org/10.1016/j.jenvman.2023.119577>
2. Fayyazbakhsh A., Bell M.L., Zhu X., Mei X., Koutný M., Hajinajaf N., Zhang Y. Engine emissions with air pollutants and greenhouse gases and their control technologies // *Journal of Cleaner Production*. – 2022. – Vol. 376, No. 134260. <https://doi.org/10.1016/j.jclepro.2022.134260>
3. Wang L., Liu Y., Bi G., Zhang L., Song J. A phenomenological model of diesel combustion characteristics under CO<sub>2</sub>/O<sub>2</sub> atmosphere // *Fuel Processing Technology*. – 2022. – Vol. 229, No. 107167. <https://doi.org/10.1016/j.fuproc.2022.107167>
4. International Energy Agency report, 2023.
5. Report of the Agency for strategic planning and reforms of the Republic of Kazakhstan: On the state of protection of atmospheric air in the Republic of Kazakhstan, 2023.
6. Wang X., Zheng H., Wang Zh., Shan Yu., Meng J., Liang X., Feng K., Guan D. Kazakhstan's CO<sub>2</sub> emissions in the post-Kyoto Protocol era: Production-and consumption-based analysis // *Journal of Environmental Management*. – 2019. – Vol. 249, No. 109393. <https://doi.org/10.1016/j.jenvman.2019.109393>
7. Obiora S.Ch., Bamisile O., Hu Y., Ozsahin D.U., Adun H. Assessing the decarbonization of electricity generation in major emitting countries by 2030 and 2050: Transition to a high share renewable energy mix // *Heliyon*. – 2024. – Vol.10, Issue 8, No. e28770. <https://doi.org/10.1016/j.heliyon.2024.e28770>
8. Addai K., Serener B., Kirikkaleli D. Complementarities in the effect of economic globalization and decarbonization technologies on carbon neutrality. Evidence from Germany using Fourier-based approaches // *World Development Sustainability*. – 2023. – Vol. 3, No. 100050. <https://doi.org/10.1016/j.wds.2023.100050>
9. Shirzadi M., Tominaga Yo. Computational fluid dynamics analysis of pollutant dispersion around a high-rise building: Impact of surrounding buildings // *Building and Environment*. – 2023. – Vol. 245, No. 110895. <https://doi.org/10.1016/j.buildenv.2023.110895>
10. Amsden A.A. Kiva-3v, release 2, improvements to kiva-3v. Los Alamos, 1999. – 34 p.

11. Gorokhovski M., Hermann M. Modeling primary atomization // *Annual Review of Fluid Mechanics*. – 2008. – Vol. 40. – P. 343–366. <https://doi.org/10.1146/annurev.fluid.40.111406.102200>
12. Amsden A.A., O'Rourke P.J., Butler T.D. KIVA-II: A computer program for chemically reactive flows with sprays. Los Alamos, 1989. – 160 p.
13. Gorokhovski M.A., Oruganti S.K. Stochastic models for the droplet motion and evaporation in under-resolved turbulent flows at a large Reynolds number // *Journal of Fluid Mechanics*. 2022. – Vol. 932, No. A18. <https://doi.org/10.1017/jfm.2021.916>
14. Amsden A.A. KIVA-3: A KIVA Program with block-structured mesh for complex geometries. Los Alamos, 1993. – 95 p.
15. Mok M.Ch., Yeoh Ch.V., Tan M.K., Foo J.J. Optimization of Reynolds stress model coefficients at multiple discrete flow regions for three-dimensional realizations of fractal-generated turbulence // *European Journal of Mechanics – B/Fluids*. – 2024. – Vol. 106. – P. 30–47. <https://doi.org/10.1016/j.euromechflu.2024.03.002>
16. Zhao Y., Akolekar H.D., Weatheritt J., Michelassi V., Sandberg R.D. RANS turbulence model development using CFD-driven machine learning // *Journal of Computational Physics*. – 2020. – Vol. 411, No. 109413. <https://doi.org/10.1016/j.jcp.2020.109413>
17. Gao N., Niu J., He Q., Zhu T., Wu J. Using RANS turbulence models and Lagrangian approach to predict particle deposition in turbulent channel flows // *Building and Environment*. – 2012. – Vol. 48. – P. 206–214. <https://doi.org/10.1016/j.buildenv.2011.09.003>
18. Bolegenova S., Askarova A., Slavinskaya N., Ospanova Sh., Maxutkhanova A., Aldiyarova A., Yerbosynov D. Statistical modeling of spray formation, combustion, and evaporation of liquid fuel droplets // *Physical Sciences and Technology*. – 2022. – Vol. 9, No. 3-4. – P. 69–82. <https://doi.org/10.26577/phst.2022.v9.i2.09>
19. Bhoite S., Windom B., Singh J., Montgomery D., Marchese A.J. A study of ignition and combustion of liquid hydrocarbon droplets in premixed fuel/air mixtures in a rapid compression machine // *Proceedings of the Combustion Institute*. – 2023. – Vol. 339, Issue 2. – P. 2533–2542 <https://doi.org/10.1016/j.proci.2022.08.125>
20. Maghbouli A., Yang W., An H., Li J., Chou S.K., Chua K.J. An advanced combustion model coupled with detailed chemical reaction mechanism for D.I diesel engine simulation // *Applied Energy*. – 2013. – Vol. 111. – P. 758–770. <https://doi.org/10.1016/j.apenergy.2013.05.031>
21. Berezovskaya I.E., Tasmukhanova A.A., Ryspaeva M.Zh., Ospanova Sh.S. Investigation of the influence of liquid fuel injection rate on the combustion process using KIVA-II software // *Eurasian Physical Technical Journal*. – 2023. – Vol. 20, Issue 3 (45). – P. 43–51. <https://doi.org/10.31489/2023No3/43-51>
22. Askarova A., Bolegenova S., Ospanova Sh., Rakhimzhanova L., Nurmukhanova A., Adilbayev N. Optimization of fuel droplet sputtering and combustion at high turbulence flows // *Russian Physics Journal*. – 2024. – Vol. 67, Issue 2. – P. 167–170. <https://doi.org/10.1007/s11182-024-03104-5>
23. Askarova A., Bolegenova S., Ospanova Sh., Slavinskaya N., Aldiyarova A., Ungarova N. Simulation of non-isothermal liquid sprays under large-scale turbulence // *Physical Sciences and Technologies*. – 2021. – Vol 8, No. 3-4. – P. 28–40. <https://doi.org/10.26577/phst.2021.v8.i2.04>
24. Askarova A., Bolegenova S., Mazhrenova N., Manatbayev R., Ospanova Sh., Bolegenova S., Berezovskaya I., Maximov V., Nugymanova A., Shortanbayeva Zh. 3D modelling of heat and mass transfer processes during the combustion of liquid fuel // *Bulgarian Chemical Communications*. – 2016. – Vol. 48, Issue E. – P. 229–235.

**Information about authors:**

*Bolegenova Saltanat, Doctor of Physical and Mathematical Sciences, is a Professor at the al-Farabi Kazakh National University (Almaty, Kazakhstan), e-mail: Saltanat.Bolegenova@kaznu.edu.kz;*

*Askarova Aliya, Doctor of Physical and Mathematical Sciences, is a Professor at the al-Farabi Kazakh National University (Almaty, Kazakhstan), e-mail: Aliya.Askarova@kaznu.edu.kz;*

*Ospanova Shynar (corresponding author), PhD, is a Senior Lecturer at the al-Farabi Kazakh National University (Almaty, Kazakhstan), e-mail: Shynar.Ospanova@kaznu.edu.kz;*

*Zhumagaliyeva Sabina, Master student at the al-Farabi Kazakh National University (Almaty, Kazakhstan), e-mail: zhumasabina@icloud.com;*

*Makanova Ayaulym, Master student at the al-Farabi Kazakh National University (Almaty, Kazakhstan), e-mail: aiko.20.20@mail.ru;*

*Aldiyarova Aliya is a Lecturer at the al-Farabi Kazakh National University (Almaty, Kazakhstan), e-mail: aliya.aldiyarova14@gmail.com;*

*Nurmukhanova Alfiya, Candidate of Technical Sciences, is Senior Lecturer at the al-Farabi Kazakh National University (Almaty, Kazakhstan), e-mail: alfiyanurmukhanova7@gmail.com;*

*Idrissova Gulzhan, is a Senior Lecturer at the al-Farabi Kazakh National University (Almaty, Kazakhstan), e-mail: alikosh.bekbayev@gmail.com*

## LES modeling of gas particle dispersion and thermal characteristics in a reacting turbulent flow

Zivile Rutkuniene 

Kaunas University of Technology, Kaunas, Lithuania  
e-mail: rutkuniene@yandex.ru

*(Received May 9, 2024; received in revised form May 18, 2024; accepted May 23, 2024)*

This paper presents the results of a 3D computer simulation of the combustion processes of gas particles (methane) in turbulent flow by applying numerical methods for calculating complex turbulent flows. The numerical model for calculating turbulent reacting flow is based on the filtered equations of conservation of mass, momentum, and internal energy using a spatial filter for calculating and modeling complex vortex structures. Aerodynamic, temperature and thermal characteristics of the flow were obtained based on the study on the influence of the Sauter mean radius of methane particles on its distribution and combustion processes. 3D visualization of the reacting flow was obtained considering the degree of its turbulence and the intensity of methane particle collision on the area of its distribution. The obtained results can be used for a deep understanding of the theory of gas combustion, in combustion chambers of various thermophysical objects and as an alternative to liquid hydrocarbon fuels due to safety and low harmful load of methane on the environment.

**Key words:** combustion, gas, turbulent, filtering, combustion, Sauter radius.

**PACS number(s):** 47.27.E.

### 1 Introduction

Nowadays, much attention is paid to the scientific design of chemical reactors and installations in which chemical transformation phenomena complicated by turbulent heat and mass transfer processes take place. In the systems under consideration, there are complex physical and chemical processes, the components of which are: gas flow motion, mass transfer, heat transfer, and chemical transformation. At the center of attention of numerous researches of chemical transformation processes in turbulence conditions is the question of the influence of gas-dynamic characteristics of mixing turbulent flows on conditions of the course of chemical processes, and also on possibilities of control of these processes through various external influences [1].

It is known that knowledge only of average values of such pulsating quantities as velocity, temperature, concentrations of reacting components, and reaction products is insufficient for a complete description of complex processes of chemical transformation under conditions of non-

exothermicity and turbulence even in those cases when the influence of the chemical reaction on the gas dynamic characteristics of the system can be neglected. The strong and ambiguous interaction between the chemistry and dynamics of liquids and gases seriously complicates both the experimental study of reacting flows and the creation of a more or less rigorous theory. Therefore, numerical simulations can be successfully used to predict and study the behavior of such complex systems.

Experimental observations and approximate theoretical models suggest laws that a physical system must obey. Using numerical experiments it is possible to check the fulfillment of these laws, obtain quantitative predictions, and compare these predictions with the results of known experiments. A rigorous quantitative calculation of a diffusive turbulent plume of finite size is very difficult, but this very task is of the greatest practical interest. As the analysis of scientific publications shows, a rigorous theory of turbulent combustion is far from being complete at the moment. There are various approaches to modeling turbulent reacting systems that require further development and refinement, as

well as their application for solving specific problems.

Modern fuel combustion modeling techniques are designed to determine high combustion efficiency and minimum emission of pollutants into the atmosphere. They are widely used in designing and optimizing practical combustion systems because, compared to experimental testing and prototyping, the development costs of mathematical and computer simulations are very low. Today, no real progress in design or optimization can be made without numerical or computer simulations [2, 3].

The work used a model of turbulent combustion, which is based on the density of the probability function, the theory of combustion of atomized fuel under combustion conditions in diesel engines. This approach, applied earlier by the authors of [4-6], takes into account the effects of turbulence and random dynamics of vaporized gas droplets, which affect the average rate of chemical kinetics of the processes. Also in the paper, a probability density function for the variables describing the gas medium is given, where vaporized gas-liquid mixture droplets are considered in terms of source terms.

Phenomenological models aim to represent the most significant characteristics of spray formation without consuming huge amounts of computational resources. The first category of phenomenological models consists of simple Lagrangian models, which have been frequently used in industrial numerical codes for the last thirty years. In such models, the precursor mechanisms for the initial breakup of a gas jet are surface instabilities [7, 8], particle distribution [9], spontaneous breakup [10], jet turbulence [11, 12], and cavitation [13-15].

The classical theory uses the assumption of the similarity of diffusion and thermal phenomena in the vicinity of gas particles. This assumption allows one to analytically determine the particle lifetime, flame temperature, distance from the particle surface to the flame front, and some other parameters. However, concerning modern problems, especially the problems of controlling the combustion of jets and reducing the output of harmful substances during combustion, such a simple model is not very effective. To solve such problems, data on the dynamics of physical and chemical processes in the particle itself and its vicinity are required. For example, [16] presents the results of the analysis of the vaporization of a single droplet using the model of independent diffusion of components – fuel vapors, oxygen, and nitrogen.

Efficient combustion of gaseous fuels in promising engines and power plants requires good mixing and, consequently, sufficient length of the burnout section. When burning hydrocarbons, it is necessary to consider that their kinetic properties are worse compared to hydrogen, which is reflected in the increase of chemical reaction times in the ignition and combustion processes by more than an order of magnitude.

Most of the 90% of harmful substances in the air of megacities are harmful waste emitted by vehicles, soot, smoke, toxic compounds emitted by burning petroleum fuels at thermal power plants, and heavy metals. Methane is considered an environmentally efficient fuel. In engines running on methane, the content of carbon monoxide is 2-3 times lower, and nitrogen oxides are emitted half as much. The amount of smoke is reduced by 9 times compared to liquid fuels, and it does not contain sulfur and lead. The high safety of methane also depends on its physical properties. In countries where natural gas vehicles are used, such as Italy and Germany, there is a reward when a vehicle is converted to natural gas. In many countries, methane vehicles also have a lower transport tax. The idea of lower taxation for owners of methane-fueled vehicles in many countries is being discussed by the Ministry of Energy.

The purpose of this research was to investigate the characteristics of methane particles in a reactive flowing gas. Numerical models for calculating complex turbulent flows were used to assist in their analysis of the intricate gas movement.

## 2 Numerical model of turbulent flow calculation

Direct numerical modeling of turbulent flows is inefficient and prohibitively expensive, as a significant number of computational resources are expended to capture small eddy structures that contain negligible amounts of turbulence kinetic energy. Large eddy modeling of turbulent flows is an intermediate method between DNS and RANS and is increasingly being used as a tool to study turbulence dynamics in technical applications.

The main difference between LES and DNS lies in the concept of the filtering procedure for LES, the separation of small-scale and large-scale structures [17-19]. In large eddy simulation, large eddies are directly resolved on the numerical grid and time, while the smallest subgrid-scale eddies are modeled.

In LES approach, large eddy structures are simulated, which depend on boundary conditions and consist of most of the kinetic energy of the flow. The basic premise of this approach is that the largest vortices carry the maximum Reynolds stresses and must be calculated. Small scales or SubGrid Scales (SGS) contain low values of Reynolds stresses, in addition, small-scale turbulence is close to isotropic and has near-universal characteristics that are more amenable to modeling.

Modeling of turbulent flows consists of four steps:

1. Spatial filtering;
2. Obtaining filtered Navier-Stokes equations;
3. Modelling of unresolved movements;
4. Numerical solution.

In LES, large scales are resolved, and only small-scale structures are simulated. Large scales are derived at the expense of the flow geometry and can change with changes in the flow geometry. Small scales, involving the dissipation of turbulence kinetic energy, are generally universal and easily simulated. The spatial filtering operation decomposes the flow field into two components, the first of which is resolvable (filtered) and the second is subgrid.

The filtered continuity, momentum, and mass equations are written as follows.

The filtered mass conservation equation is written as follows:

$$\frac{\partial \rho}{\partial t} + \frac{\partial \rho \tilde{u}_i}{\partial x_i} = \tilde{S}_{mass}. \quad (1)$$

The filtered momentum conservation equation looks like this:

$$\frac{\partial \rho \tilde{u}_i}{\partial t} + \frac{\partial \rho \tilde{u}_i \tilde{u}_j}{\partial x_j} = \rho g - \frac{\partial \tilde{p}}{\partial x_i} + \frac{\partial \tilde{\sigma}_{ij}}{\partial x_j} + \tilde{S}_{mom}. \quad (2)$$

The filtered equation of conservation of internal energy of the system is written as follows:

$$\frac{\partial \rho \tilde{E}}{\partial t} + \frac{\partial \rho \tilde{E} \tilde{u}_j}{\partial x_j} = - \frac{\partial \tilde{p} \tilde{u}_j}{\partial x_i} + \frac{\partial \tilde{u}_j \tilde{\sigma}_{ij}}{\partial x_j} + \tilde{S}_{energy}. \quad (3)$$

The anisotropic part of the Reynolds subgrid stress, whose value is unknown, can be modeled using the Boussinesq approach [20]:

$$\sigma_{ij}^s - \frac{1}{3} \delta_{ij} \tilde{\sigma}_{kk}^s = -\mu_t \tilde{S}_{ij}. \quad (4)$$

Here  $\tilde{\sigma}_{ij}$  plays a similar role in the filtered equations as the Reynolds stress tensor in RANS.  $\tilde{S}_{ij}$  denotes the strain rate tensor in the filtered scale:

$$\tilde{S}_{ij} = \left( \frac{\partial \tilde{u}}{\partial x_j} + \frac{\partial \tilde{u}_j}{\partial x_i} \right). \quad (5)$$

The choice of the function for the filter is one of the central points in the modeling of large eddies. Some of the commonly used filters are given below [21].

Volume-averaged box filter is:

$$G(x - \xi; \Delta) = \begin{cases} 1/\Delta, & |x_i - \xi_i| < \Delta x_i / 2 \\ 0, & |x_i - \xi_i| > \Delta x_i / 2 \end{cases}.$$

Gaussian filter is:

$$G(x - \xi; \Delta) = \left( \frac{6}{\pi \Delta^2} \right)^{3/2} \exp \left( -6 \frac{|x_i - \xi_i|^2}{\Delta^2} \right).$$

The shortened Fourier filter is:

$$G(x - \xi; \Delta) = \frac{1}{\Delta^3} \prod_{i=1}^3 \frac{\sin(x_i - \xi_i) / \Delta}{(x_i - \xi_i) / \Delta}.$$

### 3 Results of computer simulations

This paper presents the results of numerical modeling of the processes of atomization and combustion of gaseous methane at varying initial values of the Sauter mean radius of its particles in a

model combustion chamber. As a result of computer simulation, the graphs of particle size distribution, profiles of combustion temperature, and reaction products along the height of the combustion chamber at values of 25, 50, 75, 100, and 125  $\mu\text{m}$  droplets' Sauter mean radius were obtained.

Figure 1 shows the distribution of the longitudinal component of the velocity during

methane combustion in the combustion chamber at different values of the Sauter mean radius. As can be seen from the figure, at an initial value of 25 microns, the velocity will have a maximum value of 200 m/s. As the particle radius increases, the velocity decreases along the height of the chamber. At the last values of 100 and 125 microns, the velocity tends to a minimum (80 m/s).

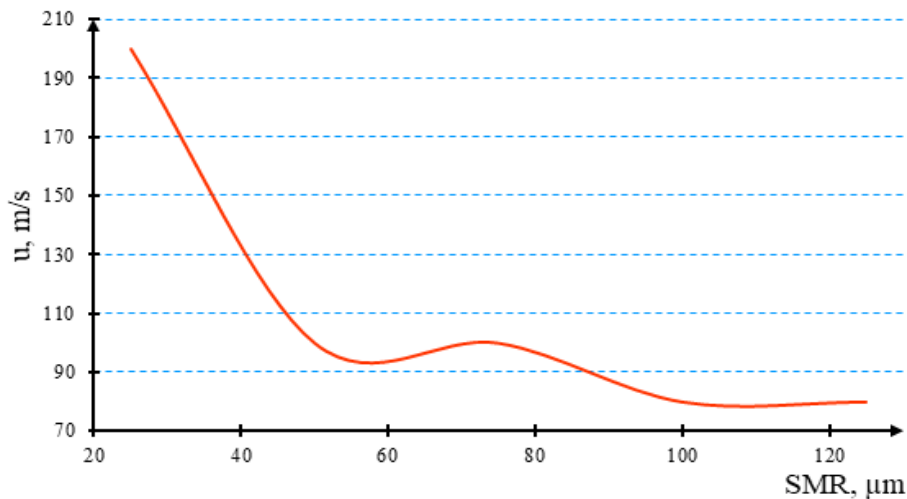


**Figure 1** – Dependence of the velocity component in the longitudinal section in the combustion chamber on the Sauter mean radius of the particles

Figure 2 shows the dependence of the transverse velocity component on the Sauter mean radius of the particles. Even in this case, the velocity component decreases monotonically as the particle size increases. At the initial 100 microns, the maximum value of the velocity was 1250 m/s, and at 50 microns was 700 m/s. These values coincide with the results published in the works of some authors [22-24]. Similar behavior of the aerodynamic characteristics of the flow in the presence of combustion can also be observed during the combustion of hydrocarbon liquid fuels in the combustion chambers of thermal power facilities

[25]. The only difference between liquid fuel and methane is that liquid fuel droplets go through a stage of evaporation and breakup, which affects the duration of their combustion process.

The following Figure 3 shows the value of the Nusselt number as a function of methane particle radius, which is one of the thermal criteria of the combustion process. At initial values of the radius, the Nusselt number will be low. As the particle size increases, its value also increases. Only at 100 microns a minimum of the Nusselt number can be observed. The maximum value of the Nusselt number was 1.9 at 125 microns.

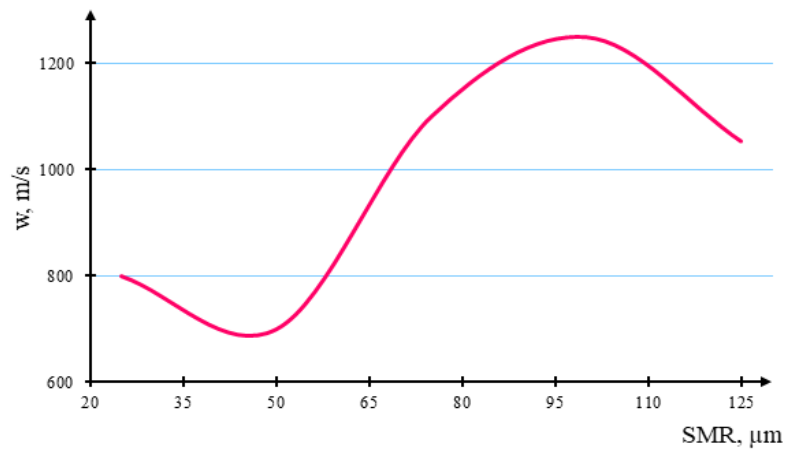


**Figure 2** – Dependence of the transverse component of the velocity in the longitudinal section in the combustion chamber on the Sauter mean radius of the particles

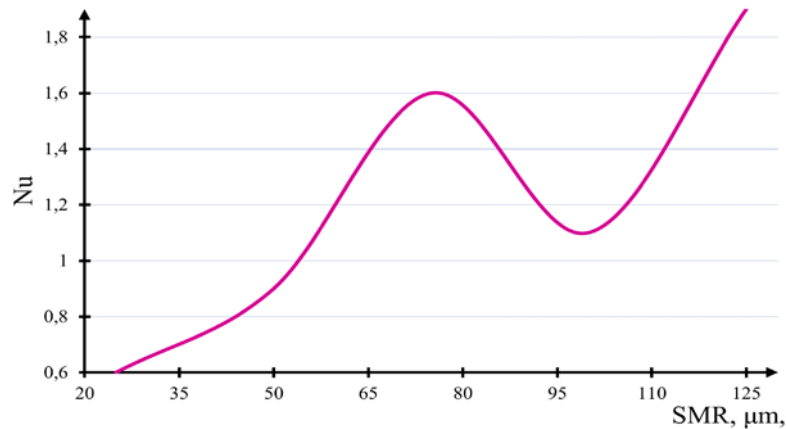


**Figure 3** – Dependence of the Nusselt number on the mean Sauter particle radius

According to the results of the performed numerical simulation, the influence of different values of the Sauter mean radius of the particles on methane combustion was studied. As a result of the numerical simulation, it was found that 125 microns corresponds to the effective combustion mode. At this value, the particle size inside the chamber under combustion reaches a maximum value and particle velocities increase. A lot of oxygen is released in the

middle of the combustion chamber, which helps the methane burn efficiently and evenly.

Since the numerical calculation program is designed for modeling not only liquid but also gaseous fuels, for the transition of the numerical calculation from liquid fuel to gas, changes were made in the values of the lines corresponding to the accounting of rupture, evaporation, and merging of liquid droplets:

**Table 1** – Modification of program sub-files for gas combustion

breakup 1.0	change to	breakup 0.0.
evapp 1.0		evapp 0.0
kolide 1		kolide 0



Through computer testing, 3D visualizations of the process of methane particle fragmentation and combustion were generated. To gain a better understanding of the combustion of methane and its specific physical and chemical characteristics was the goal of this work. Thermal, aerodynamic, and dispersion characteristics of methane particles in the combustion chamber under the efficient combustion mode were determined.

Figure 4 shows the distribution of the longitudinal component of the methane particle

velocity in the combustion chamber at different time moments. At the initial time of 0.8 ms, the velocity of methane combustion in most of the combustion chamber is 20 m/s, and at time  $t=2.5$  ms, its value reaches the maximum value of 80 m/s.

Figure 5 shows the distribution of the transverse velocity component inside the combustion chamber. At the axis of the combustion chamber, the velocity reaches its maximum value of 550 m/s. And in the rest of the combustion chamber, the velocity value was equal to 50 m/s.

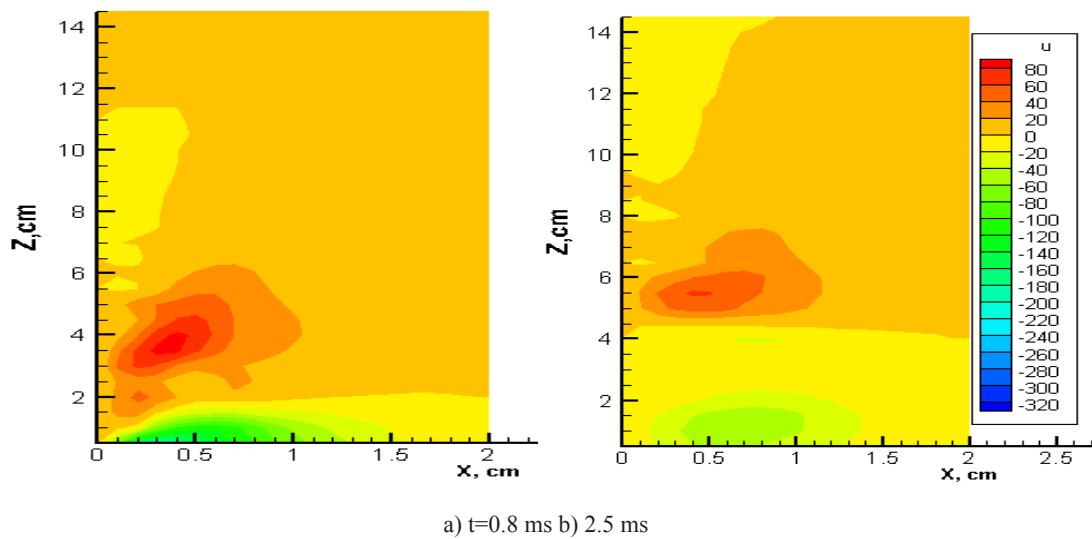


**Figure 4** – Distribution of the longitudinal component of methane particle velocity at the effective combustion mode

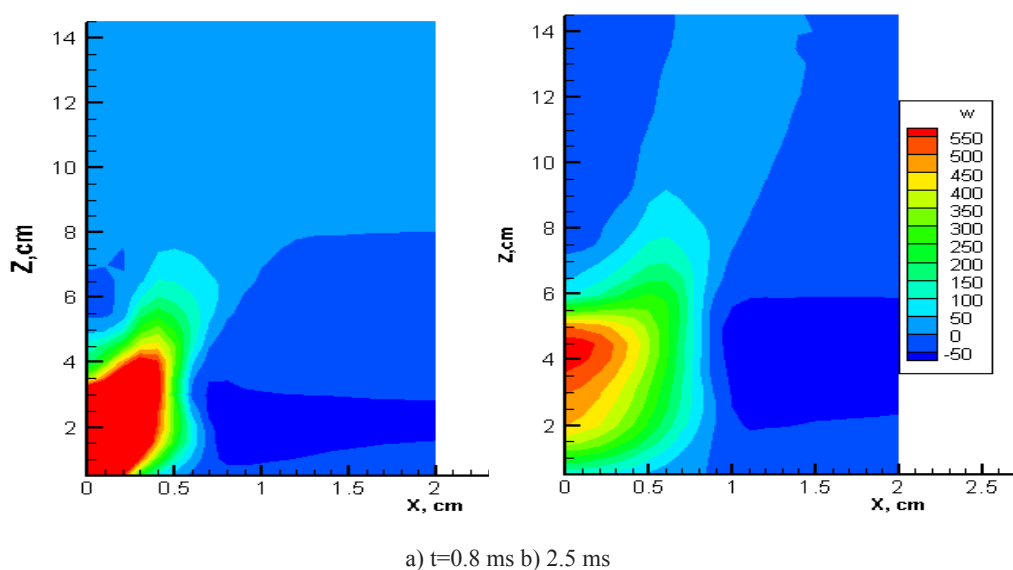


**Figure 5** – Distribution of the transverse component of methane particle velocity at the effective combustion mode

Heat convection is always accompanied by thermal conductivity, since when a liquid or gas moves, individual particles of different temperatures inevitably come into contact. The combined transfer of heat by convection and conduction is called convective heat transfer.

Figure 6 shows the intensity of convective heat transfer between the body surface and the free gas flow, which is expressed by the Nusselt number. As can be seen from the figure, at the initial moment the heat transfer intensity slowly increases and

becomes more intense upstream. With time, the value of the Nusselt number decreases because of the heat increase along the height of the combustion chamber.

Typically, laminar flows have a Nusselt number in the range of 1. That is, the heat flow due to convection always exceeds in magnitude the heat flow due to thermal conductivity. Large Nusselt numbers indicate strong convective heat flow, which is a characteristic of turbulent flows.

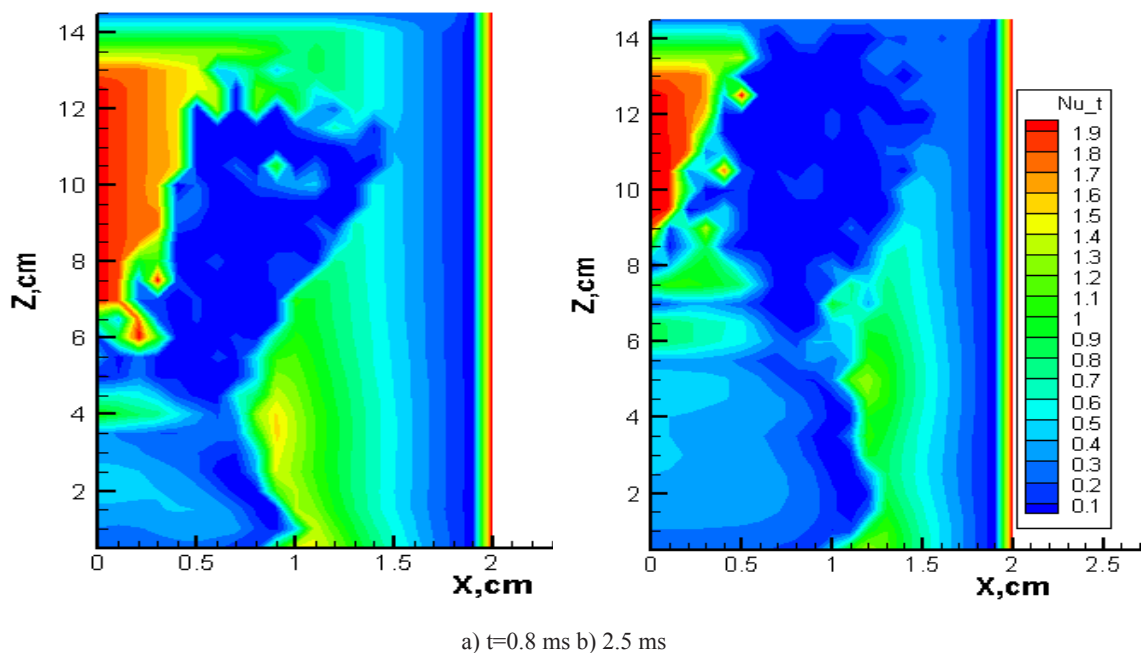


**Figure 6** – Intensity of heat exchange due to convection and heat conduction in the free flow of methane particles

Thus, in this paper, computational experiments were carried out to determine the effective mode of gas combustion when the particle size changes at the beginning of the process. Based on the results obtained, it can be said with certainty that for methane the best size of the average Sauter droplet radius is 125 microns. Since at this value, methane combustion is intensive, its particles spread over long distances, due to the intensive collision of particles the heat exchange between the environment is improved and the aerodynamics of the flow becomes stable.

#### 4 Conclusions

In this paper, computational experiments on 3D modeling were carried out to determine the thermophysical, aerodynamic, and dispersion characteristics of methane particles in a reacting gas flow in a model combustion chamber. The influence of different Sauter mean radii of methane particles on the processes of its atomization and combustion was investigated, considering the degree of flow turbulence.

The distribution of the longitudinal component of particle velocity during methane combustion in

the combustion chamber at different values of the Sauter mean radius was shown. The process of efficient combustion of methane particles occurs at  $SMR=125 \mu m$ .

The distribution of the transverse velocity component in the combustion chamber at different time moments is shown. At the initial time of 0.8 ms, the velocity of methane combustion in most of the combustion chamber was 20 m/s, while at the chamber extension,  $t=2.5$  ms its value reached its maximum value of 80 m/s. The particles reach their

maximum velocity of 550 m/s at the axis of the combustion chamber.

The intensity of heat transfer due to convection and conduction was shown by Nusselt number, which gradually decreased towards the exit of the combustion chamber.

This work has not only scientific but also used applications, as methane can be used as a substitute for liquid fuel in various internal combustion engines, as it has good physical and chemical properties and low harmful load on the environment.

## References

1. Askarova A., Bolegenova S., Ospanova Sh., Rakhimzhanova L., Nurmukhanova A., Adilbayev N. Optimization of fuel droplet sputtering and combustion at high turbulence flows // *Russian Physics Journal*. – 2024. – Vol. 67, Issue 2. – P. 167–170. <https://doi.org/10.1007/s11182-024-03104-5>
2. Falfari S., Bianchi G.M., Cazzoli G., Forte C., Negro S. Basics on Water Injection Process for Gasoline Engines // *Energy Procedia*. – 2018. – Vol. 148. – P. 50-57. <https://doi.org/10.1016/j.egypro.2018.08.018>
3. Berezovskaya I.E., Tasmukhanova A.A., Ryspaeva M.Zh., Ospanova Sh.S. Investigation of the influence of liquid fuel injection rate on the combustion process using KIVA-II software // *Eurasian Physical Technical Journal*. – 2023. – Vol. 20, Issue 3 (45). – P. 43–51. <https://doi.org/10.31489/2023No3/43-51>
4. Durand P., Gorokhovski M., Borghi R. An application of the probability density function model to diesel engine combustion // *Combustion science and technology*. – 1999. – Vol. 144, №1 (6). – P. 47-48. <https://doi.org/10.1080/00102209908924197>
5. Askarova A., Bolegenova S., Ospanova Sh., Slavinskaya N., Aldiyarova A., Ungarova N. Simulation of non-isothermal liquid sprays under large-scale turbulence // *Physical Sciences and Technologies*. – 2021. – Vol 8, No. 3-4. – P. 28-40. <https://doi.org/10.26577/phst.2021.v8.i2.04>
6. Navarro-Martinez S. Large eddy simulation of spray atomization with a probability density function method // *International Journal of Multiphase Flow*. – 2014. – Vol. 63. – P. 11-12. <https://doi.org/10.1016/j.ijmultiphaseflow.2014.02.013>
7. Villermaux E. Fragmentation // *Annual Review of Fluid Mechanics*. – 2007. – Vol. 39. – P. 419–446. <https://doi.org/10.1146/annurev.fluid.39.050905.110214>
8. Perini F., Reitz R.D. Improved atomization, collision and sub-grid scale momentum coupling models for transient vaporizing engine sprays // *International Journal of Multiphase Flow*. – 2016. – Vol. 79. – P. 107-123. <https://doi.org/10.1016/j.ijmultiphaseflow.2015.10.009>
9. Yi Y., Reitz R. Modeling the primary break-up of high-speed jets // *Atomization and Sprays*. – 2004. – Vol. 14. – P. 53–80. <http://dx.doi.org/10.1615/AtomizSpr.v14.i1.40>
10. Tanner F.X. Development and validation of a cascade atomization and drop breakup model for high-velocity dense sprays // *Atomization and Sprays*. – 2004. – Vol. 14. – P. 211–242. <http://dx.doi.org/10.1615/AtomizSpr.v14.i3.20>
11. Li Y., Huang Y., Luo K., Liang M., Lei B. Development and validation of an improved atomization model for GDI spray simulations: Coupling effects of nozzle-generated turbulence and aerodynamic force // *Fuel*. – 2021. – Vol. 299, No. 129871. <https://doi.org/10.1016/j.fuel.2021.120871>
12. Bolegenova S., Askarova A., Slavinskaya N., Ospanova Sh., Maxutkhanova A., Aldiyarova A., Yerbosynov D. Statistical modeling of spray formation, combustion, and evaporation of liquid fuel droplets // *Physical Sciences and Technology*. – 2022. – Vol. 9, No. 3-4. – P. 69–82. <https://doi.org/10.26577/phst.2022.v9.i2.09>
13. Wei Y., Fan L., Zhang H., Gu Y., Deng Y., Leng X., Fei H., He Zh. Experimental investigations into the effects of string cavitation on diesel nozzle internal flow and near field spray dynamics under different injection control strategies // *Fuel*. – 2022. – Vol. 309, No. 122021. <https://doi.org/10.1016/j.fuel.2021.122021>
14. Zhang X., He Zh., Wang Q., Tao X., Zhou Zh., Xia X., Zhang W. Effect of fuel temperature on cavitation flow inside vertical multi-hole nozzles and spray characteristics with different nozzle geometries // *Experimental Thermal and Fluid Science*. – 2018. – Vol. 91. – P. 374-387. <https://doi.org/10.1016/j.expthermflusci.2017.06.006>
15. Hong L., Weilong Zh., Ming J., Yan'an Y., Yang H. An improved method for coupling the in-nozzle cavitation with Multi-fluid-quasi-VOF model for diesel spray // *Computers & Fluids*. – 2018. – Vol. 177. – P. 20-32. <https://doi.org/10.1016/j.compfluid.2018.09.017>
16. Yu D., Chen Zh. Theoretical analysis on droplet vaporization at elevated temperatures and pressures // *International Journal of Heat and Mass Transfer*. – 2021. – Vol. 164, No. 129542. <https://doi.org/10.1016/j.ijheatmasstransfer.2020.120542>
17. Khan M.M., Helie j., Gorokhovski M., Sheikh N.A. Experimental and numerical study of flash boiling in gasoline direct injection sprays // *Applied Thermal Engineering*. – 2017. – Vol. 123. – P. 377-389. <https://doi.org/10.1016/j.applthermaleng.2017.05.102>

18. Colman H.M., Darabiha N., Veynante D., Fiorina B. A turbulent combustion model for soot formation at the LES subgrid-scale using virtual chemistry approach // *Combustion and Flame*. – 2023. – Vol. 247, No. 112496. <https://doi.org/10.1016/j.combustflame.2022.112496>
19. Kren J., Mikuz B., Tiselj I. DNS vs. LES: Turbulent flow in square duct with heated foil boundary // *International Journal of Heat and Fluid Flow*. – 2024. – Vol. 107, No. 109403. <https://doi.org/10.1016/j.ijheatfluidflow.2024.109403>
20. Poochinapan K., Wongsaijai B. Dynamic analysis of wave scenarios based on enhanced numerical models for the good Boussinesq equation // *Results in Applied Mathematics*. – 2024. – Vol. 21, No. 100416. <https://doi.org/10.1016/j.rinam.2023.100416>
21. Sun G., Domaradzki J.A. Implicit LES using adaptive filtering // *Journal of Computational Physics*. – 2018. – Vol. 359. – P.380-408. <https://doi.org/10.1016/j.jcp.2018.01.009>
22. Kamma P., Promtong M., Suvanjumrat Ch. Development of a reduced mechanism for methane combustion in OpenFOAM: A computational approach for efficient and accurate simulations // *International Journal of Thermofluids*. – 2024. – Vol. 22, No. 100654. <https://doi.org/10.1016/j.ijft.2024.100654>
23. Gulcan H.E. Effect of methane injection strategy on combustion, exergetic performance, and enviro-economic analyses in a diesel/methane CRDI engine // *Applied Thermal Engineering*. – 2024. – Vol. 243, No. 122654. <https://doi.org/10.1016/j.applthermaleng.2024.122654>
24. Gheshlaghi M.K.Gh., Tahsini A.M. Numerical investigation of hydrogen addition effects to a methane-fueled high-pressure combustion chamber // *International Journal of Hydrogen Energy*. – 2024. – Vol. 48, Issue 86. – P. 33732-33745. <https://doi.org/10.1016/j.ijhydene.2023.05.119>
25. Askarova A., Bolegenova S., Mazhrenova N., Manatbayev R., Ospanova Sh., Bolegenova S., Berezovskaya I., Maximov V., Nugymanova A., Shortanbayeva Zh. 3D modelling of heat and mass transfer processes during the combustion of liquid fuel // *Bulgarian Chemical Communications*. – 2016. – Vol. 48, Issue E. – P. 229-235.

**Information about the author:**

Zivile Rutkuniene, Doctor of Sciences, is an Associate Professor at the Kaunas University of Technology (Kaunas, Lithuania), e-mail: [rutkuniene@yandex.com](mailto:rutkuniene@yandex.com)

## Experience of noctilucent clouds registering in the near infrared spectrum region

A.A. Solodovnik<sup>1</sup> , R.O. Zyryanov<sup>1</sup> , P.I. Leontyev<sup>1</sup> , B.M. Useinov<sup>1\*</sup> ,

E.G. Gololobova<sup>1</sup> , and P.L. Zhuravlev<sup>2</sup> 

<sup>1</sup>M. Kozybayev North Kazakhstan University, Petropavlovsk, Kazakhstan

<sup>2</sup>Nazarbayev Intellectual School, Petropavlovsk, Kazakhstan

\*e-mail: buseinov@gmail.com

(Received January 29, 2024; received in revised form April, 13 2024; accepted April 23, 2024)

Some aspects of increasing the efficiency of noctilucent clouds ground-based observations are considered. The study of such objects is highly relevant in connection with the general problems of climate change. It is shown that the limitations on the possibility of registering the phenomenon in the optical range are associated both with the relatively low brightness of clouds of this type against the background of the twilight segment, and with the strong absorption of light by dust aerosol in the surface layer of the atmosphere. The paper substantiates the idea that the transition to observations of noctilucent clouds in the near infrared range will increase the contrast of their images in the twilight segment. This will make it possible to detect noctilucent clouds during civil twilight, including at low altitudes above the horizon. To test this assumption, shooting was carried out during the 2022 season using a CANON 2000 D camera and RG780 and RG830 infrared filters. The images revealed features morphologically similar to noctilucent clouds. An analysis of the images showed that they can hardly be associated with tropospheric clouds or anthropogenic formations. The results obtained were compared with ground-based observation data from other points, as well as with satellite information on the state of noctilucent cloud fields. This comparison showed that noctilucent clouds, which were not detected in visible light images, were highly likely to be detected in near-infrared images. The prospects for the application and development of the proposed method for ground-based registration of noctilucent clouds are also considered.

**Key words:** noctilucent clouds, ground-based monitoring, twilight segment, light scattering, image contrast, scattering indicatrices, infrared radiation, filters, satellite observations.

**PACS number(s):** 07.05.-1; 07.60.-1.

### 1 Introduction

Research into a wide range of phenomena manifesting itself on the celestial sphere requires obtaining high-quality observational material, including the most informative images. This statement can be fully attributed to the study of noctilucent clouds (NLC) developing in the mesosphere. The recent identification of this phenomenon connection with both large-scale tropospheric processes and, in general, with climatic changes gives special relevance to such works. At the same time, the tasks of synoptic monitoring and morphology of NLC with a further transition to identifying patterns of their genesis and evolution are relevant [1-5].

However, when solving these problems, a number of limitations arise. These limitations are

associated both with the sky illumination conditions due to the fact that observations in the visible range are effective only during navigational twilight, and with the low altitude of the object above the horizon. The first limitation is due to the fact that only during navigational twilight the brightness of the dawn segment falls below the brightness of mesospheric NLC still illuminated by the Sun. The second limitation is due to the particularly strong influence of light scattering on aerosols contained in the air near the horizon

In this regard, the task of the images contrast increasing of faintly luminous cloud formations and other extended objects on the celestial sphere appears. As we have shown earlier, one of the promising directions for its solution may be the transition to obtaining images of the studied objects not in the optical range, but in the near infrared region

of the spectrum [6]. At the same time, one can expect a decrease in the background brightness of the clear sky and, as a result, a more confident registration of NLC against the background of the twilight segment due to a lower degree of scattering of long-wave radiation in the air [7-9]. Both the ability to detect NLC with minimal immersion of the Sun's disk under the horizon before the beginning of navigation twilight and the time interval for their ground registration will increase.

## 2 Image contrast increasing as a method for detecting diffuse objects in the sky

One of the most important characteristics of images is optical contrast, which determines the ability to highlight image details from the surrounding background. In this sense, optical contrast determines the informativeness of the image under study. The ratio of the difference in brightness of some detail and background brightness to the sum of their brightnesses is most often taken as a measure of contrast. In this case, we have a dimensionless quantity varying from zero to one. This approach to image quality assessment is currently not the only one. Of the various methods for assessing image contrast, the most convenient one was chosen. In particular, when recording NLC images with their high vertical brightness gradient, it makes sense to talk not about the overall contrast of the picture, but about the local contrast of individual details. With sufficiently high local contrast values, it is not difficult to distinguish not only the presence of details of the cloud structure, but also to classify their type.

Local contrast is determined by the relation of brightness of light and dark adjacent parts of the image under study. Its value is calculated using the formula:

$$K_L = \frac{D_{\max} - D_{\min}}{G - 1}, \quad (1)$$

where  $D_{\max}$  and  $D_{\min}$  are the maximum and minimum brightness values of pixels close in position, and  $G$  is the maximum possible number of brightness gradations for the bit depth used. For example, with 8 bit pixels, it will be 256.

In turn, the overall contrast across the entire image field can be estimated as follows:

$$K_S = \frac{2\sigma_D}{G - 1}, \quad (2)$$

where  $\sigma_D$  is the standard deviation of brightness across all pixels of the picture. Thus, formulas (1) and (2) allow us to calculate dimensionless indicators characterizing the quality of the resulting picture [10-12].

In astronomical practice, the contrast of images is determined not only by the parameters of the receiving equipment, but also by the features of the shooting objects. Thus, when taking NLC images, the ratio of the brightness of cloud details (determined by the concentration of aerosol in the cloud) and the background of the twilight segment of the sky (the brightness of which can vary widely) becomes critical. Then, to highlight an object in a picture, it can be useful to reduce the brightness of the background, leading to an increase in image contrast and the overall informativity of the resulting picture.

## 3 Technique for increasing the contrast of cloud images due to the transition to the IR region of the spectrum

As noted, one of the problems in identifying the presence of NLC in images of the dawn sky segment is the slight difference in their brightness from the background brightness of the sky. Therefore, increasing the contrast of images, primarily by reducing the background brightness of the sky, becomes an urgent task. Theoretically, here we can rely on the Rayleigh law of light scattering on air molecules, namely, the inverse proportionality of the intensity of light scattering to the fourth power of the wavelength [13-15]. Based on the fact that the detectors of most cameras are most sensitive to radiation with a wavelength of about 400 nm, it is easy to determine that in order to reduce the brightness of the sky background by at least 10-15 times, it is desirable to switch to shooting the sky in the wavelength range of at least 800 nm (near infrared range) [14-16].

It is also necessary, along with the scattering of light, to take into account its absorption. The fact is that NLC, as a rule, are observed at low altitudes above the horizon, and for the most distant cloud fields the altitude can be a few degrees. In this case, the absorption of light by dust aerosols in the region

located between the object of study and the observer, that is, in the troposphere, begins to play a significant role, complicating the registration of NLC. The role of dust aerosols in the formation of the twilight segment is well studied. It is important to note here that as the wavelength of radiation increases, the transparency of the surface layer of the atmosphere increases rapidly. If the transparency of the surface layer in the visible range is maximum for red rays, then it will be even more pronounced in the near infrared range [17]. That is, it should be easier to detect NLC near the horizon in the IR range than in the optical range.

When analyzing the possibility of using the IR range to detect NLC, along with taking into account the scattering of light on air density fluctuations, it is necessary to consider the mechanisms of scattering of light radiation on the NLC particles themselves. In this case, it was necessary to make a choice between several scattering theories. Based on classical works, preference should be given to the Mie theory, and as the results of calculations and measurements have shown, the indicatrix of light scattering by NLC particles is strongly extended forward (Figure 1) [18].

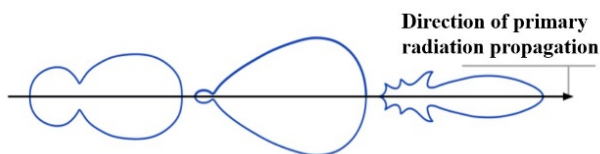


**Figure 1** – Graphic representation of Mie scattering indicatrices for particles of size: a)  $1/3 \lambda$ , b)  $1.0 \lambda$ , c) more than  $1.0 \lambda$  [17].

Confirmation of the importance of taking into account the influence of the light scattering indicatrix type when studying NLC is the fact that the maximum albedo of NLC particles is observed at altitudes of about 2 degrees. This corresponds to a light beam deflection angle no more than 10 degrees. Such deviation is described by elongated indicatrices, both in the Mie and Henyi-Gristein theories. At the same time, observations in the IR range make it possible to sharply reduce both the influence of the background of the twilight segment and the dust content of the tropospheric layer. Thus, there is reason to expect that recording the pattern of the twilight segment in the near-infrared region of the spectrum will make it possible to increase the difference in the brightness of high-altitude cloud formations and the sky background and to detail the type of cloudiness distribution in the sky.

To implement this approach in NLC photography experiments, we used RG780 and RG830 filters. The filters were standardly attached with a threaded connection to the wide-angle lens CANON EF-S LENS of the CANON 2000 D camera [19]. The general view of the camera with a filter and the transmission curves of the filters are shown in Figure 2.

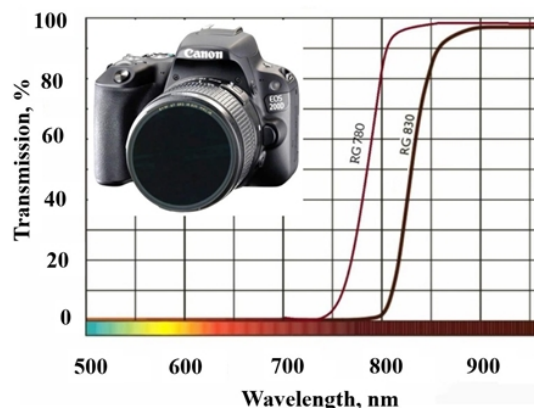


**Figure 2** – General view of CANON 2000 D camera with filter and the transmission curves of the RG780 and RG830 filters.

The assumption about the contrast increasing of the sky extended objects images when shooting in the IR range was verified by repeatedly shooting cirrus clouds in daytime conditions. The fact is that cirrus clouds are structurally closest to NLC, while they are characterized by a thin structure that is detected only on high-contrast images. Therefore, at first, the technique of shooting NLC in the IR range was practiced precisely on cirrus clouds. Examples of shooting results are shown in Figure 3.

Here, the image a) was obtained when shooting without a filter, the image b) was obtained when using a filter with a transmission boundary of 780 nm and the image c) – when using a filter with a transmission boundary of 830 nm. It is noticeable that during normal shooting, details in the lower part of the image are poorly distinguished. And in the near-infrared region of the spectrum, the detail of the picture is noticeably improved. However, it is not the overall impression of the painting that is significant, but the changes in the contrast coefficient. For the picture in the visible region of the spectrum, the local contrast  $K_L$  was 0.48, and for filter images 0.74 and 0.75, respectively. Thus, the assumption of the cloud fields images contrast increasing with the transition from their registration in the visible range to the near-IR region of the spectrum can be considered justified.



**Figure 3** - Images of the cirrus cloud field obtained in the visible range – a) and using infrared filters – b) and c), respectively.

#### **4 The results of the experiment on the registration of noctilucent clouds in the near-infrared region of the spectrum**

Images of the twilight segment in the near infrared region of the spectrum were obtained near the maximum frequency of NLC appearance in the sky of temperate latitudes in the 2022 season. In this case, a CANON 2000 D camera with an RG830 filter, installed on the south-eastern outskirts of Petropavlovsk, was used. Days with clear weather were selected, and the presence of NLC visible to the eye was not required. The shooting was carried out during civil twilight, when NLC are not yet visually observed. Of course, shooting in visible light was also carried out for control. Note that if the exposures were tenths of a second when shooting in visible light, then when using a filter the exposures increased to hundreds of seconds. The most interesting fragments of the images are shown in Figure 4 – the images in visible light are on the left, the images in the near IR range are on the right.

Note that the direction to the north is indicated in the figure. The most interesting and important details of the images are the light formations near the horizon in the images in the IR range. But are they noctilucent clouds? To answer this question, it is necessary to consider in turn the possible effects of light scattering on smoke and cloud aerosols. To do this, the heights of the Sun below the horizon were

calculated for all pairs of images and the height of the atmosphere layer that is illuminated by the Sun. The calculation was carried out according to the method adopted in atmospheric optics [17]. The results are shown in table 1.

Based on the data in the table, it is easy to see that smoke aerosols could not play the role of particles scattering IR radiation, since the heights of their distribution are much lower than the layer of the atmosphere illuminated by the Sun. For the date July 10, at heights above 5 km, cirrus or altocumulus clouds could be a possible cause of radiation scattering, but according to the weather station of Petropavlovsk and the city of Ishim located to the north, their absence was noted. Also, on the dates of July 12 and 18, this type of cloudiness was not observed. According to meteorological data, during the specified time interval, episodic appearance of low-cumulus clouds was noted at altitudes of less than 2000 meters [20]. Thus, the influence of tropospheric clouds on the appearance of bright features in infrared images should most likely be excluded.

It is also interesting that the low angular height of the light details is very close to the conditions for observing the NLC “from the edge”, for example, from spacecraft. In addition, the total angle of the light rays deflection in this case fully corresponds to the elongation of the scattering indicatrix, both in the Mie and Henyi-Gristain approximations.



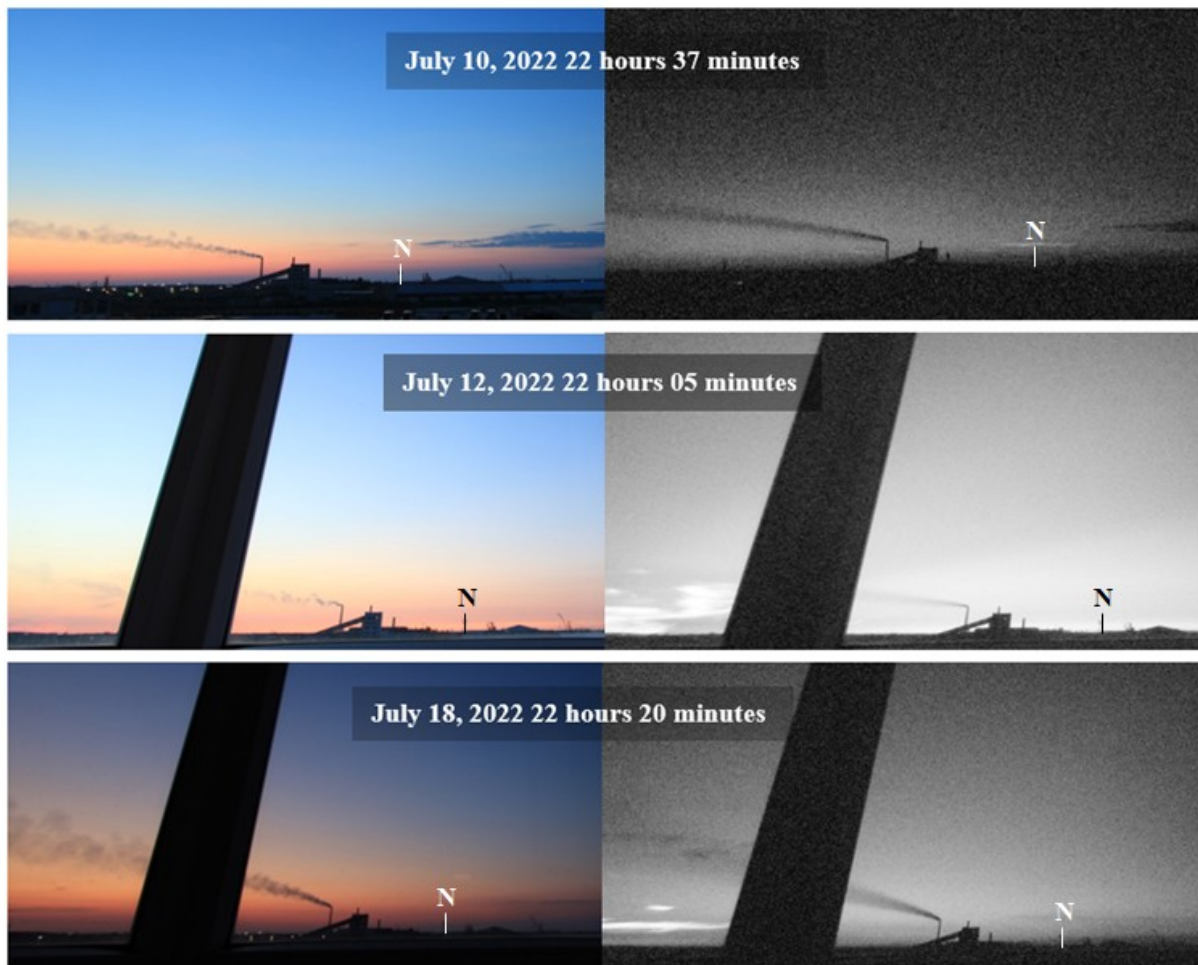


**Figure 4** - Fragments of images of the twilight segment in visible light and in the near-infrared region of the spectrum.

**Table 1** - Angular heights of the Sun at the time of shooting and extremely low heights of atmospheric illumination.

№	Date and time the image was taken	Angular height of the Sun, degrees	Height of the layer illuminated by the Sun, km
1	10.07.2022 22.37	- 4.7	5.4
2	12.07.2022 22.05	- 1.8	0.8
3	12.07.2022 22.19	- 3.2	2.5
4	12.07.2022 22.33	- 4.5	4.9
5	18.07.2022 22.07	- 2.8	1.9
6	18.07.2022 22.20	- 4.1	4.1

Using the map, it is not difficult to estimate the distance from the observation site to the thermal power station chimney, which has a height of 150 meters. The distance is 2800 meters. Therefore, the angular height of the chimney top is close to 3

degrees. At the same time, luminous formations, if they are NLC (average height 82 km), should be removed from the place of observation (latitude 54.85, longitude 69.2 degrees) for distances of about 1400 km to the north on July 10 and for distances

from 1000 to 1500 km to the north-northwest on July 12. Similarly, on July 18, 2022, the NLC should be expected to be removed from the observation point within the range of 1000 to 1400 km. It is possible to verify the presence or absence of NLC in the appropriate locations and at close points in time based on the analysis of data from the AIM mission [21] and synoptic observations of NLC on the specified dates from points in the Urals and Western Siberia. Information from the online journal meteoweb.ru [22], which noted the presence of NLC north of Petropavlovsk on July 12 and 18, was very useful.

## 5 Discussion

The absence of NLC in images taken in the visible range is explained, on the one hand, by the fact that during civil twilight NLC, as a rule, do not stand out against the background of the bright twilight segment. On the other hand, observation experience in Petropavlovsk showed that low-brightness NLC are often not recorded on images even in nautical twilight conditions when they are

located at altitudes less than 4-5 degrees above the horizon. The reason is the strong absorption of light by dust in the ground layer of the atmosphere. As noted above, the possibility of the NLC presence above the horizon of the observation point at the time of shooting can be associated with the results of ground-based observations from other points. Another source of information about the parameters and structure of the NLC field in the northern hemisphere is satellite images [23]. Using these images, it is possible to estimate the position of the southern boundary of the cloud field, the distance and azimuth of the sight line from the observation point to the clouds and make a general agreement on the results of ground and space observations. Following this logic, an analysis of the NLC presence possibility in the IR images for the required dates using satellite images was carried out.

Fragments of NLC field images projections onto the Earth's surface on the specified dates are shown in Figure 5. The position of our observation point is also indicated here. The places that correspond to the position of the light formations in the images shown in Figure 4 are highlighted here with circles.

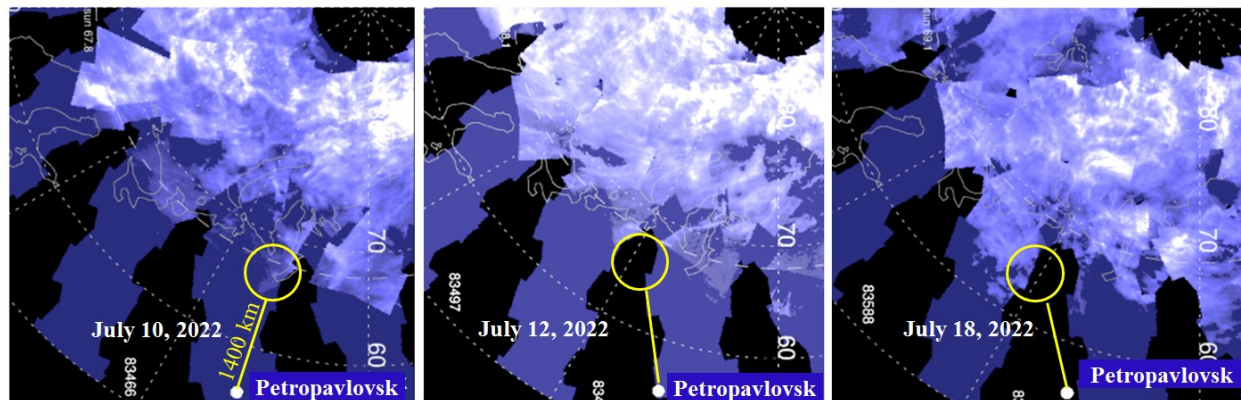


**Figure 5** - To assess the possibility of observing NLC from Petropavlovsk on July 10, 12 and 18 (according to AIM satellite shooting)

As can be seen in Figure 5, the position of the cloud field southern boundary is such that NLC could well have been present in the selected locations during the acquisition of ground-based images. The results of the image analysis are shown in Table 2, which shows the estimated distances from the observation point to the

boundaries of cloud fields and the time of obtaining the corresponding satellite images. The shooting times are given for two adjacent orbital bands. The table shows the numbers of these bands. The first indicates the time of shooting the eastern band of orbital images, the second the western.

**Table 2** - Comparison of conditions for obtaining IR and satellite images.

№	Date	Time of obtaining ground-based images, UT	Time of obtaining satellite images, UT	Distance from the observation point to the cloud field, km
1	10.07.2022	16 h 37 m	83465 06 h 30 m 83466 08 h 05 m	1200
2	12.07.2022	From 16 h 05 m to 16 h 33 m	83495 05 h 58 m 83496 07 h 33 m	1200
3	18.07.2022	From 16 h 07 m to 16 h 20 m	83586 05 h 55 m 83587 07 h 30 m	1000

Of course, attention should be paid to the difference in the time of receipt of ground images and images obtained during the flight over the relevant area of the AIM satellite. However, despite the fact that the difference was noticeable, it must be taken into account that NLC fields in most cases evolve rather slowly. In our case, this demonstrates approximately the same location of the southern cloud boundary in the images obtained over an hour and a half time interval. Therefore, the assessment of the distance between the observation point and the boundary of the cloud field, determined from satellite images, has a right to exist. The close correspondence of the distances obtained from ground-based and space-based observations indicates with a high degree of probability that it is NLC that are recorded in the images of the twilight segment taken in the near-IR range during civil twilight.

## 6 Conclusions

The results obtained are interesting, but, of course, further verification and improvement of the

NLC registration method in the near infrared region is necessary. First of all, in our opinion, improvement of the recording equipment is required. As is known, matrix receivers of digital cameras are sensitive to radiation with a wavelength up to 1200 nm with a maximum sensitivity of about 800 nm (Fig. 6a). However, to achieve sharper images, camera manufacturers usually place a glass filter in front of the sensor, which almost completely cuts off radiation with a wavelength greater than 720-740 nm (Fig. 6b). In this case, the lens optics does not prevent the shooting in the IR range (Fig. 6c).

Thus, restoring the sensitivity of the sensor of CANON cameras to radiation in the near infrared range is possible by removing such a filter. If this is done, the sensitivity of cameras in the range under consideration can be increased by at least an order of magnitude. Due to this, it is possible to reduce the exposure to acceptable values and extend the experiment on obtaining NLC infrared images not only to civil, but also to nautical twilight. This will further confirm the effectiveness of recording NLC fields in the near-infrared region of the spectrum.

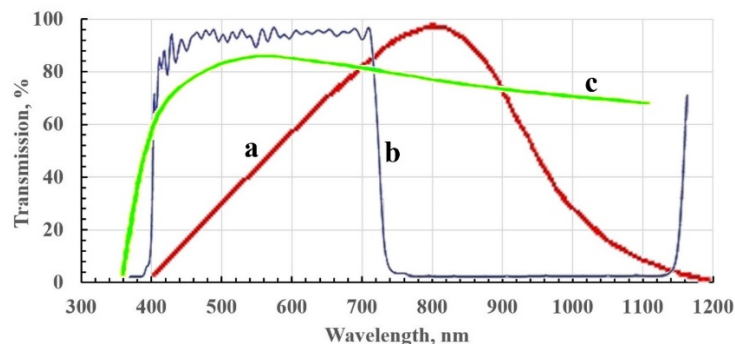


**Figure 6** – Dependence of the transmission coefficient on the wavelength of light for a) the matrix of a digital camera; b) the glass filter of the camera; c) the camera lens [24]

Increasing the long-wavelength sensitivity of cameras will allow us to move on to experiments with filters tuned to longer wavelengths. Success in this direction promises to significantly expand the possibilities of ground-based observations of NLC fields, which fully justifies the efforts being made.

### References

1. Dalin, P., Pogoreltsev, A., Pertsev, N., Perminov, V., Shevchuk, N., Dubietis, A., Zalcik, M., Kulikov, S., Zadorozhny, A., Kudabayeva, D., Solodovnik, A., Salakhutdinov, G., and Grigoryeva, I. Evidence of the formation of noctilucent clouds due to propagation of an isolated gravity wave caused by a tropospheric occluded front. // *Geophys. Res. Lett.* - 2015. Vol.42.- P. 2037–2046. <https://doi.org/10.1002/2014GL062776>
2. Dalin, P., Gavrilov, N., Pertsev, N., Perminov, V., Pogoreltsev, A., Shevchuk, N., Dubietis, A., Völger, P., Zalcik, M., Ling, A., Kulikov, S., Zadorozhny, A., Salakhutdinov, G., and Grigoryeva, I. A case study of long gravity wave crests in noctilucent clouds and their origin in the upper tropospheric jet stream // *J. Geophys. Res. Atmos.* - 2016. Vol.121. P. 23. <https://doi.org/10.1002/2016JD025422>
3. Solodovnik, A. A., Leontyev, P. I., Dalin, P., Studies of the influence of tropospheric factors on the formation of noctilucent clouds by a cartographic method // *Journal of Atmospheric and Solar-Terrestrial Physics.*- 2020. - Vol. 200.- P. 105224. <https://doi.org/10.1016/j.jastp.2020.105224>
4. Shevchuk, N., Pertsev, N., Dalin, P., Perminov, V. Wave-induced variations in noctilucent cloud brightness: model and experimental studies. *Journal of Atmospheric and Solar-Terrestrial Physics.* - 2020. Vol.203. – P. 105257. <https://doi.org/10.1016/j.jastp.2020.105257>
5. Solodovnik A., Leontiev P., Dalin P., Takenov B., Alyoshin D. Seasonal evolution and interseasonal changes in polar mesospheric clouds at high latitudes in the Southern Hemisphere // *J. of Atmospheric and Solar-Terrestrial Physics.* – 2021. – Vol.226. – Art.No 105787. <http://dx.doi.org/10.1016/j.jastp.2021.105787>
6. Solodovnik A. A., Leontyev P. I., Useinov B. M., Kadyrmin A. D., Zyryanov R. O. Application of electronic receivers for recording infrared images of celestial phenomena at the CAR of the NKU // *Physical Sciences & Technology* . – 2023. - Vol. 10.- Is. 1.- P.50-57. <https://doi.org/10.26577/ijmph.2022.v13.i2.04>
7. Evtifeev D. Experiments in the field of photography shooting. Infrared photography. URL:<https://evtifeev.com/49921-infrakrasnaya-fotosemka.html>, valid on 04.03.2023. (In Russian).
8. Emelyanov E.V. Astrophysics of the IR range. – INFO, Moscow, Russia. – 2012.– P.36. (In Russian).
9. Wolf W., Smith W., Lego R. Handbook of infrared technology // *Designing optical systems.* Trans. from English – Mir, Moscow, Russia. - 1998. Vol. 2.– P.339. (In Russian).
10. Mypresentation. Chislovye kharakteristiki izobrazhenii. Tonal'nyi diapazon. URL: <https://mypresentation.ru/presentation/chislovye-xarakteristiki-izobrazhenij>, valid on 28.04.2022.
11. NPK – Fotonika. PZS – matritsy – obshchie svedeniya. URL: <https://www.npk-photonica.ru/info/reading/18320/>, valid on 12.10.2021. (In Russian).
12. Rugography. Processing of images and video files. How to read, understand and recognize the histogram of an image. URL: <https://rugraphics.ru/photoshop/kak-chitat-ponimat-raspoznavat-gistogrammu>, valid on 04/03/2023. (In Russian).
13. Novikova V.A., Varzhel S.V. Light scattering and its application in fiber optics. // Tutorial. Editorial and Publishing Department of the University. Sankt-Peterburg, Kronverskii. – 2019. P.49. (In Russian)
14. K. S. Shifrin and A. Y. Perelman Determination of particle spectrum of atmosphere aerosol by light scattering Hydrometeorological Service. – 1965.-Vol.2.- P.566-572
15. Stephens G.L. Optical properties of eight water cloud types // *Technical Paper of CSIRO. Atmosph. Phys. Division.* Aspendale. 1979. №36.- P. 1-35.
16. Melnikova I.N., Lobanova M. Vasilyev. The phase function asymmetry parameter dependence on scattering media properties // *Modern problems of remote sensing of the earth from space* -2010.-Vol.7(4).- P.147-157
17. Zvereva S. V. In a world of sunshine L., Gidrometeoizdat .-1988. - P.160. (In Russian)
18. Gadsden M., Schröder W. Noctilucent Clouds. Springer, New York, 1989.
19. Canon Inc. Canon EOS 2000D User Manual. – Tokyo, Japan. - 2017. – 326 p. (In Russian).
20. Sensotec. Filters: light filter – 780-830nm - IR long-wave. Modification of cameras. URL: <https://photodrom.com/>, valid on 05.04.2023 (In Russian)
21. National aeronautics and space administration. Aeronomy of Ice in the Mesosphere. URL: <https://web.archive.org/web/20100324222208/http://nasascience.nasa.gov/missions/aim>, valid on 15.09.2023 (In Russian)
22. Meteoweb. The journal of observations of silvery clouds. 2006-2023. URL: <http://meteoweb.ru/astro/nlc/reports.php>, valid on 23.04.2023 (In Russian)
23. AIM Hamptonu. Aeronomy of Ice in the Mesosphere. URL: <https://aim.hamptonu.edu/>, valid on 12.05.2023
24. Fern Flower Group. Shooting in UV and IR ranges. URL: <https://www.fern-flower.org/ru/articles/semka-v-uf-i-ik-diapazonah> (In Russian)

**Information about authors:**

Solodovnik Andrey Andreevich, candidate of physical and mathematical sciences corresponding member of the Kazakhstan National Academy of Natural Sciences, is a professor at the M. Kozybaev North Kazakhstan University (Petropavlovsk, Kazakhstan), e-mail: asolodovnik@ku.edu.kz;

Zyryanov Roman Olegovich is a master's student at the M. Kozybaev North Kazakhstan University (Petropavlovsk, Kazakhstan), e-mail: romanzyryanov22@mail.ru;

Leontiev Pavel Ivanovich, candidate of physical and mathematical sciences, is an associate professor at the M. Kozybaev North Kazakhstan University (Petropavlovsk, Kazakhstan), e-mail: pleontiev@mail.ru, pleontiev@ku.edu.kz;

Useinov Beibut Meiramovich, candidate of physical and mathematical sciences, is a professor at the M. Kozybaev North Kazakhstan University (Petropavlovsk, Kazakhstan), e-mail: buseinov@gmail.com;

Gololobova Evgenia Georgievna, Master in «Information Systems in Physics», is a senior lecturer at the M. Kozybaev North Kazakhstan University (Petropavlovsk, Kazakhstan), e-mail: evgenia\_g78@mail.ru;

Zhuravlev Pavel Leonidovich, Master of Science in the specialty «Physics and Astronomy», is a laboratory assistant of AEO &quot;Nazarbayev Intellectual School&quot; branch of Petropavlovsk (Petropavlovsk, Kazakhstan), e-mail: zhuravlevpl@yandex.ru

## Analytical formula for multiple ionization cross sections of rare gas atoms by electron and positron impact

S.A. Maiorov<sup>1\*</sup>  and R.I. Golyatina<sup>2</sup> 

<sup>1</sup>Joint Institute for High Temperatures of Russian Academy of Sciences, Moscow, Russia

<sup>2</sup>Prokhorov General Physics Institute of Russian Academy of Sciences, Moscow, Russia

\*e-mail: mayorov\_sa@mail.ru

(Received March 26, 2024; received in revised form April 30, 2024; accepted May 11, 2024)

The paper presents an analysis of data on the single and multiple ionization cross sections of rare gas atoms by electron impact and single ionization cross sections by positron impact. To approximate the cross section for single ionization of atoms of rare gases, as well as a large number of atoms of other elements, a semi-empirical formula with four parameters was proposed, which gives an accuracy of several percent in a wide energy range. Here we generalize our approach to the case of multiple ionization of an atom by electron impact and single ionization by positron impact. For the selected sets of experimental data, the recommended values of the approximation coefficients for a wide range of collision energies have been calculated and determined. The approximation formula reproduces the values of the ionization cross sections for rare gases in a wide range of energies with an accuracy of the order of error of the available experimental data and it has physically reasonable asymptotics.

**Key words:** multiple ionization cross sections, electron impact, positron impact, approximation of cross sections.

**PACS number(s):** 34.80.Bm, 34.80.Dp, 51.50.+v, 52.80.Dy.

### 1 Introduction

To analyze and simulate processes in low-temperature plasma, it is necessary to know the kinetic coefficients, in particular, the cross sections for ionization of atoms by electron impact. This work is a continuation of our works [1-4], in which experimental and theoretical data on electron-atomic collision cross sections are analyzed [5-11]. In 1912, Thomson, based on the consideration of the problem of the collision of two electrons, one of which is at rest, determined the following formula for the ionization cross section [5]:

$$\sigma_{ionization}(\varepsilon) = \frac{\pi e^4}{\varepsilon} \left( \frac{1}{I} - \frac{1}{\varepsilon} \right) \equiv 4\pi a_0^2 \frac{Ry^2(\varepsilon - I)}{I\varepsilon^2}, \quad (1)$$

where  $I$  – ionization energy,  $\varepsilon > I$  – incident electron energy,  $a_0$  – Bohr radius,  $Ry=13.6$  eV. This formula gives a linear increase in the ionization cross section at a small excess of the collision energy over the ionization potential. The formula for approximating the initial part of the curve of

dependence of the ionization cross section on the energy of the incident electron was first proposed by Compton and van Voorhis in 1925 [6]:  $\sigma_{ionization}(\varepsilon) = C_i(\varepsilon - I)$ ,  $I < \varepsilon < 2I$ . Vanier in [11] took into account the interaction of the incident and bound electrons and obtained the following approximation of the initial section:

$$\sigma_{ionization}(\varepsilon) = C_i(\varepsilon - I)^{1.127}, \quad \varepsilon > I. \quad (2)$$

The first ionization potential  $I$  can serve as the natural scale of energy when an electron collides with an atom, so here and below it is convenient to pass to the dimensionless energy  $x = \varepsilon / I$ ,  $\Delta = x - 1$ ,  $x > 1$ . In the case of high energies ( $\varepsilon > 300$  eV) dependence of the ionization cross section on the electron-impact energy can be described by the Born-Bethe type formula:

$$\sigma_{ionization}(\varepsilon) \propto \frac{\ln x}{x}. \quad (3)$$

Formulas of that type are widely used for fitting the excitation and ionization cross sections (see, e.g. [12]).

In our paper [4], we proposed a formula for the electron impact ionization cross section of an atom with four approximation coefficients  $\alpha$ ,  $\beta$ ,  $\gamma$ ,  $\delta$ :

$$\sigma_{ionization}(\varepsilon) = \frac{\alpha \Delta x^\delta}{(1 + \beta \Delta x)^\gamma}. \quad (4)$$

Here the constant  $\alpha$  has the dimension of area, and the constants  $\beta$ ,  $\gamma$ ,  $\delta$  are dimensionless quantities. To search for them, the problem of minimizing the root-mean-square relative deviation of cross sections from their experimental values was solved using the coordinate descent method. For  $\alpha = 4\pi a_0^2 (Ry / I)^2$ ,  $\beta = 1$ ,  $\gamma = 2$ ,  $\delta = 1$  formula (4) coincides with Thomson's formula (1). The maximum value of the cross section according to this formula is achieved when  $\Delta x = \delta / (\beta(\gamma - \delta))$ . Formula (4) allows one to take into account the deviation of the dependence of the cross section from linearity near the threshold, and at high energies it allows one to take into account the logarithmic correction of the Bethe-Born approximation. It turns out that a power-law decrease in the ionization cross section  $\sigma_{ionization}(x) \propto 1/x^{\gamma-\delta}$  at high energies makes it possible to obtain quite satisfactory agreement with experimental and theoretical data for all inert gases. The errors of the approximation of experimental data by analytical dependence (4) for rare gases, alkali and vapors of other metals, as well as for H, Si, P, S lie in the range of 1-10% [4], which corresponds in order of magnitude to the error of the experiments themselves.

In principle, there are hundreds of experimental and theoretical works on the determination of ionization cross sections. But at the same time, errors are often not given, because, generally speaking, they cannot be determined without knowing the exact answer. By increasing the number of measurements, the statistical error can be reduced, but in the case of an experiment, a systematic error remains. Therefore, the experimental data themselves from various sources may differ tenfold, while errors in the range of 3-7% are often indicated. In addition, the ionization of an atom as a multielectronic system, based on

theoretical consideration, usually involves the use of simplifying assumptions, which makes it difficult to determine the accuracy of the result.

## 2 Approximation of the single ionization cross sections by 1 term formula

The largest amount of experimental and theoretical data is available for cross sections of single ionization of atoms. The observed variation in the experimental data for cross sections is due to the fact that the cross section is not a directly measurable quantity, but is calculated as a result of processing other measured parameters. To analyze and approximate them, we took data from [13,14], where recommended cross-section values were obtained for single ionization of rare gas atoms by analyzing experiments and theories.

The work [15] presents the results of measurements of the ionization cross sections of helium, neon, argon, krypton, and xenon upon electron impact for energies in the range from the first ionization threshold to 1000 eV. In addition to single ionization cross sections, this work obtained data on multiple ionization cross sections. Briefly, during cross-section measurement, the vacuum chamber is filled with the target gas and the electron gun generates pulses. These pulses pass through the gas between the two plates, and the electrons produced by ionization are going at a collector. The data from [15], which claim higher accuracy, confirm the correctness of the single ionization cross sections recommended in [13, 14].

The results of the approximation of experimental data [13,14] according to formula (4) for inert gases are given in [4]. In this work, for comparison, we added the results of approximation of experimental data on single ionization [15]. The root-mean-square relative error of approximation in both cases lies in the range from one to five percent, i.e. within experimental errors. As an example, Fig. 1 for Xe shows the experimental data from [14] and [15], as well as their approximations according to formula (4). The data [14] on the right tail is significantly higher than in [15]. Table 1 shows the values of the parameters for approximating the ionization cross sections of rare gas atoms as well as the values of the root-mean-square relative error, the maximum ionization cross section  $\sigma(\varepsilon_m)$  and the energy  $\varepsilon_m$ , at which it is achieved.

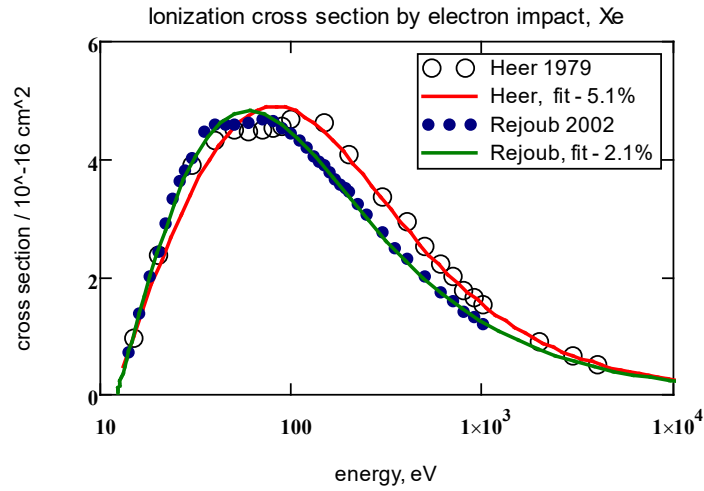


Figure 1 – Single ionization cross sections of Xe atoms by electron impact.

Table 1 – Parameter values for approximating the ionization cross sections of rare gas atoms by electron impact.

Atom, I, eV	$\alpha$ , Å <sup>2</sup>	$\beta$	$\gamma$	$\delta$	$\Delta$ , %	$\varepsilon_m$ , eV	$\sigma(\varepsilon_m)$ Å <sup>2</sup>	Reference
2, He 24.59	0.406	0.330	2.01	1.11	1.0%	116	0.35	A, Heer, [13]
	0.372	0.312	2.03	1.13	1.6%	124	0.34	B, Rejoub, [15]
10, Ne 21.57	0.451	0.23	2.22	1.33	1.3%	162	0.71	A, Heer, [14]
	0.343	0.182	2.33	1.33	4.2%	179	0.67	B, Rejoub, [15]
18, Ar 15.76	3.19	0.326	1.92	1.08	2.5%	78	2.87	A, Heer, [14]
	4.26	0.541	1.93	1.26	3.6%	71	2.66	B, Rejoub, [15]
36, Kr 14.0	3.77	0.302	1.86	1.07	2.7%	77	3.82	A, Heer, [14]
	7.08	0.641	2.19	1.52	4.3%	64	3.61	B, Rejoub, [15]
54, Xe 12.13	3.66	0.178	1.66	0.836	5.1%	81	4.90	B, Heer, [14]
	5.64	0.365	1.79	1.05	2.1%	59	4.83	A, Rejoub, [15]

The analysis of the data presented in Table 1 allows us to estimate experimental errors and improve the accuracy of determining cross sections. It can be noted that there is a correlation between the approximation error of the experimental data [13-15] by the analytical dependence (4) and the proximity of the parameter  $\beta$  to the value of 0.33. Therefore, for He, Ne, Ar, Kr we recommend data from [13,14], and for Xe from [15]. In the last column of Table 1, the letter A – marks the most accurate approximation, and B – marks the less accurate one. Note that in the recommended approximations, the values of the coefficient  $\delta$  are in the range from 1.05 to 1.33, i.e. the Vanier correction (2) with the value  $\delta = 1.127$  allows us to more correctly describe the initial part of the dependence of the ionization cross section on the collision energy.

Formula (4) approximates well the behavior of the dependence of ionization cross sections on energy for most elements (see [4]). But for some elements, as shown in Fig. 1 for Xe, this dependence has a two-humped nature due to the knocking out of electrons from the inner shells. In these cases, a fairly good accuracy is achieved by approximating experimental data with two-term formula

$$\sigma_{\text{ionization}}(\varepsilon) = \frac{\alpha_1 \Delta x_1^{\delta_1}}{(1 + \beta_1 \Delta x_1)^{\gamma_1}} + \frac{\alpha_2 \Delta x_2^{\delta_2}}{(1 + \beta_2 \Delta x_2)^{\gamma_2}},$$

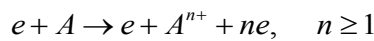
where  $x_1 = \varepsilon / I_1$ ,  $\Delta x_1 = x_1 - 1$ ,  $x_1 > 1$ ,  $x_2 = \varepsilon / E_2$ ,  $\Delta x_2 = x_2 - 1$ ,  $x_2 > 1$ ,  $E_2$  – potential from the inner shell. We used this two-term formula in [4] to approximate the single-ionization cross sections of



Xe, Cs, Cu, and U atoms, which made it possible to reduce the approximation error for these elements by one and a half times and qualitatively reproduce the two-humped nature of the dependence of the cross section on the collision energy.

### 3 Approximation of the multiple ionization cross sections of atoms by one term formula

With a sufficiently high energy of the incident electron, it can knock out several electrons at once:



Analysis of the experimental data [16] on multiple ionization (MI) cross sections  $\sigma_N$  showed that the majority of the cross sections has a similar shape and the electron-impact energy dependence can be described by the Born-Bethe type formula (3) [17]. Namely, for cases with  $n \geq 3$ , based on formula (3), a semi-empirical formula for the dependence of the cross sections MI of atoms by electron-impact is obtained [18]:

$$\sigma_n(x) = \frac{\alpha_{n,N} R y^2 (x-1) \ln x}{I_n^2 x^2}. \quad (5)$$

where dimensionless energy  $x = \varepsilon / I_n$ ,  $\Delta x = x - 1$ ,  $x > 1$ . The threshold energy  $I_n = \sum_{i=0}^{n-1} I_{i,i+1}$ ,

corresponds to the minimal ionization energy  $I_n$ , required to remove  $n$  outmost electrons,  $I_{i,i+1}$  – is the one-electron ionization energy from the charge  $i$  to  $i+1$ . The coefficient  $\alpha_{n,N}$  should depend only on two parameters: the number of ejected electrons  $n$  and the total number of the target electrons  $N$ , and a power-law approximation was found for it. Formula (5) does not allow correctly taking into account the asymptotes for  $n=1, 2$ , and for  $n > 2$  in many cases the error is very large. Semi-empirical formulas for the cross sections for the double ionization of light positive ions by electron impact were obtained in [19].

There is a large amount of experimental data for multiple ionization of rare gas atoms (see references in [20, 21]). We took more recent experimental data for multiple ionization of rare gas atoms from [15], which are in good agreement with the data from [20]. Table 2 shows the results of approximation of the cross section for multiple ionization of rare gas atoms by electron impact using formula (4). Figures 2-4 for Ne, Ar and Xe show experimental data from [14] and [15], as well as their approximations using formula (4).

**Table 2** – Parameter values for approximating the multiple ionization cross sections of rare gas atoms by electron impact.

Atom	$n, I_n, eV$	$\alpha, \text{\AA}^2$	$\beta$	$\gamma$	$\delta$	$\Delta, \%$	$\varepsilon_m, eV$	$\sigma(\varepsilon_m), \text{\AA}^2$
2, He	2, 79.01	0.005	0.643	3.59	2.25	3.7%	285	0.0013
10, Ne	2, 62.53	0.137	0.648	4.60	3.15	3.2%	272	0.0306
	3, 126.0	0.011	0.572	5.32	3.0	4.5%	411	0.0015
18, Ar	2, 43.39	12.48	1.89	4.07	3.04	6.2%	111	0.1803
	3, 84.30	0.014	0.45	2.44	1.43	32%	350	0.0089
	4, 144.1	0.005	0.63	8.76	6.96	19%	1028	0.0015
36, Kr	2, 38.36	121	2.68	4.68	3.8	3.0%	100	0.297
	3, 75.31	0.047	0.379	2.31	1.41	7.9%	387	0.039
	4, 127.8	0.078	0.94	4.75	3.84	2.5%	702	0.0097
56, Xe	2, 33.10	33.2	2.35	3.64	3.0	6.6%	99.0	0.471
	3, 64.15	127	2.35	5.69	4.78	14%	208	0.175
	4, 106.4	28.3	2.06	6.12	5.15	22%	380	0.0471
	5, 160.5	31.5	2.59	6.26	5.0	9.5%	406	0.0116
	6, 227.16	35.6	2.91	7.30	6.0	13%	587	0.0019

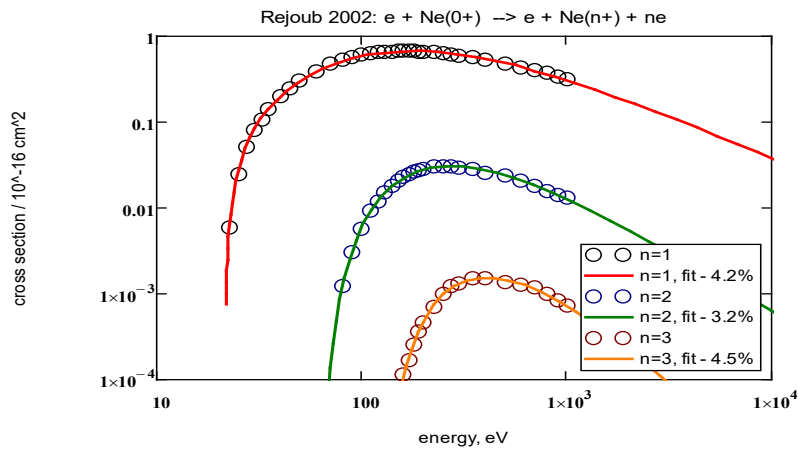


**Figure 2** – Single, double and triple cross sections for ionization of Ne atoms by electron impact.

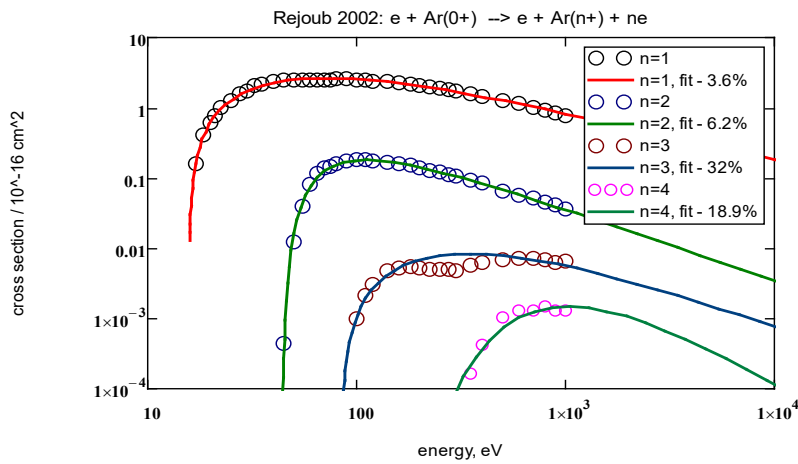


**Figure 3** – Single, double, triple and four-fold cross sections for ionization of Ar atoms by electron impact.

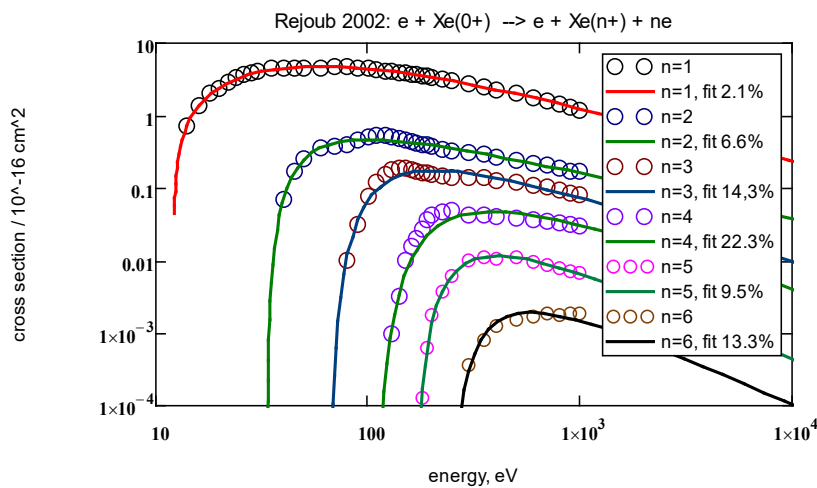


**Figure 4** – Single, double, triple, 4-, 5- and 6--fold cross sections for ionization of Xe atoms by electron impact.

For triple and 4-fold ionization of Ar atoms and two-, three-, 4-, 5- and 6-fold ionization of Xe atoms, the cross-section curve has a two-humped character due to the ionization of electrons from the inner shells. To take this effect into account more accurately, it is necessary to use two-term approximation, as we did in [4] for Xe, Cs, Cu, and U.

#### 4 Approximation of the single ionization cross sections of rare atoms by positron impact

The papers [22, 23] present the cross sections for ionization by a positron impact for atoms of rare gases. For these data, we calculated the approximation coefficients according to formula (4). The results are shown in Table 3.

**Table 3** – Parameter values for approximating the multiple ionization cross sections of rare gas atoms by positron impact.

Atom	$n, I_n$	$\alpha, \text{\AA}^2$	$\beta$	$\gamma$	$\delta$	$\Delta, \%$	$\epsilon_m, eV$	$\sigma(\epsilon_m), \text{\AA}^2$	Reference
2, He	1, 24.59	1.06	0.501	3.55	2.33	3.4%	118	0.54	Ratnavelu, [23]
10, Ne	1, 21.57	0.644	0.337	2.84	1.93	4.4%	157	0.885	Kara, [22]
		0.487	0.196	2.40	1.32	3.1%	156	0.803	Ratnavelu, [23]
18, Ar	1, 15.76	1.88	0.198	2.67	1.42	3.0%	106	2.96	Ratnavelu, [23]
36, Kr	1, 14.0	2.77	0.284	2.33	1.42	8.8%	91	3.48	Kara, [22]
		3.47	0.316	2.87	1.80	7.2%	89	4.15	Ratnavelu, [23]
56, Xe	1, 12.13	4.59	0.207	1.99	1.03	8.3%	75	5.86	Kara, [22]
		5.40	0.277	2.55	1.47	5.6%	72	6.27	Ratnavelu, [23]

Figure 5 shows cross sections of single ionization of helium atoms by electron-impact for experimental data from [13, 15] and positron impact for experimental data from [23].

Figure 6 shows cross sections of single ionization of krypton atoms by electron impact for experimental data from [14, 15] and positron impact for experimental data from [22, 23]. This

figure clearly shows the more complex nature of the dependence of the ionization cross section by positron impacts compared to electron impacts. The reason apparently lies in an additional ionization channel with the formation of positronium in a positron-atom collision. In addition, measurements of positron-atomic collisions have a large error.

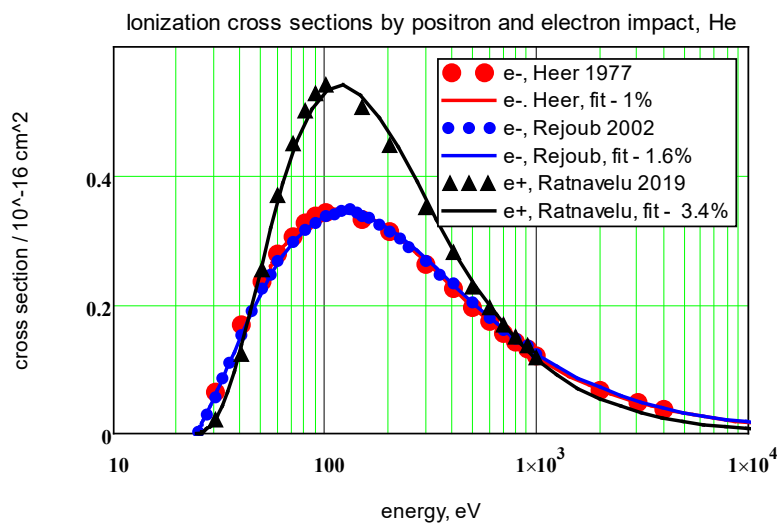


**Figure 5** – Single-ionization cross sections of He by positron (e+) and electron (e-) impact.

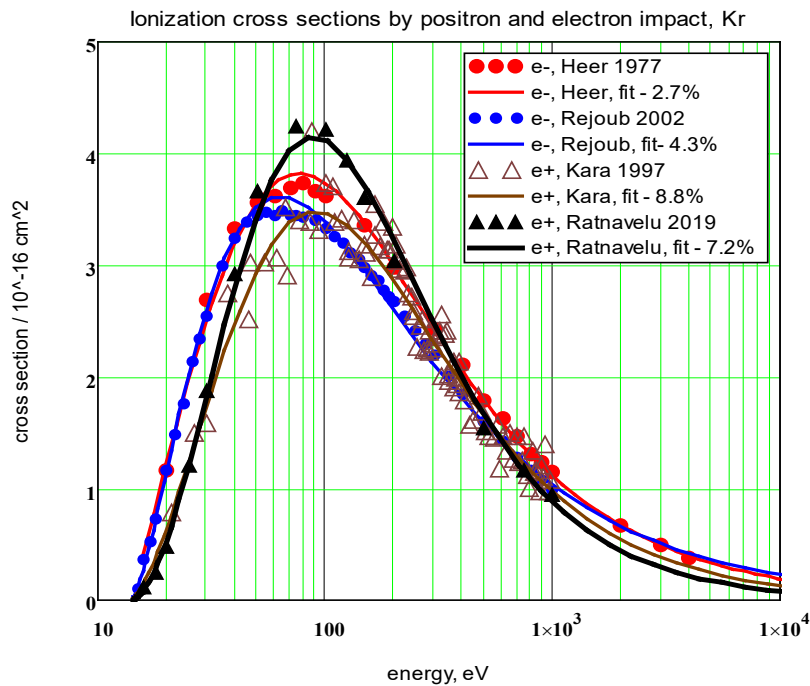


Figure 6 – Single-ionization cross sections of Kr by positron (e+) and electron (e-) impact.

## 5 Conclusions

Using the available and most reliable data on the ionization cross sections of atoms of inert gases, the cases of single and multiple ionization of atoms by electron impact and single ionization of atoms by positron impact are considered. For approximating the cross sections, a semi-empirical formula with four parameters is proposed. Smooth and asymptotically reasonable approximating dependencies make it possible to avoid errors in the numerical differentiation of experimental data, which in the mathematical sense is incorrect (that is, arbitrarily small errors in the data give an arbitrarily large error in the derivative). Therefore, the use of analytical formulas with physically reasonable asymptotes to find cross-section values by interpolation or extrapolation seems more preferable than the use of tabular experimental data.

The cross section of single ionization of atoms of rare gases by electron impact is approximated with an error of 1-3%. Since the error of the experimental data is an order of magnitude larger, the analysis of the fitting coefficients makes it possible to determine which data should be recommended for use.

Multiple ionization of atoms by electron impact is a more complex process in which the ionization of electrons from inner shells often plays an important role. But even in this case, it is possible to obtain an approximation error in the range of 3–30%. In order of magnitude, this error practically coincides with the error of the experimental data.

The cross section of single ionization of rare gas atoms by positron impact is approximated with an error of 3-9%. Since the ionization of an atom by a positron impact can be accompanied by the formation of positronium, this leads to a greater error in the experimental data.

## References

1. Golyatina R.I., Maurov S.A. Analytical cross section approximation for electron impact ionization of alkali and other metals, inert gases and hydrogen atoms // *Atoms*. – 2021. – Vol.9. – P.90. <https://doi.org/10.3390/atoms9040090>
2. Golyatina R. I., Maurov S. A. Analytical approximation of cross sections of collisions of electrons with atoms of inert gases // *Phys. Sci. Technol.* –2021. – Vol. 8. – P. 4–13. <https://doi.org/10.26577/phst.2021.v8.i1.01>
3. Golyatina R. I., Maurov S. A. Analytical approximation of cross sections of collisions of electrons with inert gas atoms // *Plasma Physics Reports*. – 2022. –Vol. 48. – P. 193–199. <https://doi.org/10.1134/S1063780X2202009X>
4. Maurov S. A., Golyatina R. I. Analytical formulas for approximating cross sections of electron collisions with hydrogen, noble gases, alkali and other atoms // *Atoms*. – 2022. –Vol.10. –P.93. <https://doi.org/10.3390/atoms10030093>
5. Thomson J.J. Ionization by moving electrified particles // *The London, Edinburgh and Dublin Philos. Mag. J. Sci.* – 1912. – Vol. 23. – P. 449–457. <https://doi.org/10.1080/14786440408637241>
6. Compton K. T., Van Voorhis C. C. Probability of ionization of gas molecules by electron impacts // *Phys. Rev.* – 1925. – Vol. 26. – P. 436. <https://doi.org/10.1103/PhysRev.26.436>
7. Zecca A., Karwasz G. P., Brusa R.S. One century of experiments on electron-atom and molecule scattering: A critical review of integral cross-sections // *Riv.Nuovo*. –1996. –Vol.19. –No.3. –P.1–146. <https://doi.org/10.1007/BF02742990>
8. Pancheshnyi S., Biagi S., Bordage M. C., Hagelaar G.J.M., Morgan W.L., Phelps A.V., Pitchford L.C. The LXCat project: Electron scattering cross sections and swarm parameters for low temperature plasma modeling // *Chemical Physics*. – 2012. – Vol. 398. – P. 148. <https://doi.org/10.1016/j.chemphys.2011.04.020>
9. Brusa R. S., Karwasz G. P., Zecca A. Analytical partitioning of total cross sections for scattering on noble gases // *Phys. D*. – 1996. – Vol. 38. – P. 279–287. <https://doi.org/10.1007/s004600050092>
10. Kaur J., Gupta D., Naghma R., Ghoshal D., Antony B. Electron impact ionization cross sections of atoms // *Canadian Journal of Physics*. – 2015. – Vol. 93. – No. 6. – P. 617–625. <http://dx.doi.org/10.1139/cjp-2014-0485>
11. Wannier G. H. The Threshold Law for Single Ionization of Atoms or Ions by Electrons // *Phys. Rev.* –1953. – Vol. 90. – P. 817– 825. <https://doi.org/10.1103/PhysRev.90.817>
12. Lotz W. Z. Electron-impact ionization cross-sections for atoms up to  $Z=108$  // *Physik*. –1970. – Vol. 232. – P. 101-107. <https://doi.org/10.1007/BF01393132>
13. Heer F. J., Jansen R. H. J. Total cross sections for electron scattering by He // *Phys. B: Atom. Mol. Phys.* – 1977. – Vol. 10. – No. 18. – P. 3741 3758.
14. Heer F. J., Jansen R. H. J., van der Kaay W. Total cross sections for electron scattering by Ne, Ar, Kr and Xe. // *J. Phys. B: At. Mol. Phys.* – 1979. – Vol. 12. – P. 979–1002. <https://doi.org/10.1088/0022-3700/12/6/016>
15. Rejoub R., Lindsay B.G., Stebbings R.F. Determination of the absolute partial and total cross sections for electron-impact ionization of the rare gases. // *Phys. Rev. A*. – 2002. –Vol. 65. – P. 042713. <https://doi.org/10.1103/PhysRevA.65.042713>
16. Tawara H., Kato T. Total and partial ionization cross sections of atoms and ions by electron impact // *At. Data Nucl. Data Tables*. – 1987. – Vol. 36. – P. 167 – 353. [https://doi.org/10.1016/0092-640X\(87\)90014-3](https://doi.org/10.1016/0092-640X(87)90014-3)
17. McGuire E. J. Electron ionization cross sections in the Born approximation // *Phys. Rev. A*. – 1977. – Vol. 16. – No. 1. – P. – 62 – 72. <https://doi.org/10.1103/PhysRevA.16.62>
18. Shevelko V. P., Tawara H. Semiempirical formula for multiple ionization cross sections of atoms by electron impact // *Phys. Scr.* – 1995. – Vol. 52. – No. 6. – P. 649–653. <https://doi.org/10.1088/0031-8949/52/6/007>
19. Shevelko V. P., Tawara H., Scheuermann F., Fabian B., Muller A. and Salzborn E. Semiempirical formulae for electron-impact double ionization cross sections of light positive ions // *J. Phys. B: At. Mol. Phys.* – 2005. – Vol. 38. – P. 525–545. <https://doi.org/10.1088/0953-4075/38/5/006>
20. Shevelko V. P., Tawara H., Salzborn E. Multiple-ionization cross sections of atoms and positive ions by electron impact // Preprint NIFS-DATA-27, Nagoya, Japan. –1995. P. 1– 40.
21. Hahn M., Muller A., Savin D. W. Electron-impact multiple-ionization cross sections for atoms and ions of helium through zinc // *The Astrophysical Journal*. – 2017. – Vol. 850. – P.122–143. <https://doi.org/10.3847/1538-4357/aa9276>
22. Kara V., Paludan K., Moxom J., Ashley P., Laricchia G. Single and double ionization of neon, krypton and xenon by positron impact // *J. Phys. B: At. Mol. Opt. Phys.* – 1997. – Vol. 30. – P. 3933–3949.
23. Ratnavelu K., Brunger M. J., Buckman S. J., Stephen J. Recommended positron scattering cross sections for atomic systems // *J. Phys. Chem. Ref. Data*. – 2019. – Vol. 48. – P. 023102. <https://doi.org/10.1063/1.5089638>

**Information about authors:**

Maurov Sergey Alekseevich (corresponding author), Doctor of Physical and Mathematical Sciences, is a leading researcher at the Joint Institute for High Temperatures of the Russian Academy of Sciences (Moscow, Russia) e-mail: [maurov\\_sa@mail.ru](mailto:maurov_sa@mail.ru);

Golyatina Rusudan Igorevna is a researcher at the Prokhorov General Physics Institute Russian Academy of Sciences (Moscow, Russia) e-mail: [rusudan@intemodino.com](mailto:rusudan@intemodino.com)

## Phase and group velocities of waves in medium of Quark-gluon plasma

K. Baiseitov<sup>1\*</sup>, D. Blaschke<sup>2,3,4</sup>, and Ye. Kuanysbailuly<sup>1</sup>

<sup>1</sup>Al-Farabi Kazakh National University, Almaty, Kazakhstan

<sup>2</sup>Institute of Theoretical Physics, University of Wrocław, Wrocław, Poland

<sup>3</sup>Helmholtzzentrum Dresden-Rossendorf (HZDR), Dresden, Germany

<sup>4</sup>Center for Advanced Systems UnderStanding (CASUS), Görlitz, Germany

\*e-mail: b.kasymkhan@gmail.com

Wave processes propagating in a medium of collisional and viscous quark-gluon plasma (QGP) are comprehensively analyzed in the paper. To investigate various optical properties of the medium, the longitudinal and transverse dielectric functions of the quark-gluon plasma are taken to study. The calculations of perturbations in these dielectric functions facilitate the derivation of dispersion relations for wave propagation within such media. Through extensive further analysis, the phase and group velocities were calculated for the considered models. The resulting graphs for phase and group velocity distinctly illustrate the dissipative properties inherent in the medium, revealing how these properties influence the propagation speed of both the wave phase and the wave packet of environmental disturbances. This article provides an in-depth analysis of the obtained results, discussing the possible behavior of waves across different models of quark-gluon plasma media. The study concludes by highlighting the achievements and contributions of this research, emphasizing its importance in advancing the understanding of wave dynamics in such extreme states of matter.

**Key words:** quark-gluon plasma, dielectric function, phase and group velocity, waves in plasma.

**PACS number(s):** - 12.38.Mh.

### 1 Introduction

The quark-gluon plasma (QGP) is a special state of matter under extreme conditions, which is formed at high temperatures and energy densities [1]. Such conditions occur naturally in the cores of massive celestial bodies [2], as well as in the early stages of the development of the Universe [3]. Moreover, such a state of matter under controlled parameters can be obtained in particle collision experiments at ultra-relativistic velocities. Such experiments are carried out at the SPS (Super Proton Synchrotron) [4], LHC (Large Hadron Collider) and RHIC [5] (Relativistic Heavy-Ion Collider).

At high energy densities, hadronic matter ceases to exist and decays into its constituent quarks and gluons. Moreover, quarks and gluons are in unbound states, which is not observed in the normal state of matter – this is the well-known phenomenon of confinement [6]. To summarize the above, the QGP is a state of matter in which free quarks and gluons are in quasi-neutral and thermodynamic equilibrium state. For a more detailed description of the QGP, the

following characteristic parameters of this state of matter can be given. When hadronic matter is compressed to high densities of the order of  $\sim 1 \text{ fm}^{-3}$  and heated to high temperatures exceeding the Hagedorn temperature [7], a transition to the QGP occurs at the pseudocritical temperature  $T_c = 156,5 \pm 1,5 \text{ MeV}$ , as shown in lattice QCD simulations [8]. It is believed that such parameters occur naturally in the state of matter in the early Universe, which lasts  $10^{-5}$  seconds after the Big Bang. [9-11]

Thus, it makes sense to study collective effects to determine the basic properties of this new state of matter. Such properties can be various static, dynamic, thermodynamic and optical properties. For this paper, optical properties were chosen to study collective effects. The problem of wave propagation in a medium determines the dispersion properties of the medium, which demonstrates the relationship between wave energy and momentum.

To characterize the medium in simulation, two QGP models are used. The first model is described by the Boltzmann equation [12-14], where the

distribution function is the probability of finding fermions with two charge values and two spin values. And the interaction between particles is described by the BGK collision integral [15]. The second model is described by the relativistic hydrodynamic equation, where collisions between particles are not taken into account, but the viscosity of the medium is taken into account as a parameter for the loss of wave energy [16-18].

By defining a model of the medium, it is possible to obtain wave dispersion equations, which are used to determine the phase and group velocities of the wave in the medium. The dispersion relations were obtained in the previous work of the authors of the article [19-21]. Thus, this article is a natural continuation of a larger research topic.

This article consists of the introduction presented in this chapter. The next chapter describes the theoretical foundations of the article and the problem statement. Below are the results of solving the problem, as well as a discussion of the results obtained. In the final chapter, the conclusions of this work are presented.

## 2 Phase velocity

In the previous chapter, two mathematical models for describing QGP were presented. The first model was usually called the collisional QGP model, since in this description the interaction between particles is described using the frequency of particle collisions. The second model was commonly called the viscous QGP model, since collisions between particles are not taken into account here, and the nonideality parameter of the system is calculated taking into account viscosity. A more detailed description of these models is available in [19-21], where the dielectric function is used to formulate the models as an expression for describing the medium. From the course of classical physics, it is known that the dielectric function describes changes in the external field inside the system, that is, it determines the properties of the system by changing the external field. Thus, by studying the properties of the dielectric function, one can find out the properties of the medium itself. Next, by equating the dielectric function to zero, the perturbations of the system are found that describe the wave dispersion in the QGP medium. Once the dispersion relation is obtained, the phase and group velocities can be calculated. In general, phase and group velocities depend on the energy and momentum of the wave, and the

properties of the medium (temperature, density, etc.). Based on this, from the values of phase velocities for various media, one can find out the properties of quarks and gluons.

To calculate these velocities, let's first define them in this part. By analogy with classical physics, the phase velocity of a wave is the speed at which the wave phase moves in space without changing the shape of the wave itself.

The phase velocity in a QGP can be significantly different compared to the phase velocity in other media due to the properties of the quarks and gluons that form this plasma.

The group velocity of a wave determines the velocity of propagation of a wave packet, the peak or front of a group of waves. Group velocity is an important property of the medium, which determines the propagation of energy and information. Therefore, studying the group velocity of waves in a QGP demonstrates how quickly disturbances propagate in this medium.

In this part of the article, we will present analytic expressions for phase and group velocity. To do this, we introduce a general expression for a plane wave:

$$\Psi = \Psi_0 \exp i(\omega t - kx - \phi_0). \quad (1)$$

Here,  $\Psi_0$  – amplitude of oscillations,  $\omega$  – frequency of collisions,  $k$  – wave number,  $\phi_0$  – initial phase of oscillations. Moreover,  $\phi(x, t) = \omega t - kx - \phi_0$  – is phase of wave. It means, it is possible to study the dependence of the change in the phase of wave oscillation over time. By definition, phase velocity is the speed at which a point of constant phase propagates

$$\frac{d\phi}{dt} = 0 = \omega - k \frac{dx}{dt} - 0. \quad (2)$$

$$\frac{dx}{dt} = \frac{\omega}{k} = v_p. \quad (3)$$

Using expression (3) one can determine the phase velocity; for this you need to find the ratio of the oscillation frequency and the wave vector.

## 3 Group velocity

Since phase velocity is formulated, let's introduce group velocity derivation. In an ideal homogeneous medium without wave attenuation (in vacuum), the phase and group velocities are equal.

However, in a real problem there is always wave attenuation due to the imperfection of the medium. That is, the plane wave equation can be modulated. In the following example, we will consider these modulations, which describe the difference between group and phase velocities. For the oscillation frequency we will write  $\omega_0 + d\omega$ , and for the wave vector we will write  $k_0 + dk$ . Next, consider the addition of two waves with a small change in modulation

$$\Psi = \exp i[(\omega_0 - d\omega)t - (k_0 - dk)x] + \exp i[(\omega_0 + d\omega)t - (k_0 + dk)x]. \quad (4)$$

After simple algebraic operations, expression (4) is reduced to the following form

$$\Psi = \exp i(\omega_0 t - k_0 x) \cos(d\omega t + dk x). \quad (5)$$

In this expression, the exponential part describes high-frequency oscillations that propagate at the carrier speed or phase velocity  $v_p = \omega/k$ . And the second term of the multiplication, cosine, describes the modulations, which can be equated to zero and the group velocity of the modulations can be found.

$$d\omega t + dk x = 0 \rightarrow v_g = \frac{d\omega}{dk} = \frac{x}{t}. \quad (6)$$

From the previous expression it follows that to find the group velocity it is necessary to find the

derivative of the oscillation frequency with respect to the wave vector. To summarize this chapter, to find the phase and group velocity, one needs to know the wave vector and oscillation frequency, the values of which are determined due to the dispersion relation of the wave.

#### 4 Results

In this part of the paper the plots of the phase and group velocity are presented. Those results were calculated according to the procedure described in the previous part of the paper [19-21].

Fig-1 shows the phase velocity values  $v_p$  over the wave number  $k$  of a collisional QGP. The values of the wave number were normalized with the plasma frequency  $\omega_p$ . Since, natural units are used in high-energy physics, the wave number and the plasma frequency have the dimension of energy, so phase and group velocities as well as wave number are dimensionless quantities. Fig-1-a) presents the absolute values of phase velocity for different collision frequencies, and Fig-1-b) presents the comparison of the different oscillation modes to the HTL approximation mode. This can be formulated in the following as  $\Delta\tilde{v}_p(v) = \frac{[v_p(v) - v_p(HTL)]}{v_p(HTL)}$ . This formula says that the difference of various oscillation modes and HTL approximation mode is divided by the HTL approximation mode. This structure of figures will be used for the next three figures as well.

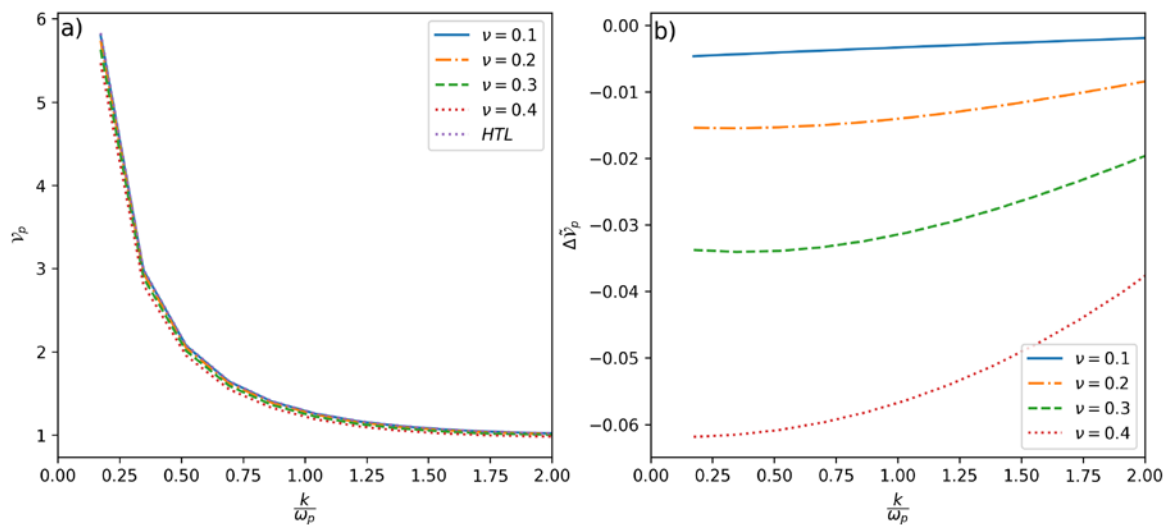


**Figure 1** – Phase velocity of collisional QGP: a) values of phase velocity  $v_p$ , b) comparison of different modes



In fig-1 and fig-2 collision oscillations were chosen to be small in comparison to oscillation frequency, because propagation waves have to have small damping coefficients.

Fig-2 describes the behavior of group velocity due to wave number in the collisional QGP; the left-hand side plot shows the absolute values and the right-hand side the difference of different oscillating modes. On the other hand, Fig-3 and fig-4 demonstrates the same results for the viscous QGP. For the viscous QGP the values of the free parameter of the model are chosen from the experiments. As it has been written before, the zero value of the viscosity is the same as HTL approximation limit. The value  $1/4\pi$  is taken from the theoretical predictions of the smallest viscosity of QGP [22]. The next three is taken from the analysis of results of the experiments, they are listed in accordance with order of the plots. [23-25]

Fig-1-b) shows that the oscillation modes are more different for the small wave number and come closer to each other at higher wave number. One can guess that for even higher wave numbers the different

modes will be the same, but the lack of computation power did not allow to calculate further. Moreover, those ranges of wave number are not feasible to analyze in current experimental setups.

Fig-2-b) shows an interesting behavior for the group velocity of collisional QGP. This plot has several points, where different modes have the same group velocity, and they differ more for small wave number and for high wave number.

Fig-3-b) has more predictable behavior with comparison to the fig-2-b). In this plot, phase velocity has the same value for the wave number equals to zero, and the difference grows with increasing wave number. At some point it reaches the extremum point and the difference gets smaller again. And again, one could say that the trend goes to the same point, but the calculation did not support such high values of wave number.

Fig-4-b) presents the comparison of group velocity of viscous QGP, and it shows predictable behavior of difference between various modes. At the small wave number, the difference is the greatest, and it becomes equal at the large wave numbers.

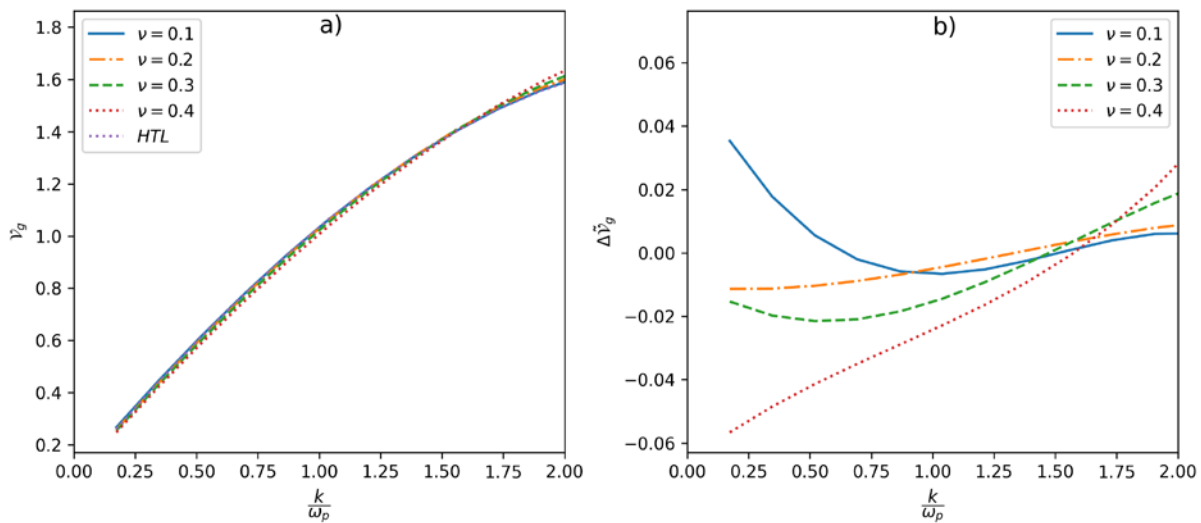
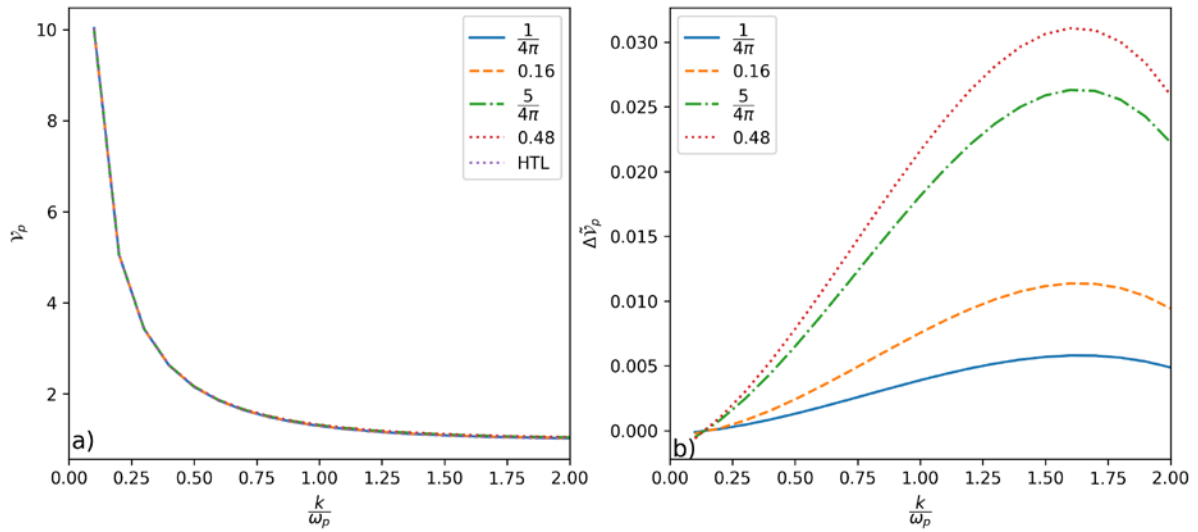
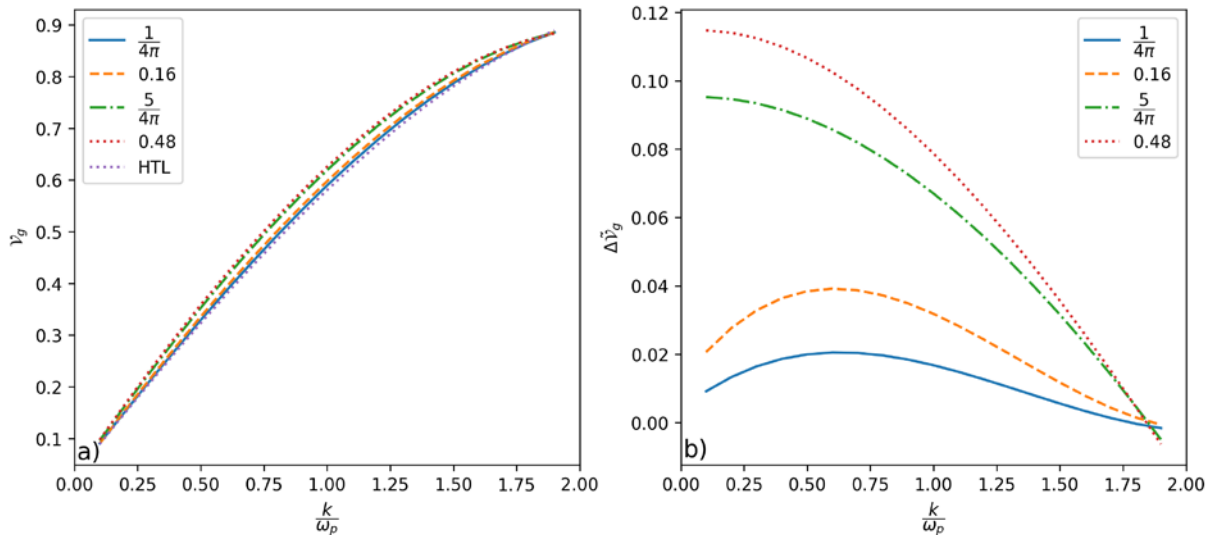


Figure 2 – Group velocity of collisional QGP: a) values of group velocity  $v_g$ , b) comparison of different modes



**Figure 3** – Phase velocity of viscous QGP: a) values of phase velocity  $v_p$ , b) comparison of different modes



**Figure 4** – Group velocity of viscous QGP: a) values of group velocity  $v_g$ , b) comparison of different modes

### 5 Conclusions

The study of phase and group velocities of waves in a quark-gluon plasma medium is an interesting area of research in modern high-energy physics. These parameters may play a key role in understanding the properties of this exotic form of matter and its behavior under extreme conditions of temperature and density. For these reasons we have calculated phase and group velocity for QGP in different models. We have compared these two

models with the HTL approximation in order to show the correspondence with other studies of wave propagation in media of QGP. That is why this article can be understood as the part of bigger studies of QGP matter. The chosen mathematical models have limitations in derivation of the dielectric function in order to get analytical results. Those limitations can be found in the original papers and those constraints apply for these results as well. However, the postulated goals of this article can be achieved in the scope of those limitations, because the existence of

the wave propagation and the difference of the phase and group velocities in two models were demonstrated. With this, the article concludes with the positive results. The presented results might be used to describe properties of the media of QGP.

### Acknowledgement

We express our gratitude to Academician of the National Academy of Sciences of the Republic of

Kazakhstan T.S. Ramazanov for valuable advice and comments during the research and revision of this article.

The work was carried out within the framework of Grant BR18574080 under the title “Research of fundamental and applied problems of plasma physics, plasma-like media for the purpose of solving problems of modern energy and obtaining new functional materials” of the Ministry of Science and Higher Education of the Republic of Kazakhstan.

### References

1. Bartke J. Introduction to Relativistic Heavy Ion Physics // World Scientific Publishing. – 2009. – P. 1-5.
2. Bauswein A., Blaschke D., and Fischer T., Effects of a strong phase transition on supernova explosions, compact stars and their mergers, in: *Astrophysics in the XXI Century with Compact Stars*, Ed. by: Vasconcellos C. A. Z., Weber F. // World Scientific Publishing. – 2023. – P. 283-320. [https://doi.org/10.1142/9789811220944\\_0008](https://doi.org/10.1142/9789811220944_0008)
3. Ellis J. From little bangs to big bangs // *J. Phys.: Conf. Ser.* – 2005. – Vol. 50, No. 8, P. 8-21. <https://doi.org/10.1088/1742-6596/50/1/002>
4. Heinz U., Jacob M. Evidence for a New State of Matter: An Assessment of the Results from the CERN Lead Beam Programme, 2000. <https://doi.org/10.48550/arXiv.nucl-th/0002042>
5. Niida T., Miake Y. Signatures of QGP at RHIC and the LHC // *AAPPS Bulletin.* – 2021. – Vol. 31, No. 12. <https://doi.org/10.1007/s43673-021-00014-3>
6. Greensite J. An introduction to the confinement problem // *Lecture Notes in Physics.* – 2011. – Vol. 821, P. 21-34. <https://doi.org/10.1007/978-3-642-14382-3>
7. Hagedorn R. Statistical thermodynamics of strong interactions at high energies // *Supplemento al Nuovo Cimento*, 1965. – P. 146-187.
8. Bazavov A., et al. (HotQCD Collaboration), Chiral crossover in QCD at zero and nonzero chemical potentials // *Phys. Lett. B.* – 2019. – Vol. 795, P. 15-21. <https://doi.org/10.1016/j.physletb.2019.05.013>
9. Rafelski J. Melting hadrons, boiling quarks // *Eur. Phys. J. A.* – 2015. – Vol. 51, No. 9, P. 87-92. <https://doi.org/10.1140/epja/i2015-15115-y>
10. Weldon H.A. Covariant calculations at finite temperature: The relativistic plasma // *Phys. Rev. D.* – 1982. – Vol. 26, No. 6, P. 1394-1407. <https://doi.org/10.1103/PhysRevD.26.1394>
11. Elze H.-Th., Heinz U. Quark-gluon transport theory // *Phys. Rep.* – 1989. – Vol. 183, No. 3, P. 81-135. [https://doi.org/10.1016/0370-1573\(89\)90059-8](https://doi.org/10.1016/0370-1573(89)90059-8)
12. Carrington M. E., Fugleberg T., Pickering D., Thoma M. H. Dielectric functions and dispersion relations of ultrarelativistic plasmas with collisions // *Can. J. Phys.* – 2004. – Vol. 82, No. 9, P. 671-678. <https://doi.org/10.1139/p04-035>
13. Chakraborty P., Mustafa M.G. Wakes in quark-gluon plasma // *Phys. Rev. D*– 2006. – Vol. 74, No. 9, P. 094002. <https://doi.org/10.1103/PhysRevD.74.094002>
14. Chakraborty P., Mustafa M.G., Ray R. Wakes in a collisional quark-gluon plasma // *J. Phys. G*– 2007. – Vol. 34, No. 10, P. 2141-2152. <https://doi.org/10.1088/0954-3899/34/10/004>
15. Bhatnagar P., Gross E., Krook M. A Model for Collision Processes in Gases. I. Small Amplitude Processes in Charged and Neutral One-Component Systems // *Phys. Rev.* – 1954. – Vol. 94, No. 3, P. 511-525. <https://doi.org/10.1103/PhysRev.94.511>
16. Bing-feng Jiang and Jia-rong Li. The dielectric function of the viscous quark-gluon plasma // *Nucl. Phys. A.* – 2010. – Vol. 847, No. 3, P. 268-282. <https://doi.org/10.1016/j.nuclphysa.2010.07.008>
17. Bing-feng Jiang, De-fu Hou, and Jia-rong Li. Polarization energy loss in hot of the viscous quark-gluon plasma // *J. Phys. G: Nucl. Part. Phys.* – 2015. – Vol. 42, No. 8, P. 085107. <https://doi.org/10.1088/0954-3899/42/8/085107>
18. Bing-feng Jiang, Shao-wu Shi, De-fu Hou, and Jia-rong Li. Color electric conductivity in a viscous quark-gluon plasma // *Chines Phys. C.* – 2021. – Vol. 45, No. 5, P. 054106. <https://doi.org/10.1088/1674-1137/abe9a2>
19. Baiseitov K., Moldabekov Z.A., Blaschke D., Djienbekov N., Ramazanov T.S. Surface Waves in a Collisional Quark-Gluon Plasma // *Physics of Particles and Nuclei Letters.* – 2020. – Vol. 17, No. 1. – P. 803-808. <https://doi.org/10.1134/S1547477120060035>
20. Baiseitov K. Dielectric function of quark-gluon plasma (in Russian: Диэлектрическая функция кварк-глюонной плазмы) // *Bulletin of NAS RK.* – 2021. – Vol. 4, No. 338, P. 15-24. <https://journals.nauka-nanrk.kz/physics-mathematics/article/view/2705>
21. Baiseitov K., Blaschke D., Ramazanov T. S. Collective bulk excitations in the QGP: From the weakly non-ideal case to the strong correlation limit // *CPP.* – 2023. – Vol. 63, No. 9-10. <https://doi.org/10.1002/ctpp.202300015>
22. Policastro G., Son D.T., Starinets A.O. Shear Viscosity of Strongly Coupled  $N=4$  Supersymmetric Yang-Mills Plasma // *Phys. Rev. Lett.* – 2001. – Vol. 87, No. 8, P. 081601. <https://doi.org/10.1103/PhysRevLett.87.081601>
23. Romatschke P., Romatschke U. Viscosity Information from Relativistic Nuclear Collisions: How Perfect is the Fluid Observed at RHIC? // *Phys. Rev. Lett.* – 2007. – Vol. 99, No. 17, P. 172301. <https://doi.org/10.1103/PhysRevLett.99.172301>

24. Song H., Heinz U. Extracting the QGP viscosity from RHIC data—a status report from viscous hydrodynamics // Journal of Physics G: Nuclear and Particle Physics. – 2009. – Vol. 36, No. 6, P. 064033 <https://doi.org/10.1088/0954-3899/36/6/064033>
25. Arnold P., Moore G.D., Yaffe L.G. Transport coefficients in high temperature gauge theories, 2. Beyond leading log // Journal of High Energy Physics. – 2003. – Vol. 2003, No. 05, P. 051. <https://doi.org/10.1088/1126-6708/2003/05/051>

**Information about authors:**

*Baiseitov Kassymkhan Mukhtaruly (corresponding author) – researcher at the Al-Farabi Kazakh National University. (Almaty, Kazakhstan) e-mail: b.kasymkhan@gmail.com*

*Blaschke David – professor at the Institute of theoretical physics, University of Wrocław. (Wrocław, Poland) e-mail: david.blaschke@gmail.com*

*Kuanyshbaiuly Yernur (corresponding author) – researcher at the Al-Farabi Kazakh National University. (Almaty, Kazakhstan) e-mail: ernursan@gmail.com*

---

## CONTENTS

SCOPE AND AIM .....	3
M.O. Tursunov, Kh.M. Iliyev, B.K. Ismaylov High-temperature analysis of silicon properties with manganese-oxygen binary complexes .....	4
Z.T. Kenzhaev, Kh.M. Iliyev, K.A. Ismailov, G.Kh. Mavlonov, S.V. Koveshnikov, B.K. Ismaylov, S.B. Isamov Physical mechanisms of gettering properties of nickel clusters in Silicon Solar Cells .....	13
I.E. Kenzhina, A.L. Kozlovskiy, P. Blynskiy, A.U. Tolenova Effect of dislocation density-associated strengthening factors on the thermal stability of composite ceramics .....	23
Zh.T. Nakysbekov, D. Ismailov, S. Bellucci, T.A. Tukhfatullin, O.V. Bogdanov, B.A. Tronin, K.N. Turmanova, S.G. Suyundykova, V.F. Grichshenko, M.I. Pshikov, A.Ye. Alzhanova Concise review of recent advances and applications of the electron linear accelerator ELU-4 in scientific and technical fields.....	32
D.A. Turlykozhaeva, W. Waldemar, A.B. Akhmetali, N.M. Ussipov, S.A. Temesheva, S.N. Akhtanov Single Gateway Placement in Wireless Mesh Networks .....	43
Zh.U. Paltusheva, Y.Y. Kedruk, L.V. Gritsenko, M.A. Tulegenova, V. Syritski, Kh.A. Abdullin The influence of synthesis parameters and thermal treatment on the optical and structural properties of zinc oxide-based nanomaterials.....	49
K. Akatan, A.K. Battalova, N.N. Sagiyeva, S.K. Kabdrakhmanova, N. Kaiyrbekov, A. Tursyngazykyzy, E. Shaimardan, M.M. Beisebekov, G.A. Kampitova Oxidized Starch/CMC based Biofilm: Synthesis and Characterization.....	58
S. Bolegenova, A. Askarova, Sh. Ospanova, S. Zhumagaliyeva, A. Makanova, A. Aldiyarova, A. Nurmukhanova, G. Idrissova Technology of reducing greenhouse gas emissions for decarbonization and decreasing anthropogenic pressure on the environment .....	64
Zivile Rutkuniene LES modeling gas particle dispersion and thermal characteristics in a reacting turbulent low .....	76
A.A. Solodovnik, R.O. Zyryanov, P.I. Leontyev, B.M. Useinov, E.G. Gololobova, P.L. Zhuravlev Experience of noctilucent clouds registering in the near infrared spectrum region .....	85
S.A. Maiorov, R.I. Golyatina Analytical formula for multiple ionization cross sections of rare gas atoms by electron and positron impact.....	94
K. Baiseitov, D. Blaschke, and Ye. Kuanyshbaiuly Phase and group velocities of waves in medium of Quark-gluon plasma .....	102